vorgelegt von

M.Sc. Matteo Chamchoum
ORCID: 0000-0001-7606-8165

Technische Universität Berlin

---

an der Fakultät II - Mathematik und Naturwissenschaften der Technischen Universität Berlin zur Erlangung des akademischen Grades Doktor der Naturwissenschaften Dr.rer.nat. vorgelegte Dissertation

Characterization of the nanoscale structure and the dynamics of polyelectrolyte complexes via neutron scattering

Promotionsausschuss:

Vorsitzender: Prof. Dr. Arne Thomas

Gutachter: Prof. Dr. Michael Gradzielski, Prof. Dr. Matthias Karg

Tag der wissenschaftlichen Aussprache: 4. Dezember 2025

Berlin 2024

Contents

List of Figures

List of Tables

List of Abbreviations

CAC	Critical Aggregation Concentration
CONTIN	Algorithm for analyzing relaxation rate distributions
D_2O	Heavy Water
DHBC	Double Hydrophilic Block Copolymer
DLS	Dynamic Light Scattering
GPC	Gel Permeation Chromatography
$g^{(2)}(\tau)$	Intensity autocorrelation function
$\Gamma(q)$	Width of the Lorentzian in neutron spectra
HM	Hydrophobic Modification
HM-length	Length of the hydrophobic moieties (from NMR)
HM-%	Percentage of hydrophobic modifications (from NMR)
IDP	Intrinsically Disordered Protein
IPEC	Interpolyelectrolyte Complex
LLPS	Liquid-Liquid Phase Separation
MCU	Molecular Weight per Unit Charge

MW	Molecular Weight (average, from NMR)
MW/charge	Molecular Weight per charged group
NaCl	Sodium Chloride
NBS	Neutron Backscattering
NMR	Nuclear Magnetic Resonance
NSE	Neutron Spin Echo
PDMAEMA	Poly(2-(dimethylamino)ethyl methacrylate)
PE	Polyelectrolyte
PEO-PMAA	Poly(ethylene oxide)-b-poly(methacrylic acid)
PDI	Polydispersity Index
QENS	Quasi Elastic Neutron Scattering
R_{g}	Radius of Gyration
SANS	Small Angle Neutron Scattering
SLS	Static Light Scattering
TOF	Time-of-Flight
U_{soft} / U_{LJ}	Interaction potentials used in computational models
z^*	Mixing ratio (ratio between negative and positive charges)

Abstract

Two oppositely charged polyelectrolytes mixed together form aggregates known as interpolyelectrolyte complexes (IPECs). These complexes are sensitive to environmental variables (e.g., pressure, pH, salt concentration) and to the architecture of the polymers. This dissertation investigates mixtures of hydrophobically modified polyelectrolytes and double-hydrophilic block copolymers. Various types and degrees of hydrophobic modifications were explored, as well as the effect of mixing ratio between the oppositely charged species.

The nanoscale structure and dynamics of this model system were studied using several techniques. Most polymers were synthesized in-house and characterized by nuclear magnetic resonance, gel permeation chromatography, and titration. The resulting IPECs were then investigated via static light scattering (SLS), small-angle neutron scattering (SANS), and cryogenic transmission electron microscopy (cryo-TEM). The resulting aggregates exhibited hierarchical morphologies. At small scales, all aggregates displayed polymeric features. A characteristic size of the aggregates of $\simeq$ 17 nm emerged around the equimolar regime, along with a non-trivial evolution in volume fraction and morphology between spheres and vesicles.

Dynamics were probed through dynamic light scattering (DLS), neutron spin echo (NSE), and neutron backscattering (NBS). The data revealed polymeric dynamics suppressed by aggregation, long-range correlation fluctuations prominent away from equimolarity, and hydrogen hopping on methyl groups at short length scales.

Zusammenfassung

Zwei entgegengesetzt geladene Polyelektrolyte bilden bei Mischung Aggregate, die als interpolyelektrolytische Komplexe (IPECs) bekannt sind. Diese Komplexe reagieren empfindlich auf Umgebungsparameter wie Druck, pH-Wert und Salzkonzentration sowie auf die Architektur der Polymere. In dieser Dissertation werden Mischungen aus hydrophob modifizierten Polyelektrolyten und doppelt-hydrophilen "Block-Copolymeren" untersucht. Verschiedene Arten und Grade der hydrophoben Modifikationen sowie das Mischungsverhältnis der entgegengesetzt geladenen Komponenten wurden systematisch analysiert.

Die nanostrukturellen Eigenschaften und die Dynamik dieses Modellsystems wurden mit verschiedenen Methoden untersucht. Die meisten Polymere wurden in unserer Arbeitsgruppe synthetisiert und mittels Kernspinresonanzspektroskopie, Gel-Permeations-Chromatographie und Titration charakterisiert. Die resultierenden IPECs wurden anschließend durch statische Lichtstreuung (SLS), Kleinwinkel-Neutronenstreuung (SANS) und Kryoelektronenmikroskopie (Cryo-TEM) analysiert. Die Aggregate zeigten hierarchische Morphologien. Im kleinen Längenbereich wiesen alle Aggregate polymerartige Eigenschaften auf, um den äquimolaren Bereich herum trat eine charakteristische Größe von $\simeq 17$ nm auf, sowie einer nicht-trivialen Entwicklung der Volumenfraktion und Morphologie zwischen Vesikeln und sphärischen Strukturen.

Die Dynamik wurde durch dynamische Lichtstreuung (DLS), Neutronen-Spin-Echo (NSE) und Neutronen-Rückstreuungsspektroskopie (NBS) untersucht. Die Daten zeigten eine durch Aggregation unterdrückte polymerartige Dynamik, weitreichende Korrelationsfluktuationen vor allem fern vom Äquimolaritätsbereich sowie Wasserstoffsprünge an

Methylgruppen auf kurzen Längenskalen.

Publications

The work presented in Chapter 3 and 4 has been published in *Macromolecules*,[16] while the results discussed in Chapter 5 were under peer review during the production of the thesis and have now been published.[17]

Acknowledgements

First, I would like to thank my supervisors, Dr. Orsolya Czakkel, Dr. Sylvain Prevost, and Prof. Dr. Michael Gradzielski, for their guidance and supervision throughout the entire project.

I am also grateful to Tilo Seydel for his help with the backscattering part of the project.

I am also grateful to the Institut Laue-Langevin and the Technische Universität Berlin for their continuous support and for providing the resources necessary to carry out this project.

I acknowledge the support of the Australian Centre for Neutron Scattering (ANSTO) and the Australian Government through the National Collaborative Research Infrastructure Strategy, which enabled part of the neutron research performed in this work. I also acknowledge the Soft Condensed Matter (PSCM) group at the Institut Laue-Langevin, as well as the University of Potsdam for the gel permeation chromatography measurements of the polyelectrolytes. I am further thankful to Ralf Biehl for the use of Jscatter.

I would like to thank my colleagues from both the Institut Laue-Langevin and Technische Universität Berlin for their insightful discussions and for the practical support provided throughout the project.

Finally, I would like to thank all those who supported me, both academically and personally, during this journey.

Chapter 1

Introduction

1.1 Polyelectrolytes

1.1.1 Pure Polyelectrolytes

The topic of polyelectrolytes (PEs) covers different aspects of mankind: DNA, the macromolecule in which the information of life is contained, is itself a PE. Moreover, PEs are exploited in drug delivery, water treatment and cosmetics [18, 19, 20, 21, 22, 23]. Their electrostatic nature allows PEs to form self-assembled structures at many different phases, from solid to liquid, depending on the environmental variables such as salt concentration, pH and temperature, but also the architecture of the macromolecule, since these polymeric structures are highly customizable [9, 4].

In the simplest architecture a PE is a chain of a fundamental unit of a single molecular group called a monomer. The monomer has a functional group that can be charged in particular conditions. To characterize the dissociation equilibrium, the monomer can be considered as an acid A and define the dissociation constant of the chemical reaction: [24]

$$HA \rightleftharpoons A^- + H^+ \tag{1.1}$$

Where HA is the acid and A^- is the conjugate base. From this equilibrium, one can calculate the dissociation constant as:

$$K_a = \frac{[A^-][H^+]}{[HA]} \tag{1.2}$$

where the square brackets represent the molar concentration. In reality, it is challenging to characterize this equilibrium, due to the various features PEs exhibits and the complex environmental conditions (such as salt addition, counterion condensation and the effect of chain connectivity). [25]

Classification Criterion	Categories / Examples
Based on the origin	Natural (e.g., proteins); Semi-natural (processed from natural components); Synthetic (e.g., all PEs studied in this dissertation)
Based on the charge	Polyanions (negatively charged); Polycations (positively charged); Polyampholytes (carry both negative and positive charges)
Based on the charge density	Strong PEs: very low pK_a (or high pK_b); Weak PEs: pH-dependent charge state (usually, the dissociation constant is in between 2 and 10)
Based on the shape	Rod-like; Globular; No defined shape (e.g., intrinsically disordered proteins)
Based on the position of the ion site	Linear PEs: ion site along the backbone; Branched PEs: dislocated ion site
Based on the composition	Homopolymers: same repeating subunit; Copolymers: different repeating subunits

Table 1.1: Classification criteria for polyelectrolytes. Adapted from [15].

Polyelectrolyte are usually called with a nomenclature based on different types of classifications, reported in table 1.1. In my project, I investigated PE dissolved in aqueous solutions. The concentration plays a crucial role in the forming structures and the dynamics of these molecules. Fig. 1.1

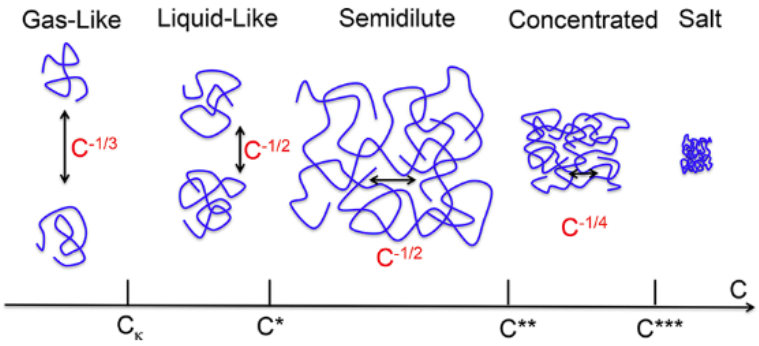

Figure 1.1: Different conformations of the polyelectrolyte chains depending on different concentrations of the solution. Taken from [1].

The investigations were performed at a concentration between 0.1 and 3% and with low salt concentration (10 mM): in this range, we observed the molecules in their "liquid like" state, where the polymer coils interact and correlations between concentration fluctuations are visible, but we expect not to see any entanglement effects. These PE solutions have been widely investigated and I report here the main considerations for the sake of clarity in the discussion. [1, 26]

The electrostatic nature of polyelectrolytes leads to many effects on their conformations and the energetics of these macromolecules is non-trivial.

The energetic of a PE is governed by the ratio of the electrostatic interactions $U_{el}(r)$ between a charged monomer and its counterion at a distance r and the thermal energy of the system:

$$\frac{U_{el}(r)}{k_B T} = z_p z_i \frac{e^2}{4\pi\epsilon_0\epsilon k_B T}\frac{\exp(-kr)}{r} \tag{1.3}$$

$$k^2 = \frac{e^2}{\epsilon_0\epsilon k_B T}\sum_i z_i^2 n_i \tag{1.4}$$

Where z_p,z_i are the valencies of the monomer and the counterion respectively, e is the elementary charge, $k_B T$ is the Boltzmann constant multiplied by the absolute temperature, ϵ_0 is the permittivity of vacuum and ϵ is the dielectric constant of the

medium. The exponential factor is a screening due to the charged environment: the summation runs over the charge species and n_i is the number density. k can be related to an inverse squared length, called the *Debye length*. For monovalent salts in water at T=298 K, the Debye length is $\xi_D \simeq 0.3/\sqrt{c_s}$ nm, where c_s is the salt concentration.

We can recognize that the factor:

$$l_B \stackrel{\text{def}}{=} \frac{e^2}{4\pi\epsilon_0\epsilon k_B T} \tag{1.5}$$

has the dimension of a length, called the *Bjerrum length*. If $l_B > r$, the electrostatic interactions are stronger than the thermal fluctuation and we consider the counterion condensed. Viceversa, if $l_B < r$, the ion is considered dissociated. For aqueous solutions at T=298 K, the Bjerrum length is $l_B \simeq 0.7$ nm.

When the ion pairing occurs, a temporary dipole is formed along the backbone. More dipoles can interact and this dipole-dipole interaction can be quite strong at short distance ($-10k_BT$ for a distance of 0.25nm). This can result in non-uniform charge density distributions along the PE and interactions between two similarly charged PEs.

Another effect studied by de Gennes, is the electrostatic interaction between interchains, leading to a correlation hole visible in the structure factor. [27] This correlation length in semidilute polyelectrolyte solution free of salt scales as $\xi_c \propto C^{-1/2}$.

Polymer dynamics

The internal dynamics of polyelectrolytes is of essential importance for their understanding. As discussed before, polyelectrolytes are rigid polymers and they preserve a similar dynamical behavior, where the electrostatic environment plays a role on the stiffness of the polymer.

One of the most important attempts to model the polymer dynamics is the well-known **Rouse model**. [28] This model starts from the hypothesis that a polymer can be modelled as a collection of n beads with a diameter b connected by $n-1$ harmonic springs, as depicted in fig. 1.2.

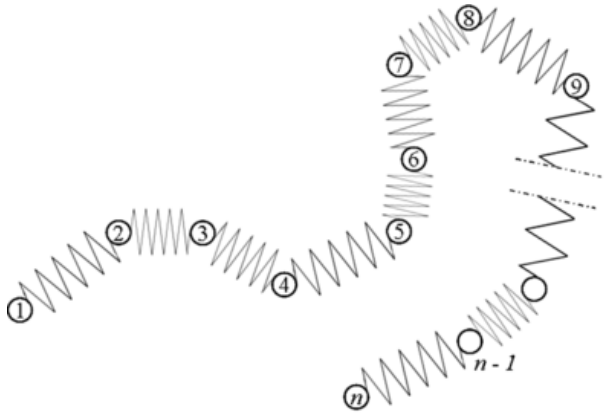

Figure 1.2: Representation of the bead-spring model, taken from [2]. The n beads are labelled.

One can then write the equation of the Brownian motion of the bead position $\mathbf{r_i(t)}$, which is ultimately the Langevin equation.

$$\frac{d\mathbf{r}_i(t)}{dt} = -\frac{1}{\zeta}\frac{\partial U}{\partial \mathbf{r}_i} + \mathbf{g}_i(t) \tag{1.6}$$

Where ζ is the friction of the bead in the solvent and $\mathbf{g_i(t)}$ is a random function which takes into account the fluctuations in velocity given by a Brownian motion. The potential U is the potential of all the springs of the polymer:

$$U = \frac{1}{2}k\sum_{i=1}^{n}(\mathbf{r}_i - \mathbf{r}_{i-1})^2 \tag{1.7}$$

With k being the spring constant. The entire derivation can be found somewhere else [29]. Inserting the potential from eq. 1.7 in the eq. 1.6, one obtain the time evolution of the beads of the polymer and the main dynamical features, such as the motion of the center of mass and the rotational characteristic time.

Although the Rouse model is a good description of concentrated unentangled polymer system, it fails to represent dilute solutions. Particularly, there is a discrepancy between the diffusion constant and the rotational time dependency from the molecular weight of the polymer. This discrepancy arises from the hypothesis that the motion of beads is independent. In reality, while an i_{th} bead is moving, the surrounding solution moves

with it and the neighboring beads experience a drag force referred to as *hydrodynamic interactions*. A new model was developed taking this interaction into account, called **Zimm model**. [30]

This model introduces the hydrodynamic interactions in a linear approximation as a tensor that describes the mobility of particle i, denoted as Him, so that the Langevin equation described in eq. 1.6 is modified as:

$$\frac{d\mathbf{r}_i(t)}{dt} = -\sum_m H_{im} \cdot \frac{\partial U}{\partial \mathbf{r}_i} + \mathbf{g}_i(t) \tag{1.8}$$

H_{im} is the hydrodynamic function of the system which depends on the position of all the particles. By introducing the potential specified in eq. 1.7, the Langevin equation becomes:

$$\frac{d\mathbf{r}_i(t)}{dt} = -\sum_m H_{im} \cdot (\mathbf{r}_{i+1}(t) + \mathbf{r}_{i-1}(t) - 2\mathbf{r}_i(t)) + \mathbf{g}_i(t) \tag{1.9}$$

This non-linear equation was even further simplified by replacing H_{im} with its equilibrium average value. Within these assumptions then, the equation of motion can be solved and one can extract the rotational relaxation time τ and the diffusion coefficient of the center of mass D of the bead spring chain. In the case of a Θ solvent, which is a solvent where the polymer assumes an ideal chain conformation, these quantities are:

$$D = \frac{0.196 k_B T}{\eta_s \sqrt{n} b} \tag{1.10}$$

$$\tau = 0.325 \frac{\eta_s (\sqrt{n} b)^3}{k_B T} \tag{1.11}$$

with η_s being the viscosity of the solvent. This model corrects the wrong dependencies of the Rouse model on the molecular weight for dilute polymer solutions.

While the Zimm model provides a good theoretical description of single-chain dynamics in many polyelectrolyte systems, experimental investigations often reveal a more complex scenario. For instance, Dynamic Light Scattering (DLS) studies have shown

that polyelectrolytes typically exhibit bimodal diffusion, indicating the presence of multiple dynamical processes. [31, 32] The slow diffusion was often explained by long-wavelength concentration fluctuations given by multichain clusters. Ermi et al. explained the faster diffusion as an electrodynamic coupling between the chain segments and the low-molecular weight counterions. While the observation of the segmental dynamics using Nuclear Magnetic Resonance (NMR), fluorescence spectroscopy or dynamic light scattering is challenging, neutron spectroscopy can overcome this limitation.

The segmental dynamics of many polymer systems [33] and polyelectrolytes have been studied [34] via Quasi-Elastic Neutron Scattering (QENS). Neutron Backscattering (NBS) QENS covers length scales in the order of nano- to sub-nanometers and timescales from pico- to tens of nanoseconds. These ranges make the technique a perfect tool to probe the self-diffusive polymeric segmental dynamics and the local dynamics of the investigated molecules. For instance, in the context of studying ionic conductors for rechargeable batteries, the dynamics within a salt mixture of poly(ethylene glycol) (PEO)-lithium has been resolved, revealing in this case the typical bimodal dynamics of entangled polymer systems. [35] The study showed a slow mode assigned to the dynamics of the PEO salt mixture, while the faster mode corresponds to the PEO dynamics.

The segmental dynamics was also resolved by Slim et al. for unentangled semidilute solutions of sodium polystyrenesulfonate (NaPSS) and Buvalaia et al. for polystyrene sulfonate (PSS). [36, 3] They both observed the segmental dynamics of the polyelectrolyte showing a minimum centered in the same q of the structure factor peak, visible via small angle scattering. This effect is also called *de Gennes Narrowing* and it is the results of the fact that the diffusion coefficient of a collection of particles can be modelled as: [27]

$$D(q) = D_{CM}\frac{H(q)}{S(q)} \tag{1.12}$$

This version of the Langevin equation where $H(q)$ is the hydrodynamic function which takes into account the hydrodynamic interaction between different polymer coils and $S(q)$ is the structure factor.

A full description of the dynamics of the polyelectrolyte solution investigated by

Buvalaia is displayed in fig. 1.3

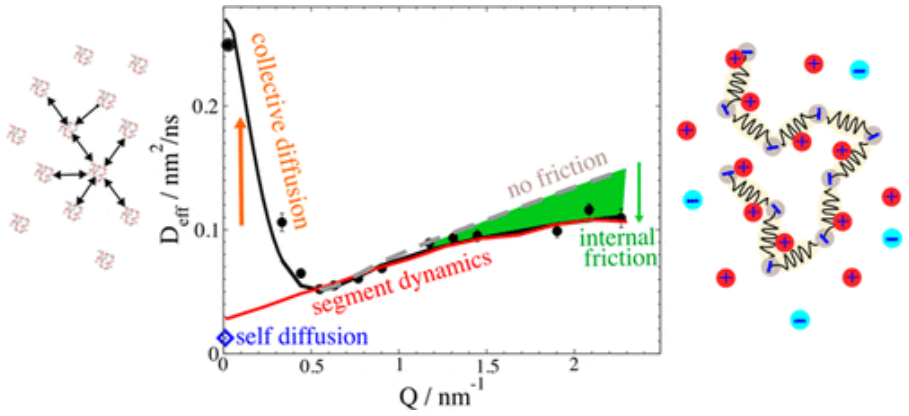

Figure 1.3: Collective diffusion coefficient D collected via neutron spin-echo and modelled with the Zimm model with the addition of a friction within neighboring beads. Taken from [3]

They modelled the observed dynamics with the Zimm model and a deviation at high-q explained with a friction within neighboring beads of the polymer chain. This deviation from the Zimm model was related to counterion condensation on the polymer chain.

1.1.2 Polyelectrolyte Complexes (PECs)

Owing to their electrostatic nature, oppositely charged polyelectrolytes form complexes upon mixing. The resulting physical properties can vary greatly depending on the polymer architecture and solution conditions [37, 38, 39, 40]. For instance, PE complexation strongly depends on **salt concentration**: from eq. 1.3 we can see that an ionic environment will induce a larger Debye length, reinforcing the screening between the ions and thus weakening the electrostatic interactions. It follows that the same mixture of PEs can be in different phases; this was experimentally observed by many investigations, an example of which is depicted in fig. 1.4.[4]

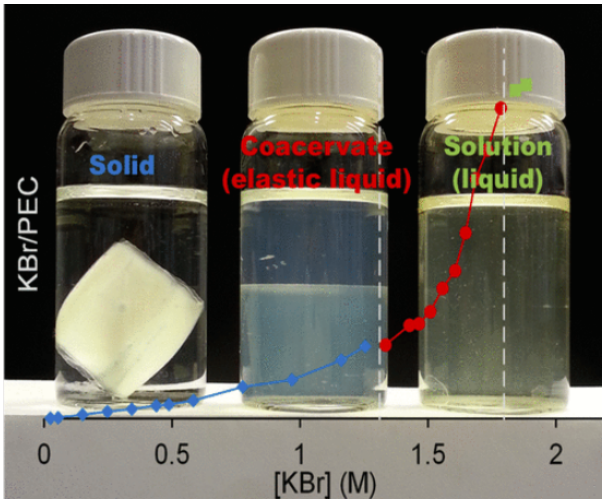

Figure 1.4: A mixture of oppositely charged polyelectrolytes dissolved in water solutions at different salt concentrations. Taken from [4]

Solid-liquid phase separation can occur in a solution with low salt concentration, while increasing the salt concentration, the aggregates become more plastic, leading to a liquid-liquid phase separation known as coacervation. By increasing further the salt concentration, the interactions between the PEs become so weak that it is possible to obtain dissolved aggregates in solution. There are other ways to weaken the interactions between the oppositely charged species, e.g. by tuning the pH, thus altering the charge density of the PEs. The ionic strength also influences the PE complexation.

To unravel the fundamental interactions of complexations, many theoretical, computational and experimental studies have been performed, and it is instructive to look at molecular dynamics simulations of oppositely charged PEs. [5, 41] An extract of the aforementioned simulations is depicted in fig. 1.5. [5]

When two salt-free solutions of oppositely charged polyelectrolytes are mixed, the species spontaneously assemble into polyelectrolyte complexes (PECs). At first glance, one might expect complexation to be driven by enthalpic ion pairing between the oppositely charged chains. However, it has been widely observed that the process is primarily entropically driven, due to the release of counterions into the solution and the reorganization of water molecules around the neutralized chains.

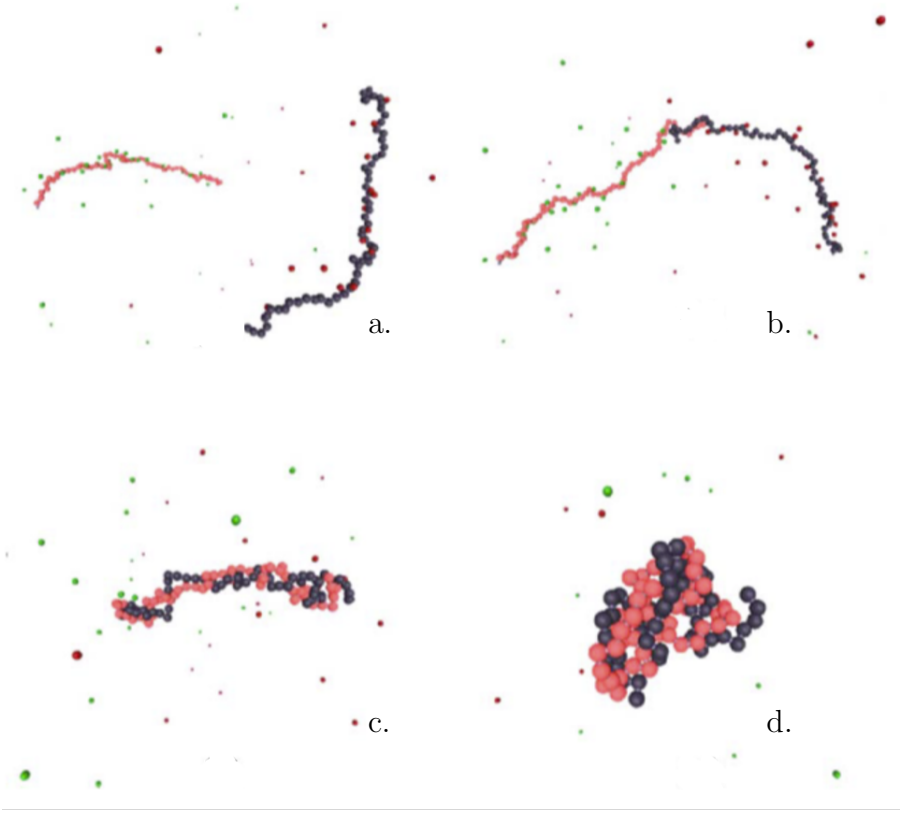

Figure 1.5: Association behavior of two oppositely charged PEs. Screenshot taken from a computational study of polyelectrolyte complexes. Taken from [5].

Fig. 1.5 shows a progressive release of the counterions. Once the PEs are in contact (panel b) they form the first ion pairing and in a cascade mechanism triggered by the dipole forces, all the other counterions are released, leading to a neutral polyelectrolyte complex. In this simulation, it was found that the entropic energy contribution was in fact greater than the enthalpic one.

Besides the environmental influences, PEs are highly tunable systems and different architectures correspond to different behaviors. For the scope of this thesis it is interesting to introduce **polysoaps**: PEs characterized by substitutions of the charged groups with hydrophobic moieties, and **double hydrophilic block copolymers**, thus copolymers characterized by one neutral hydrophilic chain and a charged chain.

1.1.3 Polysoaps

Polysoaps are a subclass of hydrophilic polymers modified with hydrophobic substitutions. These substitutions experience hydrophobic interactions in aqueous solutions, leading to aggregates at the mesoscopic scale (between the molecular and macroscopic scale). Polysoaps have been widely investigated for their interesting macroscopic properties such as low viscosity and surface activity.[42, 43]

Owing to their molecular composition, which is similar to the surfactant micelles, they are analogous to these aggregates and thus they are often referred to as "micellar polymers" or "polymeric surfactants".[6]

The two main categories of micellar polymers are illustrated in fig. 1.6 polysoaps (A) are polymeric surfactants where the surfactant moiety substitutes one or more polymeric subunits, in contrast with amphiphilic copolymers (B) where the hydrophobic subunits are a portion of the whole copolymer.

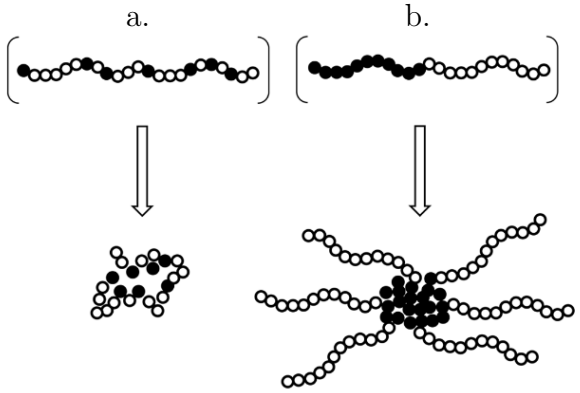

Figure 1.6: Schematic representation of the association behavior of polysoaps (a) and amphiphilic copolymers (b). Hydrophobic groups are represented in black, while hydrophilic groups are white. Image taken from [6].

This two category are not sharply defined and it is possible to find polymers with features of both categories. However it is useful to categorize polymeric micelles because polysoaps and amphiphilic copolymers usually behave differently in water solutions: while polysoaps tend to form intramolecular connections at high concentrations, amphiphilic copolymers mainly experience intermolecular connections.

To contextualize the present work, it is useful to recall the main features of polysoap engineering, which have already been extensively reviewed by Laschewsky [43]. Polysoaps are usually synthesized aiming for an appropriate hydrophilic-hydrophobic balance (HLB), such that the molecules are soluble in water but they also form aggregates. There have been many different attempts at surfactant-like substitutions. While the main variations one can operate in surfactants are to test different hydrophilic heads and different alkyl chains, polysoaps introduce a new level of complexity due to the polymeric architecture. Focusing on the surfactant-like nature of the polysoaps, the main tests involve varying of the ionic nature of the hydrophilic head and the length of the alkyl chain. In particular, it has been reported that the length of the alkyl chain at which polysoaps experience aggregation is C_8, while for at C_{18} the hydrophobic aggregates start to crystallize and they cannot be considered fluid. [44, 45] Not only the length of the alkyl chain is important to form micelles, but also the their abundance. Due to the tendency of polysoaps to form intramolecular micelles, there must be a minimum amount of hydrophobic modifications to obtain such micelles. By analogy with the critical micelle concentration, the "critical alkyl group content" has been defined as the minimum percentage of hydrophobic subunit in the polysoap. This number varies with the alkyl chain length and it has been found to be around 20 mol % for octyl chains and 10 mol % for dodecyl chains.[42, 46] Another important variable in the aggregation behavior of polysoaps is the junction between the polyelectrolyte backbone and the surfactant monomers.

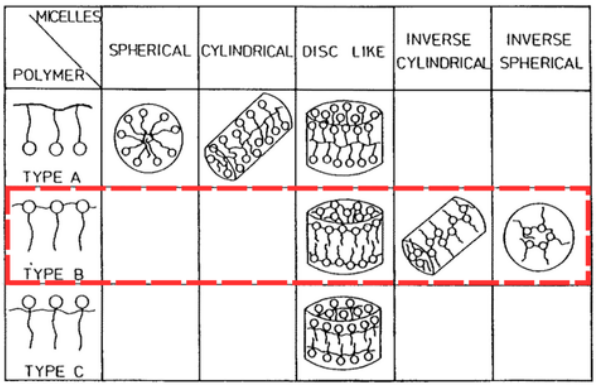

Figure 1.7: Different structure given by different isomers of the same polysoap. Image adapted from [7].

Fig. 1.7 shows different isomeric structures and the possible aggregation patterns they can have [7]. The polymers used in this dissertation have the hydrophilic head attached to the backbone, resulting in type B polysoaps.

Solubilization

Polysoaps merge a hydrophilic nature with the presence of hydrophobic pockets similarly to surfactants; however, a dilution applied to a surfactant solution will disrupt the micelles, leading to segregation, while polysoaps remain dissolved in acqueous solutions and preserve their "micellar nature" at very low concentrations.

Two main types of solubilization studies can be distinguished: the first is the solubilization of probe hydrophobic molecules, such as dyes or chromophores [47, 48]. These studies mainly focus to characterize the presence of hydrophobic domains and they are intrinsically affected by large uncertainty e.g. due to the perturbation induced by the probe molecule on the studied system [49]. A second, less frequent, type of study focuses on the solubilization of the polyelectrolytes [50, 51]. In this second approach, it has been found that the surface activity is not correlated to the solubilization capacity [52]. Moreover, high molecular weight polysoaps do not exhibit any lower solubility limit in most of the case [52], while low molecular weight polysoaps behave similarly to surfactants [53]. The length of the alkyl chains also increase the solubilization capacity [54].

Structures

The most common case of aggregates for low molecular weight polysoaps is fluctuating spherical micelles with an aggregation number in the order of 10-200, depending on the polysoap architecture. These systems have a high mobility and they experience a dynamic equilibrium with rapid exchange between aggregated and non-aggregated unimers dispersed in solution. In most of the cases, as stated above, micelles form intramolecularly, however intermolecular aggregates are observed when the critical aggregate concentration (CAC) point is not reached [49], in the case of oligomeric polysoaps [55] and in highly concentrated solutions as a secondary effect [56].

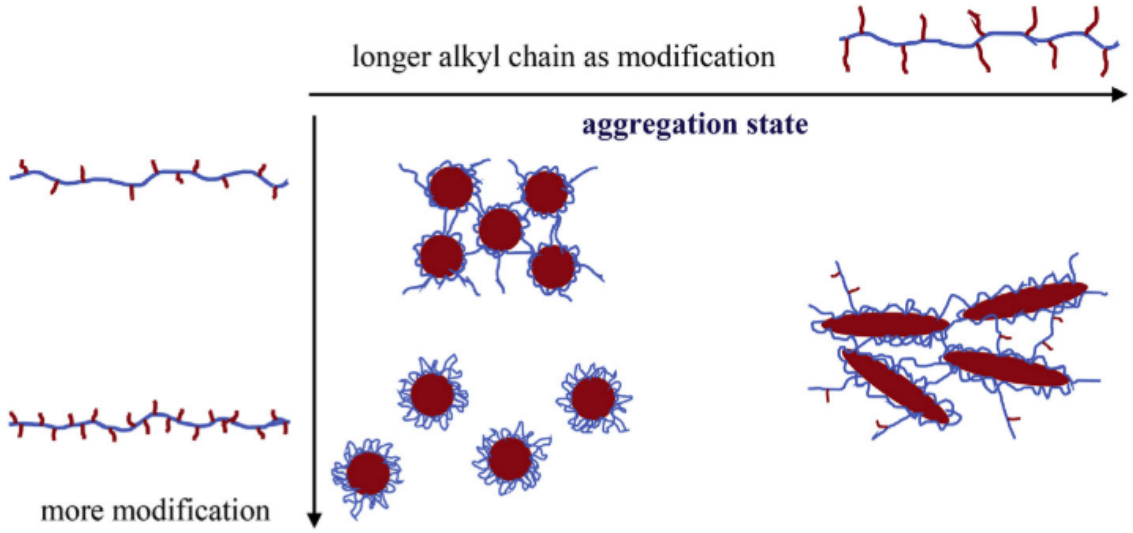

Figure 1.8: Schematic description of the behavior of polysoaps with different types and degrees of hydrophobic modifications. Taken from [8].

This twofold nature of intramolecular and intermolecular aggregations was also observed recently in our group. Riemer et al. studied a variety of polyacrylic acid (PAA) polysoaps. [57, 8] In these studies, it was observed that longer alkyl chains tend to form intramolecular micelles, while shorter alkyl chains connect different polysoaps. It was also observed that the abundance of hydrophobic modification plays a huge role in the formation of the structures: for a low degree of modification (10% mol), an interconnection between different polymers is always visible. The stiffness of a polysoap with a low

degree of modification is high due to its charge, resulting in which prevents the polymer from rearranging into intramolecular structure. This phenomenon is also observed for longer alkyl chains (C_{16}), where elongated intermolecular structures are visible. By increasing the degree of modification, the polymer becomes more flexible and there is a tendency to obtain intramolecular micelles.

Applications

There are many sectors in which polysoaps appeared to be promising, as they enhance the solubilization of hydrophobic molecules in hydrophilic environments:

- In the field of colloidal stability, only a few studies have shown promising results, such as the formation of viscoelastic fluids, [58]
- In the pharmaceutical sector, many studies proved polysoaps can improve drug efficiency and stability, and reduce toxicity, [59, 60]
- The majority of application of polysoaps have been tested in the field of micellar catalysis. [61, 62]

1.1.4 Double Hydrophilic Block Copolymer (DHBC)

Double **H**ydrophilic **B**lock **C**opolymer (DHBC) formed by a charged polyelectrolyte portion attached to a neutral hydrophilic block (usually poly(ethylene-glycol) (PEG) is used) are interesting molecules due to their self-assembly nature. As discussed for IPECs, the oppositely charged polyelectrolyte species tend to aggregate. However the PEG portion is more hydrophilic than the charged environment created by the blocks and therefore arranges itself at the interface between water and the core. The PEG portion helps to stabilize the aggregate, leading in many cases to core-shell micelles (as depicted in fig. 1.9). These aggregates are referred to in the literature in many ways e.g., complex coacervate core micelles (C3Ms), block ionomer micelles (BICs) or polyion complex micelles (PICs).[63, 64, 65]

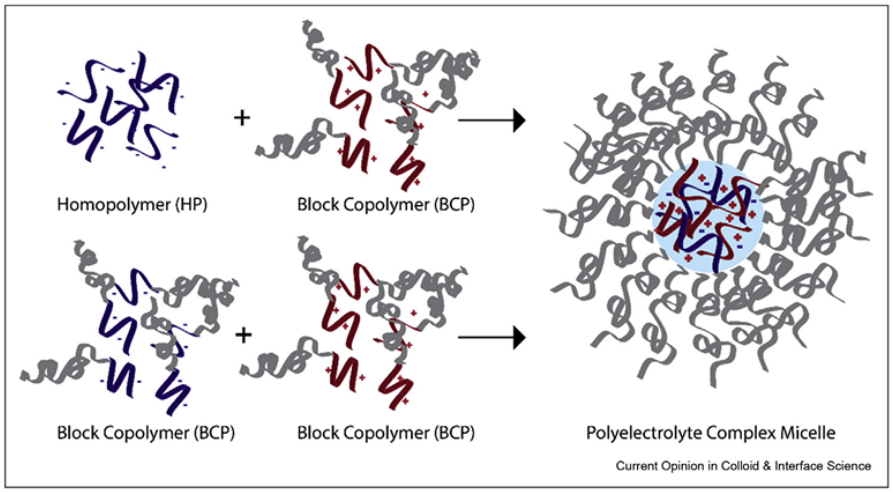

Figure 1.9: Sketch of the general assembly structure between oppositely charged double hydrophilic block copolymers. Figure taken from [9].

Since they are a subcategory of IPECs and to avoid further complicating the nomenclature, we will refer to these aggregates as IPECs throughout this dissertation.

There has been several reviews on the behavior of IPECs formed by DHBCs, here I report the main features, a more in depth description can be found in the following references [9, 23, 66].

One milestone on DHBC is the study of Cohen Stuart about a mixture of poly((dimethyl amino)-ethyl methacrylate)-co-poly(glyceryl methacrylate) (PDMAEMAco- PGMA) and poly(acrylic acid) (PAA).[63] In this study they mixed these 2 polymers in different charged ratios, finding that, after an equilibration time, the polymers were rearranging into aggregates. By light scattering, they characterized the behavior as a function of the mixing ratio and they observed for the first time the micelles via cryo-TEM.

Micelle formation, stability and responses to the environment

Understanding the kinetics of formation and disruption of polymer micelles is crucial for implementing an application as carrier nanostructures and the most widely accepted hypotheses for these two kinetic processes have been already reviewed.[9]

Although the scientific community agrees on the first formation of aggregates via

ion-pairing, the rearrengement which leads to the core-shell structure is not clear. Two main hypothesis have been made:

- Amann et al. observed that IPECs formed by poly(styrene sulfonate) (pSS) resulted in solid coacervates, leading to kinetically trapped charged aggregates that precipitate and subsequently rearrange over time via unimer exchange, leading to the core-shell structures. [67]

- Wu et al. used poly (acrylic acid) (PAA): this polymer leads to liquid-like structures. The aggregates are smaller and more flexible and appear to be neutral at the very first step of formation. The aggregates seem to grow over time by merging of small clusters. [68]

The kinetics of disruption have also been investigated and two mechanism for inducing disruption have been identified:

- By salt addition, electrostatic interactions are screened, inducing swelling effects and leading to disruption by core fragmentation. [69]

- By pH variation, the ionization of the charged sites can be controlled, leading to a decrease of the electrostatic interactions. [70]

By investigating the stability of micelles, a highly dynamical model has been proposed, where the micelles continuously exchange polyelectrolyte couples or undergo fission/fusion events. [71]

The charge ratio between the oppositely charged polyelectrolytes has been shown to affect the morphology of the aggregates: Takahashi et al. reported a transition from spherical structures at the equimolarity mixing ratio to cylindrical charged structures for the non-equimolar mixing ratio [72]. Rappoport et al. studied the effect of an unbalance of the diblock hydrophilic block copolymer, finding that an excess of diblock hydrophilic block copolymers leads to core-shell structures, while an excess of the simple polyelectrolytes leads to vescicular structures. [73]

Applications

Micellar IPECs are attractive for the pharmaceutical fields as drug carriers. The main features that make these structures interesting are the following.

- The affinity within biomolecules used as biopharmaceuticals. This permits micellar IPECs to encapsulate proteins, DNA and RNA. [74, 75]
- their response to environmental conditions. By using weak polyelectrolytes, one can construct switchable self-assemblies that respond to the ionic strength or pH. In doing so, it is possible to design drug carriers that dissolve at specific targets, such as environments with low pH (such as the gastric environment). [74] Such applications have already been explored with hydrogels. [76]
- the possibility to implement a protective switchable corona onto the micelles.[77]

1.1.5 Scope of the dissertation

Open problems on the complexation

Although polysoaps and micellar IPECs have been widely investigated in recent decades, there are still many open questions to tackle. The stability of micellar IPECs is sometimes overestimated, with the conclusions that a bigger amount of salt is needed to dissolve them; conversely, they easily dissolve to a pH different from the predicted one. This discrepancy between the conceptualization of a carrier and the actual experimental test might lead to incorrect dissolution at the application stage, leading to the drug being delivered in the wrong spot.

Another crucial point of micellar IPECs is the extent of complexation: incomplete association has been reported in the case of coacervate [78], but also micellar IPECs [79], resulting in a solution containing encapsulated and unencapsulated active agents.

Moreover, by smartly engineering the polymers forming the IPECs, one could develop multicompartment IPECs, capable of encapsulating different kinds of active agents. This dissertation aims to progress in this direction. By mixing polysoaps with oppositely

charged double hydrophilic block copolymers, the hydrophobic pockets of the polysoaps are encapsulated into the bigger micellar IPECs given by DHBC.

Similar attempts of mixing polysoaps into IPECs structures have been already investigated in our group, finding the hydrophobic moieties to form cylindrical structures which interconnect different polysoaps and increase the aggregation number by almost one order of magnitude.[80] In this dissertation, I also introduce the effect of double hydrophilic block copolymers.

This dissertation investigates the polycation Poly(2-(dimethylamino)ethyl methacrylate) (PDMAEMA), a temperature sensitive polyelectrolyte. [81, 82] Since PDMAEMA is a weak polybase, it reacts strongly to variations in pH, opening the possibility to create switchable carriers. [83]

PDMAEMA has been already exploited as a component of carriers of biomolecules. Rappoport et al. observed the capability of quaternized PDMAEMA DHBC to complex with DNA. [73] They tested the structure of the obtained aggregates in a solution mimicking the physiological condition of the blood, finding cylindrical structures organized in an hexagonal fashion.

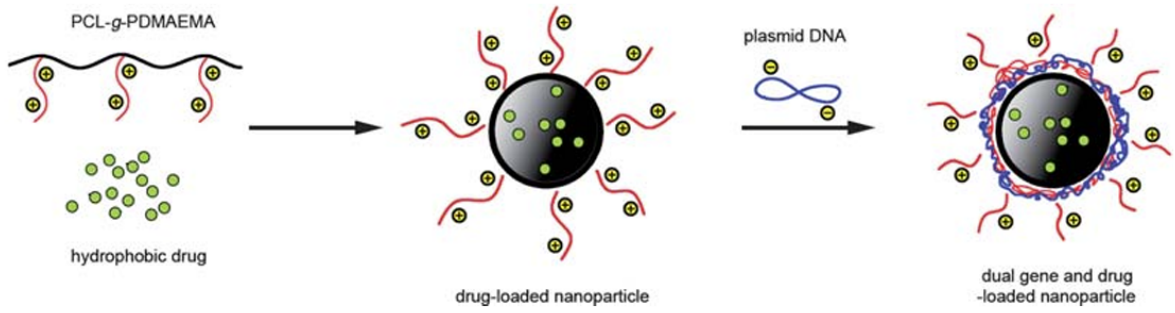

Figure 1.10: Poly(2-(dimethylamino)ethyl methacrylate) (PDMAEMA) copolymer aggregates with plasmids. Taken from [10].

Different types of Hydrophobically modified PDMAEMA have been tested as well: particularly a copolymer made by a hydrophobic backbone with grafted moieties of PDMAEMA has been used to form complexes with plasmids. This copolymer can self-assemble into structures with 2 different environments, a hydrophobic core able to en-

capsulate hydrophobic drugs, and a charged corona which hosts the plasmids, due to its electrostatic affinity (as depicted in fig. 1.10)[10].

Han et al. observed that in aqueous solution PDMAEMA can form spherical micelles, rod-like structures or fractal structures, depending on the pH.[84] In case of IPECs with PDMAEMA-based DHBCs, the DHBC content has only a mild effect, whereas the pH and the mixing ratio changes strongly the size of the formed aggregates [85].

Open problems on the Dynamics

Although these systems have been extensively studied due to their wide range of applications, a comprehensive description of their nanoscale structure and dynamics remains elusive. As it was explained above, micellar IPECs are highly dynamic systems and a dynamical equilibrium of exchanging block-copolymers has been correlated to the polymeric segmental dynamics. [86, 87] Particular attention has been given to the chain dynamics of the corona of the complexes, finding this dynamics to be related with the distance from the copolymer junction[88].

A particular point I discussed in this thesis was the effect of complexation on the polymer dynamics. Polymeric aggregation was proven to suppress the segmental dynamics of polymers, as seen in a study on PNIPAM micelles.[89] In this work, aggregation was triggered by raising the temperature above the lower critical solution temperature (LCST). Other well-known examples of nanoscale self-assembly aggregation are found in internally disordered proteins (IDPs), which are unfolded proteins that undergo liquid-liquid phase separation (LLPS). In the aggregated state, these macromolecules become more and more rigid.[90]

Recently, the segmental dynamics of complex coacervates was probed for different charge types: for ammonium cations, the increase of salt concentration was observed to enhance the dynamics, reducing the number of ion pairs. This dependency vanished when ammonium cations were substituted with guadinidium groups.[91]

In this dissertation, I used a model system of double hydrophilic block copolymers mixed with polysoaps. I characterized the resulting structure, the influence of the hy-

drophobic modifications on micellar IPECs and I tested the presence of hydrophobic domains. Secondly, I investigated the polymer dynamics, which is again subdivided into segmental dynamics and collective dynamics. As a result of the thesis, I observed the effect of implementing hydrophobic modifications and the effect of the complexation on the segmental dynamics.

1.2 Neutron Scattering Theory

A useful tool to probe the structure of matter is given by neutron scattering theory. To better understand the discussion on the polyelectrolyte investigation, I recall some basic concepts of these experimental techniques. A more detailed discussion can be found in several books [92, 93, 94].

In a neutron scattering experiment, the investigated sample is irradiated with a beam of neutrons. Through the quantum-mechanical laws, we can express a neutron with momentum $\mathbf{p}$ as a spherical wave of de Broglie wavelength $\lambda = h/p$, where h is the Planck constant, and a wave vector $\mathbf{k} = \mathbf{p}/\hbar$, with $\hbar = h/2\pi$. By using the classical definition of the kinetic energy of a particle, it follows that $E = (\hbar k)^2/2m$, with m being the mass of the particle.

In the mechanical problem of scattering, depicted in fig. 1.11 a neutron of the beam travels toward the sample, interacts with it, and is captured by a detector on a specific scattering angle θ. The momentum and energy transfer ($\mathbf{q}$, E) from the initial state of the neutron ($\mathbf{k_i}$, E_i) to the final one ($\mathbf{k_f}$, E_f) is:

$$\mathbf{q} = \mathbf{k_f} - \mathbf{k_i} \tag{1.13}$$

$$E = E_f - E_i = \hbar\omega \tag{1.14}$$

where ω is the frequency associated with the energy exchange. Based on the energy exchange E, there are two cases of scattering:

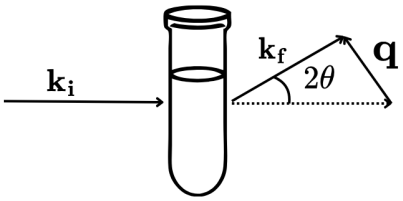

Figure 1.11: Geometrical representation of the problem of neutron scattering.

- $\mathbf{E} \neq 0$: it is called *Inelastic Neutron Scattering*. The neutron is exchanging energy with the sample. If the energy is small, it can be referred to as *QuasiElastic Neutron Scattering* (QENS) and it is the phenomenon exploited by Neutron Backscattering and Neutron Spin Echo.

- $\mathbf{E} = 0$: in this case, called *Elastic Neutron Scattering*, the sample is not exchanging energy with the neutron. Since $E_i = E_f$, it follows that $k_i = k_f = k$ and q can be calculated as:

$$q = \frac{4\pi \sin(\theta)}{\lambda} \tag{1.15}$$

  This type of scattering is the basis of Small Angle Neutron Scattering.

1.2.1 Cross section

A scattering experiment measures the *differential scattering cross section* $\frac{d\sigma}{d\Omega}$, which is represented by the ratio of neutrons deflected in a specific solid angle $\delta\Omega$ (depicted in

fig. 1.12) by the incident flux intensity Φ_0.

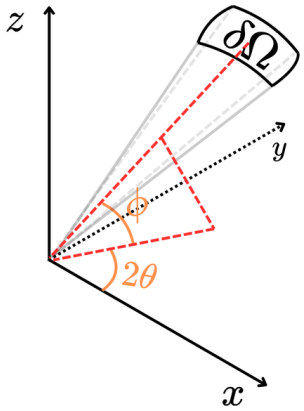

Figure 1.12: Graphical representation of the solid angle for the cross section.

To calculate the cross section, it is necessary to calculate the scattered wave function of a neutron from a nucleus. The neutron beam wave function is:

$$\psi(r) = Ae^{i\mathbf{k}\cdot\mathbf{r}} \tag{1.16}$$

with $\mathbf{k}$ being the neutron wavevector. After being scattered by a nucleus, the wave function is:

$$\psi_{sc}(r) = -\frac{b}{r}Ae^{i\mathbf{k}\cdot\mathbf{r}} \tag{1.17}$$

Where b is the *bound nuclear scattering length*, which modulates the amplitude between the incident and the scattered waves.

A typical investigated sample consists of a collection of nuclei, thus we have to sum over all the scattering events:

$$\psi_{sc}(r) = Ae^{i\mathbf{k}\cdot\mathbf{r}} \sum_j \frac{-b_j}{|\mathbf{R} - \mathbf{r_j}|} e^{-i\mathbf{q}\cdot\mathbf{r_j}} \tag{1.18}$$

where j runs over all the nuclei, $\mathbf{R}$ is the vector between the sample and the detector and $\mathbf{r_j}$ the position of the j_{th} nucleus. In our case, we consider the detector farther than

the typical distance between the nuclei of our sample ($\mathbf{R} \gg \mathbf{r_j}$), thus the scattering intensity $I(q)$:

$$I(q) = |\psi(q)\psi^*(q)| \propto \Big| \sum_j b_j e^{-i\mathbf{q}\cdot\mathbf{r_j}} \Big|^2 \tag{1.19}$$

which is also the differential cross section in the case of elastic scattering. If we introduce the *scattering length density* $SLD(\mathbf{r})$, we can express $I(\mathbf{q})$ in its integral form for elastic scattering:

$$I(\mathbf{q}) \propto \left| \int_V dV SLD(\mathbf{r}) e^{i\mathbf{q}\cdot\mathbf{r}} \right|^2 \tag{1.20}$$

where V is the sample volume. In the case of inelastic scattering, we define the *partial differential cross section*, represented by the number of neutrons scattered in a solid angle, per flux and per final energy interval (E, $E + dE$) $\frac{d\sigma}{d\Omega dE}$.

1.2.2 Coherent and Incoherent Scattering

In the previous chapter, I discussed the scattering length as a constant related to the nucleus. Since b depends on the isotope and given that the isotope distribution in our sample can be considered random, the cross section from elastic neutron scattering, as already shown in eq. 1.19 is:

$$\frac{d\sigma}{d\Omega} = \sum_{jk} \overline{b_j b_k} e^{-i\mathbf{q}\cdot(\mathbf{r_j}-\mathbf{r_k})} \tag{1.21}$$

where j and k run over all the scattering sites and the bar denotes the average over the isotope distribution. This expression can be split into two contributions: a *self* term ($j = k$) and a *cross* ($j \neq k$) term:

$$\overline{b_j b_k} = \overline{b_k^2} \qquad j = k \tag{1.22}$$

$$= \overline{b_k}\ \overline{b_j} \qquad j \neq k \tag{1.23}$$

where $\overline{b} = \sum_i p_i b_i$ is the average over the isotope distribution of the scattering length and $\overline{b^2} = \sum_i p_i b_i^2$ is its mean squared.

Separating eq. 1.21 into self and cross terms:

$$\frac{d\sigma}{d\Omega} = \sum_{j \neq k} \overline{b_j b_k} e^{-i\mathbf{q}\cdot(\mathbf{r_j}-\mathbf{r_k})} + \sum_j \overline{b_j^2} = \tag{1.24}$$

$$= \underbrace{\sum_{jk} \overline{b_j}\ \overline{b_k} e^{-i\mathbf{q}\cdot(\mathbf{r_j}-\mathbf{r_k})}}_{\left(\frac{d\sigma}{d\Omega}\right)_{coh}} + \underbrace{\sum_j (\overline{b_j^2} - \overline{b_j}^2)}_{\left(\frac{d\sigma}{d\Omega}\right)_{inc}} \tag{1.25}$$

where in eq. 1.25, we have added and subtracted $\sum_j \overline{b_j}^2$. The two additive terms are called *coherent* and *incoherent* differential cross sections. The coherent cross section $\left(\frac{d\sigma}{d\Omega}\right)_{coh}$ depends on the reciprocal position between the atom j and k, it therefore contains information on the structure. The incoherent cross section $\left(\frac{d\sigma}{d\Omega}\right)_{inc}$, however, does not depend on the atomic distribution, but only on their abundance. In elastic scattering experiments, such as SANS, the signal is composed of coherent scattering plus a flat component of noise given by the incoherent part. Later in this dissertation, I will also discuss how incoherent scattering can be informative on the dynamics of the atoms in a quasielastic investigation.

1.2.3 Structure and Form factor formalism

For simplicity, the decomposition into form and structure factor is presented in the context of elastic scattering; however, this concept can be generalized to obtain the dynamic structure factor. The elastic differential cross section, written in its integral

form in eq. 1.20, is the Fourier transform of scattering length density. The derivation is also explained considering a collection of homogeneous hard spheres in a solution (the generalization has been discussed elsewhere [94]). The scattering length density $SLD(\mathbf{r})$ can be written as:

$$SLD(\mathbf{r}) = SLD_0 + \sum_j \overline{SLD_c(\mathbf{r} - \mathbf{r_j})} \tag{1.26}$$

where SLD_0 is the scattering length density of the solvent, j runs over the spheres probed and $\overline{SLD_c(\mathbf{r})}$ is

$$\overline{SLD_c(\mathbf{r})} = \begin{cases} SLD_{sph} & \text{inside the particle} \\ 0 & \text{outside the particle} \end{cases} \tag{1.27}$$

Where SLD_{sph} represents the constant scattering length density inside the spheres. By Fourier transforming $\overline{SLD_c(\mathbf{r})}$:

$$\left(\frac{d\sigma}{d\Omega}\right)_{el} \propto \left| 2\pi^3 \delta(\mathbf{q}) + \sum_j e^{i\mathbf{q}\cdot\mathbf{r_j}} \int_V \overline{SLD_c(\mathbf{r})} e^{i\mathbf{q}\cdot\mathbf{r}} d\mathbf{r} \right|^2 \tag{1.28}$$

Where $\delta(\mathbf{q})$ is the delta function. On the right hand-side of the equation, the first term is identically 0 for $q \neq 0$. The second term includes a summation and an integral over the volume. The integral term depends solely on the characteristics of the scatterers and is often referred to as *form factor* $F(\mathbf{q})$. $\left(\frac{d\sigma}{d\Omega}\right)_{el}$ can then be rewritten as:

$$\left(\frac{d\sigma}{d\Omega}\right)_{el} \propto |F(\mathbf{q})|^2 \left[N + 2 \sum_{j>j'} \cos(\mathbf{q} \cdot (\mathbf{r_j} - \mathbf{r_{j'}})) \right] = |F(\mathbf{q})|^2 S(\mathbf{q}) \tag{1.29}$$

Where the expression in the brackets is redefined as the *structure factor* $S(\mathbf{q})$ and it depends only on the spatial correlation between the scatterers. This formulation is useful for splitting the scattering intensity into contributions from individual scatterers and from their spatial distribution.

1.3 Small Angle Scattering Theory

Small Angle Neutron Scattering (SANS) is a powerful technique for characterizing the nanostructures (typical ranging from one to several hundreds of nm, depending on the instrument) present in a sample. A SANS experiment measures the elastic scattering intensity of the sample.

1.3.1 Instrument setup

A representative example is D11, shown in fig. 1.13. The SANS instruments can widely vary in the details, however they must perform 4 fundamental actions:

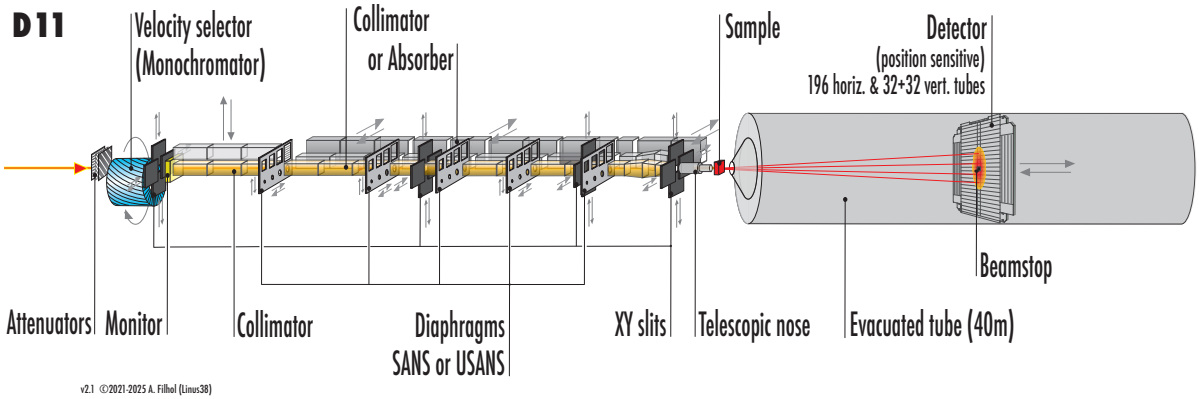

Figure 1.13: D11 setup, taken from ILL website [11]

- The first important step for SANS is to determine the wavelength of the incident beam and there are two different approaches: in the *monochromatic mode* the wavelength is typically selected using a velocity selector or a crystal monochromator. This is usually the preferred operating mode at a continuous beam sources. Alternatively, the neutron wavelength can be determined using the time-of-flight (TOF) method. This approach is commonly used in pulsed neutron sources.
- Collimation: two pinholes several meters far apart ensure that the neutron beam is aligned with the axis of the diffractometer. This step is crucial for determining the minimum accessible q-value.

- Scattering: the sample scatters the neutron to a specific angle.
- Detection: A two-dimensional detector is positioned several meters ($\simeq$ 30m) from the sample to satisfy the small angle working condition. The detector commonly uses ^{3}He gas for neutron detection. Multiple detector panels may be combined to acquire a wide q-range simultaneously.

Data from SAM, D22, and D33 were acquired in velocity selector mode, whereas data on Bilby were collected in time-of-flight (TOF) mode.

1.3.2 Data Modelling

Absolute intensity Analysis

A neutron detector counts how many neutron have been scattered on a specific angle, providing an intensity in absolute units:

$$I(\mathbf{q}) = I_0(\lambda)\eta(\lambda)T(\lambda)\Delta\Omega\left(\frac{d\sigma}{d\Omega}\right)_{el} * R(\mathbf{q}) + B(\mathbf{q}) \tag{1.30}$$

here, the first two terms are characteristics of the experimental setup (incident flux and efficiency of the detector) and $T(\lambda)$ is the transmission of the sample. $\Delta\Omega$ is the solid angle subtended by the detector, $\left(\frac{d\sigma}{d\Omega}\right)_{el}$ is the previously discussed cross section, $R(\mathbf{q})$ is the resolution function and $B(\mathbf{q})$ is the background and $*$ is the convolution operator. In this formula, the most relevant information is encoded in the elastic scattering cross section, and the normalization can be expressed using the sample concentration. The most common way to express the normalization is

$$\left(\frac{d\sigma}{d\Omega}\right)_{el}\Bigg|_{q=0} = \frac{NV_p^2(\Delta SLD)^2}{V} \tag{1.31}$$

Where V is the scattering volume, N is the amount of scatterers, V_p is the volume of the scatterers and ΔSLD is the difference between the scattering length density of the

scatterers and the solute. By definition, the volume fraction Φ is

$$\Phi = \frac{NV_p}{V} \tag{1.32}$$

And the particle volume can also be expressed in terms of macroscopic quantities:

$$V_p = \frac{MW}{\rho N_A} \tag{1.33}$$

Where MW is the molecular weight, ρ is the density of the solute and N_A is the Avogadro's constant. It follows that

$$\left(\frac{d\sigma}{d\Omega}\right)_{el}\Big|_{q=0} = \frac{\Phi MW(\Delta SLD)^2}{\rho N_A} \tag{1.34}$$

Guinier Analysis

A key step in small angle scattering data analysis is the Guinier analysis. The Guinier model is one of the most important empirical model for low-q scattering. This model can be written as:

$$I(q) = I_0 e^{-\frac{(qR_g)^2}{3}} \tag{1.35}$$

where $I_0 = I(q \to 0)$ is the forward scattering and R_g represents the radius of gyration of the observed feature. In fig. 1.14a, the Guinier model fits synthetic data and is compared with a spherical model, to highlight the limitations of this approximation. Taking the natural logarithm of this equation yields:

$$ln(I(q)) = ln(I_0) - \frac{(qR_g)^2}{3} \tag{1.36}$$

Plotting $\ln I(q)$ against q^2 gives a linear relationship, with a slope of $-R_g^2/3$ and an intercept of $ln(I(0))$. To simplify the discussion, $log(I(qR_g^2)$ has been plotted in fig. 1.14b.

From this plot, the quality of the Guinier fit can be tested. A reliable fit should be

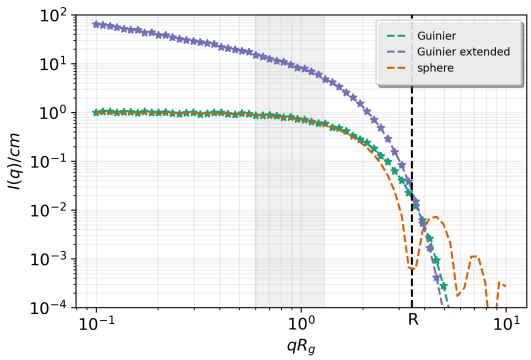

(a) Logarithmic plot with Guinier model compared with the extended version and the model of a sphere. The dashed black line represents the radius of the qR_g value corresponding to the radius of a sphere with the same size of the feature probed by Guinier.

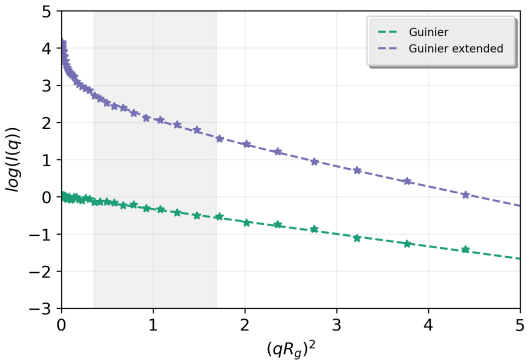

(b) Guinier plot for Guinier and the extended model.

Figure 1.14

performed in the region $0.6 < qR_g < 1.3$, where deviations between the Guinier model and the intensity of a sphere of the same size (shown in orange) are still negligible.

If the probed feature does not show a plateau, i.e., it is bigger than the maximum corresponding length explored, deviations from the linear regime appear at very low q.

$$I(q) = \frac{I_0 \exp\left(-\frac{x^2 R_g^2}{3-f(d)} - \pi f(d)\right)}{x^{f(d)}} + \pi f(d) \tag{1.37}$$

$$f(d) = 2.9 \sin\left(\frac{d\pi}{6}\right)^2 \tag{1.38}$$

This ad-hoc model describes a structure with two characteristic dimensions, where one is much larger than the other. If the larger feature has dimensionality $d = 1$, it may correspond to infinite rods (or an equivalent density distribution). If $d = 2$, it may represent an infinite disk. R_g captures the finite dimensions (e.g. the thickness of the disk or the radius of the rod). This function has been empirically extended to fractal

dimensions. The green lines and dots in fig. 1.14 represent an infinite rod with the same diameter as the spheres (shown in orange) and the Guinier model, as well as the parameter I_0, which in the latter model does not represent $I(q \to 0)$ anymore.

Porod analysis

While the Guinier analysis is helpful to characterize the low-q regime, the Porod analysis focuses on the high-q limit, where finer structural details emerge. To simplify the calculations, it is instructive to consider the case of a smooth sphere and then generalize to other geometrical objects, as done in *The Sans Toolbox* [12]. Using the pair correlation function of a sphere P(r), the intensity can be written as:

$$P(q,r) = \int d^3r e^{-i\mathbf{q}\cdot\mathbf{r}} P(\mathbf{r}) = \frac{1}{V_P} \int dr 4\pi r^2 \frac{sin(qr)}{qr} P(r) \simeq \frac{3}{2R^3} \frac{S_p}{V_p} \frac{1}{q^4} \tag{1.39}$$

Here, S_p and V_P are the surface area and the volume of the sphere and R is its radius. The right hand-side of the equation corresponds to the asymptotic limit of $q \to \infty$. From this approximation, two key points arises:

- The high-q regime exhibits a power-law behavior:

$$I(q) = \frac{A}{q^4} + B \tag{1.40}$$

  where B accounts for the incoherent scattering present in the sample.

- The parameter A can provide geometrical insights, especially in the case of aligned systems[95]

Although the derivation of the Porod law was done for spherical feature, the model can be generalized to different shapes:

$$I(q) = \frac{A}{q^d} + B \tag{1.41}$$

here, d is a generic power-law exponent that provides information about the system's density distribution, as illustrated in fig. 1.15.

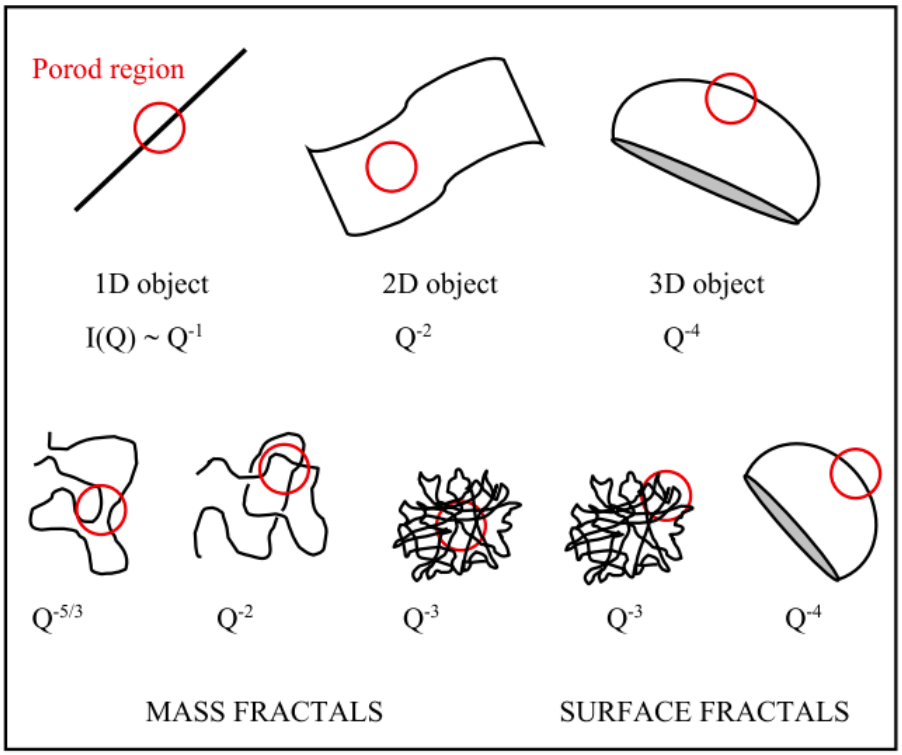

Figure 1.15: Density distributions corresponding to different power-law exponents. Illustration taken from [12].

Krakty Plot

A useful way to detect deviations from the polymer like scattering behavior is to plot $q^2 I(q)$ versus q. At high-q, a polymer typically scatters as $I(q) \propto q^{-2}$, resulting in a Kratky plot with a horizontal asymptote. More rigid structures tend to diverge, while more globular ones converge to zero.

Beaucage

Scattering intensities $I(q)$ from different types of structures-such as spheres, ellipsoids, or polymer coils-are generally characterized by a Guinier regime at low-q and a power-

law decay at high-q. While probing a sample via Small Angle Scattering (SAS) without prior structural knowledge, essential information might be missing. For this reason, the need for a flexible model capable of capturing general features emerged in the scattering community. Assuming uncorrelated low-q and high-q regime, one can rewrite the total scattering intensity as a sum of the Guinier and Porod models [96, 97, 98] in the same formulation implemented in many scattering software packages.[13, 99, 100]

$$
\begin{aligned}
I(q) &= Ge^{-q^2 R_g^2/3.} + Cq^{-d}\left[\mathrm{erf}(qR_g/6^{0.5})\right]^{3d} \\
C &= \frac{Gd}{R_g^d}\left[\frac{6d^2}{(2+d)(2+2d)}\right]^{d/2.}\Gamma(d/2)
\end{aligned}
\tag{1.42}
$$

Where R_g is the radius of gyration of the feature probed, G is the scattering forward intensity, d is the dimensionality of the power law, $\mathrm{erf}(x)$ is the errorfunction and $\Gamma(x)$ is the Gamma function. Notably, the amplitude of the power-law term does not introduce additional free parameters, as it is fully determined by structural quantities already fixed by the Guinier term, ultimately connected to the finite-size effects of the scattering feature.

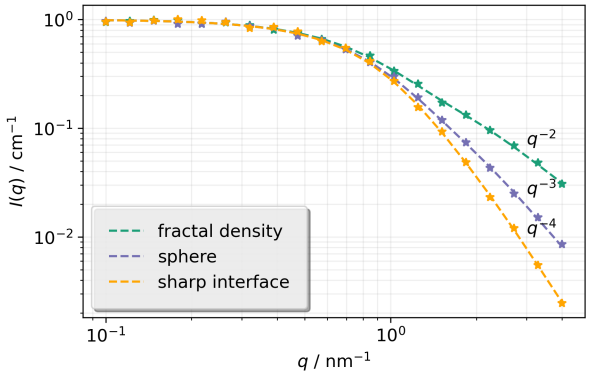

Figure 1.16: Beaucage models applied on synthetic data for different values of q. Plot inspired by the documentation of JScatter [13].

In fig. 1.16, three Beaucage models differs for their power-law exponent d. If $d = 4$, the obtained model is representative of a sharp interface. For $d = 3$, the sample is

spherical whereas for $d < 3$, the sample exhibits a fractal mass distribution.

This model has been widely used to represent polyelectrolytes complexations.[101, 102, 67, 103, 80]

Moreover, the summation of this function can model hierarchical features on the investigated sample:

$$I(q) = \text{background} + \sum_{i=1}^{M} \left[G_i e^{-q^2 R_{gi}^2/3.} + C_i q^{-d_i} \left[\text{erf}(qR_{gi}/6^{0.5}) \right]^{3d_i} \right] \tag{1.43}$$

Where I represent all the M scales observed in the multiscale structure.

Gaussian Chain

Consider a dilute solution of non-interacting polymers, modeled as N beads connected by springs, where each bead has a size l. Polymers can be more or less hydrated, depending on their affinity to interact with another bead with respect to the solvent: e.g. a polymer with very hydrophobic subunit will expose the least surface to water solution, resulting in collapsed structures, while a hydrophilic polymer will open and form bigger and more hydrated structures. This behavior is captured by the so-called *goodness of the solvent parameter* ν. For $0 < \nu < 1$, small values of ν correspond to collapsed chains, whereas big values of ν indicate swollen chains.

This structure has a radius of gyration:

$$R_g^2 = \frac{l^2 N^{2\nu}}{(2\nu + 1)(2\nu + 2)} \tag{1.44}$$

And the intensity $I(q)$ can be written as:

$$I(q) = I_0 \left(\frac{1}{\nu U^{\frac{1}{2\nu}}} \cdot g_2 - \frac{1}{\nu U^{\frac{1}{\nu}}} \cdot g_1 \right) \tag{1.45}$$

$$U = \frac{(2\nu+1)(2\nu+2)(qR_g)^2}{6}$$

$$g_2 = \Gamma_{\text{inc}} \left(\frac{1}{2\nu}, U \right) \cdot \Gamma \left(\frac{1}{2\nu} \right)$$

$$g_1 = \Gamma_{\text{inc}} \left(\frac{1}{\nu}, U \right) \cdot \Gamma \left(\frac{1}{\nu} \right)$$

where $\Gamma_{inc}(.)$ is the incomplete gamma function and $\Gamma(.)$ is the gamma function. In this framework, ν is directly related to the power-law exponent discussed earlier.

Polydispersity

Up to this point, the discussion has assumed monodisperse systems. However, real samples often exhibit a distribution of feature sizes. Consider a solution of polydisperse spheres with an average radius μ_R and a variance σ_R^2. In the monodisperse case, the scattering intensity I(q) is:

$$I(q) = n|F(q)|^2 = n\Delta SLD^2 V^2 \left[\frac{3(sin(q\mu_R) - q\mu_R cos(q\mu_R))}{(q\mu_R)^3} \right]^2 \tag{1.46}$$

Where $V = \frac{4}{3}\pi\mu_R^3$ is the mean volume of the sphere, $F(q)$ is the form factor and $n = \frac{N}{V}$ is the number density. In the polydisperse case, the scattering intensity must be averaged over the radius distribution:

$$I(q) = n \int_0^\infty pdf_{\log}(R; \mu_R, \sigma_r) F^2(q, R) dR \tag{1.47}$$

$$pdf(R; \mu, \sigma_r) = \exp\left[\frac{\ln\left(\frac{R}{\mu_R \sigma_r^2}\right) - \frac{R}{\mu_R}}{\sigma_r^2} - \ln R - \ln \Gamma \frac{1}{\sigma_r^2} \right] \tag{1.48}$$

Where $\Gamma(x)$ is the Gamma function and in the log-normal distribution has been used for computational efficiency.

1.4 Neutron BackScattering Theory

Neutron BackScattering (NBS) is a powerful technique for accessing the nanosecond time scale of atoms and/or small molecular groups by probing their QuasiElastic Neutron Scattering (QENS) spectrum. Investigation exploiting this technique can be done using a neutron spectrometer such as IN16b at ILL, Grenoble, France. A sketch of this spectrometer is shown in fig. 1.17.

1.4.1 Instrument setup

This spectrometer operates in an indirect geometry. A monochromator, consisting of a single crystal, transforms the incoming beam into a monochromatic one directed toward the sample. With the addition of a mechanical doppler unit, the incident beam at the sample acquires an energy distribution ΔE_i. Since indirect geometry implies a fixed final energy E_f, ΔE_i allows probing different energy transfers $\hbar\omega$. There are different backscattering setups; however, the Doppler mode implemented on IN16b is the one used in this dissertation and is therefore worth discussing.

The incident beam is scattered by the sample towards an array of single-crystal energy analyzers. The analyzers reflect only those neutrons that fulfill the Bragg condition. These selected neutrons are then scattered a second time from the sample and subsequently detected. In this configuration, the detected neutrons exhibit a distribution

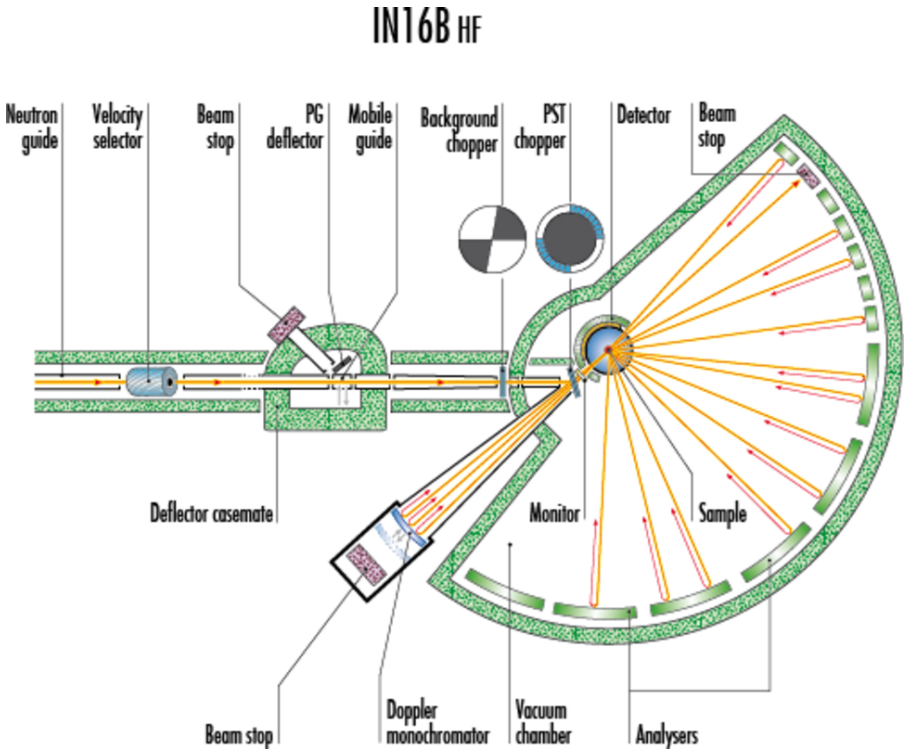

Figure 1.17: IN16b configuration in high flux mode. Image taken from ILL website [11].

in E_f, due to the second scattering by the sample; however, using the time-of-flight information, the instrument selects only the neutrons with a fixed final energy E_f.

The instrument introduces an energy resolution in the detection of the final energy E_f, which can be expressed as:

$$\frac{\delta E_f}{E_f} = \frac{\delta d}{d} + (\cot(\theta)\delta\theta) \tag{1.49}$$

Where the δ refers to the uncertainty of a quantity, d is the lattice spacing between the detectors and the $\delta\theta$ id the beam divergence. To minimize the uncertainty, the detectors must be placed behind the sample position, such that $\theta = 180°$ and that is the reason why they are called Backscattering Spectrometers.

1.4.2 Data Modelling

Diffusion of a particle

It can be shown that the time-dependent pair correlation function for the diffusion of a single particle is:

$$G(r,t) = \left(\frac{1}{4\pi D|t|}\right)^{3/2} e^{\frac{-r^2}{4D|t|}} \tag{1.50}$$

where D is the diffusion coefficient of the particle. By performing a Fourier transform of this function in time and space, we obtain the incoherent scattering intensity, which is the measured quantity in backscattering experiments. This function results in a Lorentzian

$$S^{qe}_{inc}(q,\omega) = \frac{1}{\pi}\frac{\hbar\Gamma(q)}{((\hbar\Gamma(q))^2 + (\hbar\omega)^2)} \tag{1.51}$$

where $\Gamma(q)$ is the width of the Lorentzian, which, in the case of free diffusion, can be written as

$$\Gamma(q) = Dq^2. \tag{1.52}$$

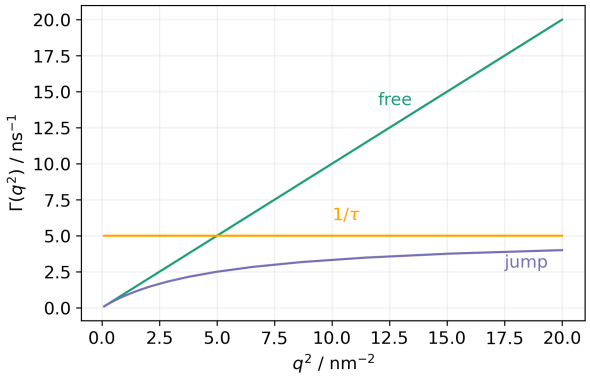

Figure 1.18: $\Gamma(q^2)$ for the case of jump and free diffusions.

The diffusion of a single particle may not be free: an example is a sub-diffusive motion, in which the particle's diffusion is constrained, as depicted in fig. 5.15. One way

to address this problem is through the so-called *jump diffusion* model. In this model, it is assumed that the particle is temporarily trapped for a time τ_0. Eq. 1.51 becomes [104]

$$S_{inc}^{qe}(q,\omega) = \frac{1}{\pi}\frac{f(q)}{((f(q))^2 + (\hbar\omega)^2)} \tag{1.53}$$

$$f(q) = \frac{D_t q^2}{1 + D_t q^2 \tau_0} \tag{1.54}$$

Here, D_t is the diffusion coefficient for free diffusion and can be extrapolated in the limit $q \to 0$, while τ_0 defines a plateau at high q.

EISF

Suppose a system experiences a perturbation at an initial $t_0 = 0$, after a transient time, it returns to equilibrium and two components can be decomposed as:

$$S_{inc}(q,\omega) = A(q)\delta(\omega) + B(q)S_{inc}^{qe}(q,\omega) \tag{1.55}$$

Here, $S_{inc}^{qe}(q,\omega)$ has already been characterized by eqs. 1.51. In a Backscattering experiment, $A(q)$ corresponds to the elastic peak of the signal, which represents all the dynamics that are too slow to be resolved and therefore appear as a static signal. For this reason, and considering $A(q) + B(q) = 1$, we can define the Elastic Incoherent Structure Factorc as $EISF(q)$.

$$EISF(q) = A(q) \tag{1.56}$$

$$B(q) = 1 - EISF(q) \tag{1.57}$$

$$\tag{1.58}$$

The $EISF(q)$ allows us to access the geometry of a particle motion. For example,

it has been derived that a particle confined in a Gaussian radial harmonic potential will exhibit an $EISF(q)$ [105]

$$EISF(q) = exp(-q^2\langle u^2\rangle) \tag{1.59}$$

where $\langle u^2\rangle$ is the variance of the Gaussian potential. This estimate can be useful for characterizing the accessible volume of hydrogen dynamics, which can be modeled as being confined within a sphere, where $\langle u^2\rangle = R^2/5$ for $(qR)^2 < 5$.

Debye-Waller factor

In a quasi-elastic investigation, the constant prefactor of $S(q,\omega)$ can be related to the vibrational density of states, which in the case of purely harmonic system is characterized by the Debye-Waller factor:

$$S(q,\omega) = e^{q^2 MSD/3} S^{trans}(q,\omega) \tag{1.60}$$

where MSD is the mean squared displacement of the vibrating atoms and $S^{trans}(q,\omega)$ is the scattering intensity defined in eq. 1.55. This MSD can provide valuable information on the mobility of the probed samples.

1.5 Neutron Spin Echo Theory

Neutron Spin Echo (NSE) spectroscopy is a powerful technique for investigating slow dynamics in materials on length scales similar to those probed by Small-Angle Neutron Scattering (SANS). NSE uses polarized neutrons and magnetic fields to encode and decode energy changes in scattered neutrons, allowing the measurement of quasi-elastic neutron scattering with extremely high energy resolution. The method was pioneered by Ferenc Mezei, who introduced the idea of using neutron spin precession to measure energy transfers, thereby circumventing the need for highly monochromatic neutron beams [106]. This innovation enables the use of a broader neutron wavelength distribution, resulting

in higher neutron flux and, consequently, improved counting statistics.

1.5.1 Instrument setup

An overview of the general instrumental setup of an NSE spectrometer is helpful to better understand its working principle. A scheme of IN15 is reported in fig. 1.19. This spectrometer was used to investigate the samples discussed in this dissertation.

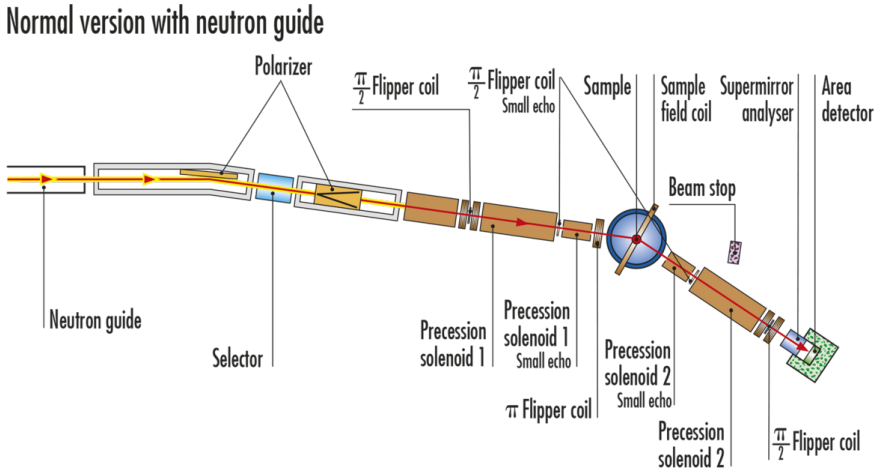

Figure 1.19: Scheme representing IN15 spectrometer, taken from ILL website [11].

The incoming neutron beam entering the setup is velocity selected to provide a wavelength distribution of a typical dispersion $\delta\lambda/\lambda \in [10, 20]\%$, polarized along the longitudinal direction with respect to the neutron guide (z-axis). A $\pi/2$ flipper rotates the polarization into the transverse direction (x-axis) before the beam enters the first solenoid. The first solenoid then induces a Larmor precession in the plane perpendicular to the beam propagation direction (x-y plane). As the neutrons pass through the solenoid, their initially aligned spins begin to precess around the magnetic field. The polarization can be express as a function of the precession angle φ:

$$P_x = \langle cos(\varphi) \rangle = \int f(v) \cos\left(\frac{\gamma_L \int B_1 dl}{v}\right) dv \tag{1.61}$$

Here, γ_L is the neutron gyromagnetic ratio and $f(v)$ is the velocity distribution of the

neutron beam. $\int_0^L B_1 dl$ is the field integral over a solenoid length L. The outer integral accounts for the velocity distribution. Due to the velocity-dependent precession, the spin ensemble dephases, and the net polarization along the x-axis decreases.

A π-flipper inverts the spin orientation, and the flipped neutrons subsequently interact with the sample. The same precession procedure is then applied by a second solenoid with identical B and L, this time in the opposite direction due to the spin flip. In the case of elastic scattering, no energy is exchanged between the neutrons and the sample, thus the velocity of the neutrons is the same, leading to the restored polarization. However, if a neutron undergoes energy exchange of an energy $\hbar\omega$ with the sample, it will accumulate a precession angle

$$\varphi_T = \frac{\gamma_L B L \hbar \omega}{m v^3} = \tau_F \omega \tag{1.62}$$

where m is the neutron mass and the prefactor in front of ω is referred to as *Fourier time* and is directly related to the field integral of the solenoid. In practice, during a beamtime experiment, the Fourier time is scanned by applying subsequently different values of currents to the solenoids, thus changing B. The q-value is set by the angle between the two branches of the instrument (before and after the sample scattering) and the wavelength of the neutrons.

Before being analyzed and detected, the neutrons spins are rotated back into the z-direction by another $\pi/2$-flipper. The spin polarization, corresponding to the amount of neutron detected at a certain Fourier time averaged over the scattering events, is the scattering intensity:

$$P_z(q, \tau_F) = \langle cos(\varphi) \rangle = \int S(q, \omega) \cos(\tau_F \omega) d\omega = I(q, \tau_F) \tag{1.63}$$

Here, the last expression corresponds to the real part of the Fourier transform of the dynamic structure factor.

It is worth mentioning that, although the probed spatial scale typically results in predominantly coherent scattering, incoherent processes do also occur. Spin-incoherent

scattering, in particular, flips the neutron spin with a probability of 2/3, leading to the following effective scattering intensity:

$$I(q,\omega) = I_{coh}(q,\omega) - 1/3 I_{inc}(q,\omega) \tag{1.64}$$

This technique is best suited for systems where coherent scattering dominates, as it probes the dynamic structure factor related to collective motions. However, in certain cases-such as hydrogen-rich samples-the coherent contribution is negligible, and the measured signal is mainly due to incoherent scattering. In such systems, the experimental outcome reflects the self-dynamics of individual particles rather than collective behavior.

1.5.2 Data modelling

By measuring $I(q,t)$ one obtains a correlation curve that provides information on the sample dynamics.

Single exponential

In the simplest case, the system exhibits a sharply monodisperse distribution of relaxation times, and $I(q,t)$ follows a simple exponential decay:

$$I(q,t) = \exp(-t/\tau) \tag{1.65}$$

The characteristic time τ corresponds to the inflection point of the decay curve and describes the dynamics probed in the sample. If the observed dynamics correspond to those of a Brownian particle, one can define $\langle\Gamma\rangle = 1/\langle\tau\rangle = Dq^2$, where D is the diffusion coefficient of the particle. Moreover, by applying the Stokes-Einstein equation, the hydrodynamic radius R_H can be obtained as:

$$R_H = \frac{k_B T}{6\pi\eta D} \tag{1.66}$$

where k_B is the Boltzmann constant, T is the temperature and η is the solvent

viscosity.

Stretched exponential

An alternative approach frequently used in NSE data modelling is the empirical Kohlrausch-Williams-Watts (KWW) model [107]:

$$I(q,t) = \exp(-t/\tau(q))^{\beta} \tag{1.67}$$

With a stretching parameter $0 < \beta < 1$. This model describes a system in which relaxation times are broadly distributed. For a diffusive particle, the average relaxation time $\langle\tau\rangle$ is given by:

$$\langle\tau\rangle(q) = \frac{\tau(q)}{\beta}\Gamma(1/\beta) \tag{1.68}$$

where Γ represents the gamma function. This function is also frequently used to model the distribution of the Rouse relaxations modes of polymer systems [34].

Zimm model

The Zimm model describes the intermediate scattering functions $I(q,t)$ of polymer systems. [29] In this model, the polymers are represented as beads connected by springs experiencing intrachain hydrodynamic interactions, with the bead size defined by the polymer's persistence length. Recent studies have shown that polyelectrolytes also experience internal friction between neighboring beads, leading to deviations in the characteristic relaxation times. [108, 109] A corresponding modified model is the ZIF model, whose intermediate scattering function ZIF $I_{ZIF}(q,t)$ can be expressed as follows:

$$\begin{aligned}
&\frac{I_{ZIF}(q,t)}{I_{ZIF}(q,0)} = \frac{\exp\left(-q^2 D_{CM} t\right)}{N} \sum_{n,m}^{N} \exp\left(\frac{-q^2 B_{n,m}(t)}{6}\right) \\
&B_{n,m}(t) = |n-m|^{2\nu} l^2 + \frac{4R_e^2}{\pi^2} \sum_{p=0.\mathrm{N}-1} \\
&\frac{A_p}{p^{2v+1}} \cos\left(\frac{\pi p n}{N}\right) \cos\left(\frac{\pi p m}{N}\right) \left(1 - \mathrm{e}^{-t/\tau_p}\right)
\end{aligned} \tag{1.69}$$

Here, l and R_e are denote the length of a segment of the polymer modeled as bead-spring chain and the end-to-end distance of the polymer, respectively. D_{CM} is the diffusion coefficient of the center of mass (CM) of the polymer, N is the number of beads and $B_{\mathrm{n,m}}(t)$ is the coefficient related to the normal mode of the dynamics of the chain, with n and m ranging from 0 to N and τ_{p} being the normal mode relaxation time. The slowest mode of the chain dynamics is given by:

$$t_z = t_{p=0} = \eta R_e^3/(\sqrt{(}3\pi)k_bT) \tag{1.70}$$

where k_bT is the thermal energy. To account for hydrodynamic friction between neighboring beads, the relaxation times are modified as follows:

$$t_{p-ZIF} = t_p p^{-3\nu} + t_{intern} \tag{1.71}$$

where t_{intern} represents the characteristic time associated with internal friction between neighboring beads. Moreover, the low-q contribution of interparticle interactions to the dynamics was considered, following the approach of Buvalaia et al. [3].

Bimodal distribution

In systems with multiple relaxation time distributions, such as a bimodal distribution, $\frac{I(q,t)}{I(q,0)}$ can be expressed as:

$$I(q,t) = (x_1 \exp(-t/\tau_1) + (1 - x_1) \exp(-t/\tau_2))^2 \tag{1.72}$$

where subscript 1 and 2 refer to the two distinct relaxation modes.

Fig. 1.20 illustrates the behavior of each model, assuming $D = 1$ nm^2/ns and $q = 5$ nm^{-1} in all cases.

1.6 Light Scattering Theory

Light scattering is a widely used technique used to characterize polymeric systems.

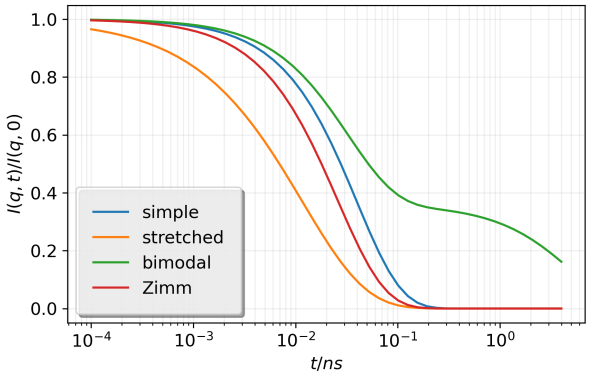

Figure 1.20: Representation of the models discussed for representing the intermediate scattering function $\frac{I(q,t)}{I(q,0)}$. In the stretched exponential model, the stretching parameter is set to $\beta = 0.7$. In the bimodal case, $x_1 = 0.4$, $\Gamma_1 = q^2 D$ and $\Gamma_2 = 0.1$.

The magnitude of the scattering vector q is given by

$$q = \frac{4\pi n_0 \sin(\theta/2)}{\lambda} \tag{1.73}$$

where n_0 is the refractive index of the solvent D_2O and θ is the scattering angle.

1.6.1 Static Light Scattering (SLS)

Analogously to neutron scattering, the molecular weight (MW) of a scatterer can be extracted by fitting the low-q region of the static scattering function with the Guinier law (eq. 1.35), from which the forward intensity $I_0 = I(q \to 0)$. I_0 is proportional to the MW of the scatterer:

$$MW = \frac{I_0}{K\, c} \tag{1.74}$$

where K is a constant related to the refractive index increment (dn/dc).

1.6.2 Dynamic Light Scattering (DLS)

DLS provides the intensity autocorrelation function $g^{(2)}(\tau)$.

$$g^{(2)}(\tau) = \langle I(t)\, I(t+\tau) \rangle \tag{1.75}$$

where $I(t)$ is the scattered intensity at a given time t and the brackets $\langle \cdot \rangle$ denotes the time average. The decay of the autocorrelation function can be related to the aggregate size and their effective interactions, provided the relaxation process arises from Brownian motion.

The models explained in the section of NSE can be applied to DLS data.

CONTIN analysis

The intensity time correlation function $g^{(2)}(q,\tau)$ can be written in terms of the field correlation function $g^{(1)}(q,\tau)$ as

$$g^{(2)}(q,\tau) = \frac{\langle I(q,t) I(q,t+\tau) \rangle}{\langle I(q,t) \rangle^2} = 1 + \beta |g^{(1)}(q,\tau)|^2 \tag{1.76}$$

where $\langle I(q,t) \rangle$ is the mean scattered intensity and β is the experimental signal-to-noise ratio. In the monodisperse case, $g^{(1)}(q,\tau) = \exp(-\Gamma\tau)$ with $\Gamma = Dq^2$ and recovering the Stokes-Einstein relations, it is possible to calculate the hydrodynamic radius. However, in the polydisperse case, there is a collection of diffusive processes and for small enough q ($qR_h < 1/2$), $g^{(1)}(q,\tau)$ can be rewritten as:

$$g(1)(q,\tau) = \int_0^\infty d\Gamma G(\Gamma) exp(-\Gamma\tau) \tag{1.77}$$

where $G(\Gamma)$ is the decay rate distribution. The CONTIN algorithm uses this integral in its discrete form and it samples $\{G(\Gamma_n)\}$ for each decay rate Γ_n.

Chapter 2

Material and Methods

2.1 Materials

To prepare the samples I used one single polyanion and a collection of polycations. The polyanion is a double hydrophilic block copolymer formed by one poly(methacrylic acid) attached to a poly(ethylene oxide) portion (PEO-PMAA). This polymer was synthethized and characterized by Dr. Kuzminskaya and the details of the characterization can be found in her dissertation [110].

As a polycation, we used a collection of statistically distributed hydrophobically modified polycations, synthethized by Dr. Özge Azeri. These polymers are hydrophobically modified versions of Poly(2-(dimethylamino)ethyl methacrylate) (PDMAEMA), where the polymerization degree, the hydrophobic modification length and abundancy are different. In table 2.1, the specifics of each polymer are reported and in the next chapter the characterization of the polycations is discussed. The general structures of the PDMAEMA and the hydrophobically modified versions are shown in fig. 2.1b-c. To complete the study on the effect of the hydrophobic moieties on the complexes, a version of PDMAEMA without hydrophobic modification was purchased from Sigma-Aldrich (product code: 909866-1G).

Stock solutions were prepared by first dissolving the polymers in heavy water (D_2O)

Table 2.1: Description of the polymers used.

ID	HM group	DP	HM-length	HM-% [g/mol]	MW/charge kDa	$\overline{MW}$ kDa	PDI
PEG-PMAA	None	45-111	0	0	0.123	10.77	1.46
C4DP175hm9	butyl	174	4	8.7	0.171	27.13	2.07
C4DP175hm4	butyl	179	4	4.3	0.164	28.03	1.99
C12DP100hm9	dodecyl	105	12	8.6	0.181	27.13	2.04
PDMAEMA	None	89	0	0	0.157	14	1.4

DP: degree of polymerisation determined from NMR
HM-length: length of the hydrophobic moieties used to modify the polycation determined from NMR measurements
HM-%: percentage of the hydrophobic modifications determined from NMR measurements
MW/charge: molecular weight per charged group determined from NMR measurements
$\overline{MW}$: average molecular weight of the polymers, estimated from NMR measurements
PDI: polydispersity index, estimated from GPC.

at a sodium chloride (NaCl) concentration of 10 mmol/kg. Concentrated solutions of deuterium chloride and sodium deuteroxide, hydrochloric acid and sodium hydroxide were used to tune the pD to the desired value. Once homogeneous stock solutions were obtained, the pD was set to 7.00 using the same acid base couple. The PDMAEMA stock solution was prepared similarly and the pD of the solution was set to 6.55. Stock solutions were prepared between 3% and 0.1% wt, depending on the investigation.

IPECs were prepared by mixing portions of the polyanion and the polycation stock solution in appropriate mixing ratio z^*.

$$z^* = \frac{[-]}{[-] + [+]} \tag{2.1}$$

Here, $[+]$ and $[-]$ are, respectively, the concentrations of the amino groups and the carboxylated groups. Here it must be pointed out that this means the maximum possible charges, while the real charges will be somewhat less and accordingly z^* is not equal to the charge ratio in the system.

To calculate z*, the experimental value of the molecular weight per charge unit M_{CU} was considered, determined from the percentage of hydrophobic modifications.

The detailed characterisation of the used PEO-PMAA is given elsewhere (precisely in the dissertation Dr. Kuzminskaya at page 23) [110] while the structure is depicted in fig. 2.1a.

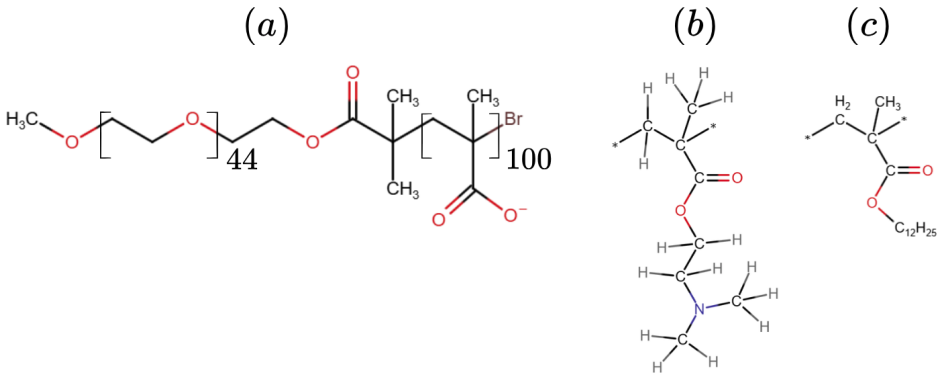

Figure 2.1: Chemical structure of the diblock copolymer PEO-PMAA (a) and polycation PDMAEMA (b) used. (c) hydrophobically modified unit in the case of HM-PDMAEMA.

Further discussions on the characterization of the polyelectrolytes are discussed in the next chapter.

In all the cases, the needed solvent have been added as first specie to the vial, which was followed by the polymer with the most abundant volume and then the other polymer. While adding the polymer solution, the vial was vortexed to avoid local overconcentration and potentially local precipitation. The samples were prepared at least 12 hours before SANS measurements and 3 days before light scattering measurement. After preparation all samples were resting on a roller for at least 12 hours to ensure homogeneity and avoid local over-concentrations.

2.2 Methods

2.2.1 Small Angle Neutron Scattering

SANS spectra of IPECs prepared from hydrophobically modified PDMAEMA were acquired using the instrument BILBY at ANSTO, Sydney, Australia [111]. The instrument was operared with a wavelength range of $\lambda \in (0.2 - 2)$ nm, and a sample to detector distances set at 18 m (rear detector), 3.5 m (horizontal curtain detector), and 2.5 m (vertical curtain detector), yielding a q-range of 0.01-5 nm^{-1}. IPECs prepared from PDMAEMA were measured on both D22 and D33 at the ILL [112, 113, 114], Grenoble,

France, exploring a similar instrumental configuration ($\lambda = 0.6nm$, detector distance of 17.6 m). Additional measurements to complete the mixing ratio scan have been performed during internal availability [115] Measurements were performed at 25 °C in both cases. Additional temperature-dependent measurements were performed at SAM, to test the stability of the structure for different temperatures. Additional concentration-dependent measurements were also performed at D22 to test the dilution laws of the polyelectrolytes.

Samples were measured in *Banjo* quartz cells (shown in fig. 2.2) of a thickness of either 2 mm or 1 mm, with respect to the availability and without noticing effects on the measurements.

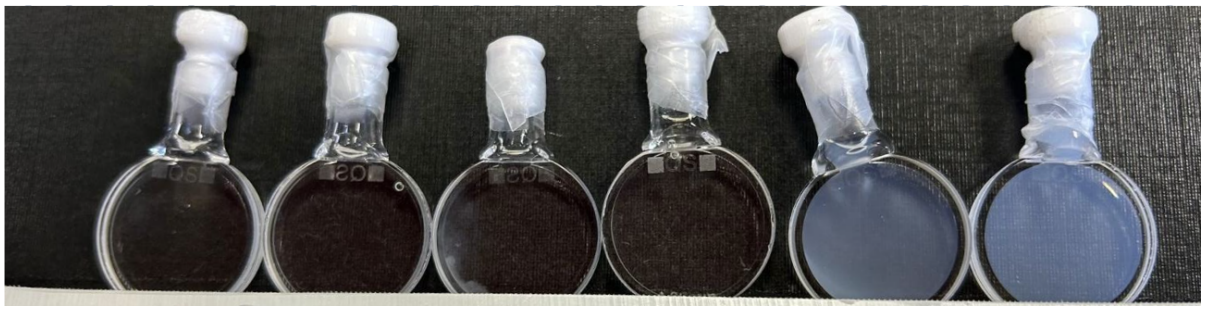

Figure 2.2: Banjo cells filled with IPECs samples made with PDMAEMA at different z^*.

After several tests, it was concluded that 3 minutes for each configuration were enough acquisition time to obtain a good quality signal for the investigation, however stock solutions were tested for longer times.

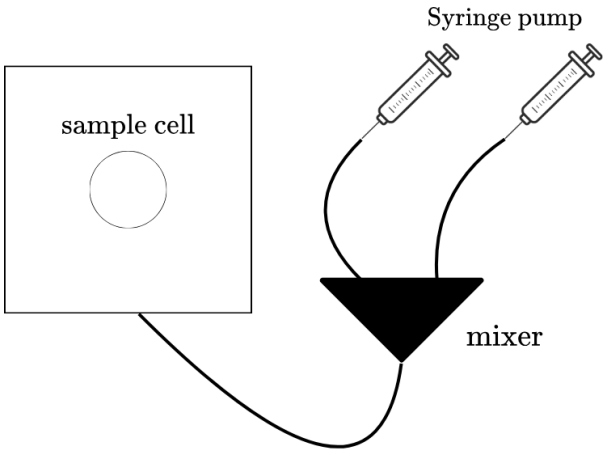

Figure 2.3: Sketch representing the instrumental setup of the in-situ mixing investigation.

To investigate the effect of sample aging, an experiment in which mixing occurred in situ was also performed, using an in situ reactor built by Avik Das (sketch of the setup depicted in fig. 2.3). In this setup, the two stock solutions were injected at different flow rates, resulting in a gradual change in the mixing ratio. Despite some issues related to the thickness of the capillaries used, the resulting data resembled those obtained from fully equilibrated samples, suggesting that equilibration does not play a significant role in the investigated q-range. Appendix A further discusses the reproducibility of the experiment.

2.2.2 Neutron Spin Echo

Samples were measured at IN15 during 3 different beamtimes at ILL.[114, 116, 112]. The instrument was set up to cover a q-range of $q \in [0.21, 1.63]$ nm^{-1} and a Fourier time range of $4.84 \times 10^{-2} < t <$ 477 ns) combining 6 different configurations ($\lambda = 6, 10, 13.5$ Å, scattering angles $\theta = 3.5, 6, 6.5, 8, 9.5°$.

The resolution functions of the instruments were determined for each experimental setup using the elastic scattering of graphite. The resulting intermediate scattering functions were corrected for the solvent background dynamics.

The investigations were performed using quartz rectangular cells with the size of 40 ×

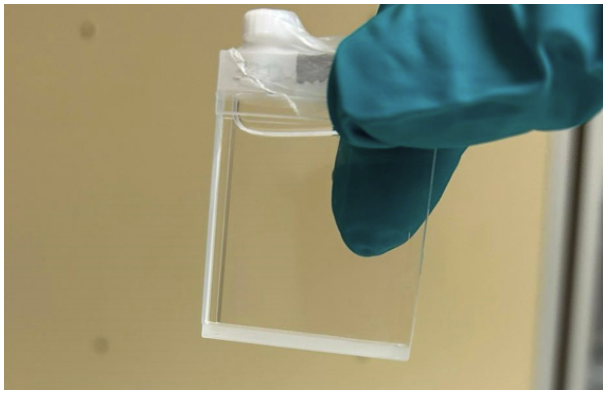

Figure 2.4: Quartz cell used during an IN15 investigation.

30mm and a thickness of $4, 2, 1$ and 0.5 mm, depending on the availability of the solution (example shown in fig. 2.4). Samples were scanned in up–down mode at IN15 to assess the scattering intensity and determine the measurement time for each configuration. Samples were measured prior equilibration on a roller, however for the sample made with C12DP100hm9 at $z^* \simeq 0.6$, we observed phase separation in the cell. The treatment of this particular sample is discussed in details.

2.2.3 Neutron Backscattering

Samples were measured at IN16b using the Doppler mode with Si(111) monochromator and analyzer crystals.[114] In this configuration, we studied S(q, ω) in a q-range of q $\in [1.91, 18.88]$ nm^{-1} and energy transfer E $= \hbar\omega \in \pm$ 30 μeV. Samples were injected in a double-walled cylindrical aluminum can with an outer diameter of 21.7 mm and a gap of $\simeq$ 0.1 mm. The can was then sealed with Indium wire and mounted in a cryofurnace allowing the control of the temperature during the entire data acquisition. After several tests, samples were scanned in both Elastic and Inelastic Fixed Window Scan mode (E/IFWS). Each sample were measured at T=280, 298 and 310 K, requiring around 4 hours of beamtime.

2.2.4 Light Scattering

Static (SLS) and Dynamic (DLS) light scattering experiments presented in this dissertation were performed using an ALV/CGS-3 instrument equipped with a He-Ne laser ($\lambda = 632.8$ nm), immersed in a toluene bath to reduce residual scattering and interface reflections. Data were acquired at a scattering angle θ ranging from 20° to 130°, using an ALV-SP goniometer.

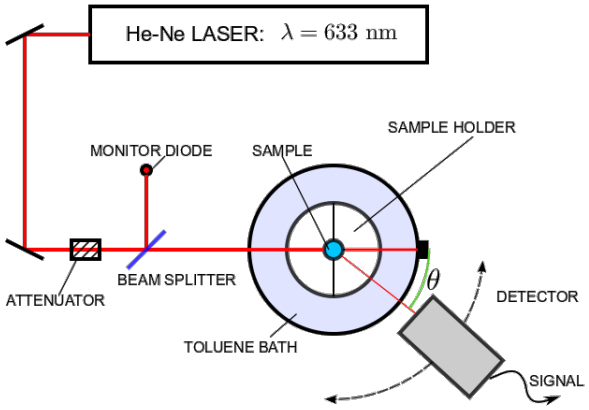

Figure 2.5: ALV setup, taken from [14].

The IPECs formed by hydrophobically modified PDMAEMA were tested by Bin Dai, at the Technische Universität Berlin. The IPEcs formed by standard PDMAEMA were probed using the same setup at ILL by the author. In the case of biphasic samples, measurements were carried out on the supernatant.

2.3 Complementary techniques

2.3.1 Gel Permeation Chromatography (GPC)

GPC was performed to characterize the molecular weight of the synthetized polymer by Özge Azeri. The measurements were carried out at the University of Potsdam, whose support is gratefully acknowledged.

2.3.2 Nuclear Magnetic Resonance (NMR)

NMR data concerning the hydrophobically modified PDMAEMA were collected by Özge Azeri and analyzed by Bin Dai.

^{1}H-NMR spectra were acquired using a Bruker Avance II 500 MHz spectrometer equipped with 5 mm probe tubes, at a temperature of 300 K. Sample solutions were prepared either in D_2O or in 16 wt% EtOD. For each measurement, around 0.6 mL of solution was used. The pH was adjusted using DCl to ensure proper dissolution of the polymer.

2.3.3 pH Titration

pH titration was carried out by Jana Lutski using a Titrando instrument (Metrohm) with tiamo-software, at room temperature. The data were analyzed by the author in collaboration with Bin Dai.

Chapter 3

Precharacterization of the polyelectrolytes

3.1 Molecular structure of the hydrophobically modified PDMAEMA

While the characterization of the double-hydrophilic block copolymer has already been extensively discussed in the dissertation of Olga Kuzminskaya [110], it was necessary to thoroughly characterize the degree of the hydrophobic modifications applied to PDMAEMA in order to determine the appropriate mixing ratio. These polymers were synthesized by Özge Azeri, and the interpretation of the results was a joint effort involving the author, Ozge Azeri and Bin Dai. Specifically, quantitative NMR data were acquired and analyzed by Bin Dai and Özge Azeri, while the titration results were discussed collaboratively.

The first valuable insights were obtained from the GPC investigation, conducted by the University of Potsdam and shown in fig. 3.1.

The most striking observation is that these polymers are highly polydisperse . From the distribution, C4DP175hm4 shows a narrower peak at a higher value, suggesting a higher degree of polymerization (DP). From the number-average molecular weight M_n and the weight-average molecular weight M_w, one can estimate the polydispersity index

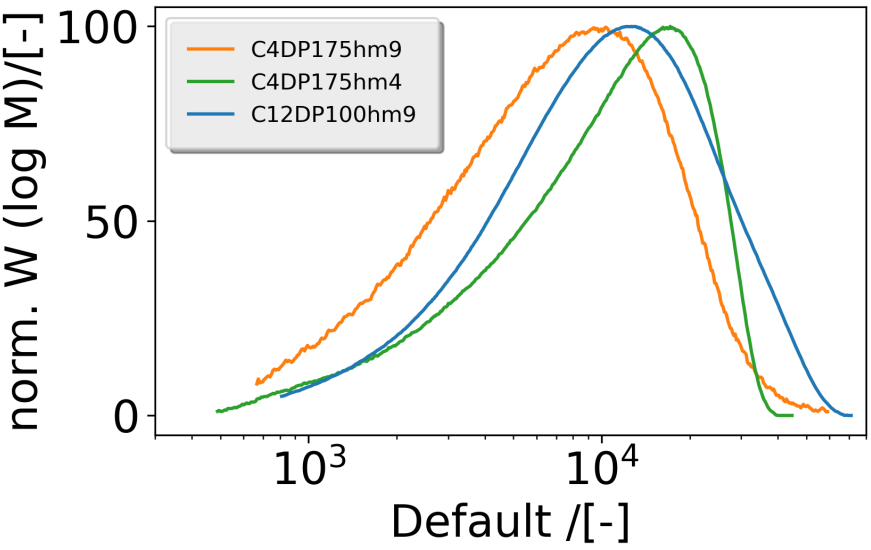

Figure 3.1: GPC applied to the hydrophobically modified PDMAEMA, from which MW and Mn have been calculated.

(PDI) as:

$$PDI = \frac{M_w}{M_n}. \tag{3.1}$$

This information is reported in table 3.1.

Table 3.1: Information extracted from Gel Permeation Chromatography (GPC) for the hydrophobically modified polymers.

	M_n	M_w	PDI
C4DP175hm9	4.50E+03	9.32E+03	2.07
C4DP175hm4	6.14E+03	1.22E+04	1.99
C12DP100hm9	6.52E+03	1.33E+04	2.04

M_n: number-average molecular weight (g/mol).
M_w: weight-average molecular weight (g/mol).
PDI: polydisperdity index.

While GPC can estimate the size of the polymer, NMR provides structural information on the molecular composition of the polymers. The ^{1}H-NMR spectra are shown in fig. 3.2.

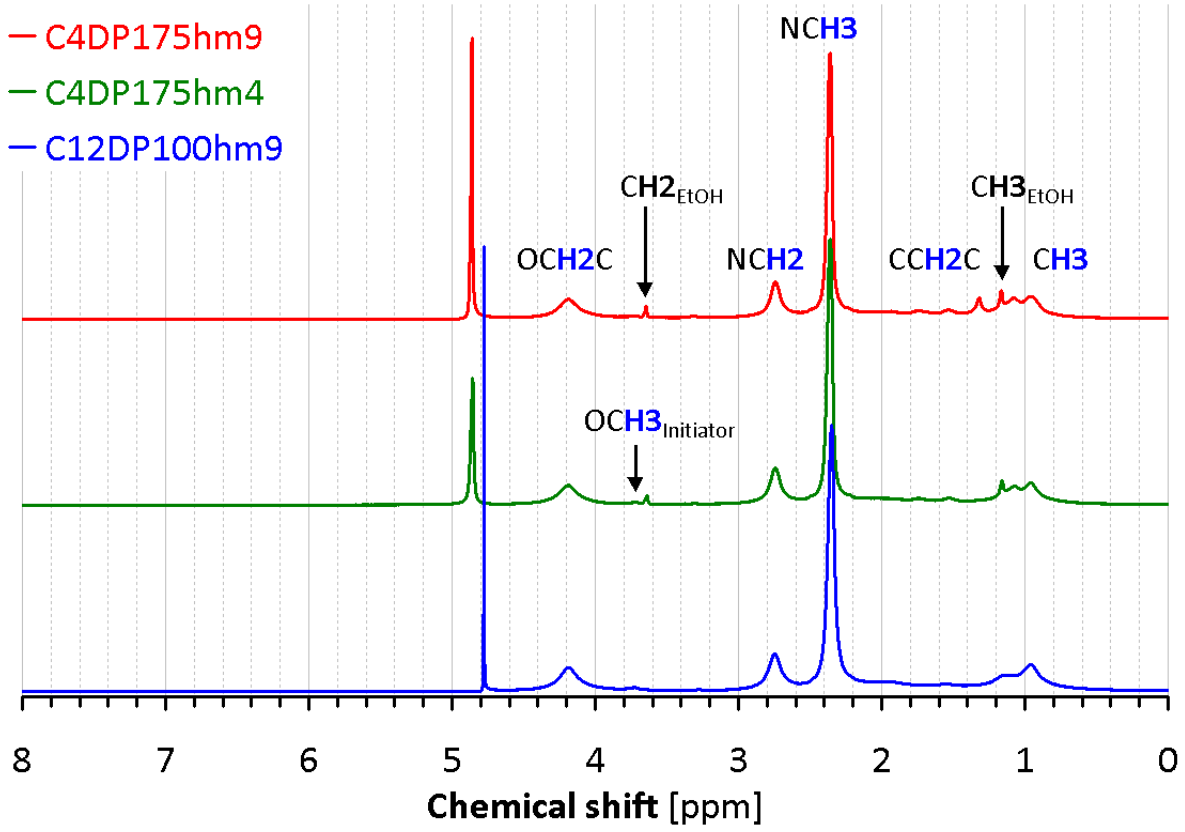

Figure 3.2: ^{1}H-NMR spectra of the three hydrophobically modified polymers, with peaks labeled according to the corresponding chemical groups. Figure produced by Bin Dai.

The molecular weight of a hydrophobically modified polymer can be expressed as

$$MW = DP \times \{MW_{DMAEMA} + x(MW_{HM} - MW_{DMAEMA})\} \tag{3.2}$$

where MW_{DMAEMA} is the molecular weight of DMAEMA while MW_{HM} is the molecular weight of the hydrophobic moiety, which can be either a butyl or a dodecyl substituent. From the NMR spectra, it was then necessary to calculate the degree of polymerization (DP) and the degree of substitution (x). While DP can be estimated by

comparing the peaks corresponding to the oxygen in each group OCH_2 and the initiator $COOCH_3$ (from the literature, $COOCH_3$ peak is at 3.71 [117]), x was estimated by comparing the bonds between the Nitrogen atom (in the unmodified group), and normalizing them over the bonds with the oxygen atom of the group $COOCH_2$. The structures of the modified and unmodified PDMAEMA are shown in fig. 2.1 By following this approach, the DP, the degree of hydrophobic modification and the molecular weight of the polymer MW have been estimated. Moreover, the M_{CU} was also estimated as the MW per charge unit assuming that all the ionizable groups are charged.

$$M_{\mathrm{CU}} = \frac{MW}{DP} \tag{3.3}$$

Finally, from pH titration, the apparent acid dissociation constant $\mathrm{p}K_{\mathrm{a}}$ of the polymers was calculated.

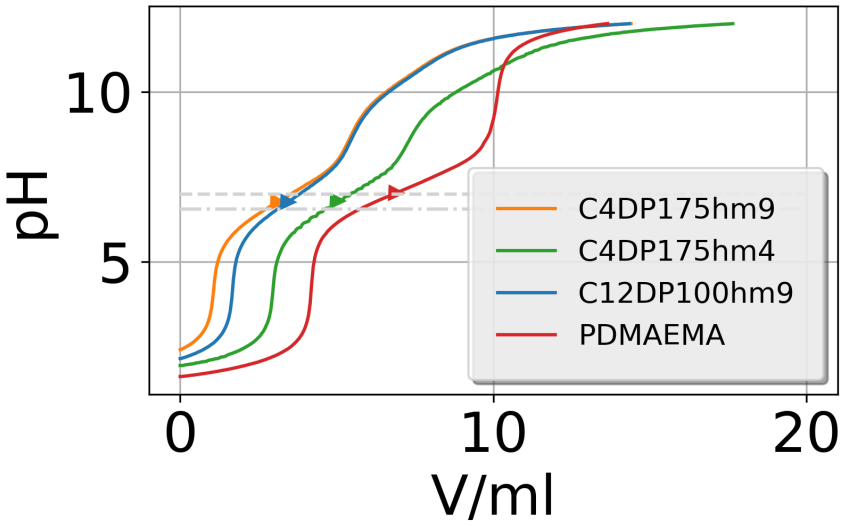

Figure 3.3: Titration curves of the investigated polycations. $\mathrm{p}K_{\mathrm{a}}$ values are marked with triangles.

In fig. 3.3, pH-titrations of the polycations are shown, where polymers were titrated with NaOH 0.1 M. The titration curves are consistent with previous observations for

PDMAEMA, which allows determining the concentration of charges along the polyelectrolyte [118]. At the beginning of titration, all the amino groups of PDMAEMA are protonated due to the excess of acid. As NaOH is added, the amino groups become unprotonated until pK_{a} is reached, where the protonated and unprotonated species are equimolar. From these titration curves, if EP1 and EP2 are the two inflection points and V_{EP1} and V_{EP2} the volume of titrating solution, the volume identifying the pK_a (V_{pK_a}) was calculated as:

$$V_{pK_a} = \frac{V_{EP1} + V_{EP2}}{2} \tag{3.4}$$

From V_{pK_a} it was possible to grafically estimate the pK_a.

An effective mean $pK_a \simeq 7$ has been estimated and reported in table 3.2 (PDMAEMA pK_{a} has been reported to be 8.4 and it was observed already a shifted towards smaller values induced by polymerization [119]).

Table 3.2: Information extracted from titration experiments

Name	M_{CU} **(g/mol)**	**p**K_{a}
C4DP175hm9	170	6.76
C12DP100hm9	150	6.79
C4DP175hm4	151	6.76
PDMAEMA	161	7.03

M_{CU}: molecular weight per charged unit, calculated from titration data.
pK_{a}: apparent acid dissociation constant derived from titration curves.

From the titration data, we calculated the molecular mass per charged unit as:

$$M_{\mathrm{CU}} = \frac{m_p}{cV} \tag{3.5}$$

where c and V are the molarity and the difference of volume added of the titrand base added between the first and second inflection points, respectively (inflection points have been estimated from the derivative of the curve). m_p is the mass of the polymer in the solution. The values of M_{CU} are shown in table 3.2, in reasonable agreement with those previously derived from NMR. A deviation is shown in the case of hydrophobically

modified polyelectrolytes.

Although pK_a is close to the pD of the prepared samples, we consider the amine groups to be protonated to a larger extent, due to the electrostatic environment within the complexes.

All the information are summarized in table 2.1.

3.2 Phase behavior of the IPEC solutions

Before delving into the nanoscale properties of the polyelectrolyte complexes, it is instructive to characterize the samples through visual inspection. A picture showing a general overview of the behavior of the complexes as a function of the mixing ratio z^* is shown in fig. 3.4.

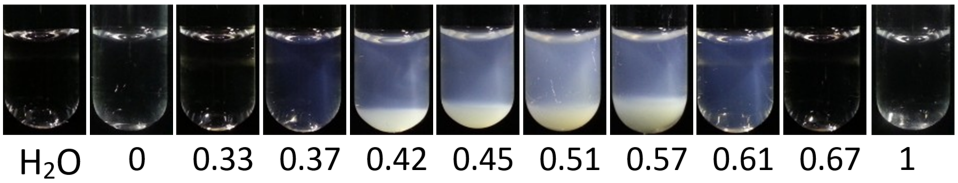

Figure 3.4: Pictures of the IPECs samples given by the polycation C4DP175hm9 for different mixing ratio z^*. Samples from DLS investigation. Pictures taken by Bin Dai.

From the image, signs of complexation become evident as the system approaches the equimolar mixing ratio.

The mixtures were consistently turbid within the range $z^* \sim [0.4, 0.6]$, transparent outside this interval and formed coacervates (liquid-liquid phase separation, LLPS) near equimolarity.

In case of LLPS, lower phase appeared white and denser than the supernatant, suggesting it contains the majority of the polymers; however, the supernatant was never fully transparent. The volume ratio between the two phases depended on both the mixing ratio and the used polycation; despite this in most of the cases, more than two-thirds of the total volume remained in the supernatant phase.

Double-hydrophilic block copolymers complexes have shown signs of complexation near the equimolar regime in several studies [23]. The nature of the complexation is typically influenced by the strength of the polyelectrolyte: weak polyelectrolytes lead to weak complexations, resulting in a more hydrated core and lower interfacial tension [9]. Another important factor affecting the phase behavior of the complexes is the length of the neutral hydrophilic block. Here, the PEG block has a degree of polymerization $DP = 45$, while the charged blocks have a $DP \simeq 100$.This appears insufficient to stabilize the complexes at equimolarity. LLPS has been observed in several studies under these conditions, leading the equimolar regime to be referred to as the *unstable region* [63].

Fig. 3.5 shows the phase behavior as a function of z^* for different polycations. This plot includes observations from the polymer prepared for for both light scattering and neutron scattering investigations. Details on sample preparation can be found in Chapter 2.

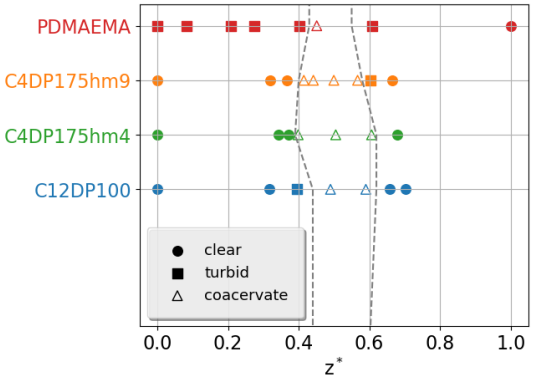

Figure 3.5: Phase behaviour of the IPECs as a function of the mixing ratio z^* at 25 °C from stock solutions at pD = 7. PDMAEMA was prepared at pD = 6.55. The dashed lines correspond to the phase boundaries. The phase plot refers to the phase behavior of the sample prepared for light scattering and neutron scattering investigations.

The pure PDMAEMA was clear after being dissolved in D_2O, but became turbid when lowering the pD towards 6.55 (we observed the change visually at pD $\simeq$ 7.9). This effect might be related to the pH responsive nature of PDMAEMA. While lowering the pH this polymer becomes more charged and compact and thus the polymer-polymer hydrophobic interaction increases. [120] Surprisingly, the hydrophobic modifications

prevent the polymer to collapse, resulting in a less packed macromolecule and a weaker polymer-polymer interaction. This polymer experiences a coil-to-globule transition while changing the degree of protonation [121]. Surprisingly, this effect was not observed in the HM-PDMAEMA polymers. Here, apparently, the conformation is dominated by the presence of the hydrophobic modification and the observed phase behavior is not sensitive to the variation of the HM.

Chapter 4

Structural characterization

In this chapter, the structure of self-assembly aggregates obtained by mixing different hydrophobically modified Poly[2 (Dimethylamino)ethyl Methacrylate] (HM-PDMAEMA) with the Double Hydrophilic Block-Copolymer (DHBC) is investigated. These structures have been investigated using Small Angle Neutron Scattering (SANS) and Static Light Scattering (SLS) for different mixing ratio z^* values defined as $z^* = \frac{[-]}{[-]+[+]}$, where $[*]$ is the molar concentration of all the chargeable species present in the systems. By testing different polycations, the role of the hydrophobic modification length and fraction, as well as the effect of mixing PEs with different degree of polymerization (DP) is investigated.

The sample preparation and the experimental methods have been already discussed in chapter 2. This chapter begins with the SLS investigation, followed by the SANS study of the individual pure polyelectrolyte solutions, and the models applied to describe the scattering intensity $I(q)$ obtained via SANS: the first model was used to identify the trends in the power-law behavior, followed by a two component Beaucage model. After these 2 *ad-hoc* models, the system was described as hydrated spheres connected in a fractal manner and finally the hypothesis of the presents of polymersomes in our samples was explored. The results discussed in this chapter have been recently published [16].

4.1 SLS

While SANS is one of the most powerful techniques to probe nanoscale structures in PE solutions, neutron scattering is a demanding and costly resource, and a strong justification is required to perform experiments in a neutron facility. In this sense, it is useful to preliminary probe the samples via light scattering.

SLS was performed in the scattering vector range 0.006<q<0.02 nm^{-1}, corresponding to features larger than $r = \frac{2\pi}{q} \simeq 300$ nm. As specified in the sample preparation, Bin Dai conducted the light scattering measurements on the IPECs formed by the hydrophobically modified polycations, while the author conducted the same investigation on the IPECs formed with unmodified PDMAEMA. The data treatment was performed by the respective experimenters and is described in section 2.

In fig. 4.1a, the SLS extracted from different mixing ratio z^* for the IPECs formed by the polycation PDMAEMA has been displayed as an example.

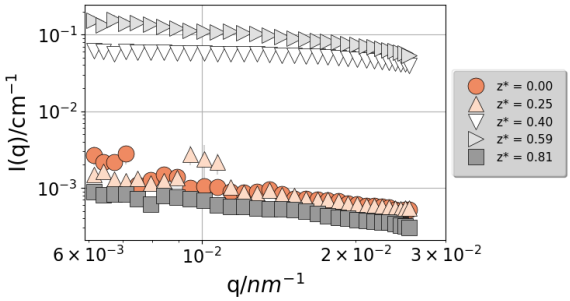

(a) SLS curves at various mixing ratios z^* for IPECs formed by the polycation PDMAEMA.

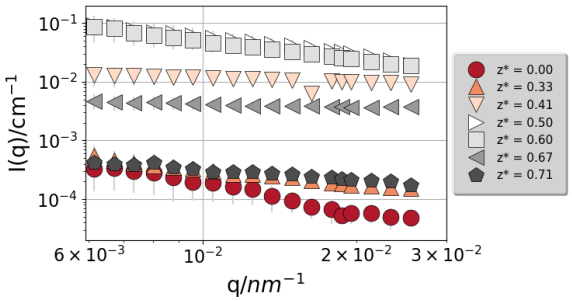

(b) SLS curves at various mixing ratios z^* for IPECs formed by the polycation C12DP100hm9.

Figure 4.1: Comparison of SLS curves for IPECs formed by different polycations: (a) PDMAEMA and (b) C12DP100hm9.

Despite the significant uncertainties, samples closer to equimolar mixing ratio showed a higher forward scattering intensity $I(q \to 0)$, consistent with the visually observed increase in turbidity. For a more quantitative interpretation of the data, Guinier Analysis was applied (explained in section 2). By comparing the same plot for the polycation

C12DP100hm9 (in fig. 4.1b) and, more generally, the IPECs formed by hydrophobically modified polycations, the plateau was not always reached.

Fig. 4.2 shows the Guinier plots of the investigated samples, with the corresponding fits superimposed. The data were fitted using the Guinier model $I(q; I_g, R_g)$ described in eq. 1.35, where I_g is the forward scattering intensity and R_g is the radius of gyration.

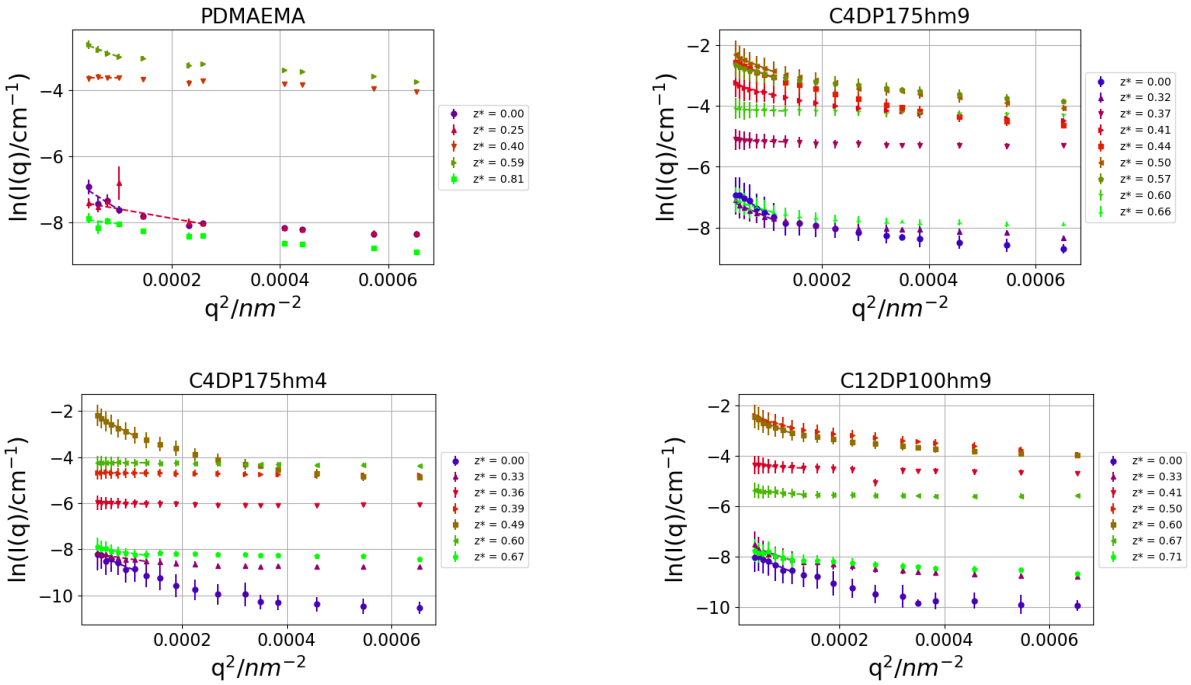

Figure 4.2: Guinier plot for the IPECs prepared at different mixing ratio ($z^* = \frac{[-]}{[-]+[+]}$) for different polycations.

Since the samples were turbid, light scattering measurements could have been affected by multiple scattering events, potentially leading to inaccurate q-dependent intensity measurements. To assess the reliability of the model, the results from the standard Guinier model and the modified version have been compared. The modified Guinier model accounts for further aggregation effects, as explained in chapter 1 and eq. 1.37. The comparison is shown in fig. 4.3. In the case of the extended Guinier approach, the condition $qR_g < 1$ was relaxed.

The two different approaches extracted similar R_g and the low-q power law D for the

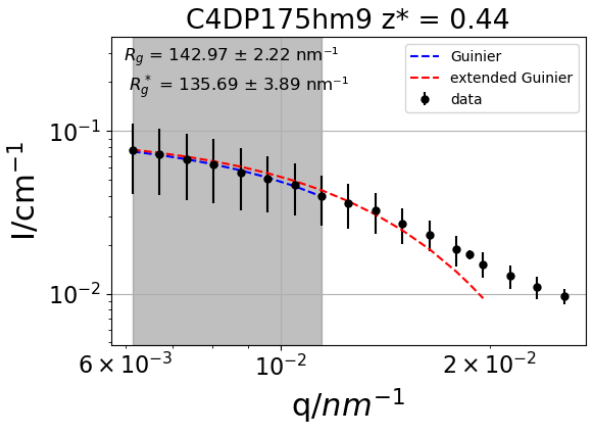

Figure 4.3: Comparison between the Guinier and the extended Guinier model. R_g represents the radius of gyration extracted with the standard Guinier while R_g^* shows the radius of gyration in the case of non-finite structures within the q-range. Data from the sample at a mixing ratio $z^* = 0.44$ and for the sample C4DP175hm9. The gray area correspond to the q-range in which the standard Guinier analysis was performed.

extended Guinier model was negligible. These observations suggested that the accessible q-range was not sufficiently low to reliably probe the larger structural features, and the extracted radius of gyration R_g represented a lower bound for the actual value in most cases.

With this assumption in mind, we analyzed the parameter extracted from the Guinier model, shown in fig. 4.4.

The forward scattering intensity I_g (b) peaked around the equimolar regime, with substantial increases in the range $0.3 < z^* < 0.7$, depending on the specific polycation used. The increase in forward intensity was associated with a transition from polymeric semidilute solutions to polymer micelles. Notably, this transition appears remarkably sharp, in agreement with the general behavior of double-hydrophilic block-copolymers [63]. The molecular weight (MW) of the PE aggregates was estimated from the forward scattering using eq. 1.74. Its behavior as a function of z^* is shown in fig. 4.5.

MW was peaked at equimolarity regime, where MW increases by a factor of 3000, showing again the transition from polyelectrolyte solutions to polymer micelles. The ratio between the peak of MW and the value at $z^* = 0.0$ can be used as a rough estimate of

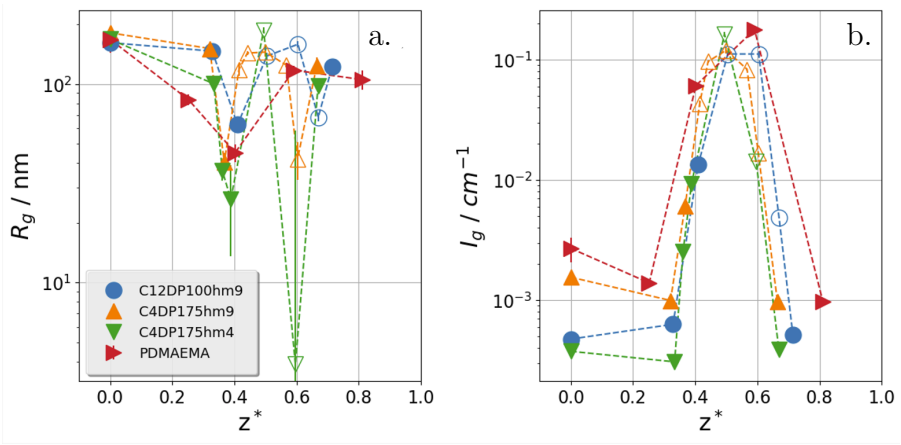

Figure 4.4: Radius of gyration R_g (a.) and forward scattering intensity I_g (b.) extracted at different values of mixing ratio z^* and for various IPECs. Empty symbols indicates samples undergoing LLPS, as discussed in chapter 3.

the maximum aggregation number N.

To understand the size of the polymeric features and the aggregates formed, R_g (shown in fig. 4.4-a) can be examined; however, pure PE solutions are known to be affected by long-range density fluctuation correlations, which explains why R_g appeared larger far from the equimolar regime. [122, 123] As the system approached the equimolar regime, the scattering from the density fluctuations disappeared and the aggregates were still small, resulting in a minimum of R_g where I_g began to increase. Ultimately, within $0.3 < z^* < 0.7$, R_g exhibited a maximum at equimolar regime for most of the IPECs investigated.

From R_g and N one can also estimate the apparent density of the aggregates, assuming they are spherical. Let N_1 and N_2 be the aggregation numbers of the polycation and polyanion, respectively, such that $N = N_1 + N_2$, the volume occupied by the polymer is then:

$$V_p = V_1 N_1 + V_2 N_2 \tag{4.1}$$

Where V_1 and V_2 are the volumes of a single polycation and polyanion respectively.

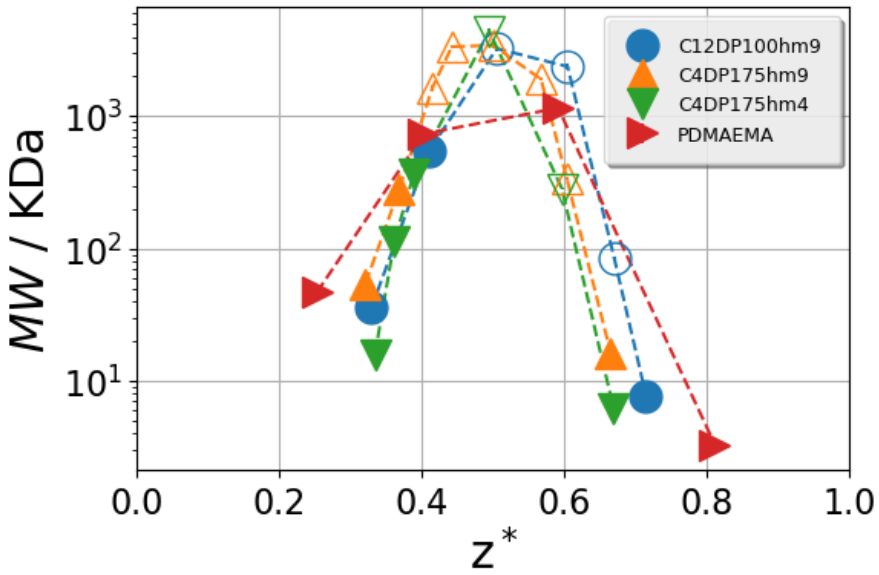

Figure 4.5: Molecular weight MW extracted for different values of mixing ratio z^* and for different IPECs. Empty simbols indicate samples undergoing LLPS, as discussed in section 3.

Knowing that the radius of a sphere $R = \sqrt{5/3}R_g$, the volume of the aggregate V_{agg} and the volume fraction occupied by the polymer material ϕ_p are:

$$V_{agg} = \frac{4\pi}{3}R^3 \tag{4.2}$$

$$\phi_p = V_p/V_{agg} \tag{4.3}$$

$$\tag{4.4}$$

the *average density* is then the weighted average of the polymer and D_2O densities:

$$d_a = \phi_p d_p + (1 - \phi_p)d_{D_2O} \tag{4.5}$$

Here, d_a is the average density between the two PEs, weighted by their molar concentrations, and d_{D_2O} is the density of D_2O. The specific density of the polymer was estimated from the monomer density; however, a more systematic approach would in-

volve performing densitometric measurements on the individual components and the complexes.

Furthermore, it can be shown that the relative error in the volume of a sphere is three times the relative error in its radius:

$$\frac{dV}{V} = \frac{V_{shell}}{V_{sphere}} = \frac{4\pi R^2 dR}{\frac{4\pi R^3}{3}} = 3\frac{dR}{R} \tag{4.6}$$

where V_{shell} represents the volume of a spherical shell with $R < r < R + dR$ and V_{sphere} is the volume of a sphere of radius R. Additionally, the error in I_g must also be propagated, resulting in a final relative uncertainty in d_a that is inherently large. Given the uncertainties in this analysis, estimating an accurate apparent density was difficult.

4.2 SANS

4.2.1 Characterization of the Polyelectrolytes

In this section, the SANS data from the pure polyelectrolyte solutions are discussed. By looking at the scattering intensity (shown in fig. 4.6), we saw the typical low-q upturn of polyelectrolyte semidilute solutions: this contribution is still debated; however the most accreditated hypothesis is this upturn to reflect long-range concentration fluctuations arising from multichain domains [122].

The high-q regime ($q > 0.1\,\mathrm{nm}^{-1}$) showed a broad peak followed by a power law, typical of semidilute polyelectrolyte solutions: the broad peak represents the electrostatic repulsion between chains while the power law represents the polymeric structure. A proper model to represent polyelectrolytes is a gaussian chain, where excluded volume effect and the interaction with the solvent is taken into account, as described in the section 2 and depicted in equation 1.45. This model was applied to the investigated polyelectrolyte solutions.

The high-q and low-q are spaced enough to expose the correlation peak for all the sample but the C4DP175hm9, where the low-q power law occurs at higher q-values. In

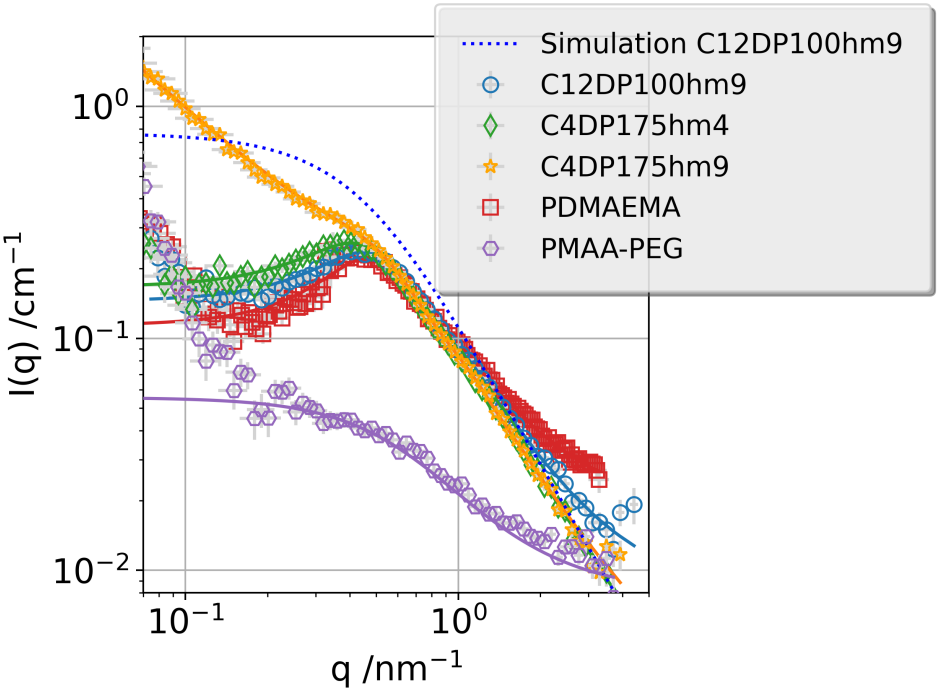

Figure 4.6: SANS data from the pure polymer solutions, measured at c=1.0%wt at ANSTO. Errorbars are shown in grey and solid lines represent the fit results of the stock solution model. A simulation of the Debye model from C12DP100hm9 architecture is displayed in light-blue dotted line.

this case, it was necessary to fit and divide the power law, to extract information from the correlation peak.

The correlation peak was observed around 0.4 nm^{-1} for all samples. However, a small shift towards lower q-values was observed for the HM-polymers, which simply can be explained by the fact that the chain concentration decreases due to the higher MW per monomer unit. To describe the correlation peak we applied a structure factor of hard spheres $S(q)$ [124, 125] with a generalized Gaussian coil intensity $P(q)$ (detailed in eq. 1.45).

To test the spatial reorganization of the polymers, SANS measurements on dilution series of the samples C12DP100hm9 and C4DP175hm4 have been made (data are shown in fig. 4.7. From the concentration dependence of the position of the correlation peak

Table 4.1: Results from fitting the structure factor model on the SANS response of the pure polycation solutions.

Sample	I_0/cm^{-1}	R_g/nm	ν	ϕ	R_{HS}/nm	c/wt%	MW_{Sq}/kDa
C12DP100hm9	0.33 ± 0.01	2.59 ± 0.07	0.48 ± 0.02	0.114 ± 0.004	5.40 ± 0.07	1.0	8.3 ± 0.7
C4DP175hm4	0.39 ± 0.01	2.95 ± 0.08	0.53 ± 0.02	0.107 ± 0.003	5.87 ± 0.07	1.0	12.7 ± 1.1
C4DP175hm9	1.1 ± 0.1	1.48 ± 0.08	0.6 ± 0.2	0.08 ± 0.01	5.3 ± 0.2	1.0	2.2 ± 0.5
PDMAEMA	0.28 ± 0.01	2.44 ± 0.08	0.47 ± 0.03	0.138 ± 0.005	5.63 ± 0.09	1.0	5.7 ± 0.6

I_0: scattered in intensity at q→0
R_g: radius of gyration from the Debye model
ν: the parameter assessed as the goodness of the solvent
ϕ: volume fraction
R_{HS}: characteristic length of interaction
c: weight concentration
MW_{Sq}: molecular weight calculated from the structure factor as shown in the main text.

q_{peak} i.e. the mean spacing d_{peak} we extracted a power law $D \simeq 1/3$ ($D_{C12DP100hm9} = 0.398 \pm 0.004$ and $D_{\text{C4DP175hm4}} = 0.367 \pm 0.07$), which is characteristic of isotropically distributed scatterers. This observation reinforces the hypothesis of the scatterers being represented as single chains of PE in solution.

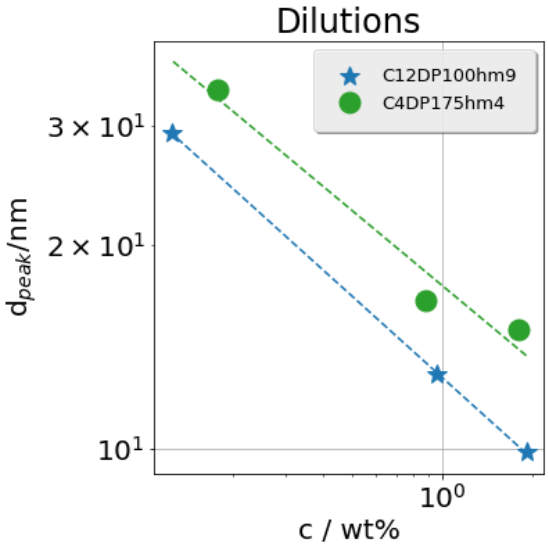

Figure 4.7: Position of the correlation peak in the real space as a function of the concentration.

All the extracted parameter, representingthe characterization of the polycations so-

lutions from the SANS data, are reported in table 4.1.

One of the justification of our investigation was the application of PE in the drug delivery: it has been shown that HM-PE can form aggregates where the hydrophobic moieties assemble into pockets and such pockets can load hydrophobic molecules. These structures are interesting in the context of solubilization of active agents [59, 60]. $I(q)$ did not show any feature compatible with the presence of hydrophobic pockets; however, to test the contrast of these features we calculated what would be the scattering contribution.

Noda et al. described a micellar structure formed by hydrophobic moieties in HM-PEs at modification percentage $\simeq 9$ mol% with an aggregation number $N_{agg} \simeq 195$.[126] We computed the theoretical SANS signal with the following conditions: the size of a micelle would be given by the Tanford length [127], we would have a radius $R = 1.67$ nm and so the estimated aggregation number N_{agg} would be:

$$N_{agg} = V/V_{chain} \simeq 58 \tag{4.7}$$

where V_{chain} is the volume of a chain and V is the volume of the micelle. We simulated the scattering of a single chain of C12DP100hm9 from the Debye model where I_0 is estimated using 1.31 and $R_g = DP^{\nu}b$, where DP is the degree of polymerization and b is the monomer length. Owing to the charge environment, it was difficult to deduce ν analytically, therefore we fitted it from the data. This simulation proved that the scattering curves are compatible with single polymers. Calculating the forward intensity, we found $I(0) \simeq 1.2 \times 10^{-3}$ cm^{-1} where n_d is the number density of hydrophobic micelles and ΔSLD is the scattering length density. This calculation confirmed that, even if all alkyl chains would reorganize into micelles, they would not be visible via SANS. Surprisingly, the hydrophobic modifications are showing a stronger effect in the dynamics of the same samples, as it is discussed in the next section.

In fig. 4.6, the violet curve represents the scattering of the double-hydrophilic block-copolymer. Two different regimes can be observed: at low-q, the intensity grows as a power law, while at q $\simeq 0.2$ nm^{-1} I observed a plateau at I(q) $= 0.04$ cm^{-1} and the typical

polymer behavior is visible at higher q-values. A similar low-q scattering was observed by Uchman et al. [128], on similar DHBC at pH = 9.3, indicating aggregation due to attractive PEG-PMAA interactions. PMAA can either exist in its protonated form (thus, neutral) or in its ionised form, where the COO^- group is in close contact with an Na ion. Different studies show that these two forms vary in the density [129, 130], thus in the SLD. The pKA of PMAA is $\simeq 4.8$ and one would expect all the chargeable group to be deprotonated at neutral pH; however, from the gaussian coil model, we obtained a plateau at $I_0 = 0.048 \pm 0.003 \text{cm}^{-1}$. This value of the platueau was in between the theoretical values calculated assuming all the group either ionized ($SLD = 3.1 \times 10^{-4}$ nm^{-2}-higher plateau), or neutral ($SLD = 2.0 \times 10^{-4}$ nm^{-2}-lower plateau). Assuming the scattering a mixture of a single chain in either one state or the other, this observed I_0 suggested that 30% of the monomer in solution must be present in their ionised form; however, the low-q upturn might hinder the exact value of the plateau.

4.2.2 Interpolyelectrolyte Complexes (IPECs)

By looking at the SANS curves, (fig. 4.8) we observed for all four sets of samples that with increasing z^* the scattering intensity increased, especially for q-values below the correlation peak. This indicated a significantly reduced electrostatic repulsion due to the presence of the oppositely charged DHBC. However, the increase of scattering intensity remains rather small below $z^* \simeq 0.35$. Above this value it increased substantially and the shape of these scattering curves indicates the presence of globular structures with radii ranging around 20 nm. At about equimolar mixing ratio, a marked intensity increase can be observed at low-q, showing the ongoing phase separation. In general, the intensity changed below $q = 0.25$ nm^{-1} corresponding to was observed using light scattering and resembling data previously reported for DHBC IPECs [63, 131, 23].

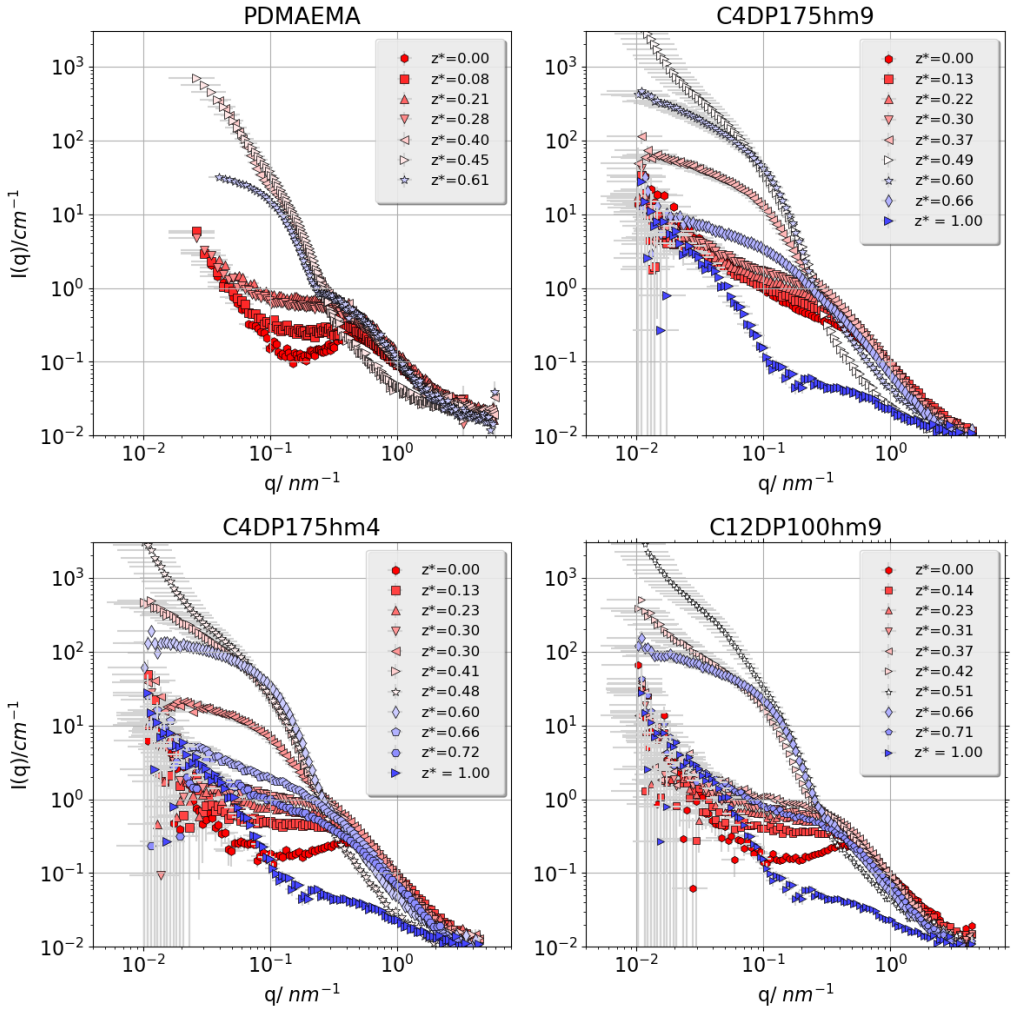

Figure 4.8: Intensity profiles I(q) extracted from IPECs made by different polycations.

4.2.3 First ad-hoc model

The aim of the first model applied to the SANS curves was to understand the evolution of the geometry of the features along the mixing ratio, without assuming any shape *a priori*. Fig. 4.9 shows a typical SANS curve obtained from the investigated IPECs:

The SANS data were usually characterized by mainly two different features: at high-q we saw a power law which was also present in the single polyelectrolyte samples. The power law exponent, however, was not fixed to a certain value. At low-q, the experimental data concerning the aggregates showed a sharp increase of intensity. For most of the

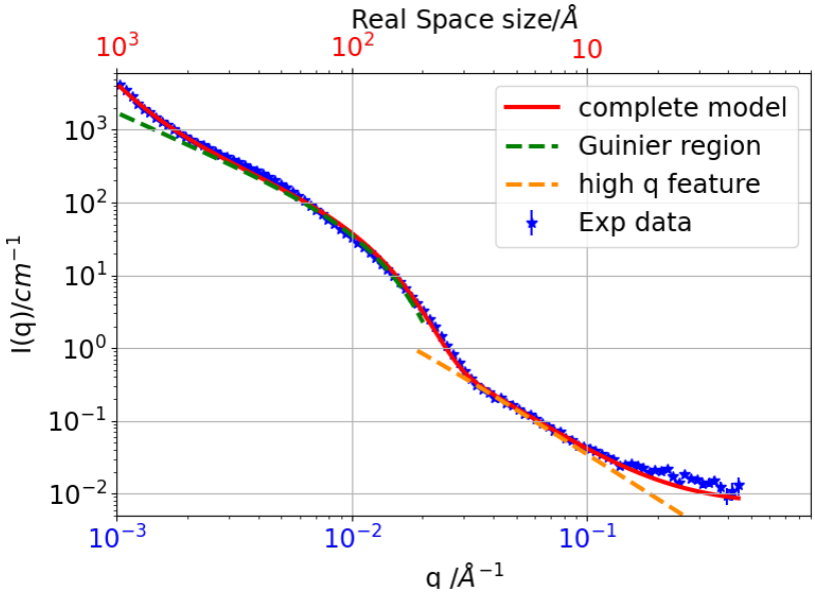

Figure 4.9: Example of a typical scattering intensity for interpolyelectrolyte complexes around equimolarity regime. The experimental concerns the sample obtained using the polycation C12DP100hm9 at a mixing ratio $z^* \simeq 0.5$.

sample, this low-q increase did not reach a plateau, which is in accordance with previous studies [132, 57, 123]. In the case of the samples close to a mixing ratio $z^* = 0.6$, a low-q plateau is observed, which suggests the presence of more defined structures.

The first model we applied on $I(q)$ was then a two component model.

$$I(q) = I_0(e^{-\pi\alpha} + \pi\alpha)q^{-\alpha}e^{-\frac{(R_a * q)^2}{3-\alpha}} + \frac{I_1(\xi q)^{-d}}{(1+(\xi q)^{m-d})} + I_{bkg} \tag{4.8}$$

Here, the first contribution is the Generalized Guinier model discussed in the section 2 and described at eq. 1.37. From this component (depicted in green in fig. 4.9), we extracted the radius of gyration of the aggregates R_g, the forward intensity $I_0 = I(q \to 0)$ and a power law α which is informative on the shape of the aggregation pattern exceeding the q-range explored. This componente was only useful in the presence of a low-q shoulder in the data, thus around equimolar mixing ratio. In the samples far from equimolar regime, we switched off this component to gain robustness in the fit.

The second component is a variation of the broad peak model, an empirical model

frequently used to model isotropic features [133]. The broad peak model was modified with the addition of a low-q power law d to take into account the low-q upturn.

By scanning the mixing ratio, we realized there was a sharp increase of the low-q $I(q)$ around equimolarity regime. Far from this regime, the scattering pattern resembled the one of a polymer. The high-q power law m is informative on the structure of the polymer, while d can suggest how these polymers were aggregating far from equimolarity regime. d was switched of when the first component was considered and viceversa. ξ is the characteristic size of the polymer structures, which defined the center of the peak. I_{bkg} is a flat background.

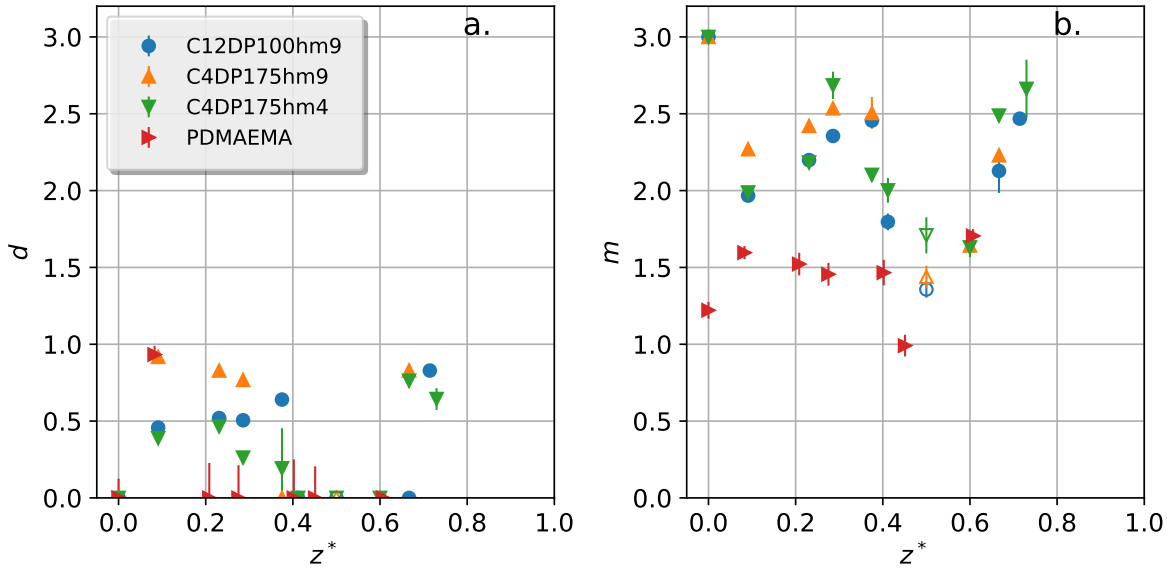

Figure 4.10: The power law representing the polymer-like aggregation d (a) and the power law representing the polymer features m (b) from the model described in eq. 4.8 for IPECs made by different polycations.

In fig. 4.10, d (a) and m (b) are displayed. d is particularly interesting for the polyelectrolyte mixtures given by hydrophobically modified polycations. This parameter suggests that hydrophobic modifications are promoting the formation of cilidrical aggregates, as observed previously in our group [80, 8, 57].m showed a minimum value for PDMAEMA. The hydrophobic modifications are removing some charged groups, lower-

ing the charge density around the polymer backbone and thus decreasing the polymer rigidity. We saw that around equimolarity, this parameter generally decreased, possibly due to the ion pairing given by the interaction between oppositely charged groups [5].

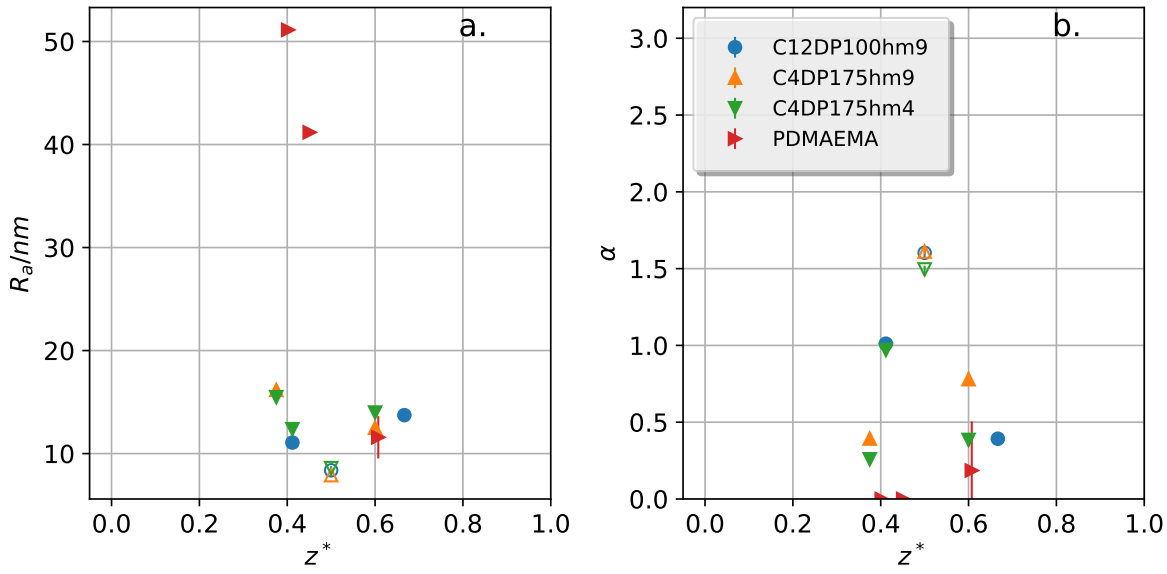

Figure 4.11: The radius of gyration of the aggregate feature R_a (a) and the power law α (b) from the model described in eq. 4.8 for IPECs made by different polycations.

In fig. 4.11, the radius of gyration of the aggregate feature R_a (a) and the power law α (b) are shown. R_a shows a minimum at equimolarity regime, but in general we find the size of the aggregates between 10 and 20 nm. On the contrary: we see that α is peaked at equimolarity regime for all the IPECs with the hydrophobically modified polycations. Once again, the hydrophobic moieties are involved in a bigger complexations. In the case of PDMAEMA, we see a quite different behavior, with higher values of R_a in the polycation excess and α compatible with 0.

It is also interesting to discuss the correlation between the forward intensity extracted from the high-q I_1 and the correlation length $\xi = 2\pi/q_0$, depicted in fig. 4.12 for the IPECs formed with the polycation PDMAEMA. I_1 increased from $z^* = 0.0$ to $z^* = 0.4$ and characteristic size $2\pi/q_0$ followed a similar behavior. This pattern is indicative to a complexation in progress: the local structures were getting bigger and more massive. By

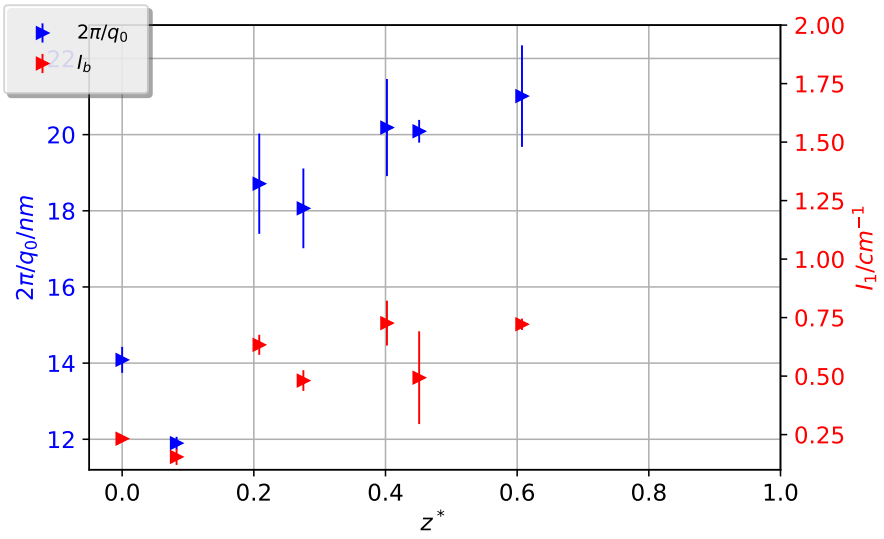

Figure 4.12: Spatial correlation $2\pi/q_0$ (in blue) and intensity related to the polymer feature I_b plotted as a function of z^* for the aggregates formed by the polycation PDMAEMA.

looking at the the power law, we also saw that within this z^*-range, m increased from 2 to 3. Polymers with a power law $m = 2$ can be either gaussian coils or rigid rod, while $m = 3$ suggests the presence of spherical denser structures. In conclusion, the aggregates became larger in mass but also more compact. This compaction is attributed to the release of counterions.

4.2.4 Second ad-hoc model: Beaucage model

Another empirical model developed to represent polymer systems is the Beaucage model (recalled in eq. 1.42). [96, 98] We used a model composed of two structural levels to describe our data. One Beaucage function was used to describe the smaller polymeric features while we used a second contribution applied on the q-range $0.03 < q < 4\ \mathrm{nm}^{-1}$ to describe the structures of the aggregates for z^* between $0.3 - 0.7$. The intensity function for this model is:

$$I(q) = B_{agg}(q; R_{agg}, G_{agg}, d_{agg}) + B_{poly}(q; R_{poly}, G_{poly}, d_{poly}) + bkg \tag{4.9}$$

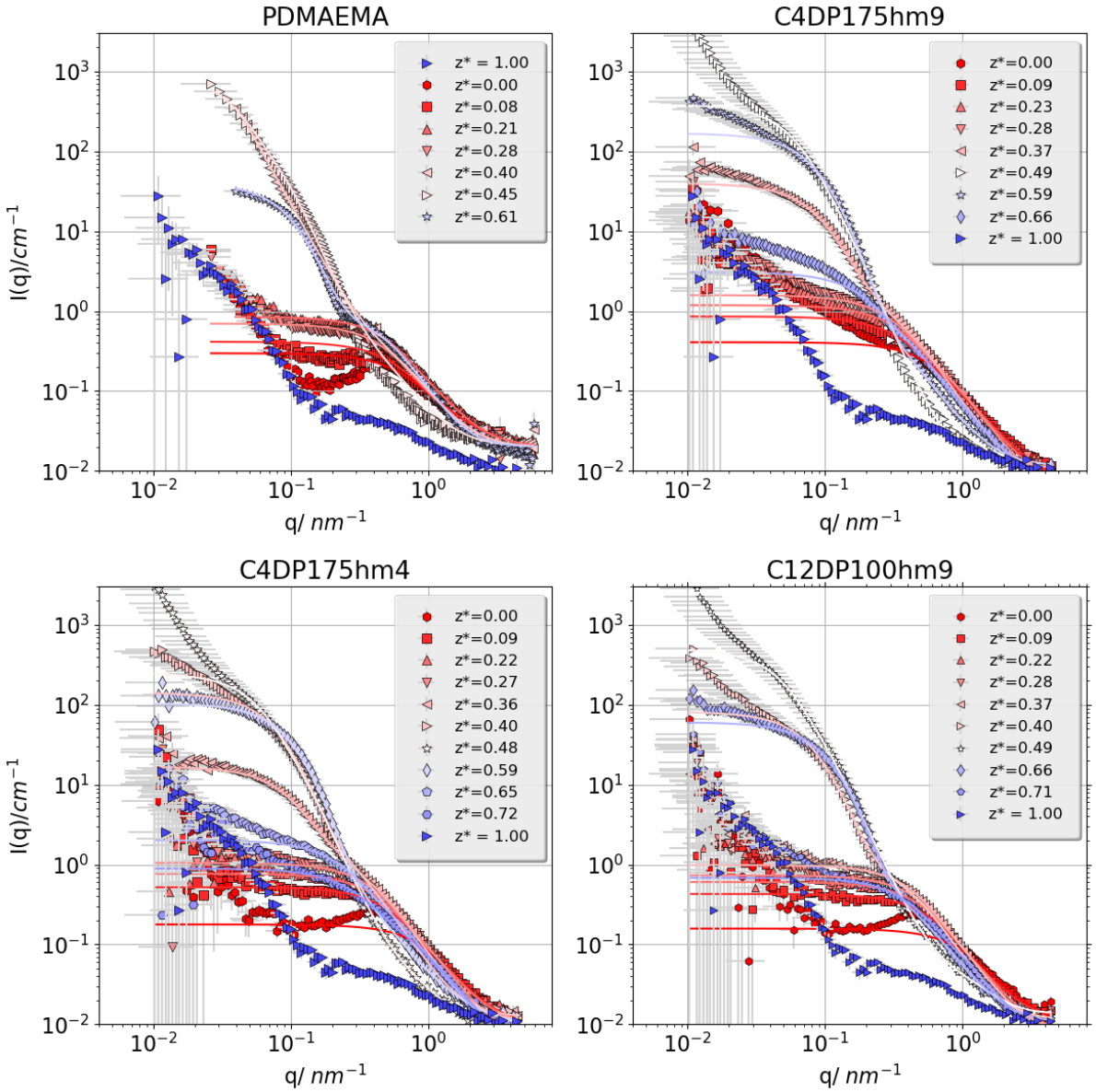

Figure 4.13: Fits of the Beaucage model applied on SANS data. Each fit is coupled with the relative residues displayed below.

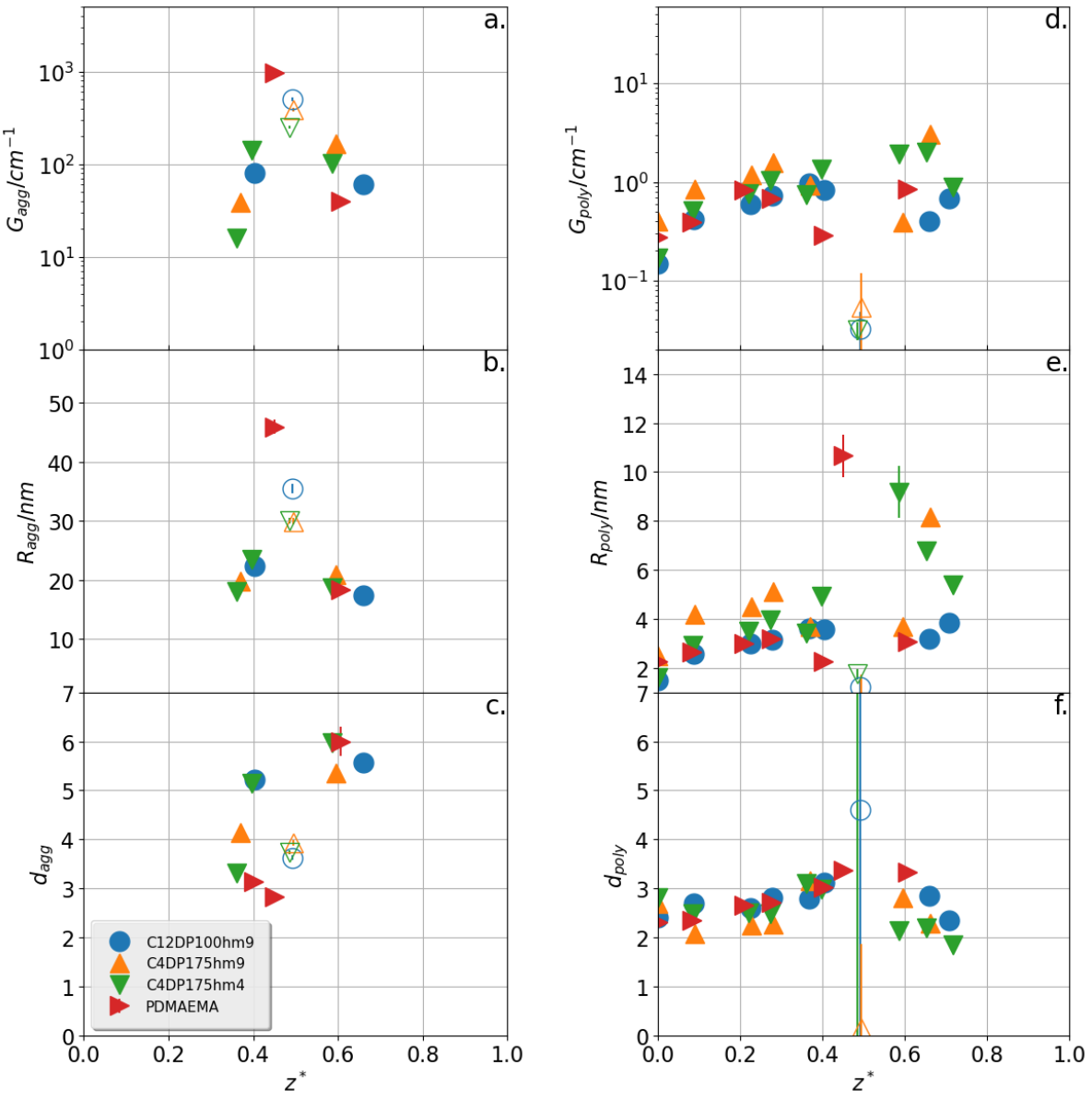

1: G_{agg}, R_{agg}, d_{agg} 2: G_{poly}, R_{poly}, d_{poly}

Figure 4.14: Beaucage parameters as a function of z^* for the four IPEC types. Panel 1: G_{agg}, R_{poly}, and d_{poly}. Panel 2: G_{poly}, R_{agg}, and d_{agg}. Empty symbols refer to biphasic solutions.

where the two sets of parameters G, d and R_g are the I(q→0), the power law exponent, and the radius of gyration, respectively, for each structural level. B_{agg} describes the

contribution from the aggregates while B_{poly} models the scattering from the polymer chains. erf() is the error function. The fits are shown in 4.13. Starting from $z^* = 0.0$, the structure factor peak was not captured and for low values of z^*, the model did not include any parameter for capturing the low-q power laws. Despite this limitations, this model accurately captured the feature arising around equimolar mixing ratio.

The most important parameters are shown in fig. 4.14.

The prefactor G_{agg} (fig. 4.14a) is higher while approaching equimolarity, in line with the light scattering investigation. Looking at R_{agg} (4.14b), the behavior for the IPECs formed with HM-PDMAEMA and the ones formed with PDMAEMA was different. For IPECs formed by PDMAEMA R_{agg} was higher in the case of polycation excess than for excess of polyanion, while the size of the HM-IPECs was symmetric around equimolarity. The z^* dependency of R_g of the IPECs from PDMAEMA is similar to what Rappoport et al. observed in similar IPECs [73]: they observed a transition from polymersomes to denser and smaller aggregates when increasing the ratio of DHBC. This behavior was not observed in the case of HM-IPECs: this may be caused by the hydrophobic modifications that connect the polycations and prevent the polymersomes to form, but this hypothesis is investigated later. The power law d_{agg} (4.14c) was estimated larger than three in most of the cases and is bigger for polyanion excess, meaning that the aggregate structure was more compact.

Towards higher value of z^*, we saw the magnitude of the high-q feature G_{poly} (fig. 4.14d) increasing while approaching the equimolarity condition: this behavior suggested that small clusters of oppositely charged polymers were aggregating. While aggregating, the power law of the same feature d_{poly} (fig. 4.14f) also increased, suggesting the formation of denser objects. R_{poly} (fig. 4.14e) is also increasing drastically while approaching the equimolar regime. For R_{poly} (fig. 4.14e), we observed systematically smaller values the more hydrophobically modified the PDMAEMA was. This can be explained by the fact that the hydrophobic modifications counteract the electrostatic repulsion that wants to extend the chains, and thereby less extended conformations are formed.

4.2.5 Fractal Aggregation of Smaller Aggregates

The ad-hoc models enlighted two important observations:

- there was always a polymer-like components present at high-q
- while reaching equimolar regime, a second component arose, depending on the mixing ratio, this component showed a plateau or not, suggesting the presence of further aggregation processes or, more generally, bigger structures.

From these observations, we developed a geometrical model that could represent the nanoscale structures. This model was based on the fractal aggregation of spherical object observed in the Krakty region for equimolar mixing ratio. In our model we employed the fractal structure factor originating from Teixeira [134] as for instance successfully employed to describe aggregation on similar systems [135] $S(q; R, D, \Xi)$:

$$S(q) = 1 + \frac{1}{(qR)^D} \frac{D\Gamma(D-1)}{\left(1 + (q\Xi)^{-2}\right)^{\frac{D-1}{2}}} sin((D-1)tg^{-1}(q\Xi)) \tag{4.10}$$

where $\Gamma(x)$ is the gamma function, D is the fractal dimension, Ξ the characteristic dimension of the cluster and R the size of the object subjected to the clustering process, which in our case is the average radius of a hydrated sphere (see below).

As a first attempt, a model with a radial linear density distribution of polymer material inside a sphere was considered:

$$\Delta\text{SLD}(r) = \Delta\text{SLD}\left(f_i - (f_i - f_f)\frac{r}{R}\right) \tag{4.11}$$

where R is the overall radius, f_i the initial volume fraction of material, f_f the final one at $r = R$, and ΔSLD the dry contrast.

The volume of material is:

$$V_{\text{dry}} = 4\pi \int_0^R \left(f_i - (f_i - f_f)\frac{r}{R}\right) r^2\, dr = \frac{\pi}{3}(f_i + 3f_f)R^3 \tag{4.12}$$

In case of a constant SLD, $f_f = f_i$ and $V = \frac{4\pi}{3} f_i R^3$ is recovered. The average volume fraction of material is $\langle f \rangle = \frac{f_i + 3f_f}{4}$.

The scattering amplitude is:

$$\begin{aligned} F(q,R) &= 4\pi\Delta\text{SLD} \int_0^R \left(f_i - (f_i - f_f)\frac{r}{R} \right) \frac{\sin(qr)}{qr} r^2 \, dr \\ &= 4\pi\Delta\text{SLD} \left[f_f \frac{\sin(qR) - qR\cos(qR)}{q^3} + (f_f - f_i) \frac{\sin(qR) + 2\frac{\cos(qR)-1}{qR}}{q^3} \right] \end{aligned} \tag{4.13}$$

where the first term is the form factor amplitude of a homogeneous sphere and the second term cancels out if $f_i = f_f$.

Since $F(0) = \Delta\text{SLD} V_{\text{dry}}$, the normalized form factor amplitude reads:

$$F_{\text{norm}}(q,R) = \frac{4}{f_i + 3f_f} \left(f_f \frac{3j_1(qR)}{qR} + (f_f - f_i) 3 \frac{\sin(qR) + 2\frac{\cos(qR)-1}{qR}}{(qR)^3} \right) \tag{4.14}$$

This model has one more parameter to fit than the homogeneous sphere, which is essentially the slope of the linear distribution. Some tests of the model are shown in fig. 4.15. After several test, this model did not improve the quality of the fit with respect to the homogeneous sphere, thus I relaxed this parameter and the polymer concentration was assumed to be constant across the radius. The form factor used was the one of homogeneous hydrated spheres.

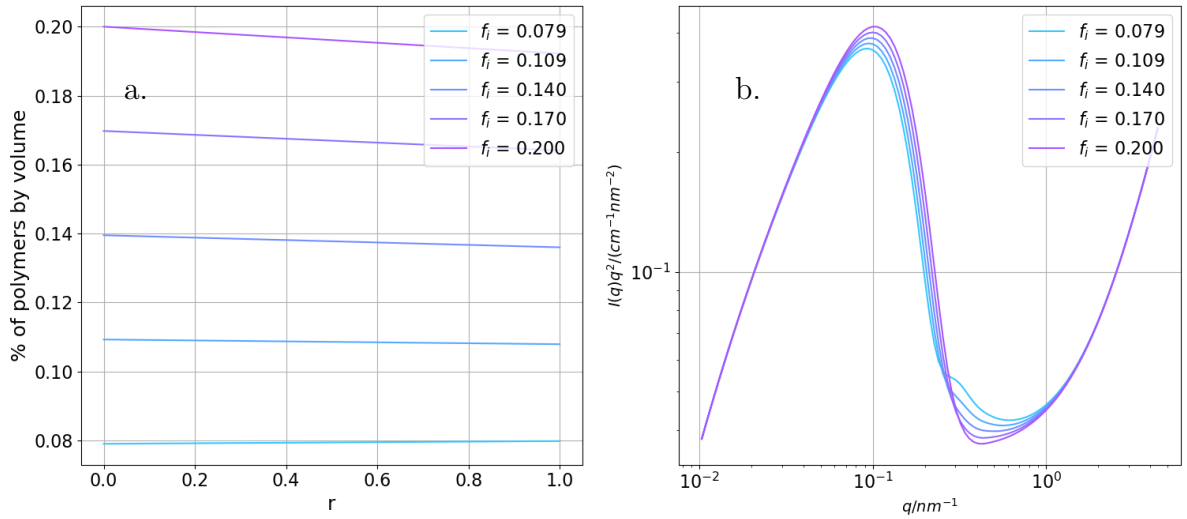

Figure 4.15: Test with different linear density distributions. Panel (a) shows the linear density distribution, while panel (b) shows the Krakty plot of the normalized $I(q)$ of such a distribution.

$$F_{\text{Sphere}}(q, R) = 4\pi\Delta\text{SLD}\frac{\sin(qR) - qR\cos(qR)}{q^3} \tag{4.15}$$

To calculate the SLD, and more generally, the absolute intensity of the aggregates, the two polymer species were considered.

The two polymers polymer species are characterized by concentrations c_1 and c_2 in $\text{g}\,\text{cm}^{-3}$, molecular weights MW_1 and MW_2 in $\text{g}\,\text{mol}^{-1}$ and molecular volumes v_1 and v_2 in nm^3. Assuming that all polymer chains aggregate, the total volume fraction is:

$$\phi_{\text{dry}} = N_A 10^{-21}\left(\frac{c_1 v_1}{MW_1} + \frac{c_2 v_2}{MW_2}\right) \tag{4.16}$$

the aggregation number $N_{\text{agg}} = N_{\text{agg},1} + N_{\text{agg},2}$ will be such that $\frac{N_{\text{agg},2}}{N_{\text{agg},1}} = \frac{c_2}{c_1}\frac{MW_1}{MW_2}$, therefore $N_{\text{agg}} = N_{\text{agg},1}\left(1 + \frac{c_2}{c_1}\frac{MW_1}{MW_2}\right)$.

The volume of the aggregated material in nm^3 is:

$$V_{\text{dry}} = N_{\text{agg},1} v_1 + N_{\text{agg},2} v_2 = N_{\text{agg},1} \left[v_1 + \left(\frac{c_2}{c_1} \frac{MW_1}{MW_2} \right) v_2 \right] = \frac{c_1 v_1 MW_2 + c_2 v_2 MW_1}{c_1 MW_2 + c_2 MW_1} \tag{4.17}$$

The number density in nm^{-3} is:

$$^1 n = \frac{\phi_{\text{dry}}}{V_{\text{dry}}} = \frac{N_A 10^{-21}}{N_{\text{agg},1}} \frac{\frac{c_1 v_1}{MW_1} + \frac{c_2 v_2}{MW_2}}{v_1 + \left(\frac{c_2}{c_1} \frac{MW_1}{MW_2} \right) v_2} = N_A 10^{-21} \frac{\frac{c_1}{MW_1} + \frac{c_2}{MW_2}}{N_{\text{agg}}} \tag{4.18}$$

here, the molecular volume were estimated from the monomeric tabulated values and the characterization of the polyelectrolytes discussed in the chapter 3.

Considering the copolymer, it is formed by units A and B. From the specifics of these two units, the molecular volume v, molecular weight MW, apparent density d and scattering length SL of the copolymer were estimated. The scattering length density SLD is then:

$$\begin{aligned} v &= n_A v_A + n_B v_B \\ MW &= n_A MW_A + n_B MW_B \\ \text{SL} &= n_A \text{SL}_A + n_B \text{SL}_B \\ d &= \frac{1}{N_A 10^{-21}} \frac{MW}{v} = \frac{1}{N_A 10^{-21}} \frac{n_A MW_A + n_B MW_B}{n_A v_A + n_B v_B} \\ \text{SLD} &= \frac{\text{SL}}{v} = \frac{n_A \text{SL}_A + n_B \text{SL}_B}{n_A v_A + n_B v_B} \end{aligned} \tag{4.19}$$

Being SLD the weighted average of the volume fraction $\{\phi_i\}$ (where i refers to the different polymers), then:

$$\Delta\text{SLD} = \frac{\sum_i \phi_i \text{SLD}_i}{\phi} - SLD_{D2O} = \frac{\frac{c_1 \text{SLD}_1}{d_1} + \frac{c_2 \text{SLD}_2}{d_2}}{\frac{c_1}{d_1} + \frac{c_2}{d_2}} - SLD_{D2O} \tag{4.20}$$

In addition to this form factor, we introduced the generalized version of the Debye model $I_{poly}(q; \nu, R_g, I_p)$ (which has the same functional form of the I(q) used for pure polyelectrolyte solutions), to take into account the scattering from polymer chains seen

in the high-q region, which is described by Gaussian coils with a radius of gyration R_g and a parameter ν that describes the solvent quality (as in eq. 1.45). I_p is a scaling factor.

Summing up all the contributions, the scattering intensity is given as:

$$I(q) = n\left[\int_0^\infty pdf(N_{\text{agg}};\mu,\sigma_r)F^2_{\text{Sphere}}(q,R)S(q;R)d\,R\right] + I_{\text{poly}}(q) + \text{bkg} \tag{4.21}$$

Where pdf(μ_N, σ_N) is the Schulz-Zimm distribution [136] which introduces a polydispersity applied in the local monodisperse approximation (as explained in the eq. 1.48 and in [137]) on the aggregation number of both the PE species N_{agg} (with μ_N and σ_N being the mean value and the standard deviation). Such a polydispersity (PD) is reflected in a smearing effect of the typical oscillations of the spherical form factors because $N_{\text{agg}} \propto R^{1/3}$, e.g. a PD of σ_r of N_{agg}=20% corresponds to σ_r of R=7%. The polydispersity on the total aggregation number was set at 60%.

Since the model assumed that the aggregates are hydrated spheres, it was possible to calculate the water content inside the aggregates.

$$H = 1 - f_p \tag{4.22}$$

Here, f_p is the fitted volume fraction of polymeric material inside the spheres, since the average radius of the spheres is calculated as

$$R = \left(\frac{3V_p}{4\pi f_p}\right)^{1/3} \tag{4.23}$$

Where V_p is the volume of polymeric material calculated from N_{agg}. We observed values around 85 and for some cases, even above 99%), similar systems showed H $\simeq$ 85% [138].

In this model we assumed that all polymers present in the system contribute to the formation of the spherical aggregates. Due to the high hydration, we consider this as-

sumption unlikely and, as an alternative model, we made the hypothesis that an equimolar polymeric mass c_{agg} is forming aggregates while the rest of the polymer is in solution or interconnecting them. The behavior of the polymer distribution in the hydrated spheres and outside is depicted in fig. 4.16

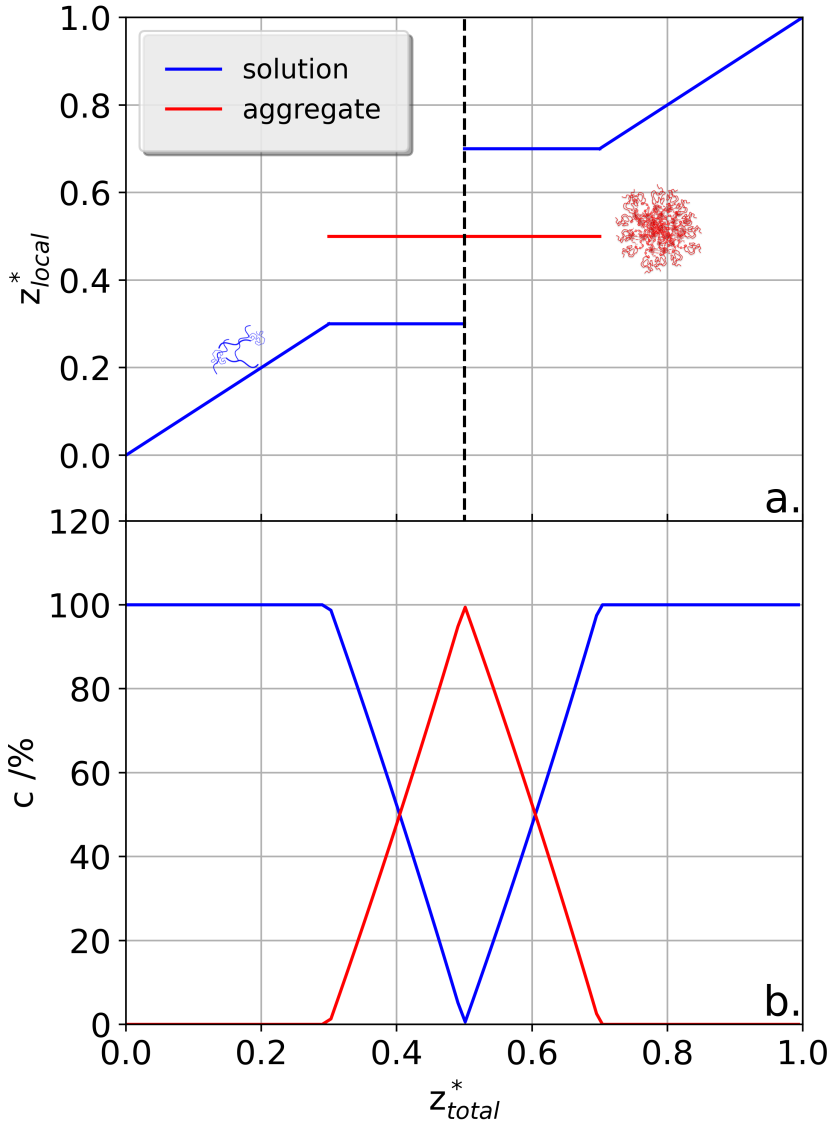

Figure 4.16: (a) Schematic behavior of charge ratios in the bulk z_b and in the aggregates z_{agg}. (b) The percentage of polymeric material in the 2 phases along z^*.

To distinguish two populations we have to make an hypothesis on the net charge of the spherical aggregates, which is driven by previous investigations on coacervates and DHBC micelles [78, 79], however we do not exclude that this hypothesis might not hold and the redistribution of polymeric material between the two populations could be different.

This model results in denser systems, in line with what Carl et al observed [138]. This model was also justified by the presence of a non-vanishing high-q scattering which resembled the scattering of a polymer at equimolar mixing ratio.

With this model, we fitted the samples around equimolar mixing ratio. The corresponding Krakty plots, with the constant background subtracted and the residues are shown in fig. 4.17

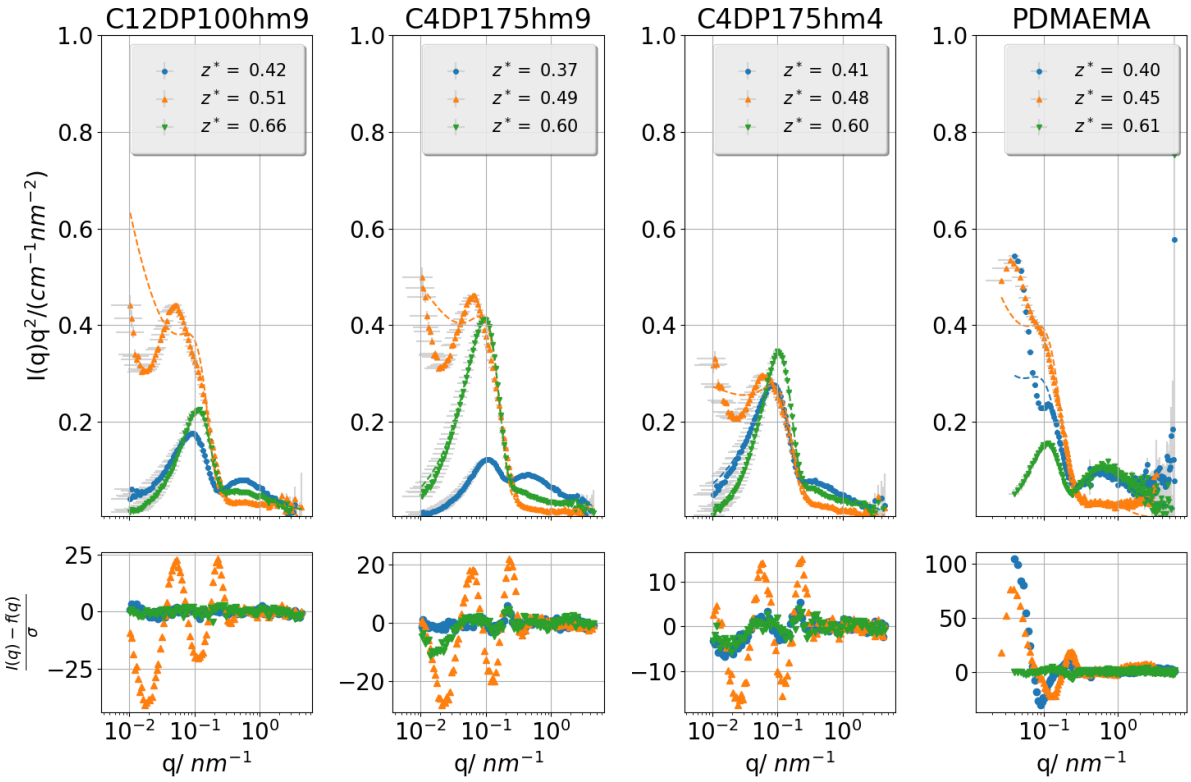

Figure 4.17: Krakty plots of the IPECs around equimolar mixing ratio with the corresponding model of fractal aggregates represented with dotted lines.

In this figure, the blue curves correspond to samples at polycation excess, the orange

curves correspond to the closest samples to equimolarity and the green curves represent the samples at polyanion excess. The model failed to represent the low-q behavior of the samples at polycation excess. These feature are further discussed in the next section, where we combine SANS with a Cryo-TEM investigation to extend to larger size our investigation. In the rest of the samples, the model successfully fitted the features of the data.

Most of the aggregates in the polycation regime (in orange) were showing a low-q maximum, indicative of bigger aggregation process. However, for the rest of the curves, a bell shape characterized by a second feature was observed. This second feature was associated the scattering of the polymers.

From the fit, we extracted the parameters of the model, shown in fig. 4.18

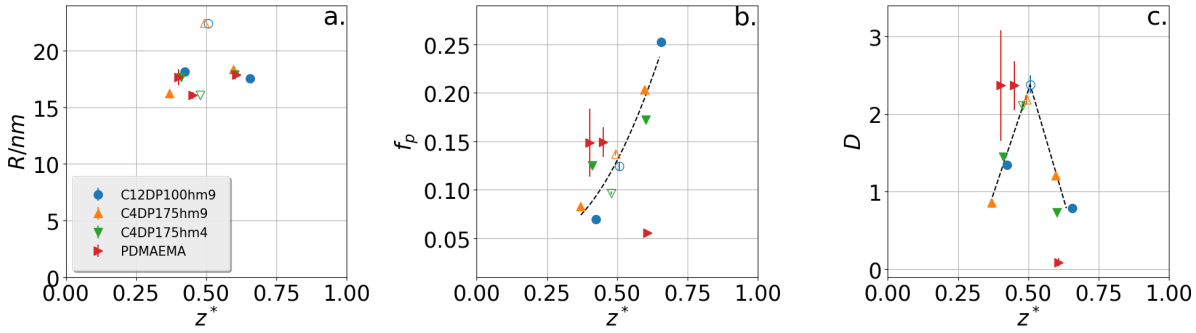

Figure 4.18: Behavior of the parameters fitted from the fractal aggregates model: the radius of the spherical mid-q structures (a), the volume fraction of the polymer inside the spherical aggregates (b) and the power law assessed to the fractal aggregates (c). A black dotted line shows the general behavior of HM-IPECs. Empty symbols refer to the biphasic solutions.

Our most important finding is that in the range of $z^* \sim [0.3 - 0.7]$ the radius remains constant at 16-18 nm, i.e. it is apparently determined by the length of the polyelectrolyte block of the PMAA-PEO and not affected much by the type and extent of the hydrophobic modification of the PDMAEMA. This means that this system has a marked tendency to form such well defined spherical complexes, which are essentially unaffected by the hydrophobic modifications. Note that in the case of PDMAEMA R_{agg} extracted from the Beaucage model at $z^* \simeq 0.4$ was bigger than the rest of the samples: in the

fractal model, R is lowered down to R$\simeq$ 17 nm. This is the consequence of the low-q and mid-q contributions being entangled, due to the low-q range explored, it is challenging to determine what is the geometry of the low-q contribution.

While looking at the polymer volume concentration f_p (fig. 4.18b), IPECs tend to be denser in the DHBC excess. This was already observed in the Beaucage modelling, but now we can estimate quantitatively the water content of the spherical objects. For polyanion excess one may assume that an excess PEG chains lead to a more well-defined interface between the spheres and the solvent, where the IPEC core and the neutral hydrophilic PEG portion are separated. The interchange between looser and denser structures is interesting as z^* becomes a parameter for fine tuning different structures.

The fractal dimension D (fig. 4.18c) is generally lower when $z^* \simeq 0.6$: at this mixing ratio, I(q) shows in most of the cases a plateau and it is particularly evident while the hydrophobic modification fraction decreases. The low-q behavior and the D trend of IPECs at this z^* suggest that the samples at $z^* \simeq 0.6$ are well defined globular structures that start aggregating while introducing hydrophobic modifications.

4.2.6 Cryo-TEM and polymersomes

Most of the explored SANS data did not show a plateau at the lowest q: the absence of a plateau suggested that the structures observed extended to larger scales and to obtain more informations on larger scale, the samples were investigated via Cryo-TEM. This investigation was done by Sapir Rappoport which I thank for the kind collaboration.

To explore the mixing ratio and the effect of the hydrophobic modifications, different IPECs formed with PDMAEMA and C12DP100hm9 at $z^* \simeq [0.2, 0.4, 0.6]$ were tested.

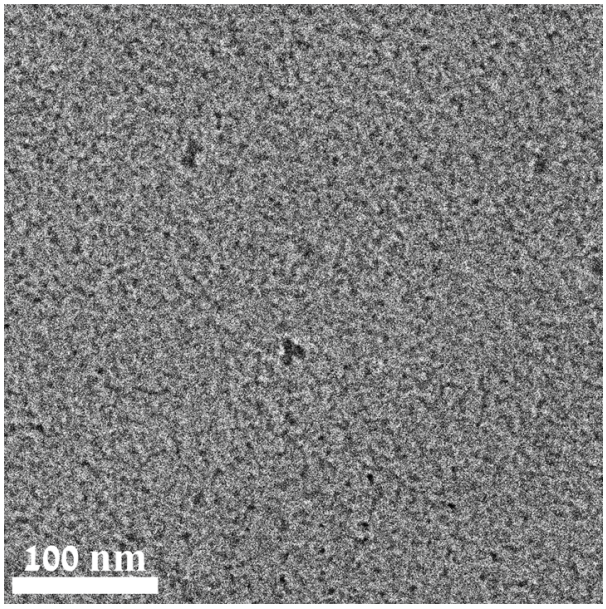

Figure 4.19: Cryo-TEM images of the IPECs produced with the polycation C12DP100hm9 at a mixing ratio $z^* \simeq 0.2$ acquired and produced by Sapir Rappoport.

Fig. 4.19 showed small aggregates of an average size of $d_p \simeq 5.6$ nm, compatible with the polymeric feature observed via SANS.

Fig. 4.20 shows two different acquisitions of the IPECs made with a PDMAEMA at $z^* \simeq 0.4$. In this pictures two different shapes were observed: in the left panel, solid micelles of an average size $d_m \simeq 20$ nm were observed, while the right panel shows polymersomes broadly distributed in their total size. The vesicles had a similar thickness of $d_v \simeq 20$ nm. Similar structure were sampled in the case of IPECs with the same mixing ratio made with the hydrophobically modified polycation.

SANS data showed the presence of bigger structures than the accessible one and a simulation of a mixture of micelles and polymersomes can elucidate the compatibility between SANS and cryo-TEM data.

Supposing we have a mixture of spherical aggregates of a radius r=17 nm and vesicles of an inner radius of R=100 nm and a thickness of l=17 nm. Then one can write the scattering intensity per scattering vector I(q) as:

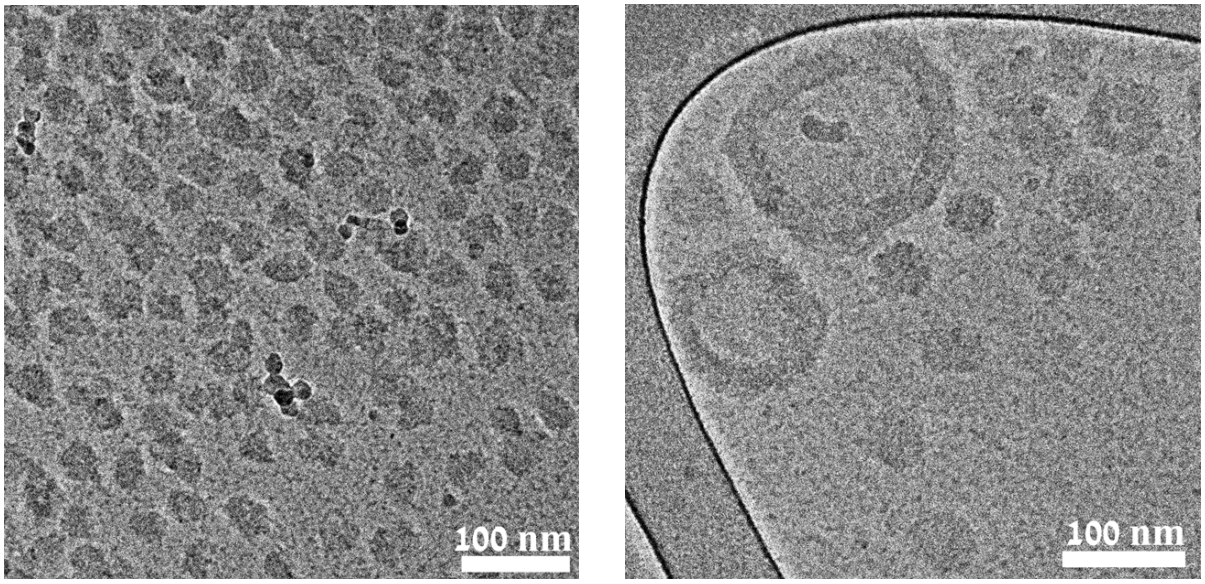

Figure 4.20: Two different Cryo-TEM images of the IPECs produced with the polycation PDMAEMA at a mixing ratio $z^* \simeq 0.4$, acquired and produced by Sapir Rappoport.

$$F_{\text{sphere}}(q) = 3V\Delta\rho \cdot \frac{\sin(qr) - qr\cos(qr)}{(qr)^3} \tag{4.24}$$

$$F_{\text{core-shell}}(q) = 3\left[V_s\Delta\rho\frac{\sin(qr_s) - qr_s\cos(qr_s)}{(qr_s)^3} - V_c\Delta\rho\frac{\sin(qr_c) - qr_c\cos(qr_c)}{(qr_c)^3}\right] \tag{4.25}$$

$$P(q) = n_{\text{core-shell}}F^2_{\text{core-shell}}(q) + n_{\text{sphere}}F^2_{\text{sphere}}(q) + \text{background} \tag{4.26}$$

Where $\Delta\rho$ is the scattering length density contrast between the polymers and the solvent, V and r are the volume and the radius of the spheres, V_s and r_s are respectively the volume and the radius of the vesicles (considering the inner core as well), V_c and r_c are respectively the volume and the radius of the core. $n_{\text{core-shell}}$ and n_{sphere} are the number densities of the core-shell and the spheres.

If one calculates the forward scattering I(q $\to$ 0):

$$I(q \to 0) = n_{\text{core-shell}}\Delta\rho^2(V_s^2 - V_c^2) + n_{\text{sphere}}\Delta\rho^2V^2 + \text{background} \tag{4.27}$$

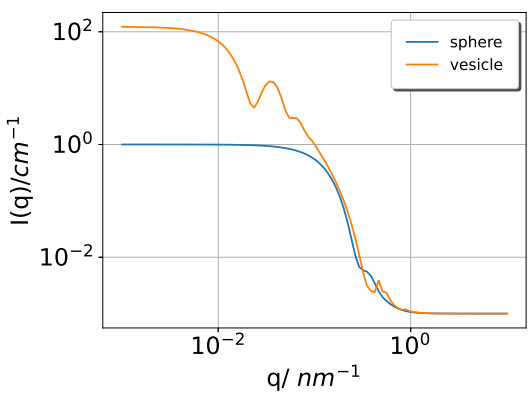

(a) Normalized I(q) contributions for same numbers of vesicles and spheres in the system.

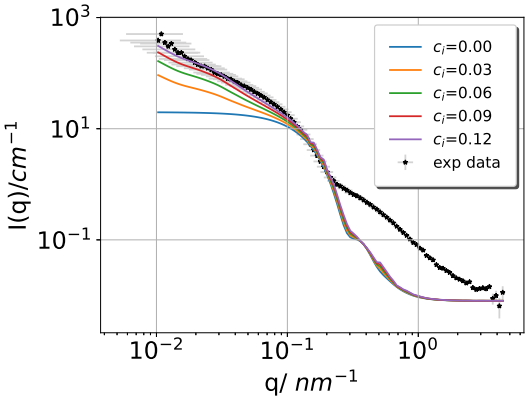

(b) I(q) simulations of different ratios of vesicles and spheres.

The 2 contributions are plotted in fig. 4.21a, to show the features normalized over the forward scattering contribution of the spheres in the condition $n_{\text{core-shell}} = n_{\text{sphere}}$. A polydispersity on the thickness, the radius of the vescicle and the radius of the sphere has been introduced.

Fig. 4.21b shows how these 2 contribution would look like in different ratios $c_i = n_{\text{core-shell}}/n_{\text{spheres}}$. To observed better the feature of such structures, we did not include the high-q features related to the polymeric contribution to better expose how the features of this model would look like in this q-range. Experimental data are taken from the IPECs made by the polymer C12DP100 with $z^* \simeq 0.6$. I(q) has been normalized on the experimental data.

By introducing a small portion of vesicles, the plateau of the solid micelles was hindered by the upturn given by the vesicles. Due to the high polydispersity and the high surface activity of polyelectrolytes, these vescicle can corresponds to the fractal aggregates modelled in the section before.

Furthermore, it is interesting to observe the IPECs formed in the polyanion excess, thus at a mixing ratio $z^* \simeq 0.6$. Fig. 5.20 shows the IPECs at this z^* formed by PDMAMEA (a) and C12DP100hm9 (b).

By looking at the two different images, the nanoscale structures were similar to what

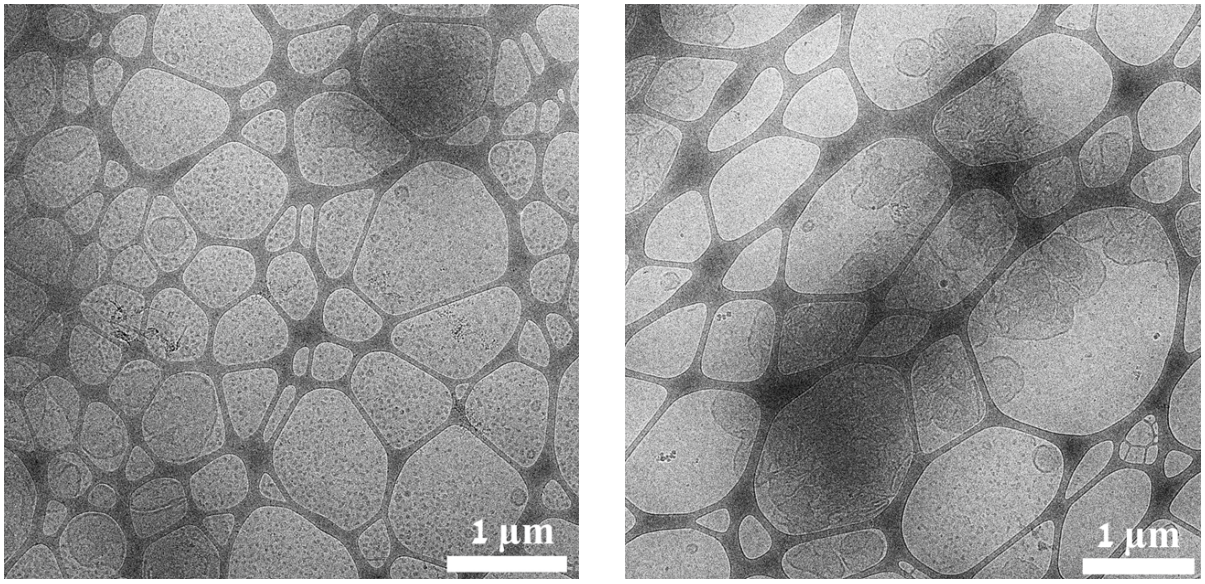

(a) IPECs formed with PDMAEMA. (b) IPECs formed with C12DP100hm9.

Figure 4.22: Two different Cryo-TEM images of the IPECs produced with the polycation PDMAEMA and C12DP100hm9 at a mixing ratio $z^* \simeq 0.6$, acquired and produced by Sapir Rappoport.

has been observed in the case of polycation excess; however, in this case the IPECs formed with C12DP100hm9 showed larger structures, in line with our observation of hydrophobic modifications connecting different aggregates and different observed also during different investigations [80, 57].

4.2.7 Conclusions on the structure

A sketch of the supposed structure is depicted in 4.23.

$z^* < 0.3, z^* > 0.7$ $0.3 < z^* < 0.7$

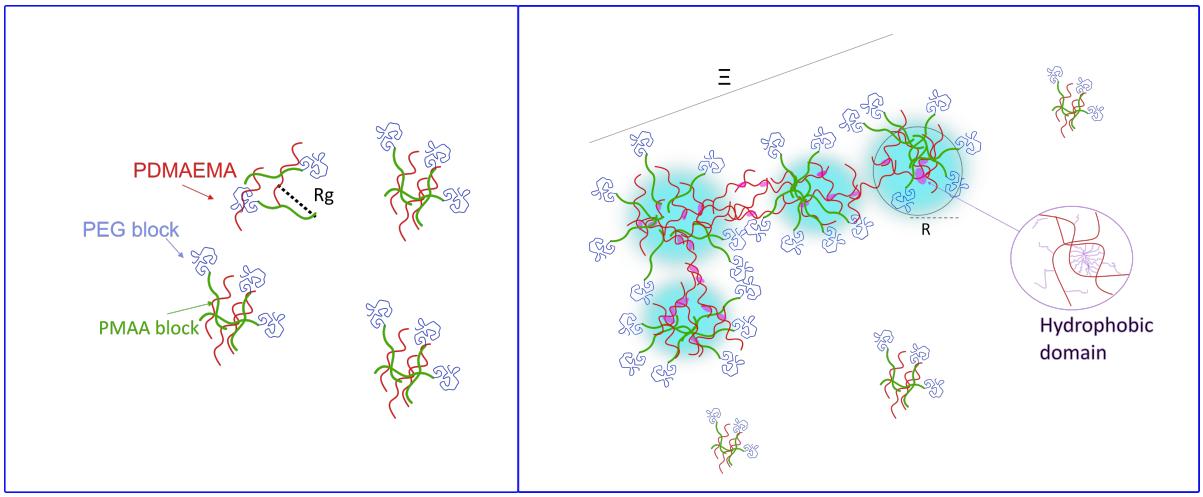

Figure 4.23: Structural representation of the analytical statistical model: z^* is the mixing ratio, PDMAEMA is represented by the red drawings while the DHBC appears in light blue (PEG block) and green (PMAA block). The cyan background represents an increase of the concentration in the bigger aggregates and the connecting hydrophobic interactions are represented by violet ellipsis.

In this study we used light and neutron scattering techniques to characterize the structures of a particular case of IPECs, where hydrophobic moieties are attached to the polycation PDMAEMA, which becomes complexated by a double-hydrophilic polyanion (DHBC) PEG-PMAA. These hydrophobically modified systems were compared to IPECs formed by non modified PDMAEMA. For mixing ratios z* below 0.3 and above 0.7 only a low tendency for aggregation is observed. Only in the z* range of 0.3-0.7 one observes a large increase of scattering intensity, i.e., formation of larger aggregates and despite the use of a DHBC, we observed phase separation (coacervation) at about equimolar mixing ratio of the polyelectrolytes. The most interesting observation is that this transition from polymer-like aggregates to larger structures occurs sharply over a rather small change of z^*. From intensity and shape of the scattering curves one can conclude to the formation of globular aggregates with a radius of 16-18 nm. The analysis of the data shows that the formed aggregates contain a high amount of water (85-95%), but the water content becomes largely reduced and the structures become less interconnected on the side of

polyanion excess.

Moreover in this system we observed a non trivial effect of changing z^*. In the range of z^* between 0.3 and 0.7 the sudden formation of larger and well-defined globular aggregates is best described by a model where they are composed of a neutralized IPEC and the excess polyelectrolyte interconnecting such aggregates or dangling free in the aqueous environment. The suggested fractal aggregation could be connected to the formation of polymersomes with a thickness compatible with the size of the micelles; however, these structure were broadly polydisperse in their size observed with cryo-TEM. Moreover, cryo-TEM is a surface investigation and one could argue that these polymers could behave slightly different in bulk. Despite this detail, the two techniques provided us a complete description of the nanoscale structures as a function of the mixing ratio and with and without hydrophobic modifications.

Chapter 5

Dynamics of Interpolyelectrolyte complexes

Once the nanoscale structures have been characterized, the dynamics remained a compelling analyisis on our systems. In this sense, the system was investigated using three different techniques: dynamic light scattering (DLS), neutron spin echo spectroscopy (NSE) and neutron backscattering (NBS). This chapter is based on a manuscript recently published in *The Journal of Chemical Physics*.[17]

5.1 Dynamic Light Scattering

The same sample discussed in the previous chapter via SLS have been analysed using DLS as well, with the same apparatus. As in the case of SLS, the IPECs formed using hydrophobically modified polycations have been investigated by Bin Dai, while the author performed the experiment on the IPECs formed by the PDMAEMA.

It has been shown that polyelectrolyte complexes experience a bimodal diffusion [31, 132]. In the investigated samples for z^* far from equimolarity regime, a bimodal pattern was observed, as displayed in fig. 5.1; however, this pattern vanishes while approaching equimolarity regime. To avoid to insert many parameters over the entire z^*, all the DLS data were modeled with a stretched exponential function.

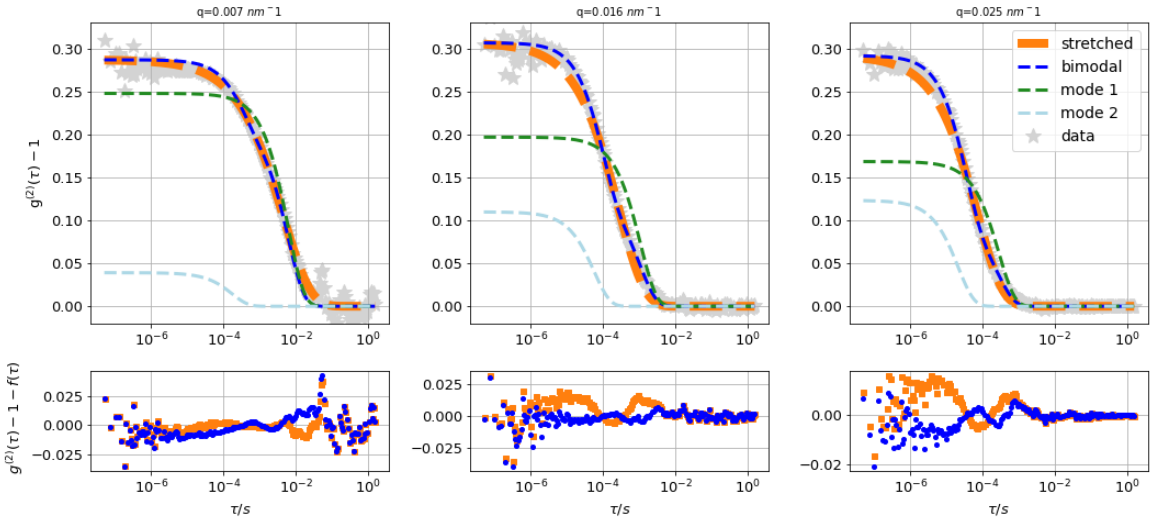

Figure 5.1: DLS data $g^{(2)}(\tau) - 1$ fitted with a bimodal distribution and a stretched distribution: the 3 different plots correspond to 3 different q. The 2 modes of the bimodal distribution are also displayed. The data correspond to the IPECs at z^*=0.32 formed by the polycation C12DP100hm4. Residuals are shown below the plots.

$$g^{(2)}(\tau) - 1 = \beta \exp(-2(\overline{\Gamma}\tau)^{\alpha}) + \text{bkg} \tag{5.1}$$

Here, the stretching parameter α can be converted to the polydispersity index PDI, $\overline{\Gamma}$ is the average value of Γ, β is a scaling factor and bkg is a constant arising from the uncertainty in the absolute mean intensity of scattered light and potential electronic noise.

The deviation between a bimodal and a stretched exponential is negligible form most of the samples.

To check the reliability of the stretched exponential function, the CONTIN analyisis was also performed on the DLS data [139, 140].

Moreover, looking at the stretching parameter α, this is close to 1 for the majority of samples at equimolarity regime (shown in fig. 5.2).

The weights extracted with the CONTIN analysis for each decay rate from IPECs made with different polycations and at different mixing ratio are displayed in fig. 5.3.

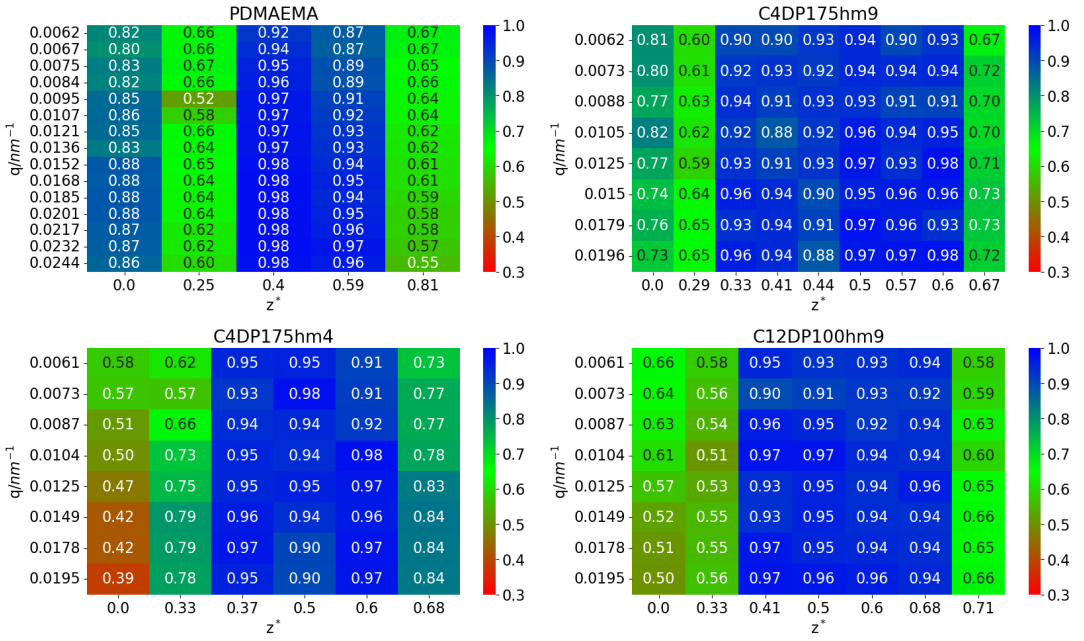

Figure 5.2: The stretching parameters for the IPECs formed by the 4 different polycations at differem q values and mixing ratios z^*.

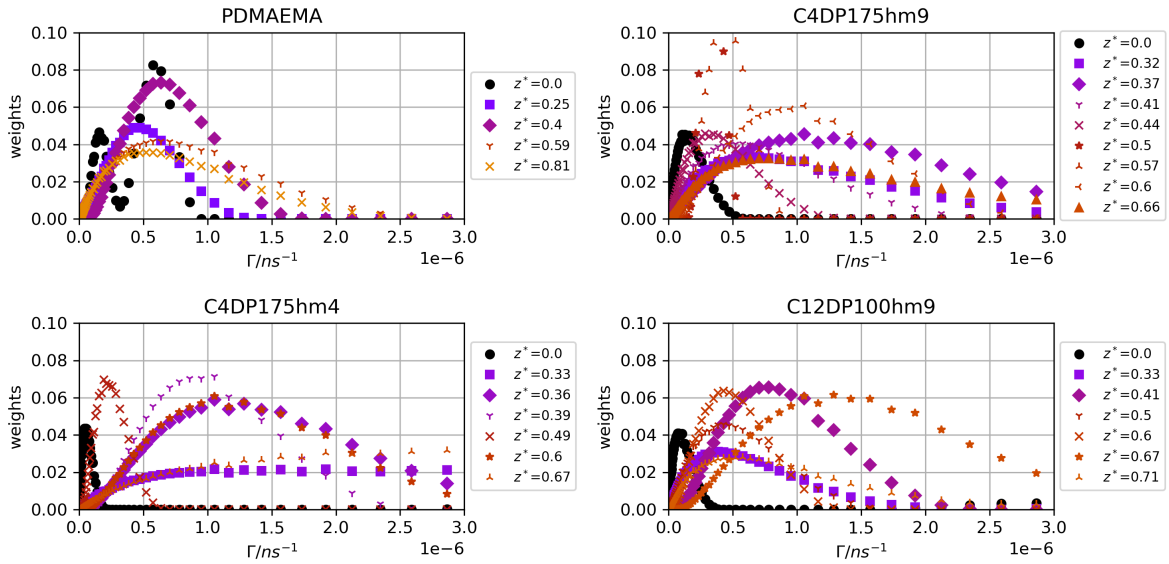

Figure 5.3: Distributions of the the relaxation Γ extracted from the CONTIN analysis from the DLS data at an angle $\theta = 42°$ for all the samples.

Most of the samples showed a distribution of weights monomodal, which reinforced the choice of representing the DLS data with a stretched exponential function.

Fig. 5.4 shows an example of the angular distribution for one sample.

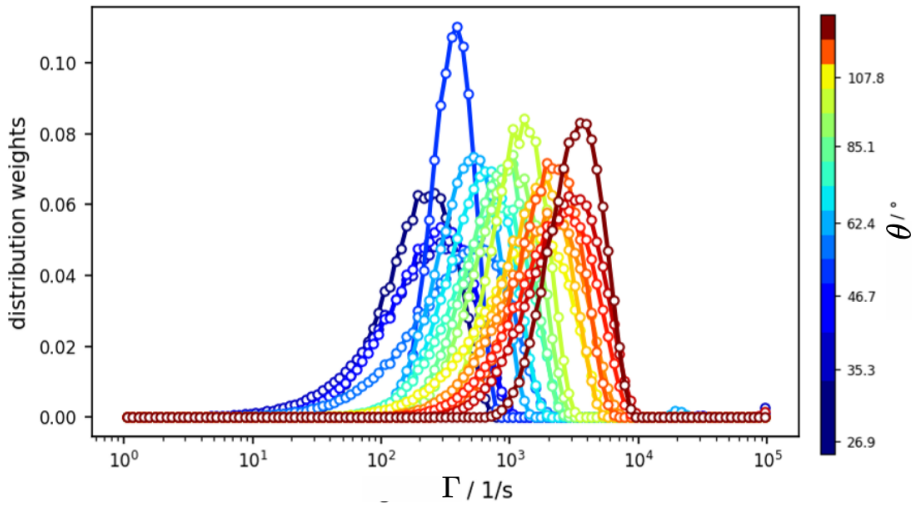

Figure 5.4: The distributions of the relaxation weights for different values of q for the IPECs made by the polycation C4DP175hm4 at z^* =0.36.

The angular distribution resembled a Fickian diffusion: weight distributions of higher q-values were peaked at higher Γ.

Once $\Gamma(q)$ was obtained from each sample, it was fitted in the assumption of the diffusion being Fickian:

$$\overline{\Gamma} = Dq^2 + \Gamma_0 \tag{5.2}$$

Here, Γ_0 was taking into account any slow diffusion unable to be resolved and it was close to 0 for all the samples.

An example of this fit is shown in fig. 5.5

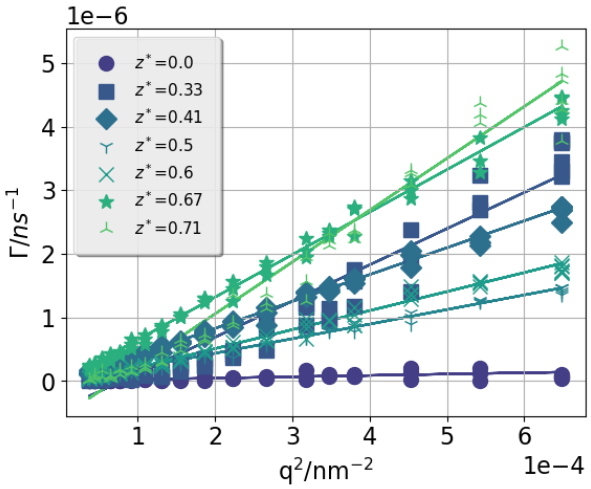

Figure 5.5: Γ for the IPECs with the polycation C12DP100hm9 (b). In the assumption of a Brownian motion, D has been extracted and plotted over q^2.

From the described fit, the effective diffusion coefficient D was extracted and the hydrodynamic radius R_H was estimated, according to eq. 1.66.

As reported earlier [80], hydrophobically modified IPECS can form structures with larger R_H than IPECs made by PDMAEMA. The reason for this is that hydrophobic moieties tend to form cross-links between different aggregates.[126, 141, 142] The aggregates showed the behavior of standard IPECs made of DHBCs, with the addition of interconnection given by the hydrophobic moieties. This was also clear from the fact that the stretched length of a PEG-PMAA molecule is about 40 nm, and therefore no simple aggregates of R_H values greater than 40 nm can be formed here.

5.2 Neutron spectroscopy

In this section, the investigation using neutron backscattering and neutron spin echo spectroscopy are discussed. Neutron spectroscopy investigations can be quite expensive, thus it was possible to only test two sets of IPECs and the standard IPECs made with PDMAEMA and the IPECs made with the polycation C12DP100hm9 were probed.

5.2.1 Pure Polyelectrolytes

To better understand the behavior of interpolyelectrolyte complexes, the dynamics of the components must be clarified. As discussed in the introduction, polyelectrolyte dynamics is characterized by different concentration regimes [1]. This first part of the section aims to estimate the polymeric regime.

Following the calculations of Masao Doi [29], the concentration of segments per unit volume can be written as c_s, and thus the concentration of polymer per unit volume as c_s/DP (where DP is the degree of polymerization). The condition for the polymer coils to overlap is:

$$\frac{c_s^* R_g^3}{DP} \simeq 1 \tag{5.3}$$

The radius of gyration is given by $R_g \simeq bDP^{\nu}$, where ν is the solvent quality, and $b = 0.45$ nm is the monomer length for PDMAEMA.

To assess the regime for the investigated system, the relevant parameters were determined from the experimental conditions. In the case of a solution at $c = 1\%$ wt of PDMAEMA with a $DP = 89$, and knowing from the NSE investigation $\nu \simeq 0.7$, the concentration of segments per volume resulted:

$$c_s = \frac{Na \cdot c \cdot d_{\mathrm{D_2O}}}{MW_{DMAEMA}} = 1.27 \times 10^{20}\mathrm{cm}^{-3} \tag{5.4}$$

The overlap concentration can be expressed as

$$c_s^* = \frac{DP^{1-3\nu}}{b^3} = 0.79 \times 10^{20}\mathrm{cm}^{-3} \tag{5.5}$$

The system lies therefore in the semidilute regime.

It was instructive to first examine the spectroscopic data of the pure polycation solutions, before analysing the complexes.

To further investigate the dynamics, the effective diffusion coefficient D_{eff} was extracted by assuming a simple exponential decay, $I(q,t)/I(q,0) = \exp(-q^2 D_{eff} t)$. This

parameter represents the diffusion coefficient associated with the collective motion of the system.

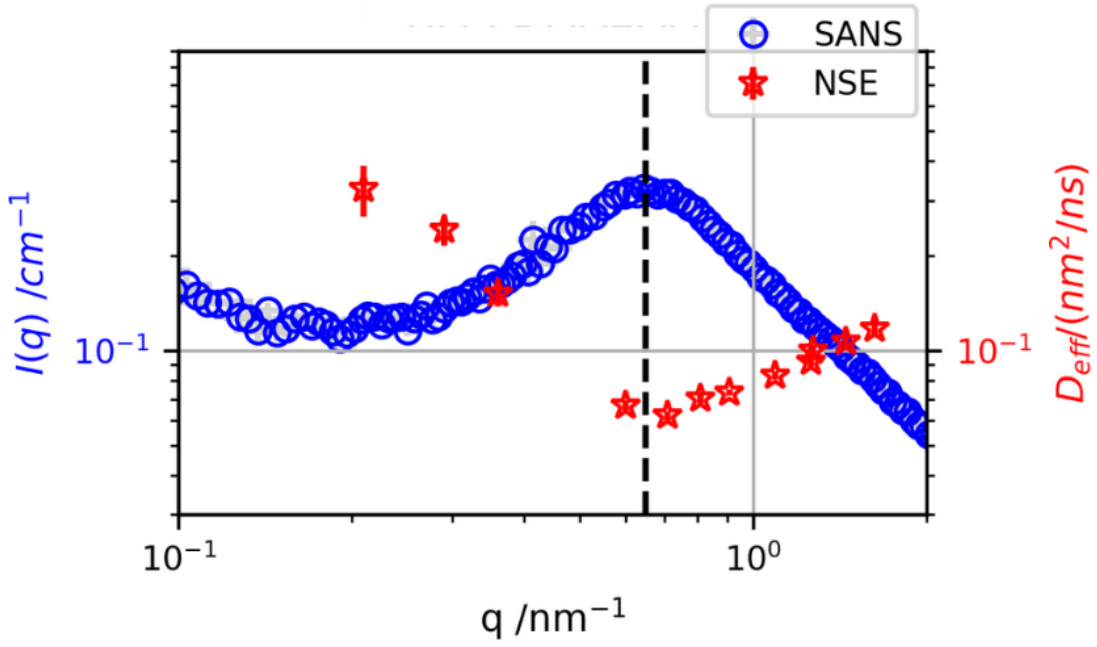

Figure 5.6: Small Angle Neutron Scattering (SANS) data superimposed to the effective diffusion coefficient from Neutron Spin-echo (NSE) for the C12DP100hm9. T was 298 K and the polymer concentration c = 2 % wt.

By looking at fig. 5.6, the so-called "de Gennes narrowing" was observed: [27]. When comparing the q-dependence of $D_{\text{eff}}(q)$ with the static scattering signal from the SANS investigation [16], a perfect overlap was observed between the $S(q)$ peak and a local minimum in $D_{\text{eff}}(q)$, as expected from eq. 1.12. This suggested that the low-q data reflect the interaction between the polymer coils.

Polyelectrolytes (PEs) are electrostatically charged macromolecules that repel each others, [143, 144] and are well-known to give rise to a structure factor peak, as previously reported and confirmed by molecular dynamics (MD) simulations[145, 3, 36, 146]. The $S(q)$ peak was centered at $q \simeq 0.65$ nm^{-1}, corresponding to a characteristic spacing of $l = 2\pi/q_{\text{peak}} \simeq 9.67$ nm, in agreement with the guessed structures. Moreover, the

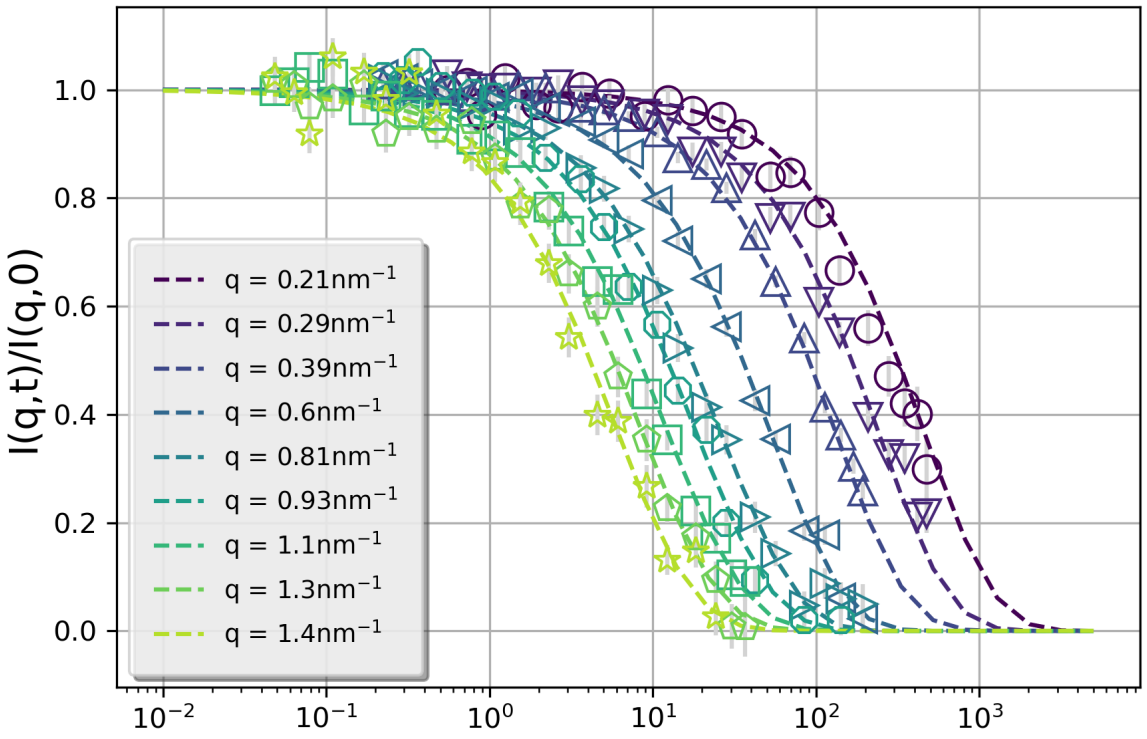

Figure 5.7: Example of fit with the ZIF model for the BICs formed by PDMAEMA at $z^* \simeq 0.2$.

emergence of an $S(q)$ peak is indicative of the PEs forming a semidilute polymer solution.

To extract further insights from the collective diffusion observed via NSE, the behavior of $D_{\text{eff}}(q)$ was modelled by attributing the low-q feature to a combination of hydrodynamic interactions between the polymers and the de Gennes narrowing [3]. The high-q regime ($q > 0.65$ nm^{-1}), where chain dynamics dominates, was described by the ZIF model. When compared with the data (an example of a global fit is shown in fig. 5.7 and all the fits are shown in Appendix B). [108, 109], this model was used to fully describe the bidimensional dynamical structure factor $S(q,t)$ varying only three parameters: the characteristic time τ_{int}, which represents the timescale over which neighboring beads experience internal friction; the hydrodynamic radius R_h, related to intermolecular hydrodynamic interactions; and a parameter ν that quantifies the goodness of the

solvent.

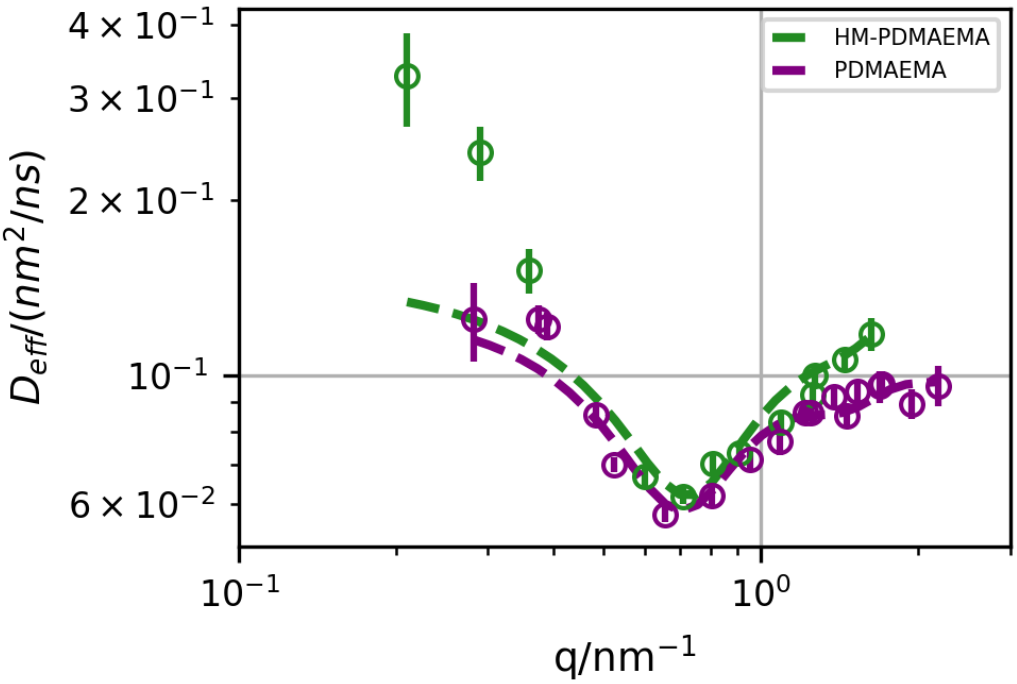

Figure 5.8: Effective diffusion coefficient $D_{\text{eff}}(q)$ of PDMAEMA and C12DP100hm9. Values have been shifted as discussed in the main text.

The results of the model applied to the PDMAEMA and C12DP100hm9 solutions are shown in fig. 5.8, and the corresponding parameters are listed in table 5.1.

Table 5.1: Parameters for fits of the C12DP100hm9 and PDMAEMA solutions: characteristic time τ_{int} of the internal friction between neighboring beads; hydrodynamic radius R_h of the polymer coil; goodness of the solvent ν; and diffusion coefficient D_{cm} of the center of mass of the polymer coil.

Sample	τ_{int} [ns]	R_h [nm]	ν	D_{cm} [nm^2/ns]
PDMAEMA	36(8)	5.2(3)	0.66(3)	0.09(1)
C12DP100hm9	7(2)	4.61(6)	0.53(1)	0.16(1)

The goodness of the solvent parameter ν (table 5.1) is consistent with the expected polymer-solvent interaction for charged macromolecules in aqueous solution ($\nu \simeq$[0.5, 0.8]).[3] Focusing on chain dynamics, a higher τ_{int} (table 5.1) was reported in the case of PDMAEMA. Hydrophobic moieties may promote inter-polymer associations, which would be expected to slow down the dynamics accordingly [147, **?**]. However, a substitution at the charged groups reduced the electrostatic charge density of the polymer (also visible in the titration curve in fig. 3.3) which resulted in a decrease in τ_{int}. The reduced value of ν indicates the higher hydrophobicity of C12DP100hm9. The values of R_h (table 5.1) are comparable within experimental uncertainties.

To evaluate the role of internal friction, it is instructive to compare the characteristic time t_{int} with the overall timescales of polymer chain dynamics. From table 5.1, although t_{int} was appreciable, the characteristic time for the chain dynamics t_{z}, calculated in eq. 1.70, remained higher ($t_{\text{zimm}} \simeq 64$ ns) and therefore dominated the dynamics. The internal friction associated with t_{int} has been attributed to counterion condensation around the polymer backbone [3, 36]. This observation supported the hypothesis that local interactions contribute significantly to the internal friction.

For better visualisation of the data, a shift to the q-values to align the de Gennes narrowing was applied. This shift can be attributed to the different concentrations of the samples, which are not expected to alter the nature of the internal dynamics.

The theoretical relation between the scattering peak position and polymer concentra-

tion can explain this shift: In the case of isotropically distributed, unentangled polymers in a semidilute solution, the structure peak position q_{peak} is related to the average distance between two centers via $d = 2\pi/q_{peak}$.

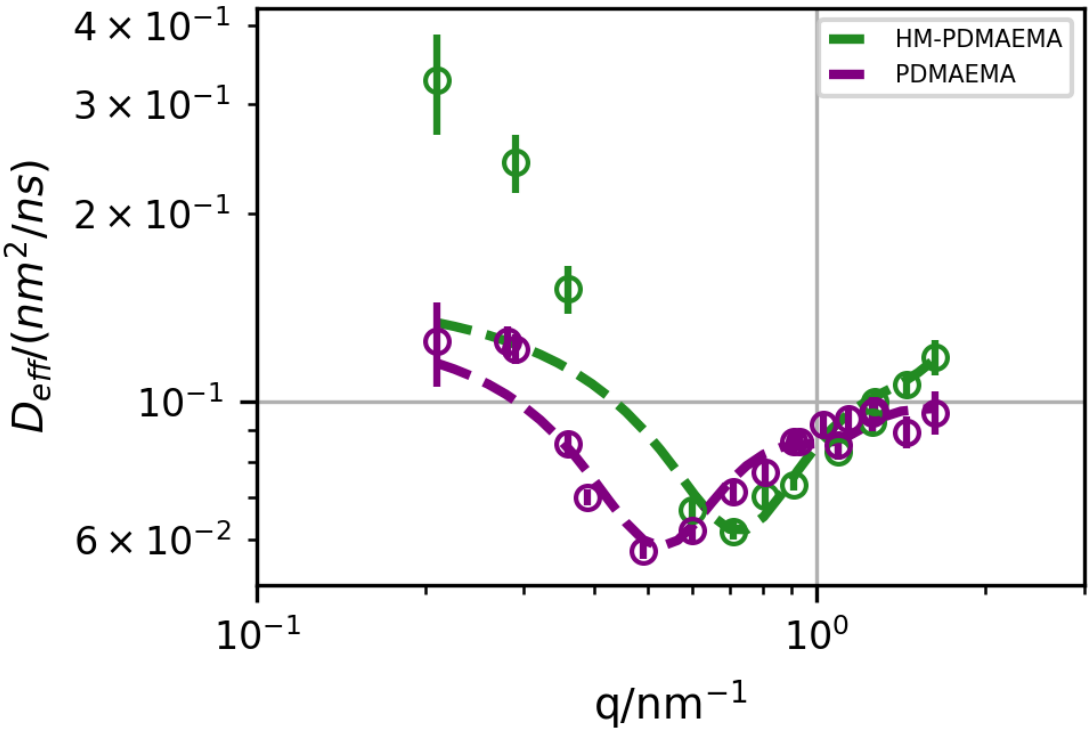

Figure 5.9: D_{eff}(q) calculated from the ZIF model and from the simple exponential fit to both PDMAEMA and C12DP100hm9. A careful reader may notice a different number of q-points in the two datasets: for C12DP100hm9, two measurements were discarded due to power supply failure.

The number density n can then be expressed as:

$$n = \frac{1}{d^3} = \left(\frac{q_{peak}}{2\pi}\right)^3 \tag{5.6}$$

Since $c \propto nMW$, where MW is the molecular weight of a polymer coil, the ratio between the positions of the structure peak can be written as:

$$\frac{q_1}{q_2} = \sqrt[3]{\frac{c_1}{c_2}}\frac{MW_2}{MW_1} \tag{5.7}$$

Here, indices 1 and 2 correspond to the PDMAEMA and C12DP100hm9 solutions investigate at IN15, respectively. Assuming $MW_1 \simeq MW_2$, $K = q_2/q_1 = 1.26$. From the data comparison, the extracted constant resulted $K = 1.37$. By comparing the curves, a ratio $K = 1.37$ was estimated. For completeness, the data without any applied shift were reported in fig. 5.9

To further support that the polymers are in the same regime, it was instructive to estimate the degree of polymerization. By once again relating the average spacing to the nominal concentration, MW was expressed as:

$$MW = \left(\frac{2\pi}{q_{peak}}\right)^3 cN_A 10^{-21}\text{g/mol} \tag{5.8}$$

where N_A is the Avogadro's number and c is the concentration in g/mL. This calculation yelded $MW_{PDMAEMA} = 6032$ g/mol and $MW_{C12DP100hm9} = 4700$ g/mol.

To further explore the effect of concentration, a comparison on the effective diffusion coefficient extracted from two solutions of C12DP100hm9 prepared at $c = 2\%, 3\%$ wt is shown in fig. 5.10

The data showed that increasing concentration shifts the minimum of the de Gennes narrowing, consistent with a more crowded environment.

The effect of the **temperature** on the polymer dynamics was also investigated by measuring the polymer C12DP100hm9 at c = 3% wt at 3 different temperatures ($T = 280, 298, 310$ K). In fig. 5.11, the effective diffusion coefficient for the 2 datasets are compared and the extracted parameters from the ZIF model are shown.

To optimize beamtime usage, a reduced set of q-values was collected at $T = 280$ and 310 K. For a consistent comparison, only the shared q-values were considered. Due to this limited q-range sampling, the fitting parameters were restricted to τ_{int} and ν, fixing R_h to the value estimated from previous SANS measurements.

The trend of segmental dynamics coupled with the structure factor feature was con-

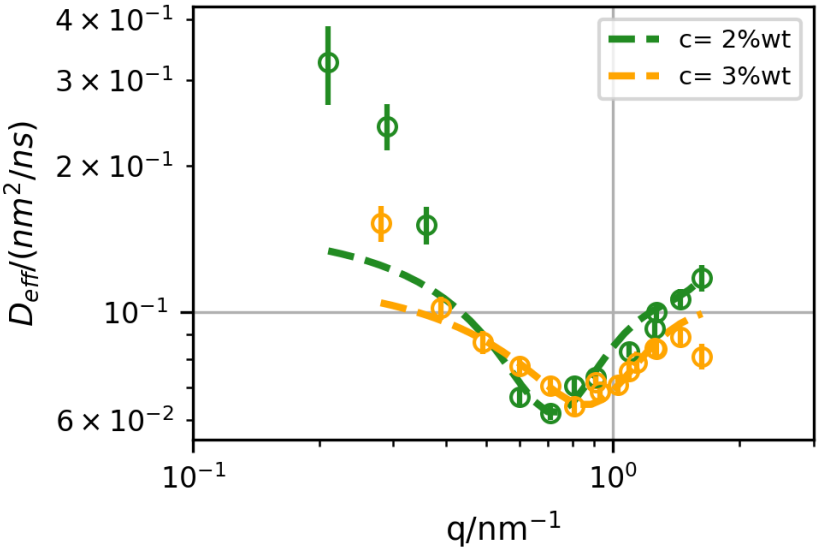

Figure 5.10: D_{eff}(q) applied to C12DP100hm9 measured at c=2% and 3% wt.

served across different temperatures, as shown by $D_{eff}(q)$ in fig. 5.11a. The diffusion coefficient of the center of mass D_{CM} (panel b) increased with temperature, in agreement with the Stokes–Einstein prediction. The characteristic time for friction between neighboring beads, τ_{int} (panel c), decreased with temperature, while the solvent quality parameter ν (panel d) showed a slight decrease. The increased kinetic energy at higher temperatures may destabilize counterion condensation, resulting in more flexible polymer chains.

Neutron Backscattering

While NSE provides access to collective motions over relatively large length scales, it is also instructive to probe the local segmental dynamics using backscattering techniques.

NSE offers valuable insight into the collective chain dynamics of the studied macromolecules. However, to better characterize chain mobility, it is also important to investigate local segmental dynamics.

Backscattering, in contrast, probes dynamics on smaller length scales than NSE and

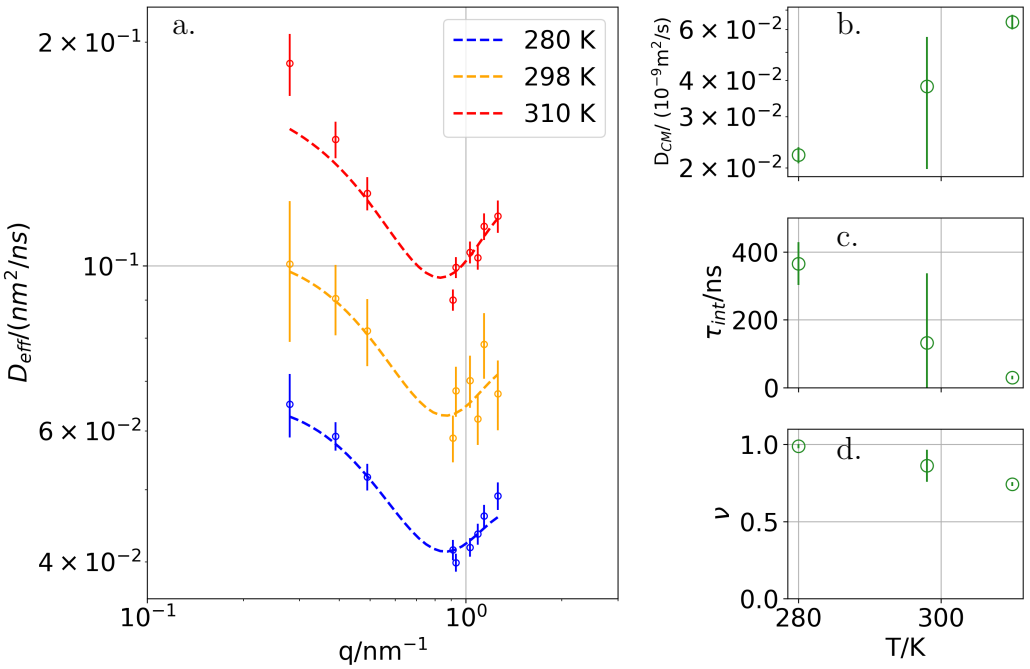

Figure 5.11: (a) Effective diffusion coefficient $D_{eff}(q)$ for C12DP100hm9 at 3% wt. Panels (b–d) show, respectively, the diffusion coefficient of the center of mass D_{CM}, the characteristic time for internal friction τ_{int}, and the solvent quality parameter ν at different temperatures.

provides information corresponding to the ensemble-averaged self-diffusion dynamics.

The local dynamics of similar systems have previously been studied via neutron backscattering. For PANAM dendrimers, an increase in protonation level led to faster dynamics, attributed to a local swelling effect [148, 149].

In the context of thermoresponsive hydrogels, which may exhibit similar features as our systems, the local segmental dynamics inside the hydrogels structures have been probed via neutron backscattering, finding an average characteristic distance of 0.5 nm. [150]

Samples were measured at IN16b in Doppler mode using Si(111) monochromator and analyzer crystals, with an elastic wavelength of 6.27 Å[151].In this configuration, $S(q,\omega)$ was measured in a q-range of $[1.91, 18.88]$ nm^{-1} and energy transfer $E = \hbar\omega \in$

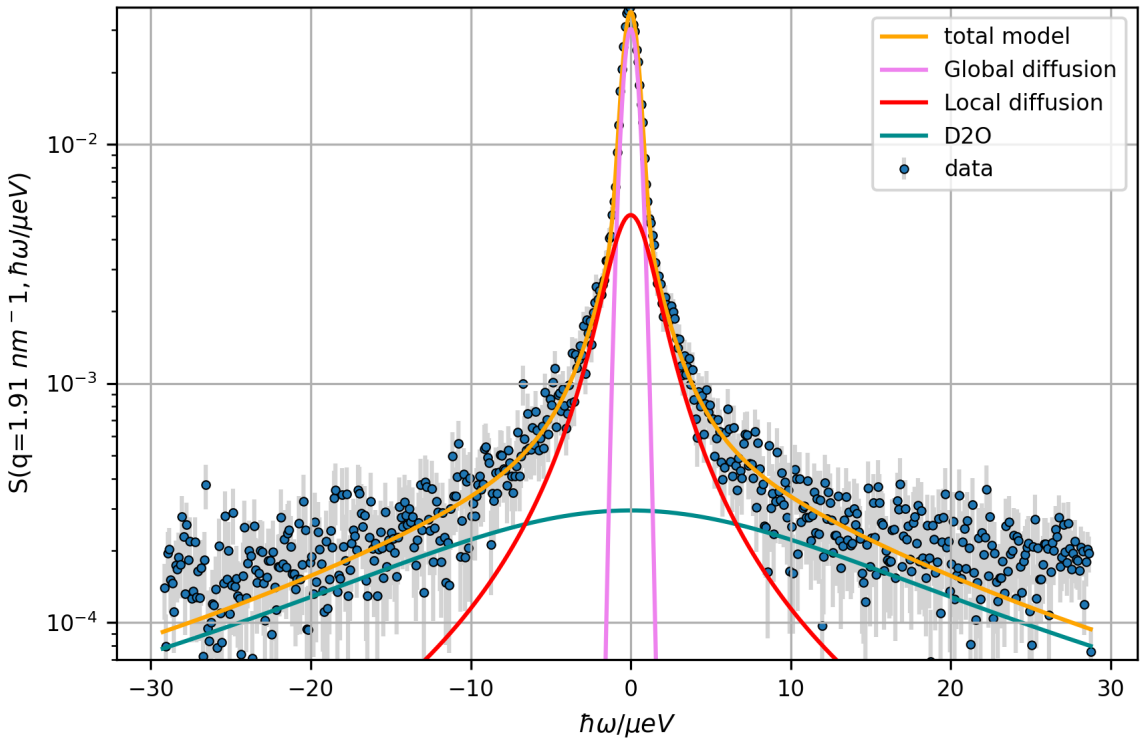

Figure 5.12: Backscattering data from the PDMAEMA sample at T=280 K and q=1.91 nm^{-1}, overlaid with the fitted model.

± 30 μeV. The effective diffusion coefficient is given by eq. 1.12. For high-q $H(q)/S(q) \approx 1$; moreover, the incoherent scattering of the hydrogen dominates over the coherent contributions of the rest of the atomic species in our samples, thus, the self diffusion dynamics was observed. The observed signal reflected the self-dynamics of the hydrogen atoms in the polymeric species. The corresponding scattering function can be written as:

$$\frac{d^2\sigma}{d\Omega d\omega} \propto \sigma_{\text{inc}} S_{\text{inc}}(q,\omega) \tag{5.9}$$

with σ_{inc} being the scattering length density of the hydrogen.

The total scattering function $S(q,\omega)$ comprised contributions from internal motions of the polymer and the motion of its center of mass (CM). Another contribution to

$S(q,\omega)$ was given by anything that was slower than the timescales imposed by the energy resolution, called the elastic peak and represented by a delta function $\delta(\omega)$. Finally, the D_2O scattering gives a broad background.

The energy resolution is well described by a Gaussian function with standard deviation σ, which is approximately 0.45 μeV at the lowest q, and decreases to about 0.38 μeV for $q > 4$ nm^{-1}. The diffusion coefficient of the center of mass of the studied polymers is typically $D_{CM} \simeq 0.02$ nm^2/ns. Since the resolution and the expected width of the CM motion are comparable, the elastic peak contribution was suppressed in this q-range.

These contributions must then be convoluted with the resolution function.

The resolution function was extracted by measuring a vanadium standard, and is well described by a single Gaussian distribution:

$$\begin{aligned} S(q,\omega) = & \\ & = S_{th}(q,\omega) * \mathcal{R}(q,\omega_0) = \\ & = \int S_{th}(q,\omega-\omega_0)\mathcal{R}(q,\omega_0)d\omega_0 = \\ & = \int S_{th}(q,\omega-\omega_0)e^{-\frac{1}{2}\left(\frac{\omega_0}{\alpha(q)}\right)^2}d\omega_0 \end{aligned}$$

where $*$ denotes the convolution operator, $S_{th}(q,\omega)$ is the theoretical model derived from knowledge of the sample, and $\mathcal{R}(q,\omega)$ is the Gaussian distribution with variance $\alpha(q)^2$ representing the instrument resolution.

The final expression for the model $S(q,\omega)$ reads:

$$\begin{aligned} S(q,\omega) =& \beta(q)\big\{A_0(q)D_{CM}q^2 + (1-A_0(q))\mathcal{L}(\Gamma(q),\omega) && (5.10)\\ & + \beta_{\mathrm{D_2O}}(q)\mathcal{L}(\Gamma_{\mathrm{D_2O}}(q),\omega) + \beta_{line}(q)\delta(\omega)\big\} * \mathcal{R}(q,\omega) && (5.11) \end{aligned}$$

Here, $A_0(q)$ is the elastic incoherent structure factor (EISF), $\beta(q)$ is the Debye–Waller factor including an arbitrary amplitude scaling, and $\mathcal{L}(\Gamma(q),\omega)$ is a Lorentzian function

whose width encodes the dynamics under investigation.

$$\mathcal{L}(\Gamma(q),\omega) = \frac{\Gamma(q)}{\pi(\Gamma(q)^2+\omega^2)} \tag{5.12}$$

Similarly, $\beta_{\mathrm{D_2O}}(q)\mathcal{L}(\Gamma_{\mathrm{D_2O}}(q),\omega)$ represents the contribution from the D_2O background. The center-of-mass dynamics is modeled as a Lorentzian with width $D_{CM}q^2$, assuming Brownian free diffusion.

Similarly $\beta_{\mathrm{D_2O}}(q)\mathcal{L}(\Gamma_{\mathrm{D_2O}}(q),\omega))$ are the same quantities related to the D_2O contribution. The dynamics of the CM is then represented by the delta $D_{CM}q^2$ in the assumption of a Brownian free diffusion. $\beta_{line}(q)\delta(\omega)$ is the elastic contribution of the cell and everything that is too slow to be resolved.

The simple model in eq. 5.11 provided a satisfactory description of the data; an example of a spectrum at a single q-value is shown in fig. 5.12. In this figure, the contribution of D_2O is an order of magnitude less than any other contributions. In between the elastic peak and the D_2O contribution a broadening appears, which corresponds to the internal dynamics of the polymer. Looking at the chemical structure of PDMAEMA (fig. **??**b), a bigger fraction of H atoms are attached to the side chains (8 on the side chains against 5 on the backbone). The same fit for all samples at all q-values are shown in Appendix C.

In C12DP100hm9, 8.6% of the carboxylic groups were substituted with dodecyl (C12), which contains 25 hydrogen atoms. This led to a ratio between the C12 and amine group contributions of $Q := \frac{0.086\times 25}{(1-0.086)\times 10} \simeq 0.24$, thus for both polymers, the dynamics of the side chains was observed.

To support the validity of the chosen form of $S(q,\omega)$, alternative interpretations of the experimental data were also considered. A common approach to model $S(q,\omega)$ is to use the empirical Kohlrausch–Williams–Watts KWW function developed to represent a distribution of relaxations in the intermediate scattering function. For polymers, the Zimm model is effectively described by a KWW function, where the relaxation time distribution arises from the internal modes of the polymer chains.

To directly compare the timescales observed with NSE and backscattering, a Fourier

transform was applied to the ZIF model fitted to the NSE data.

$$S_{ZIF}(q,\omega) = \frac{1}{2\pi I_{ZIF}(q,0)} \int I_{ZIF}(q,t) e^{i\omega t} dt \tag{5.13}$$

The BS data were fitted with the model $S(q,\omega) = AS_{ZIF}(q,\omega) + S_{D_2O}(q,\omega)$.

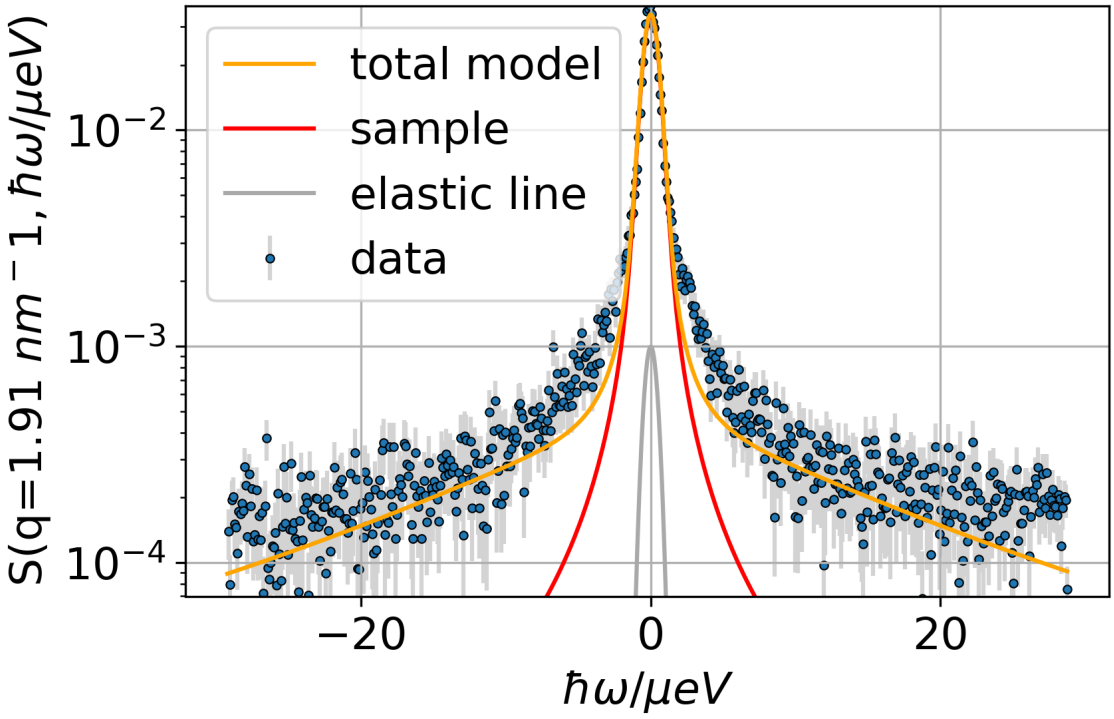

Figure 5.13: $S(q,\omega)$ for the pure polyelectrolyte PDMAEMA at temperature 280 K and c = 3 % wt. modelled by the ZIF model.

Fig. 5.13 shows the data and the ZIF model transformed and fitted on top: this model generally represented well the global dynamics of the center of mass, however a broader contribution suggested a dynamics which is not captured by NSE and thus by the ZIF model. It was concluded that the bead spring representation was not sufficient to model the investigated data. The purpose of the model in eq. 5.11 is to capture internal dynamics that are not accounted for by the bead-spring representation.

The energy resolution is directly correlated to the nanosecond timescale probed in

this investigation by the energy-time uncertainty. By analyzing the q-dependence of the Lorentzian width $\Gamma(q)$, the nature of internal dynamics of the polymers on the nanosecond timescale was characterized.

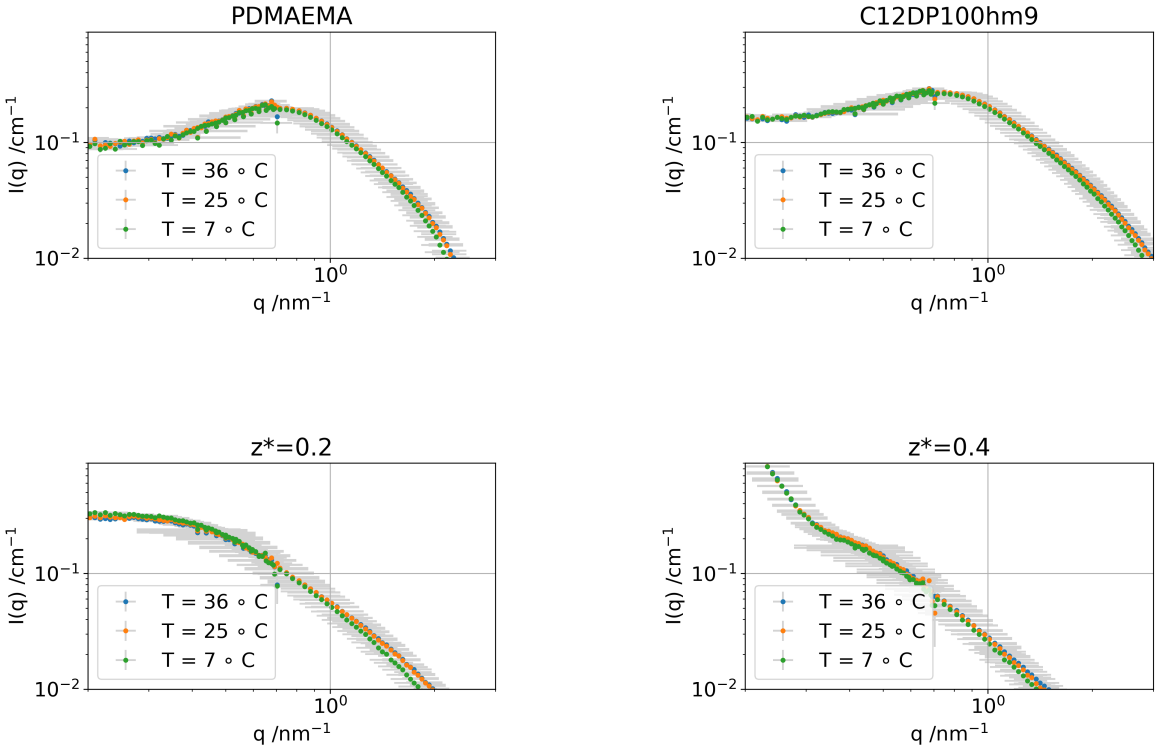

Figure 5.14: SANS spectra for different samples prepared at 3% measured at SAM. z^* is the mixing ratio defined as $z^* = \frac{[-]}{[-]+[+]}$, where [*] is the molar concentration of the charged species.

In this investigation, three temperatures were explored (280, 290, and 310 K) to characterize the dynamical behavior. Complementary SANS measurements were performed to verify that no structural changes occurred within this temperature range, as shown in fig 5.14.

The width of the Lorentzian modeling the internal polymer dynamics, $\Gamma(q)$, was extracted by fitting $S(q,\omega)$ with eq. 5.11, as shown in fig. 5.15. $\Gamma(q)$ deviated from linearity at high-q and this deviation was more marked in the case of PDMAEMA.

The nature of the deviation suggested the presence of anomalous dynamics, primarily observed at high q-values: this effect has been observed in many biological systems such as antibodies [152] or proteins in general, [153] but also polymer networks. [154, 155, 156, 157] This type of dynamics has been modeled as a distribution of discrete jumps of specific lengths. With a similar approach to what has been done on Intrinsically Disordered Proteins (IDPs),[158] the model proposed by Singwi and Sjölander was applied to the investigated system. This model describes a particle jumping between a harmonic motion of period τ_h and free Brownian diffusion with a diffusion coefficient D. [104] In the condition $\tau_h \ll \tau$, where τ is the characteristic time of the brownian diffusion, Γ(q) can be modelled as: [159, 160]

$$\Gamma(q) = \Gamma_0 + \frac{D_{self} q^2}{1 + D_{self} \tau q^2} \tag{5.14}$$

Γ_0 is a parameter ensuring a finite value at low q, accounting for any global diffusion not included in the elastic peak. This parameter should be close to 0 and this was in fact true for all the fits. D_{self} is the characteristic self-diffusion coefficient of the dynamics under investigation, and τ is the persistence time. The parameters are shown in fig. 5.15 and in table **??**.

The self-diffusion coefficient D (inset in fig. 5.15) is significantly higher for PDMAEMA compared to C12DP100hm9, confirming that the presence of the hydrophobic modification drastically reduces chain mobility, likely due to the hydrophobic interaction. Additionally, for C12DP100hm9, D increases with temperature, in agreement with the Stokes-Einstein relation,[29] while for PDMAEMA no such trend is seen (potentially due to the rather large errorbars on D).

Another difference between C12DP100hm9 and PDMAEMA lies in the persistence time τ (table **??**), which is larger for PDMAEMA, suggesting stronger confinement. This feature was once again related to the lower charge density along the polymer backbone in the case of C12DP100hm9, enhancing the flexibility of the polymer and thus the mobility of the side groups. Other studies have explained the confinement in similar systems as a three site jump in between the H of the methyl groups. [161, 162] The fact that this

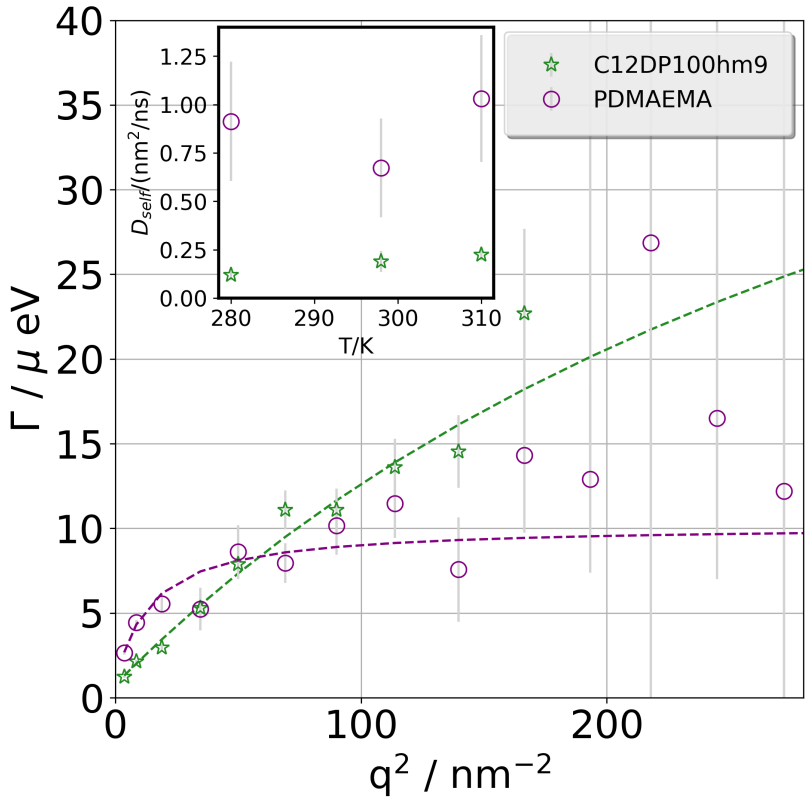

Figure 5.15: $\Gamma(q)$ with respect to q^2 for C12DP100hm9 and PDMAEMA: the inset shows the diffusion coefficient D_{self} extracted from the jump diffusion model as a function of T. Dotted lines are fits with eq. 5.14.

confinement effect is more pronounced for PDMAEMA, where there are more methyl groups, reinforced this hypothesis.

$S(q, \omega = 0)$ is connected with the vibrational modes of our system and in the case of an harmonic process the intensity is proportional to the populations of the different modes, which results in the well-known Debye-Waller factor: [163, 164]

$$S(q, \omega = 0) = \beta(q) = Ae^{-\langle MSD \rangle q^2/3} \tag{5.15}$$

Where $\langle MSD \rangle$ is the mean square displacement of the vibrations and $\beta(q)$, as ex-

Table 5.2: Parameters extracted from the analysis of the BackScattering investigation of the pure polycation solutions at c = 3 % wt at different temperatures.

	D	τ	$\sqrt{\langle MSD \rangle}$	$\sqrt{\langle R^2 \rangle}$
C12DP100hm9 (280 K)	0.12 ± 0.03	0.04 ± 0.01	0.143 ± 0.008	0.47 ± 0.05
C12DP100hm9 (298 K)	0.19 ± 0.05	0.06 ± 0.02	0.171 ± 0.010	0.47 ± 0.07
C12DP100hm9 (310 K)	0.22 ± 0.03	0.011 ± 0.007	0.158 ± 0.007	0.41 ± 0.06
PDMAEMA (280 K)	0.9 ± 0.3	0.081 ± 0.007	0.153 ± 0.014	0.42 ± 0.07
PDMAEMA (298 K)	0.7 ± 0.3	0.05 ± 0.01	0.163 ± 0.025	0.47 ± 0.07
PDMAEMA (310 K)	1.0 ± 0.3	0.070 ± 0.007	0.156 ± 0.016	0.50 ± 0.06

D: Diffusion coefficient.
τ: jump diffusion time.
$\sqrt{\text{MSD}}$: root square of the mean square displacement calculated from the Debye-Waller factor.
$\sqrt{\langle R^2 \rangle}$: Radius of the gaussian potential calculated from the Elastic Incoherent Structure Factor.

tracted from the model, is shown in fig. 5.16. The first two points have been excluded from data fitting due to the broader energy resolution of the lowest two detectors compared to all others, resulting from the geometry of their mounting inside the spectrometer. A deviation from the exponential behavior was observed and explained by contamination of the elastic contribution of the empty can. From this analysis, $\sqrt{\langle MSD \rangle} \simeq 0.16$ nm. A previous investigation on the denaturation of bovine serum albumin (BSA) obtained values in the same order. [165] As pointed out there, the magnitude of $\sqrt{\langle MSD \rangle}$ was much higher than typical atomic vibrations, due to the diffusive modes of the investigated macromolecules (BSA in their case, polyelectrolytes in this investigation). Surprisingly, looking at the temperature behavior and the influence of hydrophobic modifications, no particular trend was observed between C12DP100hm9 and PDMAEMA.

Another insightful quantity present in our model is the Elastic Incoherent Structure Factor EISF(q), described by the parameter $A_0(q)$ shown in Fig. 8. This parameter decays to zero around $q \simeq 7.5$ nm^{-1}. As explained in the Experimental section, the amplitude ratio of the center-of-mass and internal Lorentzians is identified as the elastic incoherent structure factor $A_0(q)$ (eq. 5.11), carrying information on the geometry of confinement.[162] Assuming the particles being confined in a Gaussian profile centered

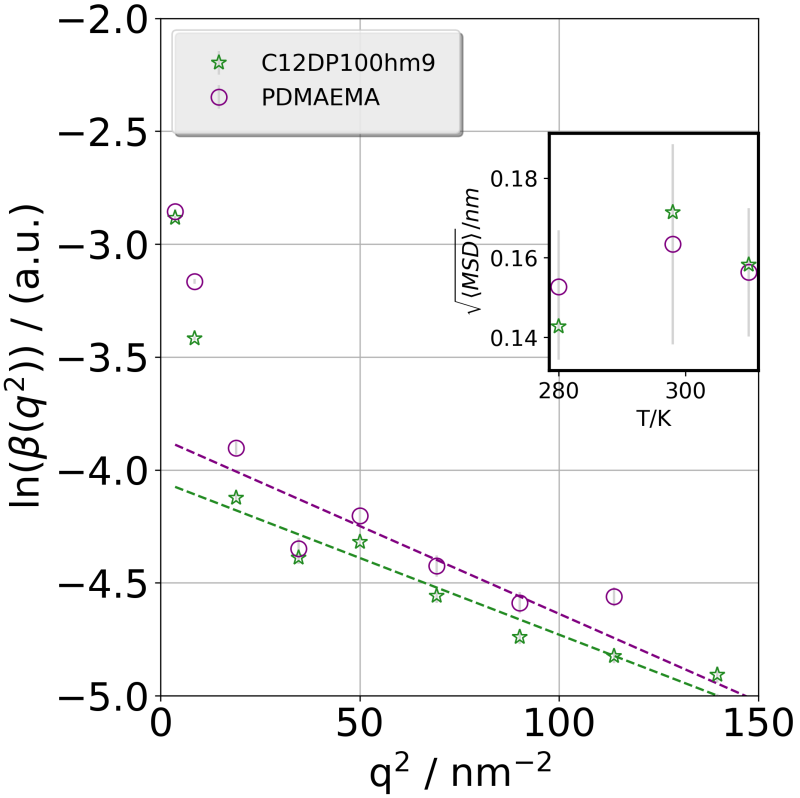

Figure 5.16: Debye-Waller factor calculated for PDMAEMA and C12DP100hm9 at T=280 K. Fits are represented with dashed lines. From the fits for each T $\langle MSD \rangle$ was extracted and shown in the inset plot.

at a distance $\sqrt{\langle R^2 \rangle}$: [105]

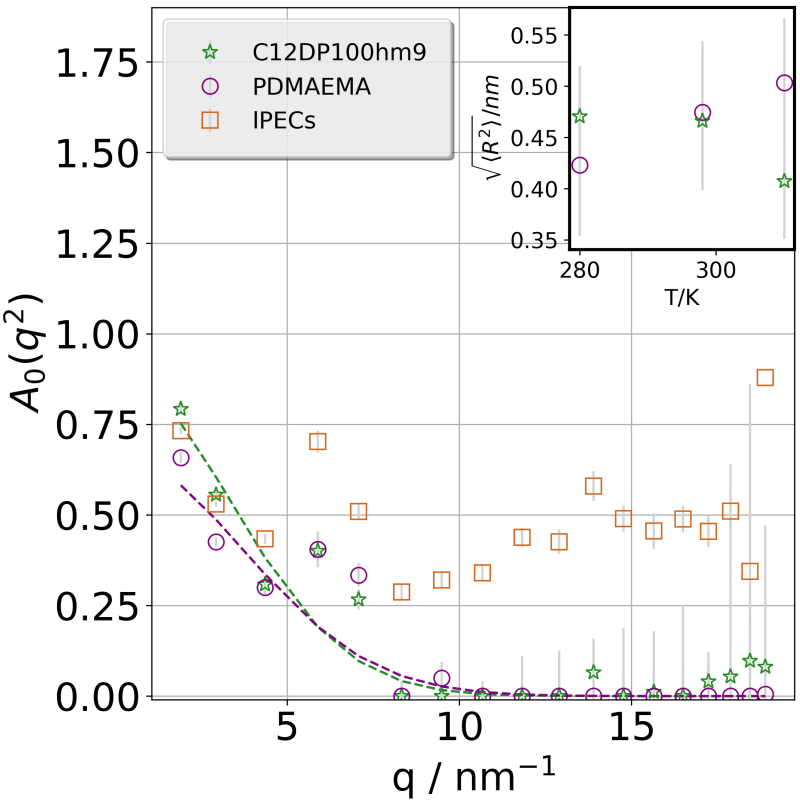

Figure 5.17: Elastic Incoherent Structure Factor calculated for polyelectrolyte solutions of PDMAEMA, C12DP100hm9 and interpolyelectrolyte complexes using the polycation PDMAEMA. All the curves correspond to the data measured at T=280 K. Fits are represented with dashed lines. From the fits for each T $\langle R \rangle$ was extracted and shown in the inset plot.

$$A_0(q) = Ae^{-q^2\langle R^2 \rangle/5} \tag{5.16}$$

In this model, the distance $\sqrt{\langle R^2 \rangle} \simeq 0.45$ nm corresponds to the diameter of the PDMAEMA subunit, suggesting the H-atoms to be trapped in a region compatible with the monomer size. The error bars are too large to allow a conclusive assessment of temperature dependence.

Interpolyelectrolyte Complexes

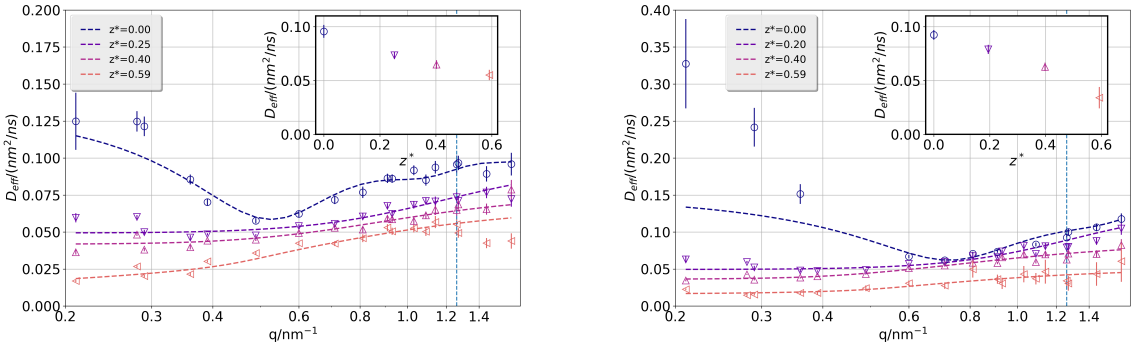

(a) IPECs made from PDMAEMA

(b) IPECs made from C12DP100hm9

Figure 5.18: $D_{eff}(q)$ for IPECs made from PDMAEMA (a) and C12DP100hm9 (b) at different mixing ratios z^*, represented as hollow points. Dotted lines show the ZIF model fitted to the experimental data. The inset displays the behavior of $D_{\text{eff}}(z^*)$ at $q = 1.26$ nm^{-1} (vertical line).

Hydration influences polymer dynamics; to better understand aggregate properties, it is crucial to probe this behavior. Using NSE, a q-range from 0.21 to 1.63 nm^{-1} was explored, corresponding to length scales of approximately 3.8 to 29.9 nm. As pointed out in the graphical abstract, this q-range corresponds to zooming inside the aggregates, focusing on the chain dynamics of the aggregated polymers. The resulting q-dependence of the effective diffusion coefficient $D_{eff}(q)$ (as described in the above) is shown in fig. 5.18a for PDMAEMA IPECs and fig. 5.18b for C12DP100hm9 IPECs.

Upon forming aggregates (increasing z^*), the de Gennes narrowing disappeared. Since this feature originates from electrostatic repulsion, adding an oppositely charged component neutralizes the system and reduces repulsion. This observation is in agreement with the model published earlier.[16]

Approaching equimolarity, $D_{eff}(q)$ decreased across all q-values: the complexation of oppositely charged PEs forms larger aggregates, which diffuse more slowly. High-q dynamics also slowed down, as shown in the inset of fig. 5.18a. At q = 1.26 nm^{-1}, $D_{eff}(q)$ decreased by a factor $\simeq 0.5$. This is an effect of the electrostatic interactions

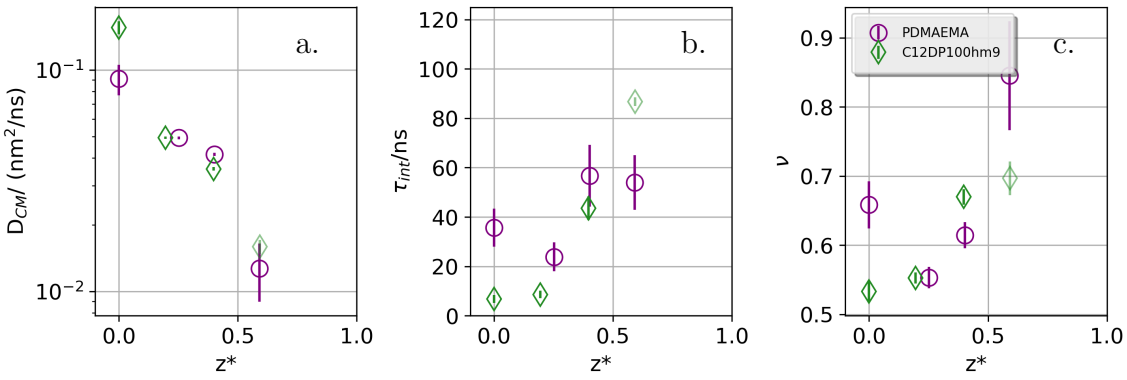

Figure 5.19: Diffusion coefficient of the center of mass D_{CM} (a), characteristic time for internal friction τ_{int} (b), and solvent quality parameter ν (c). Parameters were extracted using the NSE model of eq. 1.69 applied to IPECs investigated at IN15, ILL. The C12DP100hm9 IPEC sample at $z^* \simeq 0.6$ appears faded to represent the poor data quality.

suppressing the chain dynamics and similarly seen for the two pure polycations.

By applying the ZIF model to the IPECs, the hypothesis drawn was that the aggregates can be modelled as polymer species in semidilute conditions. As the aggregates are highly hydrated, they can be considered as being "polymer like" objects. The extracted features are an ensemble average over the 2 polymeric species forming the aggregate. With this model, it was possible to quantitatively determine how the dynamics of the IPECs is influenced by the complexation: fig. 5.19 shows the parameteres resulting from the fits.

Being close to equimolarity, it can happen that the samples experience phase separation. A detailed characterization of the phase behavior was already discussed. In the case of the NSE investigation, a biphasic separation during the measurement was noticed for the IPECs formed by C12DP100hm9 around equimolarity. Due low signal-to-noise ratio, the sample of IPECs made by C12DP100hm9 at $z^* = 0.6$ was probed in two different beamtime, obtaining the same results: during the measurement, a phase separation occurred. By checking the static intensity $I(q)$ of the sample, stable values were registered during the investigation, meaning that the separation did not happen

during the measurements.

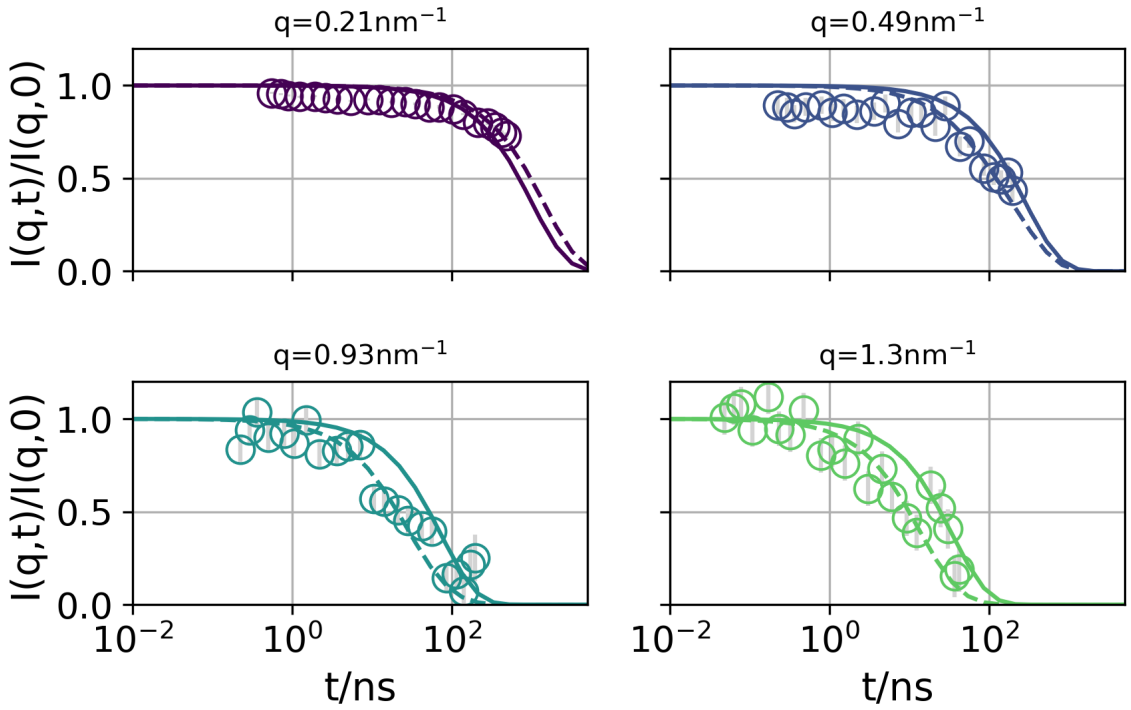

Figure 5.20: Intermediate scattering function $I(q,t)$ for IPECs at $z^* \simeq 0.6$, measured at selected q-values. Solid lines: single exponential fit; dotted lines: ZIF fit.

Fig. 5.20 shows fits at different q-values. At low q, $I(q,t)$ did not decay reliably, complicating the fit. At higher q, data noise prevented reliable interpretation of chain dynamics. Moreover, at higher q, the data were too noisy to discuss the chain dynamics extracted from this sample. Due to these issues, τ_{int} was not fitted, but only the remaining parameters of the ZIF model for this sample.

The application of the ZIF model to the experimental data for the IPECs formed with PDMAEMA with and without hydrophobic modification allowed to describe the complexation effect in detail. First, the diffusion coefficient of the center of mass D_{CM} (Fig. 10a) decreased upon approaching equimolarity in a similar fashion for PDMAEMA and C12DP100hm9. Aggregation yielded larger structures in both cases, leading to

slower center-of-mass diffusion.

The characteristic time for internal friction, t_{int} (fig. 5.19B), increased slightly upon approaching equimolarity for both C12DP100hm9 and PDMAEMA. The internal friction has been associated to the short-range backbone dihedral rotation for IDPs.[166, 167, 168] the ion pairing between oppositely charged PEs stiffened the polymer backbone, suppressing dihedral motions and slowing polymer dynamics.

The solvent quality parameter ν, which quantifies polymer–solvent interactions, decreased from 0.8 to 0.5 with increasing z^*, then increased again at higher z^*. Around equimolarity the dynamics was suppressed by the electrostatic interactions, leading to noisy data and thus big errorbars on ν and in general for all the fitted parameters.

The estimation of D_{CM} is taken from Jscatter documentation [13].

$$D_{CM} = 0.203 k_b T/(R_e \mu) \tag{5.17}$$

Here, R_e is the end-to-end distance, while μ is the viscosity of the solvent (D_2O). For IPECs at $z^* \simeq 0.6$ formed with PDMAEMA it was found $D_{\mathrm{CM}} \simeq 0.0127 \pm 0.004$ nm^2/ns. The dynamics of the center of mass shows a substantial difference given by the hydrophobic modifications. In the case of IPECs at $z \simeq 0.6$ formed with PDMAEMA, a $D_{CM} \simeq 0.0127(40)$ nm^2/ns is observed. Using the Stokes–Einstein relation, the hydrodynamic radius resulted $R_H \simeq 14 \pm 4$ nm. This agrees with previous SANS measurements reporting an aggregate radius of $R \simeq 17$ nm (and thus $R_g \simeq 13$ nm).

Using NSE, dynamics were probed at length scales where polymer substructure is mostly averaged out; backscattering, however, accesses more local dynamics, revealing molecular-level processes that mainly affect the elastic peak.

A comparison of PDMAEMA and the IPEC at z* = 0.6 (fig. 5.22a) showed the superposition of a pure polyelectrolyte and an IPECs (at a mixing ratio $z^* \simeq 0.6$) $S(q, \omega)$ summed over the q-range. The IPEC data showed a narrower peak, which suggested a reduced internal dynamics. Moreover, in fig. 5.22b, the same comparison is shown for IPECs made by C12DP100hm9 and PDMAEMA, where the hydrophobic modification suppressed even further the dynamics.

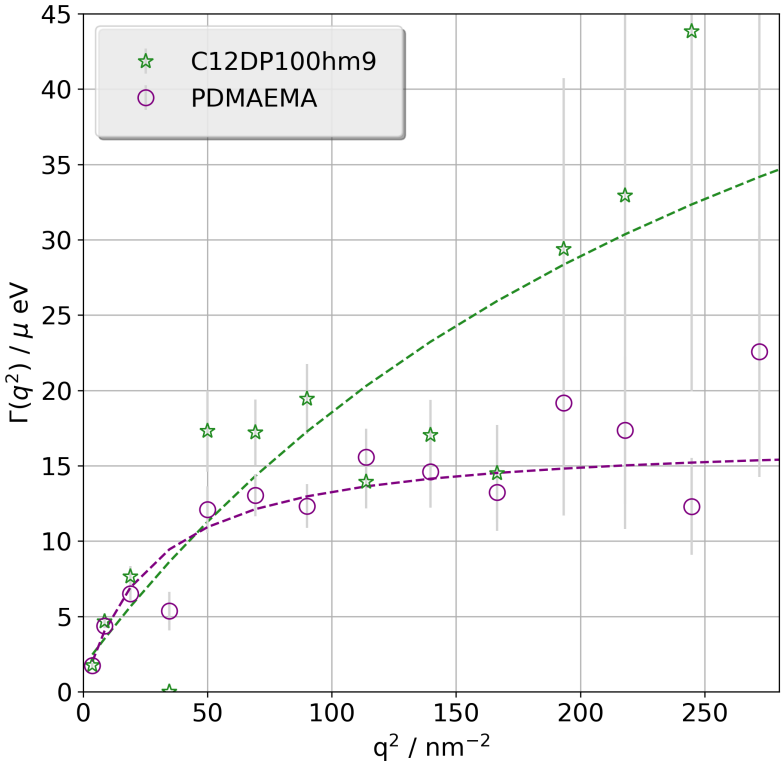

Figure 5.21: Width of $S(q,\omega)$ $\Gamma(q)$ extracted for the IPECs at a mixing ratio $z^* \simeq 0.6$ and at $T = 280$K.

By modelling $S(q,\omega)$ for IPECs at $z^* \simeq 0.6$ with the model given by eq. 5.11, the fits were satisfactory. Fig. 5.21 shows the comparison between the Lorenzian width $\Gamma(q)$ calculated from the IPECs made by PDMAEMA and C12DP100hm9 and the main parameters extracted from fitting $S(q,\omega)$ are given in table 5.1, with the values of the pure polyelectrolyte solutions for a comparison.

Looking at the results, the dynamics does not show effects of the aggregation process. The deviation to a sub-linear regime at high-q is once again more pronounced in the case of unmodified PDMAEMA, as before for the pure polymers (fig. 6), reinforcing the hypothesis that the confinement of the dynamics can be described by a three-site jump of the methyl groups. This sub-linear deviation was also appreciable in the persistence

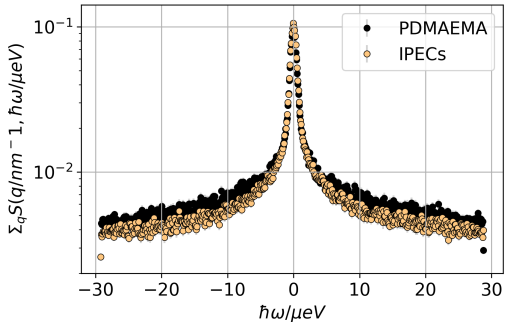

(a) Sum over q of $S(q,\omega)$ of the pure polyelectrolyte solution and the IPECs (at a $z^* = 0.6$) formed by PDMAEMA. Temperature at 280 K and c = 3 % wt.

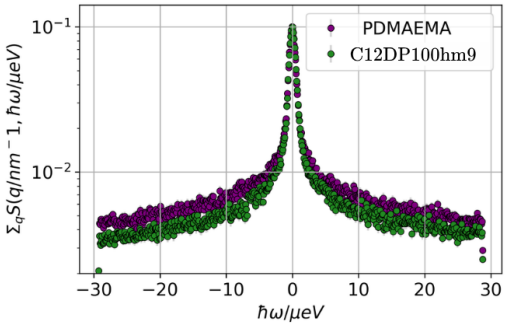

(b) Sum over q of $S(q,\omega)$ of the pure polyelectrolyte solutions of PDMAEMA and C12DP100hm9. Temperature at 280 K and c = 3 % wt.

Figure 5.22

	PDMAEMA	**IPECs** ($z^* \simeq 0.6$)	**C12DP100hm9**	**HM-IPECs** ($z^* \simeq 0.6$)
$D_{self}/(\mathrm{nm}^2/\mathrm{ns})$	0.9 ± 0.3	0.9 ± 0.2	0.12 ± 0.03	0.34 ± 0.19
$D_{CM}/(\mathrm{nm}^2/\mathrm{ns})$	0.027 ± 0.003	0.0208 ± 0.0007	0.019 ± 0.002	0.0125 ± 0.0003
τ/ns	0.081 ± 0.007	0.039 ± 0.004	0.04 ± 0.01	0.1 ± 0.1

Table 5.3: Parameters extracted from the backscattering data of the PDMAEMA, C12DP100hm9 and their IPECs close to equimolarity, measured at 280 K and at c=3% wt. Given are the self-diffusion coefficient, the center-of-mass diffusion coefficient, and the characteristic time.

time τ, which is smaller for samples with C12DP100hm9. Interesting is also that the values of $\Gamma(q)$ are consistently lower for the IPECs compared to the homopolymer.

Despite complexation not significantly affecting local dynamics, comparison of the EISF(q) (fig. 5.17), represented by $A_0(q)$ in eq. 5.11, shows that $A_0(q)$ is substantially higher for the complexes. This observation suggested that the slower mode of the center of mass predominated the IPECs $S(q,\omega)$, while this is not the case for the pure polyelectrolyte solutions, where the internal dynamics (the inelastic part of $S(q,\omega)$ within the energy window investigated) had a higher contribution. For a comparison, a high amplitude of the slow modes assessed to the center of mass motions was also observed in a similar investigation of β-Casein, where the local dynamics of the hydrogens was also

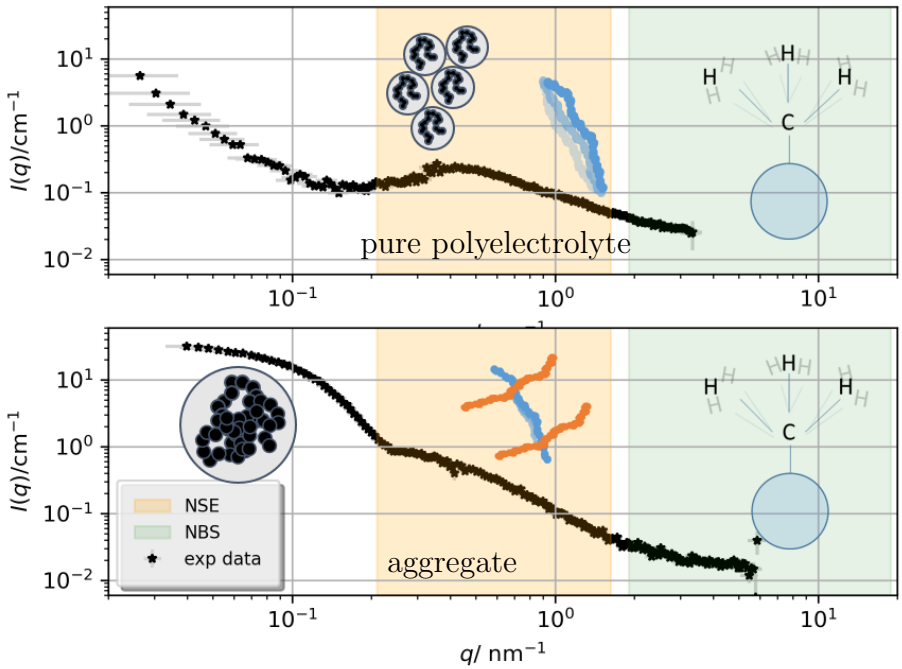

Figure 5.23: SANS scattering intensity $I(q)$ for a sample of pure polycation PDMAEMA at 1% wt and the corresponding IPECs close to equimolarity regime. On top of the plots, the different features are drown of the systems and the q-ranges in which the neutron spectroscopy investigations have been performed are underlined.

not dramatically affected by the micellization. [169]

5.2.2 Conclusions

In this study, the local dynamics of the polycation PDMAEMA was investigated, both in its pure form and hydrophobically modified (8.6 mol% C_{12}), in aqueous solution and in complex with the oppositely charged double-hydrophilic PEO–PMAA. Two complementary neutron scattering techniques were employed, suited to probing nanoscale dynamics, combined with DLS measurements. The interaction between the two types of polyelectrolytes leads to the formation of interpolyelectrolyte complexes (IPECs). Our focus was on the effect of IPEC formation and hydrophobic interaction on the dynamics. These

insights may prove useful for future applications of IPECs as nanocarriers, for instance in drug delivery systems.

Fig. 5.23 illustrates the relationship between nanoscale structure and dynamics. It displays SANS curves of a pure polyelectrolyte samples and IPECs samples near equimolarity, along with schematic drawings representing the corresponding dynamics. The q-range limits of the two neutron spectroscopy techniques are crucial for understanding which features are probed: NSE is sensitive to dynamics on the scale of polymer chains and does not extend to full aggregate size, whereas NBS captures the local dynamics of chain segments. In our data analysis, the intermediate scattering function was successfully described using a model of interacting polymer chains. Chain dynamics is reduced in the IPEC samples, with internal friction increasing as equimolarity is approached. Electrostatic interactions between oppositely charged monomers promote the formation of larger aggregates. This leads to the disappearance of the correlation peak, as individual polymer chains are no longer correlated in solution.

The incoherent $S(q, \omega)$ revealed that hydrophobic modifications induce a slowdown in dynamics and hinder the mobility of PDMAEMA segments. While probing structure and collective dynamics, no clear effect of the hydrophobic modifications was detected at high q, suggesting that hydrophobic interactions play only a minor role at these scales. Moreover, any hydrophobic clusters potentially present would scatter weakly and thus contribute little to the observed signal.

This study exemplifies how combining different QENS techniques enables the investigation of nanoscale dynamics in complex polymeric systems. Notably, local chain dynamics is predominantly slowed by electrostatic interactions, while additional hydrophobic interactions have only a marginal impact. These insights contribute to a better understanding of the aggregation behavior of IPECs.

Chapter 6

Computational model

This computational model was initially developed to represent the hydrophobic domains in IPECs formed by hydrophobically modified polyelectrolytes. These molecular aggregates exhibit a hierarchical structure, with distinguishable levels of aggregation. Prior to the structural investigation, the hydrophobic domains were expected to be observable within polymer aggregates. Although the SANS investigation revealed that the hydrophobic domains are not detectable and that only the polymer behavior is observed, it remains instructive to discuss this model in the context of different applications. One example is the case of polyelectrolyte microemulsion complexes (PEMECs), where the spherical micelles provided by the microemulsion are more defined than the aggregates formed by hydrophobic moieties.

6.1 The model

With the rise of computational resources, in silico simulations of molecular systems have been increasingly employed to extract their behavior and compare it with experimental results. In the conceptualization of the potential, all the units are Lennard-Jones units, which are arbitrary units. A system of N particles has $6N$ coordinates from which the thermodynamic variables can be calculated. Every configuration is called *a microstate* and assuming the system is ergodic, the average features of the system are extracted

from the ensemble average performed on the set of the microstates.

In this context, two main computational approaches are commonly used:

- **Molecular dynamics:** by solving the equations of motion using a discrete-time approach, the dynamics of the molecular system can be reproduced. A typical example is the Verlet integration [170]. These algorithms aim to capture the true dynamics of the system but are limited by energy barriers present in its energy landscape.

- **Monte Carlo:** A well-known example is the Metropolis algorithm [171]. These methods do not aim to reproduce the system dynamics and are not intended to simulate trajectories. Since the exploration of phase space is stochastic, a careful design of the sampling procedure can overcome limitations imposed by the ruggedness of the energy landscape.

The hydrophobic domain is defined as the fundamental unit of the system and is represented as a sphere. These spheres interact via an exponential potential $U_{soft}(r)$.

$$U_{soft}(r) = \begin{cases} A\exp(-r/\rho) + c & r \leq r_c \\ 0 & r > r_c \end{cases} \tag{6.1}$$

Here, A denotes the interaction strength, ρ the characteristic interaction length, and r_c the cutoff distance beyond which the potential is set to zero. The potential is illustrated in Fig. 6.1.

By adjusting these parameters, one can define the *softness* of the spheres. As a preliminary step, a short simulation was performed to determine the effective radius. In this simulation, all interactions between particles were switched off, except for those between a single reference particle and the surrounding medium. This setup mimics Brownian motion, in which many point-like particles influence a single finite-size particle. From the simulation, the radial pair distribution function $g(r)$ was calculated, representing the number of particles found within the shell $r + dr$.

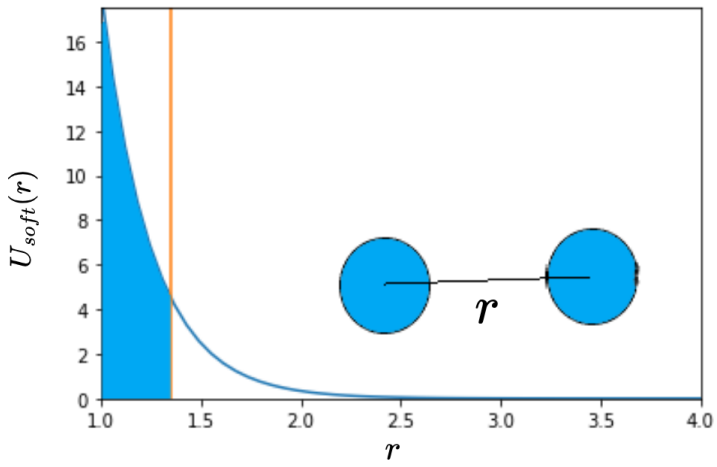

Figure 6.1: Interaction potential between the units of the systems. The colored subtended area represents the region where the two particles compenetrates each other. Values in Lennard-Jones units.

From fig. 6.3a, no particles are found closer than $l \simeq 1.35$, corresponding to a particle radius of $r = d/2 = 0.675$. All variables are expressed in Lennard-Jones units, which are arbitrarily rescaled according to the potential.

After defining the elementary unit, a confining potential was introduced to simulate the aggregation pattern. As a first approximation, the aggregation was assumed to be spherical, and a spherical wall was used to confine the particles within a specific region. The entire confining shell interacts with the particles via a Lennard-Jones potential:

$$U_{LJ}(r) = \begin{cases} 4\varepsilon \left[\left(\frac{\sigma}{r}\right)^{12} - \left(\frac{\sigma}{r}\right)^{6} \right] + c & r \leq r_c \\ 0 & r > r_c \end{cases} \tag{6.2}$$

Where ε is the strength of the potential and σ is the typical length of interaction. The strength of the Lennard-Jones potential, compared to the exponential potential, is shown in fig. 6.2

The plot clearly shows that the Lennard-Jones potential is significantly sharper than

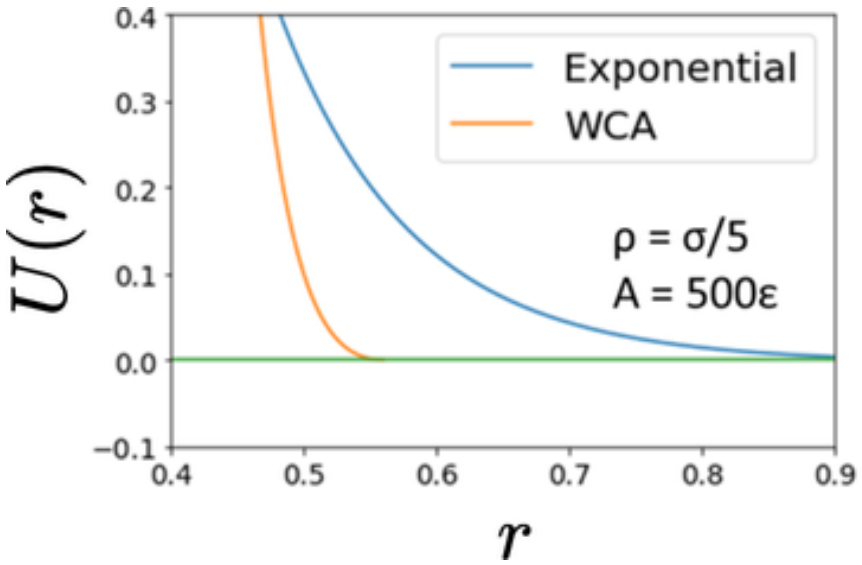

Figure 6.2: Lennard-Jones and exponential potential, the relation of the strengths of the two potentials is depicted in the figure. Values in Lennard-Jones units.

the exponential one. By applying this potential, the hydrophobic domains are spatially brought together. Fig. 6.4 shows, on the left, the hypothesized structure of multicompartment IPECs, and on the right, a screenshot from a representative simulation.

To test this model, several simulations were performed by varying the number of particles confined within the caging potential, thereby changing the volume fraction ϕ, calculated as:

$$\phi = \frac{V_p}{V_T} N_p \tag{6.3}$$

Here, V_p is the volume of a single particle, V_T is the total volume of the confining sphere, and N_p is the number of particles in the system. See table 6.1.

From the simulated trajectories, the static coherent scattering function $I(q)$ can be computed. For a system of N_p spherical scatterers, $I(q)$ can be estimated using the Debye formula, which represents the discrete analogue of eq. 1.28, averaged over all orientations:

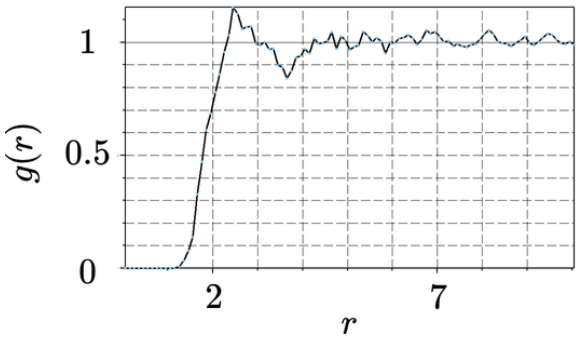

(a) Radial pair distribution function $g(r)$ extracted from 2500 frames, sampled every 10 frames, from a properly equilibrated simulation. Calculations for the $g(r)$ were performed using VMD, while the simulation were performed using LAMMPS [172, 173]. Values in Lennard-Jones units.

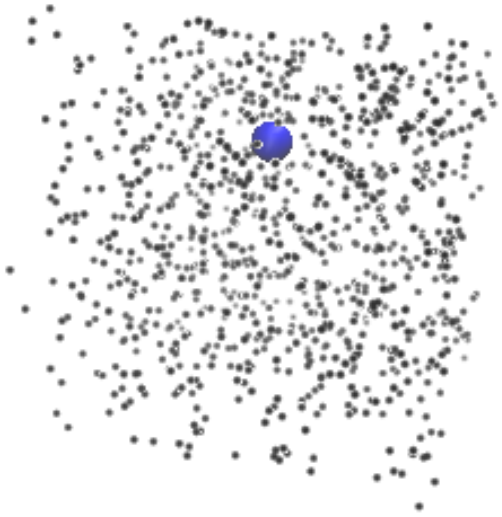

(b) Screenshot of the simulation used to extract the particle radius. Taken from VMD.

Figure 6.3: Radial pair distribution function (a) and screenshot of the simulation (b) to calculate the radius of the particles.

$$I(q) = c^* \sum_{ij}^{N} F_i(q) b_j F_j(q) \frac{\sin(qr_{ij})}{qr_{ij}} = c^* \sum_{ij}^{N} F_i(q) F_j(q) \frac{\sin(qr_{ij})}{qr_{ij}} \tag{6.4}$$

Here, the indices i and j run from 1 to N; c^* is a renormalization factor that depends on the concentration and scattering length density of the scatterers; and $F(q)$ is the form factor, which in this case corresponds to the spherical form factor.

In fig. 6.5, the scattering intensity for various numbers of scatterers is shown, averaged over 100 frames. As the volume fraction increases, the effect of spherical confinement becomes increasingly evident, and all frames exhibit the same scattering pattern.

The outcome of the simulation was also modeled theoretically by combining the form factor of a sphere with the Ornstein-Zernike structure factor $S(q)$. In this specific case,

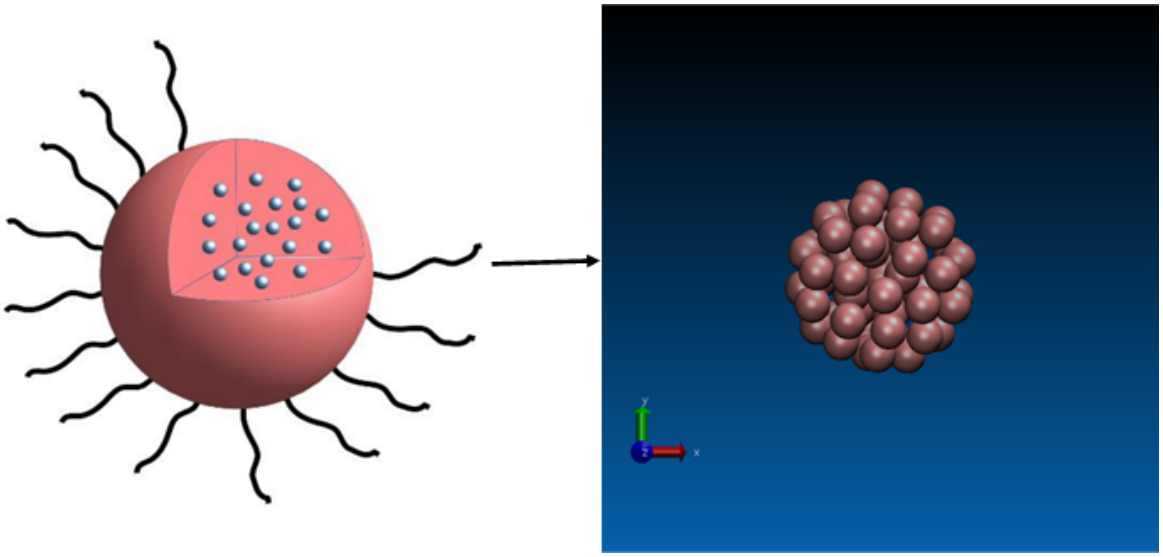

Figure 6.4: Left side: sketch of the structure of multicompartment polyelectrolyte complexes. Right side: Screenshot from a simulation performed with a number of particle $N = 109$.

N_p	R_{cage}	ϕ
8	7	0.7%
17	7	1.5%
51	7	4.6%
100	7	9.0%

Table 6.1: Condition of the simulations performed with a caging potential at different volume fractions ϕ.

its closure for hard spheres, as derived by Percus and Yevick [124], has been employed.

However, the system may exhibit a **clustered structure**. To better represent this configuration, the inter-particle correlation can be complemented by the structure factor of fractal aggregates. This structure factor is described by a power-law characterized by a fractal dimension [174].

In this model, the expression reported in [175] was used, where

$$S(\mathbf{q}) = \int g(\mathbf{r}) exp(i\mathbf{q} \cdot \mathbf{r}) \tag{6.5}$$

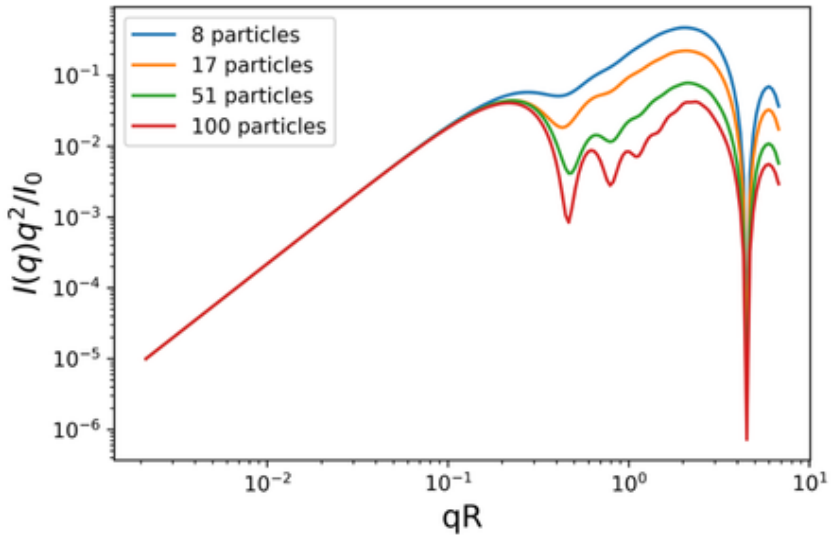

Figure 6.5: Normalized kratky plot averaged over 100 configurations for different number of particles N_p.

and the function $g(\mathbf{r})$ is expressed as:

$$g(\mathbf{r}) = r^{D-3}h(r/R) \tag{6.6}$$

The function $h(r/R)$ is defined as:

$$h(r/R) = \begin{cases} (\frac{4}{3}\pi R^3)(1-\frac{r}{4R})(1+\frac{r}{4R})^2 & r < 2R \\ 0 & \text{otherwise} \end{cases} \tag{6.7}$$

Here, R denotes the cluster radius.

By combining all contributions, the scattering intensity can be expressed as:

$$I(q) = c^* P(q)\Big[S(q) + \Big(N_p - S(0)\Big)F(q)\Big] \tag{6.8}$$

Here, $F(q)$ denotes the structure factor of a fractal aggregate.

Fig. 6.6 shows the behavior of the fitted confinement size R and the power-law exponent D as functions of N_p. The estimated confinement size converges to the actual value at higher densities, where the presence of the cage becomes more pronounced. The

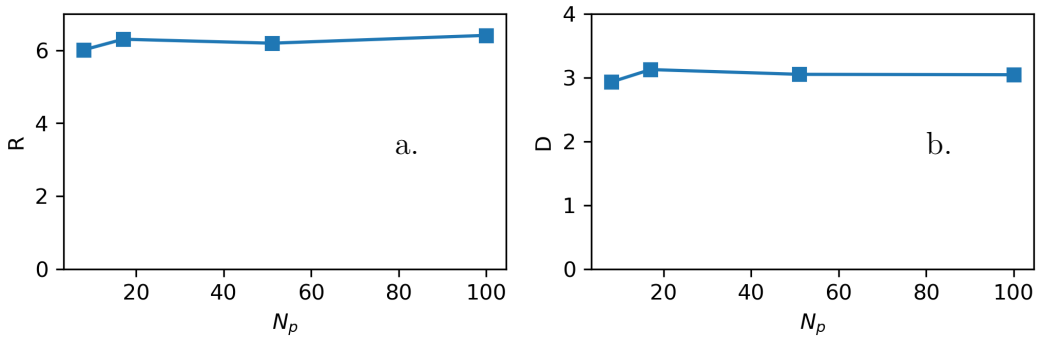

Figure 6.6: Estimated radius R of the confinement (a), and estimated power law D (b). Values in Lennard-Jones units.

fractal dimension obtained from the structure factor D suggests a spherical confinement, which is the shape of the caging potential.

As an alternative approach, the confining potential was replaced by a radial potential directed towards the center of the simulation box. Fig. 6.7 displays a schematic representation of the radial force field and the corresponding potential as a function of the radial distance.

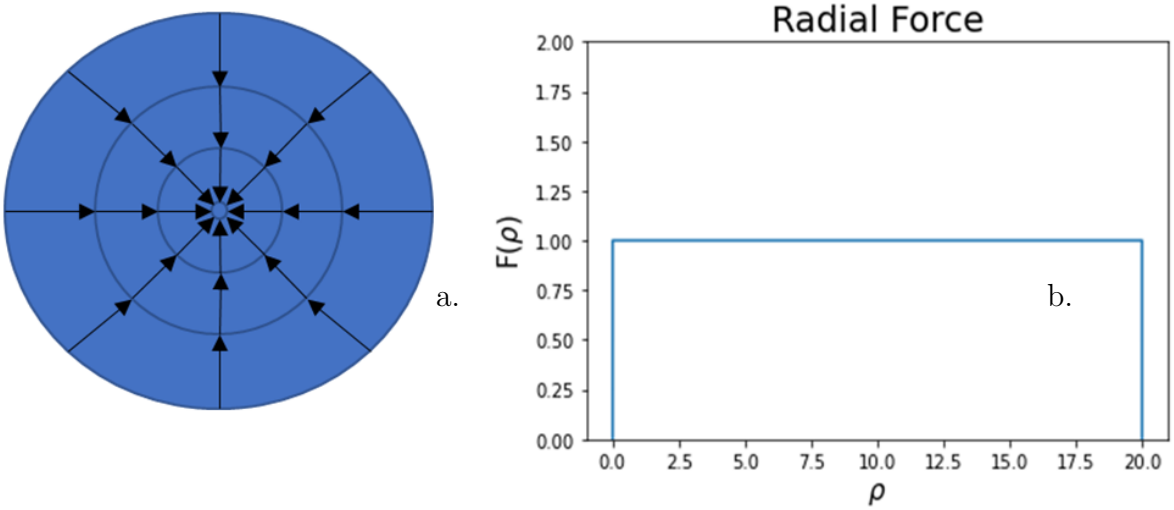

Figure 6.7: Sketch of the force fields on the simulation (a). Plot of the constant potential over the radial variable ρ (b). Values in Lennard-Jones units.

The advantage of using this type of potential lies in the ability to control the compactness of the structures independently of the scatterer concentration.

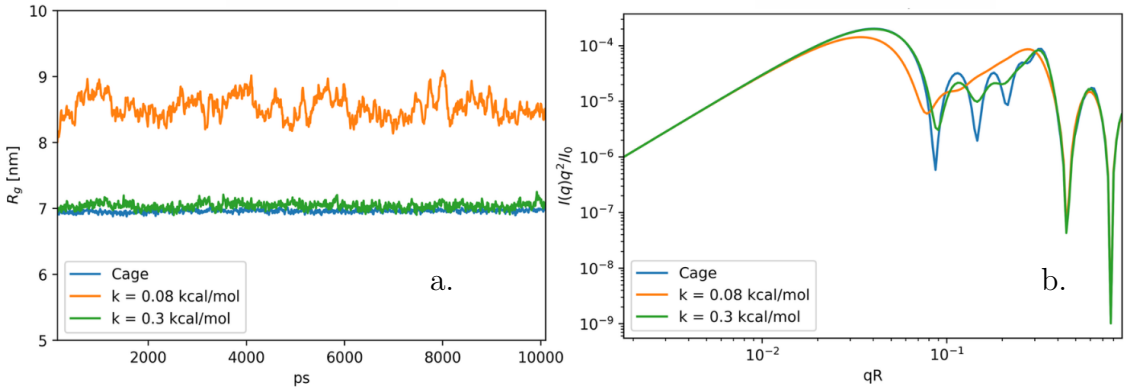

Figure 6.8: Radius of gyration for the cage potential and different strenght of the radial potential(a). Relative scattering intensity $I(q)$ as a Krakty plot (b).

Fig. 6.8 shows the radius of gyration, calculated as:

$$R_g^2 = \frac{1}{N}\sum_{j=1}^{N} r_j^2 \tag{6.9}$$

When the strength of the potential is reduced, R_g exhibits larger fluctuations. Consequently, the scatterers are distributed differently across frames, and the average over the trajectory results in less pronounced oscillations, reflecting weaker structural features of the aggregates.

6.2 Applications

6.2.1 PEMECs

As previously discussed, although the model does not efficiently describe the investigated system, it can still be applied to the study of PEMECs. Microemulsions are ordered structures and tend to exhibit strong scattering features [176, 177].

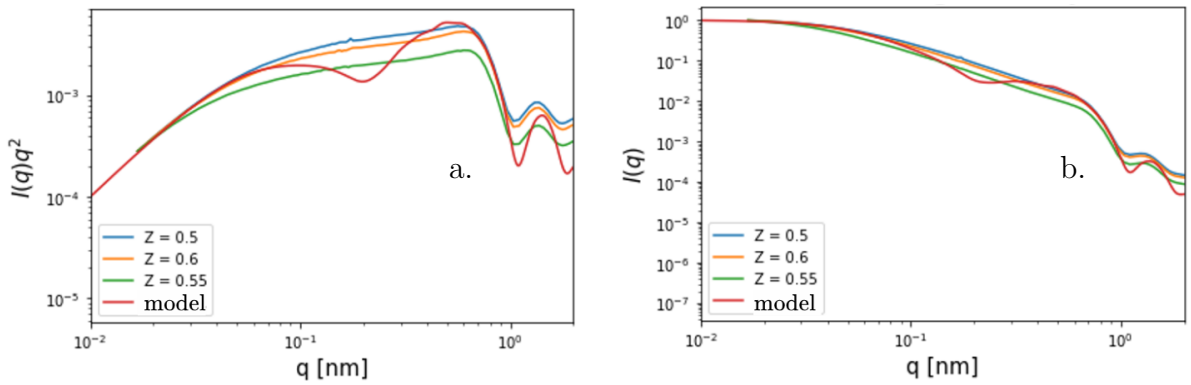

Figure 6.9: Kratky plot of the PEMECs and the model (a). Standard representation of the scattering intensity (b).

As an example, it is instructive to model the microemulsions investigated by Miriam Simon. These PEMECs are formed by mixing TTAB with a double-hydrophilic diblock copolymer (PEG-PAA), exploring a mixing ratio z^* as previously defined. To represent this system, several simulations were performed with a number of particles ranging from 5 to 50, using an interaction strength of the global radial potential of $k = 0.1$ kcal/mol. The results are shown in fig. 6.9

As visible in the figure, the feature rising from the confinement is still more marked then the features of the samples.

6.2.2 Amphiphilic Blockcopolymers

A similar model have been developed for representing the LCST behavior of amphiphilic blockcopolymers [178]. The model is fully implemented in Jscatter and it represents a collection of spheres confined in a sphere. This model we implemented could offer a vision on the dynamics of such structures and by modifying the forcefield, we can obtain different shapes of aggregates.

6.3 Further developments

Regarding its application on IPECs, after analyzing the SANS data, it emerged that the observed features are the polymer chains more than the hydrophobic domains and the structures are lesse oredered than expected. A solution to obtain a more representative description of the system is to introduce a finer model, where the polymer chains are represented in their bead spring fashion. We explored briefly this opportunities as a project of an intern, Leopold Bilder.

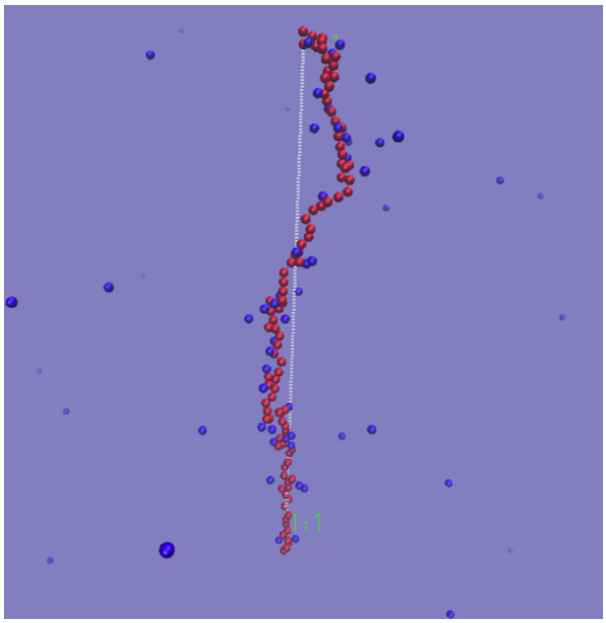

Figure 6.10: Snapshot of an equilibrated molecule of PDMAEMA with its counterions explicitly represented.

As a first step, we dimensionate two polymers: a PMAA chain of 100 beads and 100 beads of PDMAEMA, with their counterions. Every bead interacts with a WCA potential described in eq. 6.2, electrostatic interactions were represented by a Coulombic potential:

$$U_c = \frac{C q_1 q_2}{\epsilon r} \tag{6.10}$$

Where C is the bead-specific strength of the interactions, q_i are the charges, ϵ is the

dielectric constant of the water and r is the distance between the center of the two beads.

Covalent bonds were modeled as springs

$$U = k(r - r_0)^2 \tag{6.11}$$

The parameters were taken from the literature [179]. A snapshot of a simulation of a PDMAEMA molecule is presented in fig. 6.10.

Chapter 7

Conclusion and Future Works

This thesis primarily focuses on the characterization of the nanoscale structure and dynamics of IPECs formed by two specific polyelectrolytes: the first is a double-hydrophilic block copolymer; the second is a set of polysoaps with varying hydrophobic modifications.

Typically, double-hydrophilic block copolymers (DHBCs) stabilize polyelectrolyte complexes in solution by forming dispersed colloids and, depending on parameters such as concentration, mixing ratio, and PEG chain length, may retain partial phase separation.

In contrast, polysoaps behave similarly to surfactants, forming micelles depending on the extent of hydrophobic modification (commonly referred to as the critical aggregation concentration-CAC) and the length of the hydrophobic side chains. When polysoaps were mixed with DHBCs, the resulting structures appeared to be highly hydrated, with the polysoaps forming interchain aggregates even at higher degrees of hydrophobic modification (e.g., C_{12}).

Although such polysoaps would typically be expected to form intrachain associations, leading to surfactant-like behavior, the presence of DHBCs appears to inhibit this pattern, instead promoting a higher-order hierarchical aggregation. As a result, larger structures are formed when hydrophobic modifications are present in the system.

By combining small-angle scattering techniques with microscopy investigations, it was observed that the mixing ratio also plays a crucial role in determining the shape of the resulting complexes. While polycations tend to repel each other, the addition of a

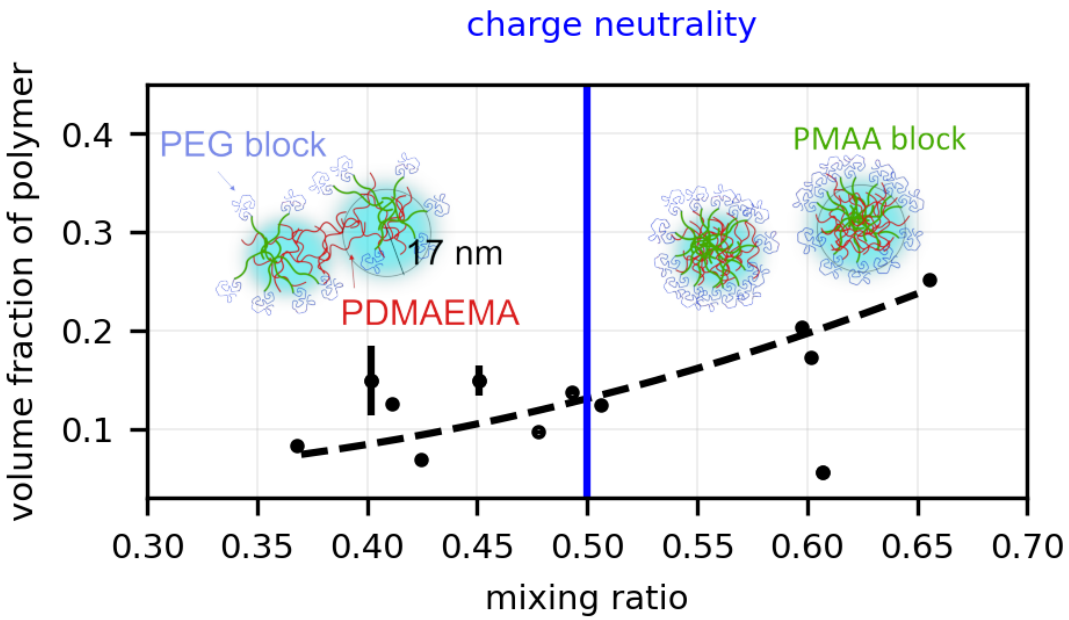

Figure 7.1: Sketch of the behavior of the density as a function of the mixing ratio.

small amount of polyanion (i.e., DHBC) rapidly neutralizes this repulsion, leading to the formation of small, polymer-like aggregates.

Approaching the equimolarity regime, the behavior resembled that of polyelectrolyte complexes without polysoaps, characterized by a rapid increase in the absolute scattering intensity. Since the PEG stabilizer was only attached to the polyanion, we also observed a peculiar transition in the shape of these objects. Although the shape transition is not sharply defined, the structures formed around equimolarity in the polycation-rich regime ($z^* \simeq 0.4$) appear more hydrated, with the polymers forming either polymersomes with a thickness of approximately $d \simeq 17$ nm or spherical micelles of comparable radius.

The presence of both structures was supported by cryo-TEM imaging and the low-q behavior observed in the SANS measurements. The same investigations showed less vesicle formation in the DBHC excess. This behavior was interpreted as a consequence of the higher PEG content, which better stabilizes the structures in solution and leads to the formation of less hydrated spherical objects.

It should be noted that the absence of features corresponding to the hydrophobic micelles does not necessarily imply that such features are absent; the hydrophobic moieties are still expected to associate with one another.

The aggregation effects were also reflected in the dynamics of the polymer chains, as revealed by NSE spectroscopy. The experiments revealed a dynamic behavior characteristic of polymer chains, well described by modifications of the Zimm model. In line with the repulsion observed on the structures, a de Gennes narrowing feature was also observed in the pure polyelectrolyte solutions. These features rapidly disappeared upon the addition of oppositely charged polyelectrolytes. Chain dynamics were also suppressed as the system approached equimolarity.

While structural investigations did not reveal significant differences between polymers with and without hydrophobic modifications at the high-q regime, neutron backscattering was able to detect such differences.

Each PDMAEMA unit contains three methyl groups, and backscattering measurements revealed sub-diffusive features associated with hydrogen hopping in these groups. This feature was more pronounced in the PDMAEMA, while the hydrophobically modified PDMAEMA was generally less affected by the methyl group effect. Conversely, hydrophobic modifications were found to reduce the mobility of the hydrogen atoms.

Although backscattering primarily probes the self-dynamics of hydrogen atoms, the aggregation pattern was still evident, influencing the relative intensity contributions between internal and global dynamics.

As an interesting future direction, one could investigate the effect of using two DHBCs, with both the polycation and the polyanion functionalized with PEG: A higher abundance of PEG stabilizer resulted in more compact aggregates, and this behavior is

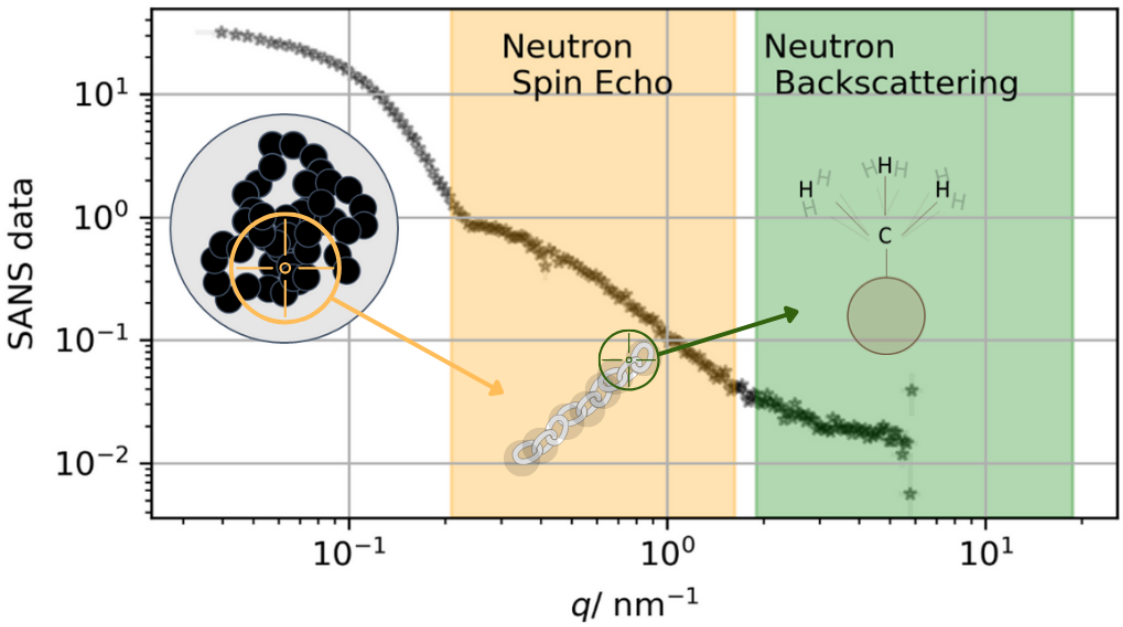

Figure 7.2: Sketch of the representation of the various features observed via dynamics over a SANS curve. The two regions in which the different neutron spectroscopy investigations were performed are enhanced with a color background.

expected to occur symmetrically with respect to the mixing ratio when both polymers are DHBCs.

Another point would be to push further the concentration of the polyelectrolytes, to see when the polymer starts to behave as an entangled solution. This approach could help identify the maximum concentration at which such polymers remain dispersed in solution. In the backscattering measurements, the instrumental limit was approached, and operating at higher concentrations could potentially overcome this constraint.

From a computational standpoint, efforts were initiated to develop a bead-spring model of the polymer system. Such a model could eventually be used to reproduce the neutron spin echo results by adapting the MDanse software to coarse-grained particles and extracting the coherent dynamic structure factor.

Appendix A

In this appendix I explore the reproducibility of the samples. To do so, fig. 7.3 shows SANS data of IPECs made with the polycation C12DP100hm9 prepared at a mixing ratio $z^* = 0.6$. Here three conditions are tested: a sample *freshly* prepared, a sample measured after the *standard* equilibration time and the same sample, *aged* for almost a month (this sample was measured during a separate internal beamtime with slightly different setup, which is the reason of the shift in the measured q-range). As a comparison, I also show the data for the same IPECs analyzed at ANSTO, where the closest measured $z^* = 0.66$. The plot shows that the fresh sample does not show the polymeric feature at high-q and there is a small fluctuation in the forward scattering. Despite that, the measurements look reproducible.

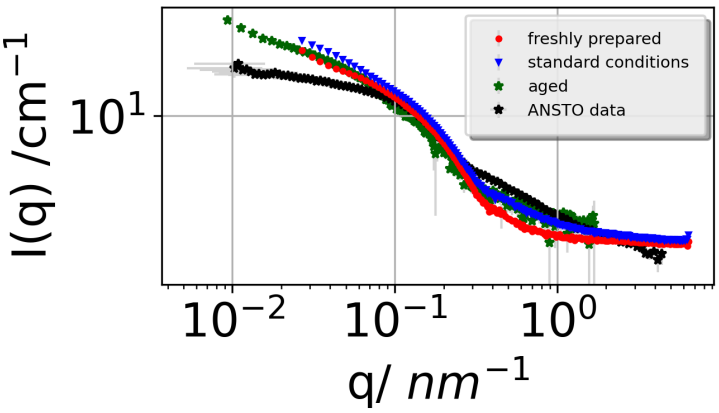

Figure 7.3: SANS intensity of IPECs made with the polycation C12DP100hm9 prepared at a mixing ratio $z^* = 0.6$.

Appendix B

This appendix is useful to elucidate the fit on the Neutron Spin Echo data. Here the fits superimposed to the experimental values of the dynamic structure factor $S(q,t)$ are shown. For each sample, the residues are calculated as $\frac{S_{exp}(q,t)-S_{fit}(q,t)}{\sigma}$, where $S_{exp}(q,t)$ is the experimental structure factor, $S_{fit}(q,t)$ is the value from the model in eq. 5.11 and σ is the experimental error.

PDMAEMA at $c = 1\%$wt and $T = 298$K.

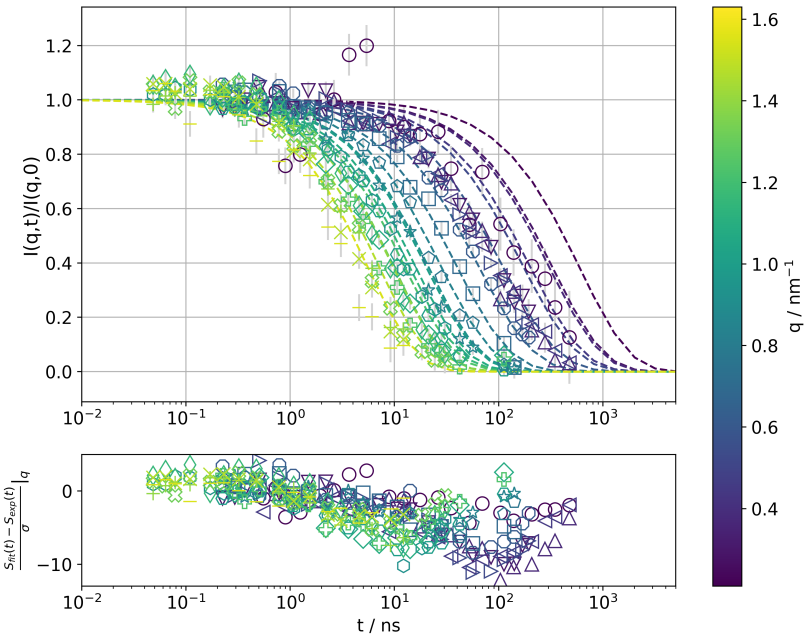

Figure 7.4: $S(q,t)$ for every q analyzed and its relative residues.

IPECs made with PDMAEMA at $c = 1\%$wt and $T = 298$K, $z^* = 0.2$.

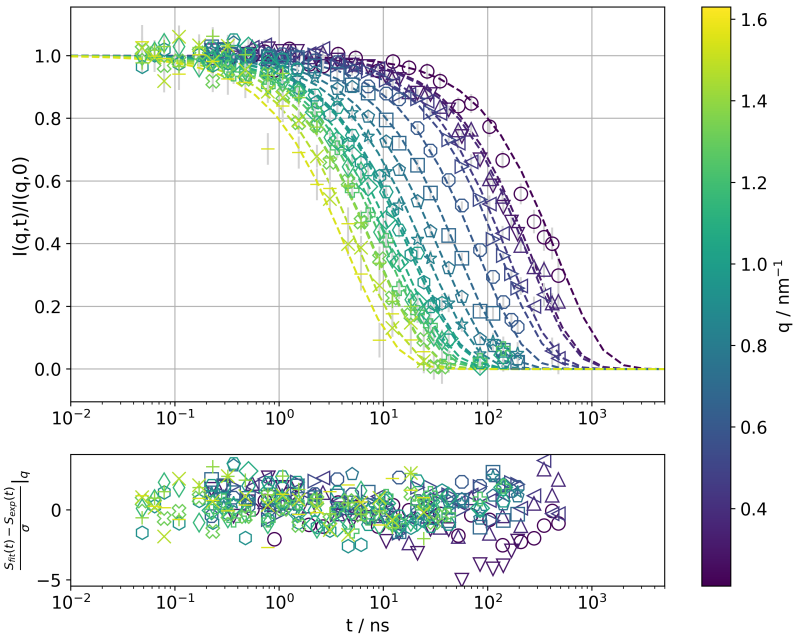

Figure 7.5: $S(q,t)$ for every q analyzed and its relative residues.

IPECs made with PDMAEMA at $c = 1\%$wt and $T = 298$K, $z^* = 0.4$.

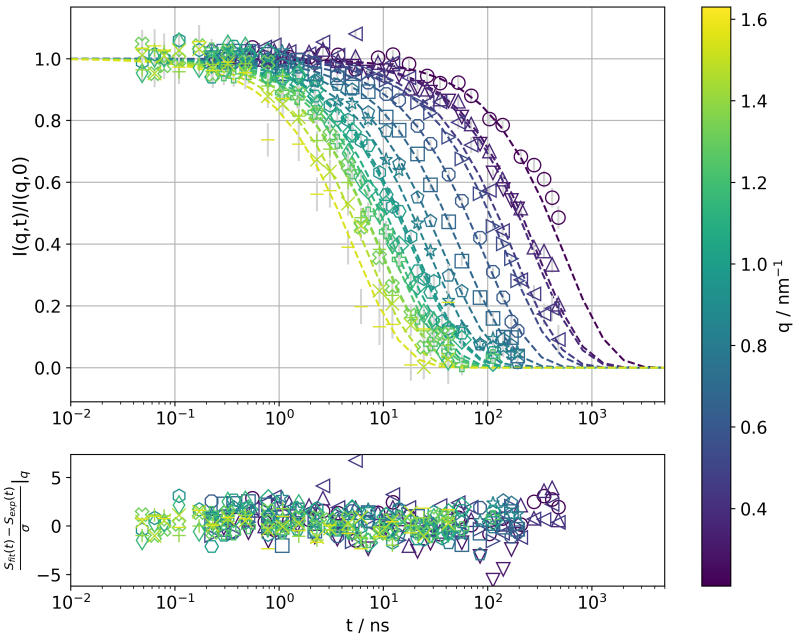

Figure 7.6: $S(q,t)$ for every q analyzed and its relative residues.

IPECs made with PDMAEMA at $c = 1\%$wt and $T = 298$K, $z^* = 0.6$.

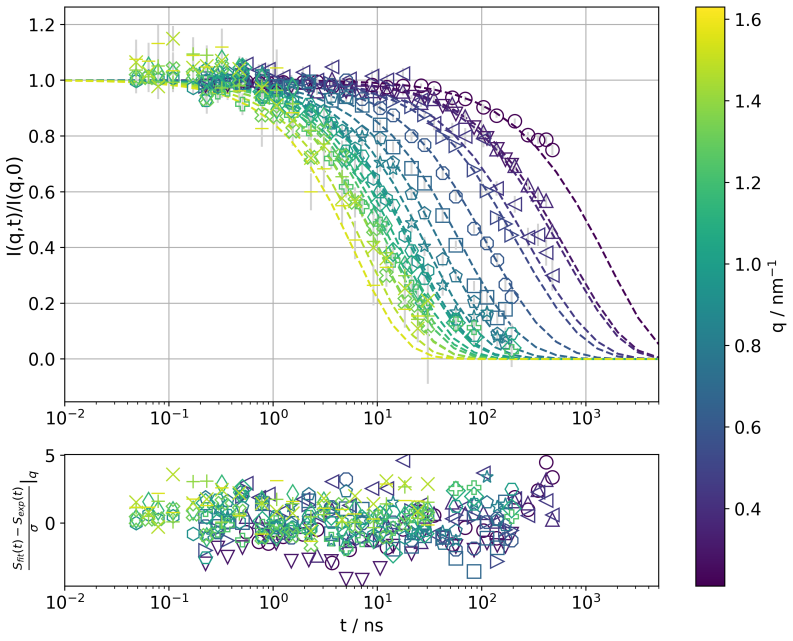

Figure 7.7: $S(q,t)$ for every q analyzed and its relative residues.

C12DP100hm9 at $c = 2\%$wt and $T = 298$K.

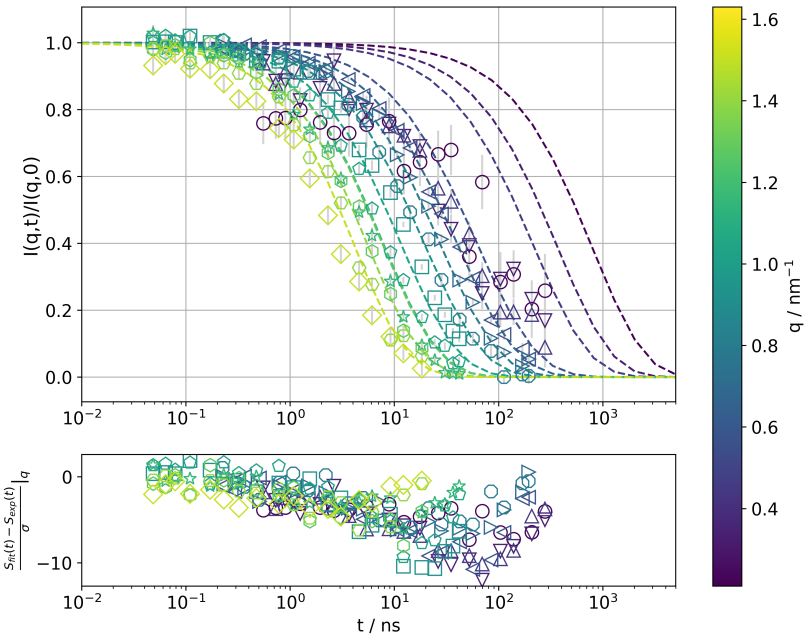

Figure 7.8: $S(q,t)$ for every q analyzed and its relative residues.

IPECs made with C12DP100hm9 at $c = 1\%$wt and $T = 298$K, $z^* = 0.2$.

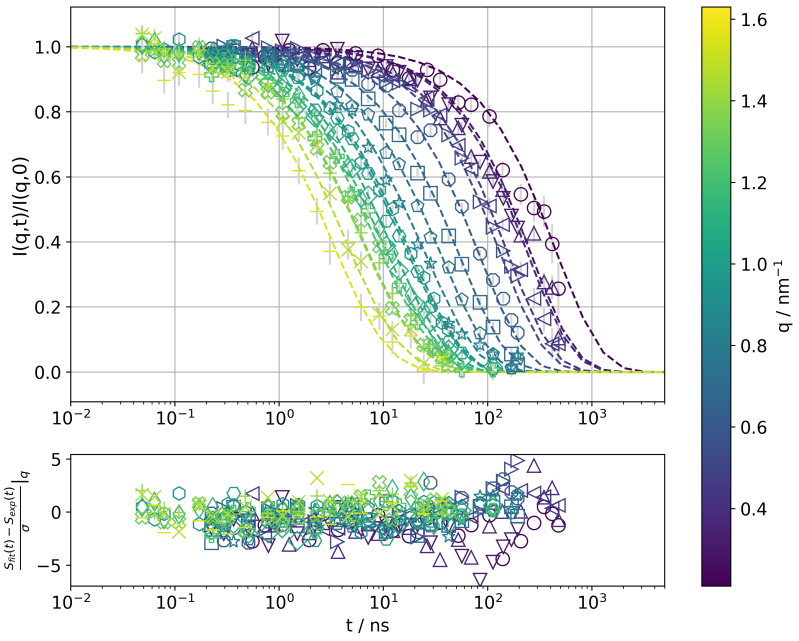

Figure 7.9: $S(q,t)$ for every q analyzed and its relative residues.

IPECs made with C12DP100hm9 at $c = 1\%$wt and $T = 298$K, $z^* = 0.4$.

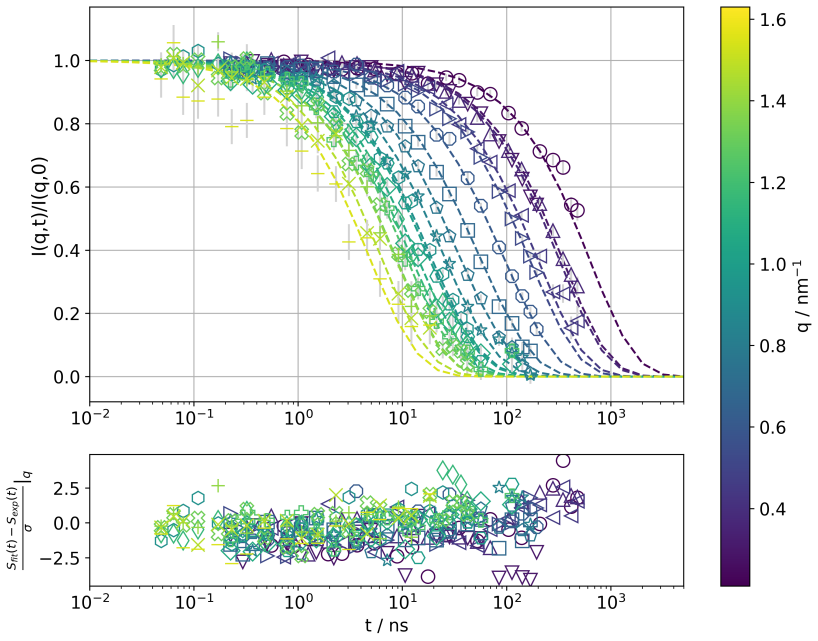

Figure 7.10: $S(q,t)$ for every q analyzed and its relative residues.

IPECs made with C12DP100hm9 at $c = 1\%$wt and $T = 298$K, $z^* = 0.6$.

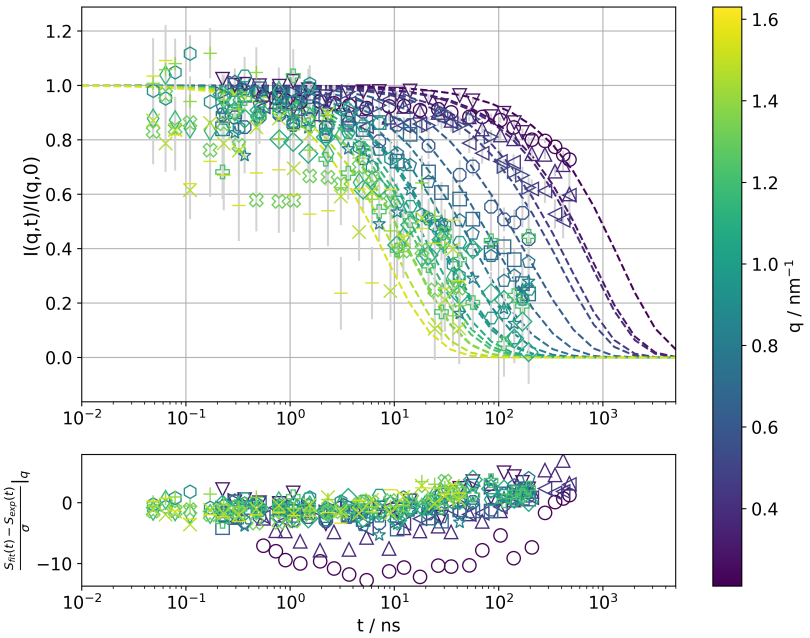

Figure 7.11: $S(q,t)$ for every q analyzed and its relative residues.

C12DP100hm9 at $c = 3\%$wt and $T = 280$K.

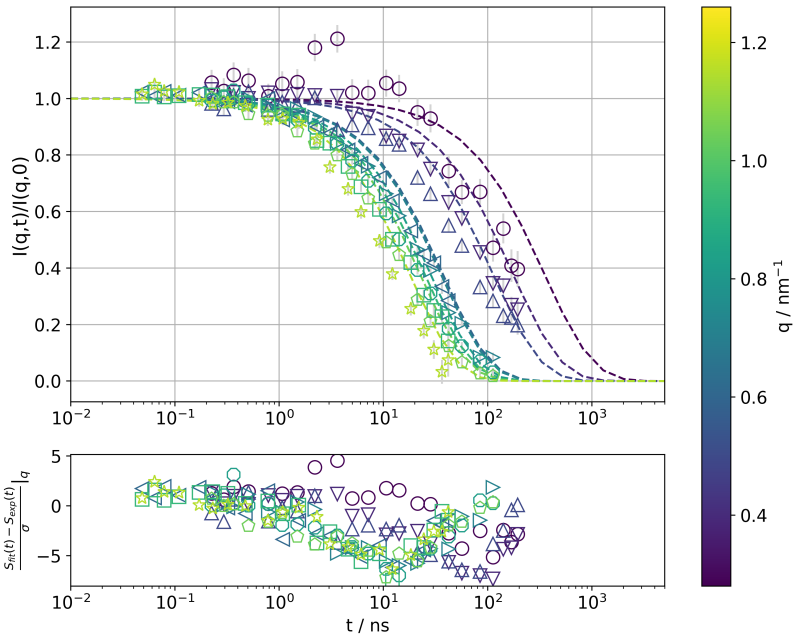

Figure 7.12: $S(q,t)$ for every q analyzed and its relative residues.

C12DP100hm9 at $c = 3\%$wt and $T = 298$K.

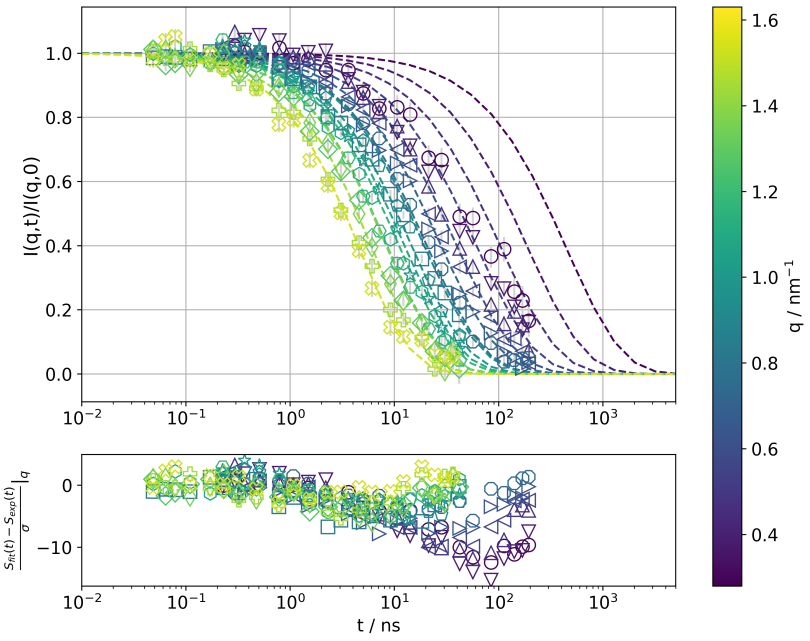

Figure 7.13: $S(q,t)$ for every q analyzed and its relative residues.

C12DP100hm9 at $c = 3\%$wt and $T = 310$K.

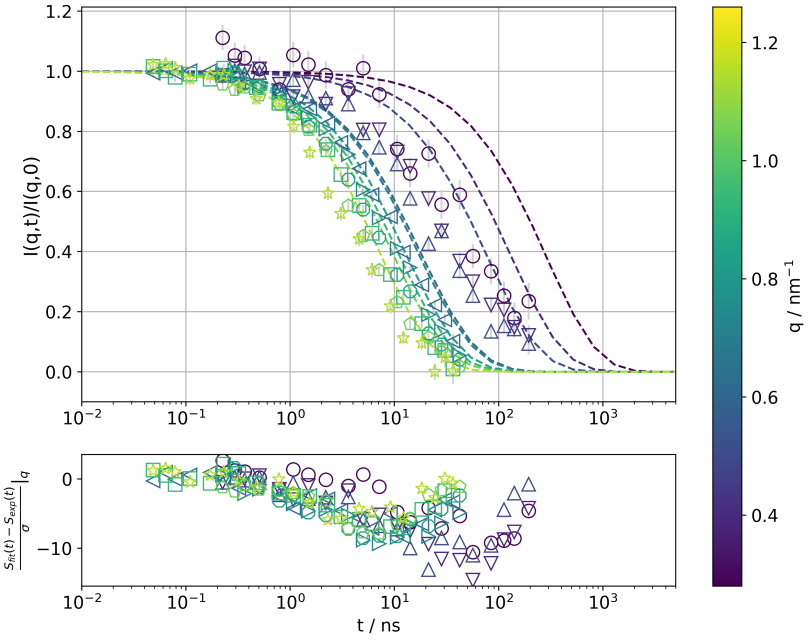

Figure 7.14: $S(q,t)$ for every q analyzed and its relative residues.

Appendix C

This appendix is useful to elucidate the fit on the Backscattering data. Here the fits superimposed to the experimental values of the dynamic structure factor $S(q,\omega)$ are shown. For each sample, the residues are calculated as $\frac{S_{exp}(q,\omega)-S_{fit}(q,\omega)}{\sigma}$, where $S_{exp}(q,\omega)$ is the experimental structure factor, $S_{fit}(q,\omega)$ is the value from the model in eq. 5.11 and σ is the experimental error.

PDMAEMA at $c = 3\%$wt and $T = 280$K

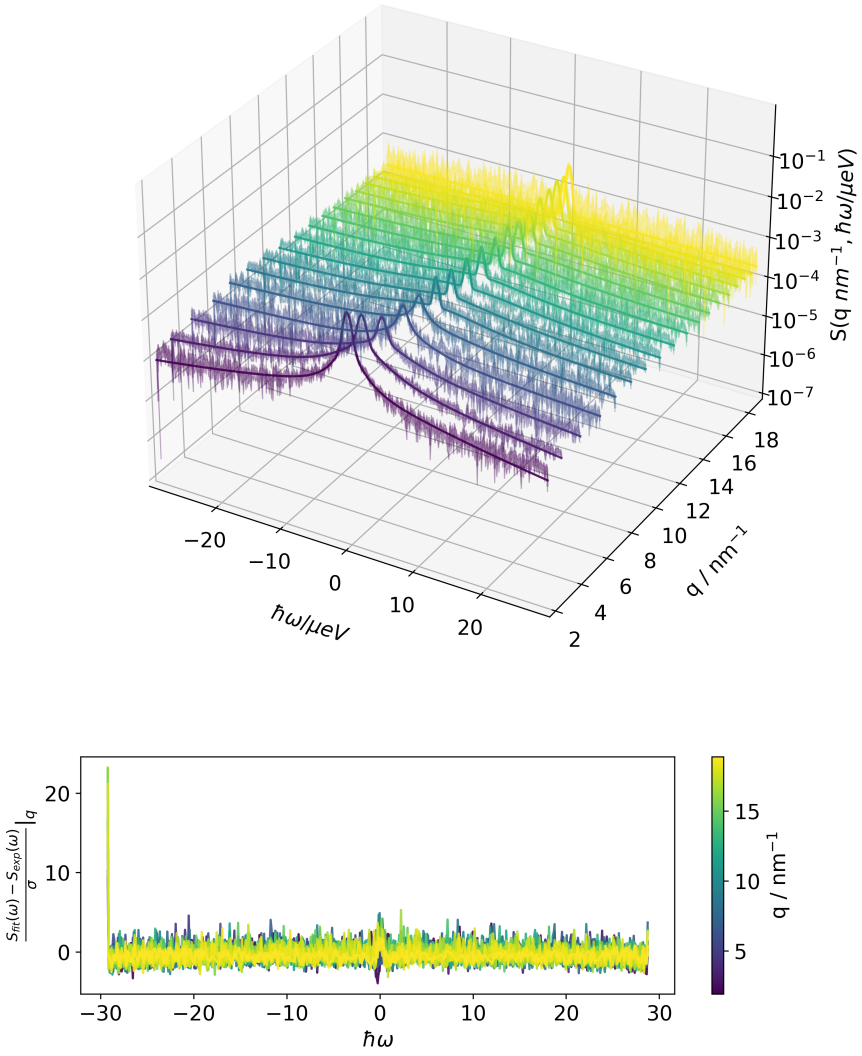

Figure 7.15: $S(q, \omega)$ for every q analyzed and its relative residues.

PDMAEMA at $c = 3\%$wt and $T = 298$K

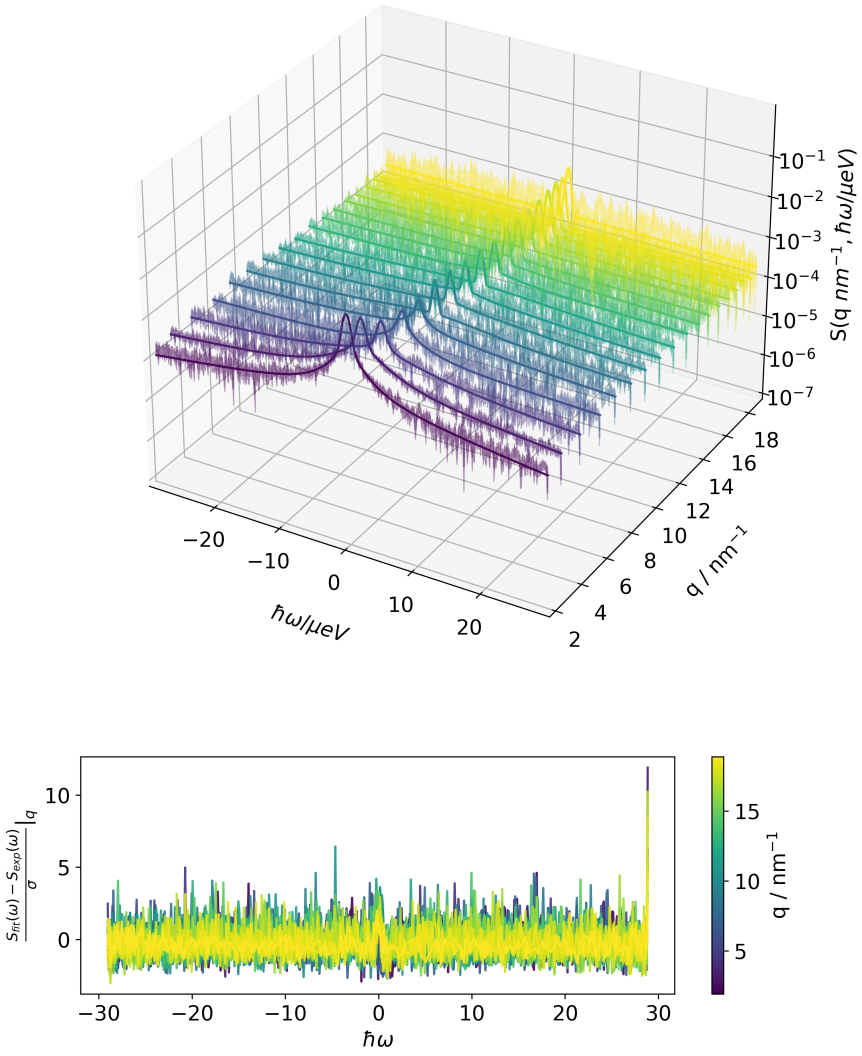

Figure 7.16: $S(q, \omega)$ for every q analyzed and its relative residues.

PDMAEMA at $c = 3\%$wt and $T = 310$K

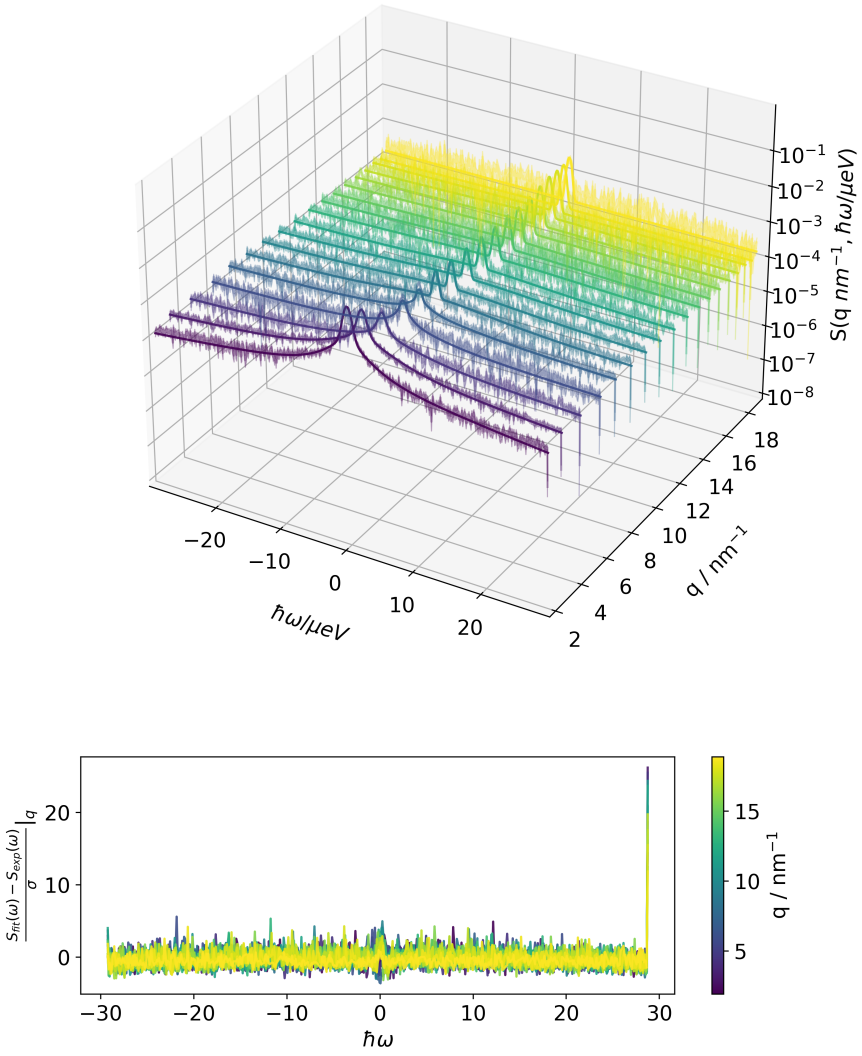

Figure 7.17: $S(q, \omega)$ for every q analyzed and its relative residues.

C12DP100hm9 at $c = 3\%$wt and $T = 280$K

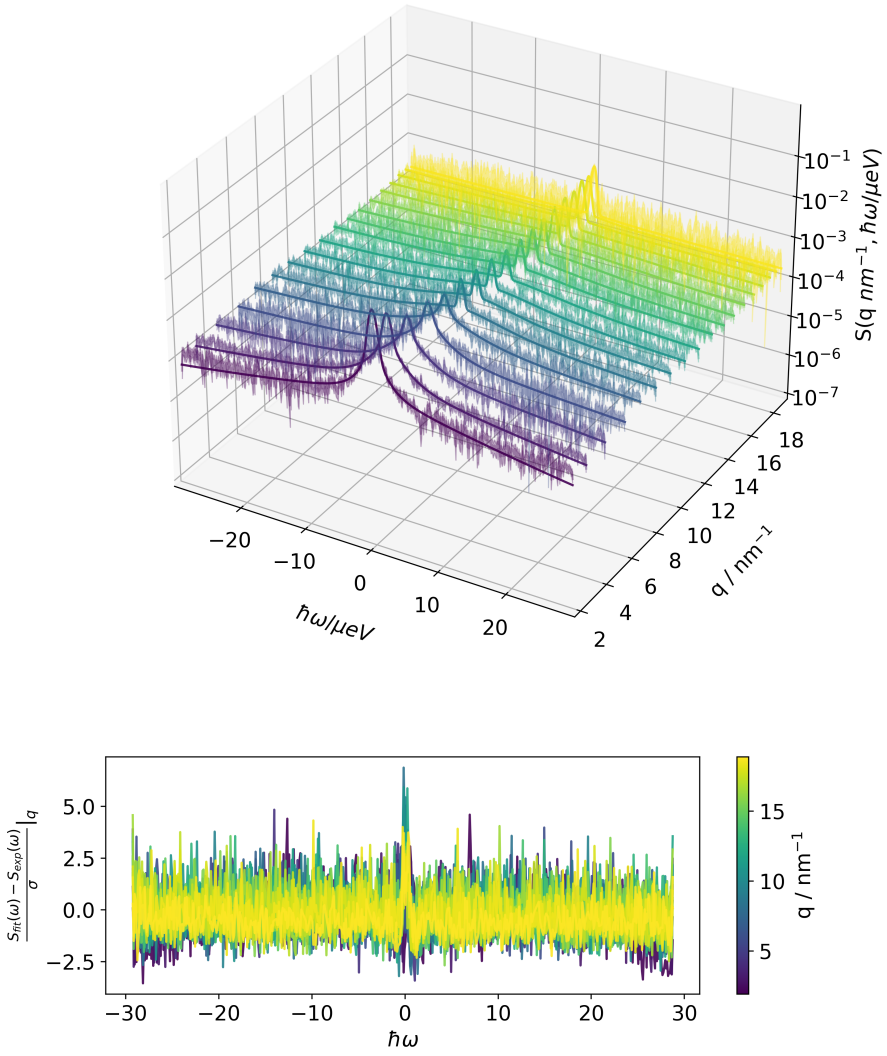

Figure 7.18: $S(q, \omega)$ for every q analyzed and its relative residues.

C12DP100hm9 at $c = 3\%$wt and $T = 298$K

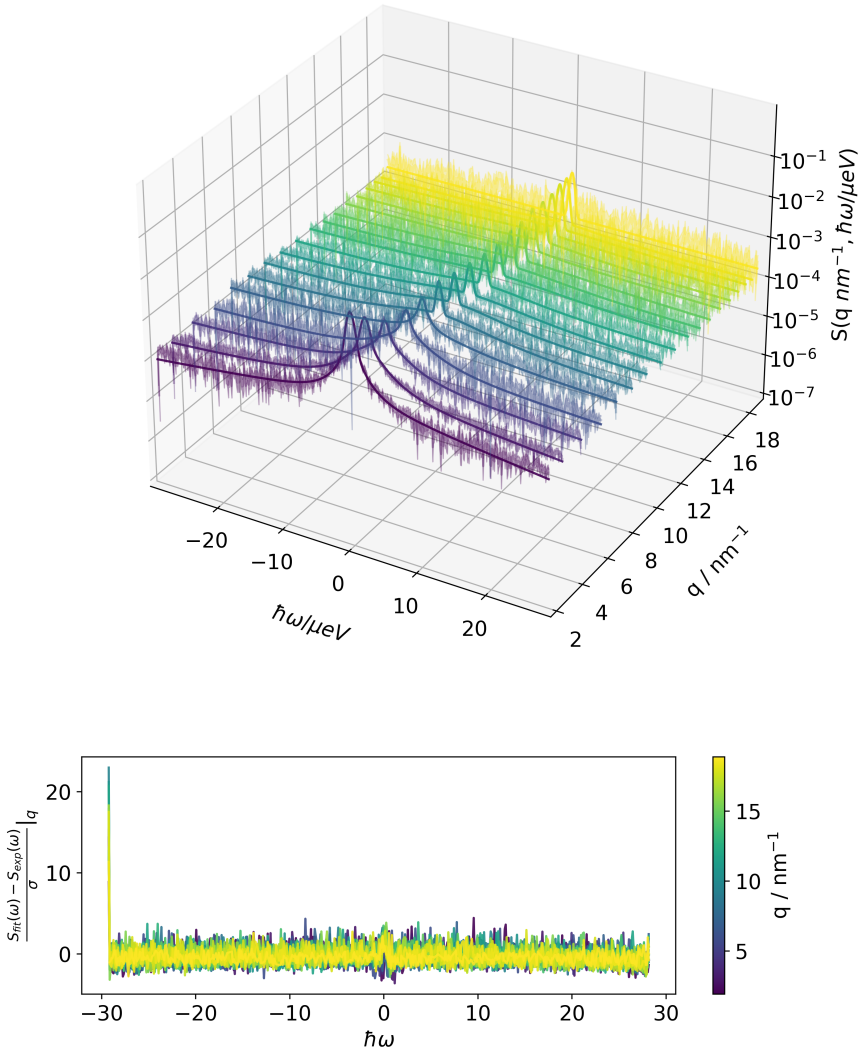

Figure 7.19: $S(q, \omega)$ for every q analyzed and its relative residues.

C12DP100hm9 at $c = 3\%$wt and $T = 310$K

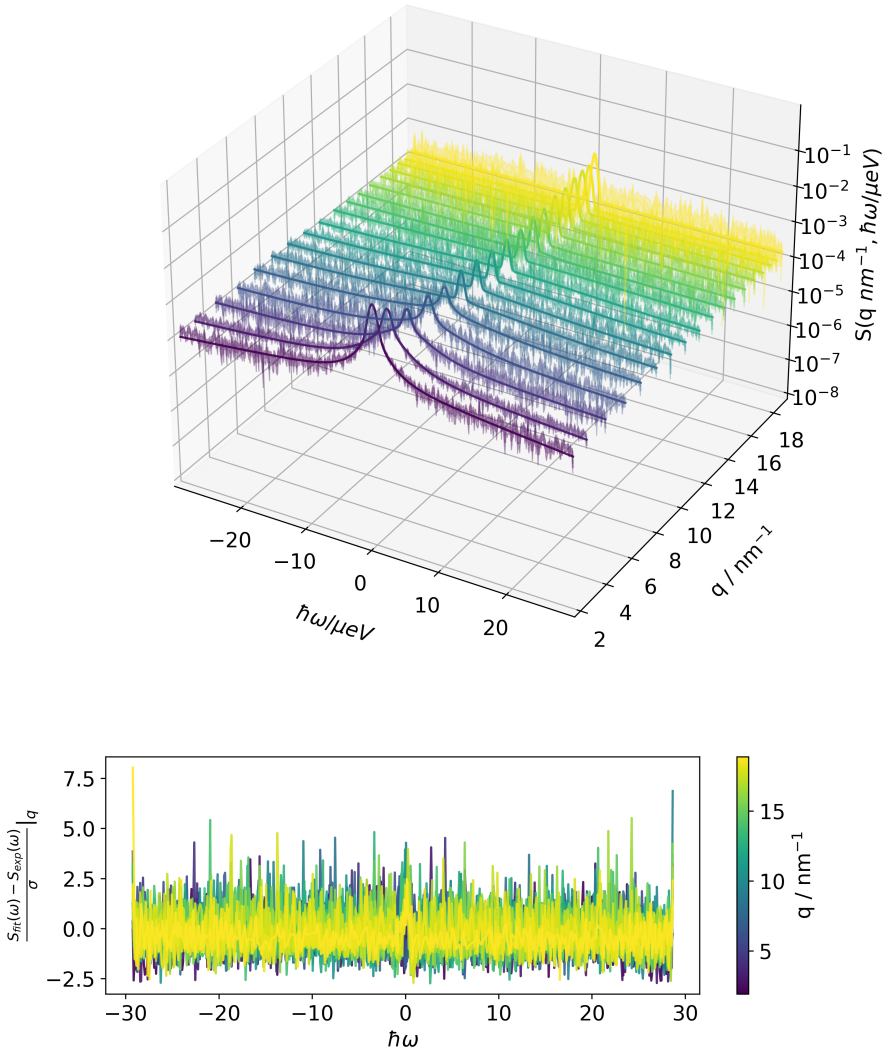

Figure 7.20: $S(q, \omega)$ for every q analyzed and its relative residues.

IPECs made with the polycation PDMAEMA at $c = 3\%$wt and $T = 298$K at a mixing ratio $z^* = 0.6$

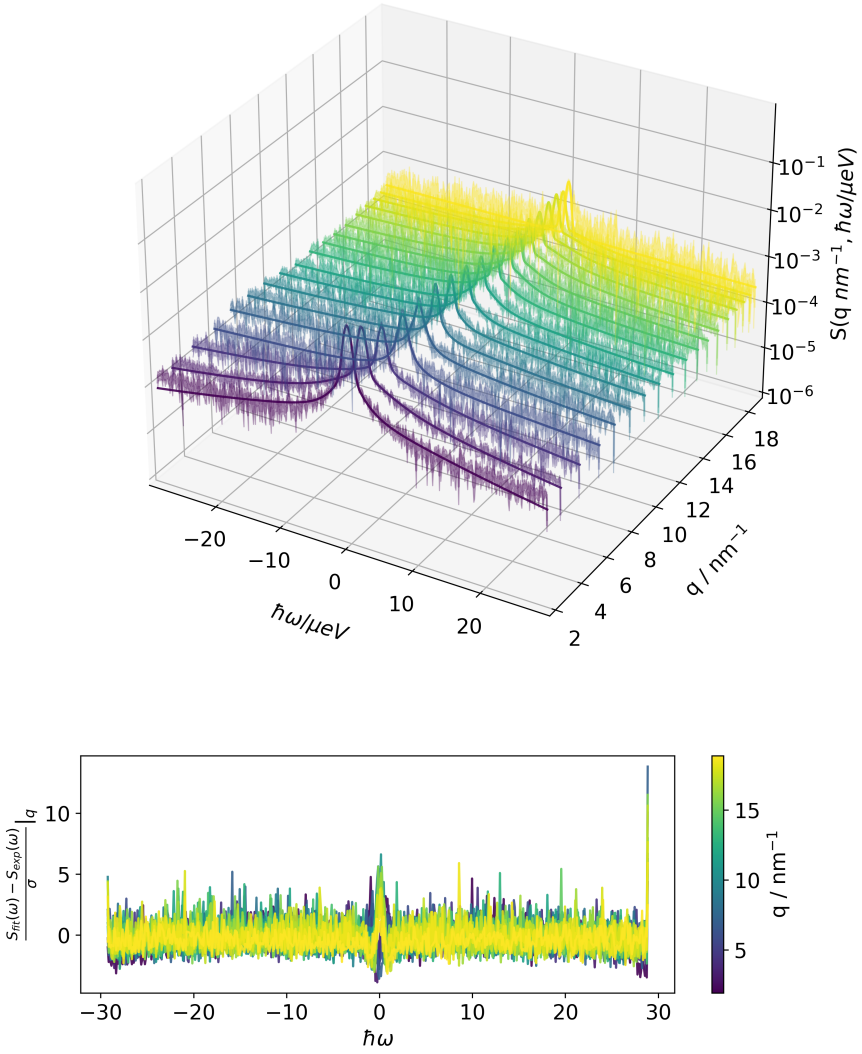

Figure 7.21: $S(q, \omega)$ for every q analyzed and its relative residues.

IPECs made with the polycation C12DP100hm9 at $c = 3\%$wt and $T = 298$K at a mixing ratio $z^* = 0.6$

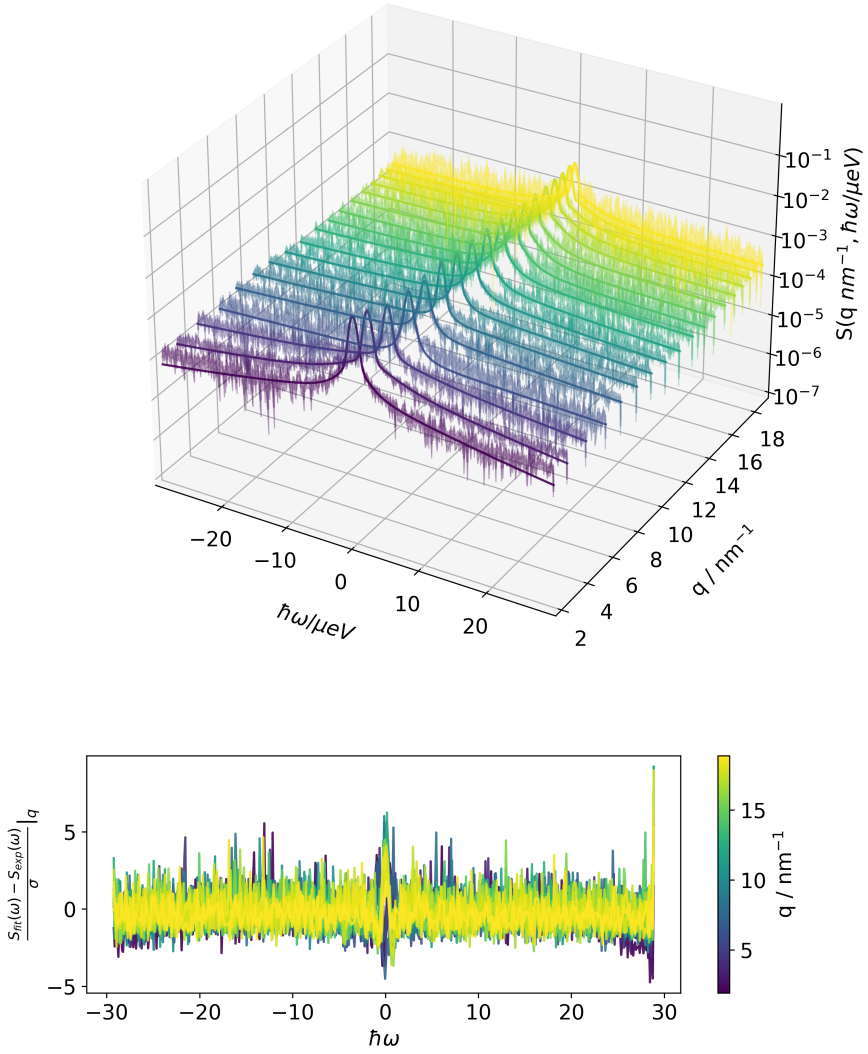

Figure 7.22: $S(q, \omega)$ for every q analyzed and its relative residues.

Usage of AI

The generative artificial intelligence (AI) software ChatGPT-4 by OpenAI and the integrated AI tool in Overleaf were used to check grammar and syntax, and to improve the wording of individual text sections. The author takes full responsibility for their use and for the final outcome.

Bibliography

[1] M. Muthukumar, "50th Anniversary Perspective: A Perspective on Polyelectrolyte Solutions," *Macromolecules*, vol. 50, no. 24, pp. 9528–9560, 2017. doi: 10.1021/acs.macromol.7b01929 .

[2] C. Cruz, F. Chinesta, and G. Regnier, "Review on the brownian dynamics simulation of bead-rod-spring models encountered in computational rheology," *Archives of Computational Methods in Engineering*, vol. 19, pp. 227–259, 2012. doi: https://doi.org/10.1007/s11831-012-9072-2 .

[3] E. Buvalaia, M. Kruteva, I. Hoffmann, A. Radulescu, S. Förster, and R. Biehl, "Interchain Hydrodynamic Interaction and Internal Friction of Polyelectrolytes," *ACS Macro Letters*, vol. 12, no. 9, pp. 1218–1223, 2023. doi: 10.1021/acsmacrolett.3c00409 .

[4] J. K. Bediako, E. S. M. Mouele, Y. El Ouardi, and E. Repo, "Saloplastics and the polyelectrolyte complex continuum: Advances, challenges and prospects," *Chemical Engineering Journal*, vol. 462, p. 142322, 2023. doi: 10.1016/j.cej.2023.142322 .

[5] Z. Ou and M. Muthukumar, "Entropy and enthalpy of polyelectrolyte complexation: Langevin dynamics simulations," *The Journal of Chemical Physics*, vol. 124, no. 15, p. 154902, 2006. doi: 10.1063/1.2178803 .

[6] P. Raffa, D. A. Z. Wever, F. Picchioni, and A. A. Broekhuis, "Polymeric surfactants: Synthesis, properties, and links to applications," *Chemical Reviews*, vol. 115, no. 16, pp. 8504–8563, 2015. doi: 10.1021/cr500129h .

[7] E. Jahns and H. Finkelmann, "Lyotropic liquid crystalline phase behavior of a polymeric amphiphile polymerized via their hydrophilic ends," *Colloid and Polymer Science*, vol. 265, pp. 304–311, 1987. doi: 10.1007/BF01417929 .

[8] S. Riemer, S. Prévost, M. Dzionara, U. Gasser, and M. Gradzielski, "Hydrophobically modified polyacrylates (hmPAAs) with long alkyl chains - Self-assembly in aqueous solution," *Polymer*, vol. 128, pp. 78–86, 2017. doi: 10.1016/j.polymer.2017.09.005 .

[9] S. Shah and L. Leon, "Structural dynamics, phase behavior, and applications of polyelectrolyte complex micelles," *Current Opinion in Colloid and Interface Science*, vol. 53, 2021. doi: 10.1016/j.cocis.2021.101424 .

[10] S. Guo, Y. Qiao, W. Wang, H. He, L. Deng, J. Xing, J. Xu, X. J. Liang, and A. Dong, "Poly(ϵ-caprolactone)-graft-poly(2-(N, N-dimethylamino) ethyl methacrylate) nanoparticles: PH dependent thermo-sensitive multifunctional carriers for gene and drug delivery," *Journal of Materials Chemistry*, vol. 20, no. 33, pp. 6935–6941, 2010. doi: 10.1039/c0jm00506a .

[11] "Institut Laue-Langevin website," https://www.ill.eu/.

[12] B. Hammouda, "PROBING NANOSCALE STRUCTURES-THE SANS TOOLBOX." [Online]. Available: https://www.nist.gov/ncnr/neutron-instruments/small-angle-neutron-scattering-sans

[13] R. Biehl, "Jscatter, a program for evaluation and analysis of experimental data," *PLoS ONE*, vol. 14, no. 6, 2019. doi: 10.1371/journal.pone.0218789 .

[14] "Institut für Angewandte Physik - Universität Tübingen website," https://www.soft-matter.uni-tuebingen.de/dls.html#principle.

[15] V. S. Meka, M. K. Sing, M. R. Pichika, S. R. Nali, V. R. Kolapalli, and P. Kesharwani, "A comprehensive review on polyelectrolyte complexes," *Drug Discovery Today*, vol. 22, no. 11, pp. 1697–1706, 2017. doi: 10.1016/j.drudis.2017.06.008 .

[16] M. Chamchoum, O. Czakkel, O. Azeri, B. Dai, S. Prevost, O. Kuzminskaya, O. Matsarskaia, A. E. Whitten, and M. Gradzielski, "Formation of interpolyelectrolyte complexes (IPECs) between double-hydrophilic block copolymers and polysoaps: The role of hydrophobic modification and mixing ratio as structural control parameters," *Macromolecules*, vol. 58, no. 5, pp. 2619–2629, 2025. doi: 10.1021/acs.macromol.4c02187 .

[17] M. Chamchoum, O. Czakkel, S. Prevost, T. Seydel, N. Martin, Azeri, O. Kuzminskaya, B. Dai, and M. Gradzielski, "Effect of polyelectrolyte mixing ratio and hydrophobic interactions on dynamics of (hm-)pdmaema/peo-pmaa complexes," *The Journal of Chemical Physics*, vol. 164, no. 2, p. 024908, 01 2026. doi: 10.1063/5.0285727 .

[18] Y. Luo, X. Yao, J. Yuan, T. Ding, and Q. Gao, "Preparation and drug controlled-release of polyion complex micelles as drug delivery systems," *Colloids and Surfaces B: Biointerfaces*, vol. 68, no. 2, pp. 218–224, 2009. doi: 10.1016/j.colsurfb.2008.10.014 .

[19] K. Kuperkar, D. Patel, L. I. Atanase, and P. Bahadur, "Amphiphilic Block Copolymers: Their Structures, and Self-Assembly to Polymeric Micelles and Polymersomes as Drug Delivery Vehicles," *Polymers*, vol. 14, no. 21, p. 4702, 2022. doi: 10.3390/polym14214702 .

[20] K. T. Oh, T. K. Bronich, L. Bromberg, T. A. Hatton, and A. V. Kabanov, "Block ionomer complexes as prospective nanocontainers for drug delivery," *Journal of Controlled Release*, vol. 115, no. 1, pp. 9–17, 2006. doi: 10.1016/j.jconrel.2006.06.030 .

[21] P. Loganathan, M. Gradzielski, H. Bustamante, and S. Vigneswaran, "Progress, challenges, and opportunities in enhancing nom flocculation using chemically modified chitosan: a review towards future development," *Environmental Science: Water Research and Technology*, vol. 6, pp. 45–61, 2020. doi: 10.1039/C9EW00596J .

[22] P. D. Pickett, C. R. Kasprzak, D. T. Siefker, B. A. Abel, M. A. Dearborn, and C. L. McCormick, "Amphoteric, Sulfonamide-Functionalized "polysoaps": CO2-Induced Phase Separation for Water Remediation," *Macromolecules*, vol. 51, no. 21, pp. 9052–9059, 2018. doi: 10.1021/acs.macromol.8b01613 .

[23] I. K. Voets, A. de Keizer, and M. A. Cohen Stuart, "Complex coacervate core micelles," *Advances in Colloid and Interface Science*, vol. 147-148, no. C, pp. 300–318, 2009. doi: 10.1016/j.cis.2008.09.012 .

[24] A. Katchalsky and P. Spitnik, "Potentiometric titrations of polymethacrylic acid," *Journal of Polymer Science*, vol. 2, no. 4, pp. 432–446, 1947. doi: 10.1002/pol.1947.120020409 .

[25] U. Lappan, U. Geißler, M. Oelmann, and S. Schwarz, "Apparent dissociation constants of polycarboxylic acids in presence of polycations," *Colloid and Polymer Science*, vol. 290, pp. 1665–1670, 2012. doi: 10.1007/s00396-012-2702-2 .

[26] A. V. Dobrynin and M. Rubinstein, "Theory of polyelectrolytes in solutions and at surfaces," *Progress in Polymer Science (Oxford)*, vol. 30, no. 11, pp. 1049–1118, 2005. doi: 10.1016/j.progpolymsci.2005.07.006 .

[27] P. G. De Gennes, "Liquid dynamics and inelastic scattering of neutrons," *Physica*, vol. 25, pp. 825–839, 1959. doi: 10.1016/0031-8914(59)90006-0 .

[28] J. Rouse, Prince E., "A theory of the linear viscoelastic properties of dilute solutions of coiling polymers," *The Journal of Chemical Physics*, vol. 21, no. 7, pp. 1272–1280, 1953. doi: 10.1063/1.1699180 .

[29] M. Doi, *Introduction to polymer physics*. Oxford: Oxford University Press, 2001. [Online]. Available: https://global.oup.com/academic/product/introduction-to-polymer-physics-9780198517894?cc=it&lang=en&

[30] B. H. Zimm, "Dynamics of polymer molecules in dilute solution: viscoelasticity, flow birefringence and dielectric loss," *The journal of chemical physics*, vol. 24, no. 2, pp. 269–278, 1956. doi: 10.1063/1.1742462 .

[31] S. Förster, M. Schmidt, and M. Antonietti, "Static and dynamic light scattering by aqueous polyelectrolyte solutions: effect of molecular weight, charge density and added salt," *Polymer*, vol. 31, no. 5, pp. 781–792, 1990. doi: 10.1016/0032-3861(90)90036-X .

[32] M. Sedlák, Č. Koňák, P. Štěpánek, and J. Jakeš, "Semidilute solutions of poly(methacrylic acid) in the absence of salt: Dynamic light-scattering study," *Polymer*, vol. 28, no. 6, pp. 873–880, 1987. doi: 10.1016/0032-3861(87)90156-X .

[33] M. Kruteva, "Dynamics studied by Quasielastic Neutron Scattering (QENS)," *Adsorption*, vol. 27, no. 5, pp. 875–889, 2021. doi: 10.1007/s10450-020-00295-4 .

[34] J. Colmenero and A. Arbe, "Recent progress on polymer dynamics by neutron scattering: From simple polymers to complex materials," *Journal of Polymer Science, Part B: Polymer Physics*, vol. 51, no. 2, pp. 87–113, 2013. doi: 10.1002/polb.23178 .

[35] A. Triolo, F. Lo Celso, S. Passerini, V. Arrighi, R. E. Lechner, B. Frick, and R. Triolo, "Segmental dynamics in polymer electrolytes," *Applied Physics A: Materials Science and Processing*, vol. 74, no. SUPPL.I, 2002. doi: 10.1007/s003390201882 .

[36] A. H. Slim, W. H. Shi, F. Safi Samghabadi, A. Faraone, A. B. Marciel, R. Poling-Skutvik, and J. C. Conrad, "Electrostatic Repulsion Slows Relaxations of Polyelectrolytes in Semidilute Solutions," *ACS Macro Letters*, vol. 11, no. 7, pp. 854–860, 2022. doi: 10.1021/acsmacrolett.2c00213 .

[37] M. Tirrell, "Polyelectrolyte Complexes: Fluid or Solid?" *ACS Central Science*, vol. 4, no. 5, pp. 532–533, 2018. doi: 10.1021/acscentsci.8b00284 .

[38] V. A. Kabanov, "Polyelectrolyte complexes in solution and in bulk," *Uspekhi Khimii*, vol. 74, no. 1, pp. 5–23, 2005. doi: 10.1070/rc2005v074n01abeh001165 .

[39] E. Spruijt, A. H. Westphal, J. W. Borst, M. A. Cohen Stuart, and J. Van Der Gucht, "Binodal compositions of polyelectrolyte complexes," *Macromolecules*, vol. 43, no. 15, pp. 6476–6484, 2010. doi: 10.1021/ma101031t .

[40] J. Van Der Gucht, E. Spruijt, M. Lemmers, and M. A. Cohen Stuart, "Polyelectrolyte complexes: Bulk phases and colloidal systems," *Journal of Colloid and Interface Science*, vol. 361, no. 2, pp. 407–422, 2011. doi: 10.1016/j.jcis.2011.05.080 .

[41] Q. Wang and J. B. Schlenoff, "The polyelectrolyte complex/coacervate continuum," *Macromolecules*, vol. 47, no. 9, pp. 3108–3116, 2014. doi: 10.1021/ma500500q .

[42] D. Woermann and F. T. Wall, "Reactions of polysoaps with chloride and bromide ions," *The Journal of Physical Chemistry*, vol. 64, no. 5, pp. 581–584, 1960. doi: 10.1021/j100834a016 .

[43] A. Laschewsky, *Molecular concepts, self-organisation and properties of polysoaps*. Berlin, Heidelberg: Springer Berlin Heidelberg, 1995, pp. 1–86. doi: 10.1007/BFb0025228 .

[44] D. Cochin and A. Laschewsky, "Layer-by-layer self-assembly of hydrophobically modified polyelectrolytes," *Macromolecular Chemistry and Physics*, vol. 200, no. 3, pp. 609–615, 1999. doi: 10.1002/(SICI)1521-3935(19990301)200:3-609::AID-MACP609-3.0.CO;2-X .

[45] S. Abid, S. Hamid, and D. Sherrington, "Micellization and surface activity of long-chain monoquaternary and diquaternary ammonium salts," *Journal of Colloid and Interface Science*, vol. 120, no. 1, pp. 245–255, 1987. doi: 10.1016/0021-9797(87)90346-8 .

[46] U. P. Strauss, N. L. Gershfeld, and E. H. Crook, "The transition from typical polyelectrolyte to polysoap. ii. viscosity studies of poly-4-vinylpyridine derivatives

in aqueous kbr solutions." *The Journal of Physical Chemistry*, vol. 60, no. 5, pp. 577–584, 1956. doi: 10.1021/j150539a016 .

[47] F. Grieser and C. J. Drummond, "The physicochemical properties of self-assembled surfactant aggregates as determined by some molecular spectroscopic probe techniques," *The Journal of Physical Chemistry*, vol. 92, no. 20, pp. 5580–5593, 1988. doi: 10.1021/j100331a012 .

[48] F. M. Winnik, "Photophysics of preassociated pyrenes in aqueous polymer solutions and in other organized media," *Chemical reviews*, vol. 93, no. 2, pp. 587–614, 1993. doi: 10.1021/cr00018a001 .

[49] R. Varadaraj, J. Bock, N. Brons, and S. Pace, "Probing hydrophobic microdomains of hydrophobically associating acrylamide-n-alkylacrylamide copolymers in solution using a solvatochromic absorption dye probe," *The Journal of Physical Chemistry*, vol. 97, no. 49, pp. 12 991–12 994, 1993. doi: 10.1021/j100151a056 .

[50] U. P. Strauss and E. G. Jackson, "Polysoaps. i. viscosity and solubilization studies on an n-dodecyl bromide addition compound of poly-2-vinylpyridine," *Journal of polymer Science*, vol. 6, no. 5, pp. 649–659, 1951. doi: 10.1002/pol.1951.120060515 .

[51] A. Medalia, H. Freedman, and S. Sinha, "Polysoaps. iii. polysoaps and related materials prepared by chemical modification of polystyrene," *Journal of Polymer Science*, vol. 40, no. 136, pp. 15–33, 1959.

[52] P. Anton, P. Köberle, and A. Laschewsky, "Recent developments in the field of micellar polymers," *Die Makromolekulare Chemie: Macromolecular Chemistry and Physics*, vol. 194, no. 1, pp. 1–27, 1993. doi: 10.1002/macp.1993.021940101 .

[53] K. Arai, J. Sugita, and Y. Ogiwara, "Polymerization of sodium 10-undecenoate under irradiation of uv light," *Die Makromolekulare Chemie: Macromolecular Chemistry and Physics*, vol. 188, no. 11, pp. 2511–2516, 1987. doi: 10.1002/macp.1987.021881102 .

[54] I. M. Klotz, G. P. Royer, and A. Sloniewsky, "Macromolecule-small molecule interactions. strong binding and cooperativity in a model synthetic polymer," *Biochemistry*, vol. 8, no. 12, pp. 4752–4756, 1969. doi: 10.1021/bi00840a015 .

[55] K. Arai and S. Miyahara, "Preparation of sodium 5-methyl-3, 7-octadienoate and its polymerization under irradiation with uv light," *Die Makromolekulare Chemie: Macromolecular Chemistry and Physics*, vol. 191, no. 11, pp. 2647–2652, 1990. doi: 10.1002/macp.1990.021911113 .

[56] D. Tsiourvas, C. Paleos, and A. Malliaris, "Aggregational behavior in water, of some polyamphiphiles derived from reactive polymers," *Journal of Polymer Science Part A: Polymer Chemistry*, vol. 31, no. 2, pp. 387–393, 1993. doi: 10.1021/ma00101a029 .

[57] S. Riemer, S. Prévost, M. Dzionara, M. S. Appavou, R. Schweins, and M. Gradzielski, "Aggregation behaviour of hydrophobically modified polyacrylate - Variation of alkyl chain length," *Polymer*, vol. 70, pp. 194–206, 2015. doi: 10.1016/j.polymer.2015.06.010 .

[58] D. Peiffer, "Polymerizable viscoelastic fluids," *Journal of Polymer Science Part A: Polymer Chemistry*, vol. 28, no. 3, pp. 619–627, 1990. doi: 10.1002/pola.1990.080280313 .

[59] H.-G. Batz, "Polymeric drugs," in *Reactivities*. Berlin, Heidelberg: Springer Berlin Heidelberg, 1977, pp. 25–53. doi: 10.1007/3-540-07943-2 .

[60] P. Ferruti, F. Danusso, G. Franchi, N. Polentarutti, and S. Garattini, "Effects of a series of new synthetic high polymers on cancer metastases," *Journal of Medicinal Chemistry*, vol. 16, no. 5, pp. 496–499, 1973. doi: 10.1021/jm00263a018 .

[61] S. Shinkai, "Coenzyme catalyses in micelles, polymers and host molecules," *Progress in Polymer Science*, vol. 8, no. 1-2, pp. 1–59, 1982. doi: 10.1016/0079-6700(82)90007-7 .

[62] C. A. Bunton, F. Nome, F. H. Quina, and L. S. Romsted, "Ion binding and reactivity at charged aqueous interfaces," *Accounts of chemical research*, vol. 24, no. 12, pp. 357–364, 1991. doi: 10.1021/ar00012a001 .

[63] M. A. Cohen Stuart, N. A. Besseling, and R. G. Fokkink, "Formation of micelles with complex coacervate cores," *Langmuir*, vol. 14, no. 24, pp. 6846–6849, 1998. doi: 10.1021/la980778m .

[64] A. Harada and K. Kataoka, "Formation of polyion complex micelles in an aqueous milieu from a pair of oppositely-charged block copolymers with poly (ethylene glycol) segments," *Macromolecules*, vol. 28, no. 15, pp. 5294–5299, 1995. doi: 10.1021/ma00119a019 .

[65] A. V. Kabanov, T. K. Bronich, V. A. Kabanov, K. Yu, and A. Eisenberg, "Soluble stoichiometric complexes from poly (n-ethyl-4-vinylpyridinium) cations and poly (ethylene oxide)-block-polymethacrylate anions," *Macromolecules*, vol. 29, no. 21, pp. 6797–6802, 1996. doi: 10.1021/ma960120k .

[66] D. V. Pergushov, A. H. Müller, and F. H. Schacher, "Micellar interpolyelectrolyte complexes," *Chemical Society Reviews*, vol. 41, no. 21, pp. 6888–6901, 2012. doi: 10.1039/c2cs35135h .

[67] M. Amann, J. S. Diget, J. Lyngsø, J. S. Pedersen, T. Narayanan, and R. Lund, "Kinetic Pathways for Polyelectrolyte Coacervate Micelle Formation Revealed by Time-Resolved Synchrotron SAXS," *Macromolecules*, vol. 52, no. 21, pp. 8227–8237, 2019. doi: 10.1021/acs.macromol.9b01072 .

[68] H. Wu, J. M. Ting, B. Yu, N. E. Jackson, S. Meng, J. J. De Pablo, and M. V. Tirrell, "Spatiotemporal Formation and Growth Kinetics of Polyelectrolyte Complex Micelles with Millisecond Resolution," *ACS Macro Letters*, vol. 9, no. 11, pp. 1674–1680, 2020. doi: 10.1021/acsmacrolett.0c00543 .

[69] H. Wu, J. M. Ting, and M. V. Tirrell, "Mechanism of dissociation kinetics in polyelectrolyte complex micelles," *Macromolecules*, vol. 53, no. 1, pp. 102–111, 2020. doi: 10.1021/acs.macromol.9b01814 .

[70] H. E. Cingil, N. C. Meertens, and I. K. Voets, "Temporally programmed disassembly and reassembly of c3ms," *Small*, vol. 14, no. 46, p. 1802089, 2018. doi: 10.1002/smll.201802089 .

[71] I. Bos and J. Sprakel, "Langevin Dynamics Simulations of the Exchange of Complex Coacervate Core Micelles: The Role of Nonelectrostatic Attraction and Polyelectrolyte Length," *Macromolecules*, vol. 52, no. 22, pp. 8923–8931, 2019. doi: 10.1021/acs.macromol.9b01442 .

[72] R. Takahashi, T. Sato, K. Terao, and S. I. Yusa, "Reversible Vesicle-Spherical Micelle Transition in a Polyion Complex Micellar System Induced by Changing the Mixing Ratio of Copolymer Components," *Macromolecules*, vol. 49, no. 8, 2016. doi: 10.1021/acs.macromol.6b00308 .

[73] S. Rappoport, V. Chrysostomou, S. Pispas, and Y. Talmon, "The nanostructure of polyelectrolyte complexes of QPDMAEMA-b-POEGMA copolymers and oppositely charged polyelectrolytes, and their stability in the presence of serum albumin," *Soft Matter*, vol. 19, no. 20, pp. 3688–3699, 2023. doi: 10.1039/d3sm00467h .

[74] Y. Lee and K. Kataoka, "Biosignal-sensitive polyion complex micelles for the delivery of biopharmaceuticals," *Soft Matter*, vol. 5, no. 20, pp. 3810–3817, 2009. doi: 10.1039/B909934D .

[75] K. T. Oh, T. K. Bronich, L. Bromberg, T. A. Hatton, and A. V. Kabanov, "Block ionomer complexes as prospective nanocontainers for drug delivery," *Journal of Controlled Release*, vol. 115, no. 1, pp. 9–17, 2006. doi: 10.1016/j.jconrel.2006.06.030 .

[76] F. Taktak, "Rapid deswelling of pdmaema hydrogel in response to ph and temperature changes and its application in controlled drug delivery," *Afyon Kocatepe Üniversitesi Fen Ve Mühendislik Bilimleri Dergisi*, vol. 16, no. 1, pp. 68–75, 2016. doi: 10.5578/fmbd.26306 .

[77] N. Bayó-Puxan, M. H. Dufresne, A. E. Felber, B. Castagner, and J. C. Leroux, "Preparation of polyion complex micelles from poly(ethylene glycol)-block-polyions," *Journal of Controlled Release*, vol. 156, no. 2, pp. 118–127, 2011. doi: 10.1016/j.jconrel.2011.07.027 .

[78] G. Allegri, J. Huskens, R. P. Martinho, and S. Lindhoud, "Distribution of polyelectrolytes and counterions upon polyelectrolyte complexation," *Journal of Colloid and Interface Science*, vol. 672, pp. 654–663, 2024. doi: 10.1016/j.jcis.2024.06.062 .

[79] T. D. Vogelaar, S. M. Szostak, and R. Lund, "Coacervation in Slow Motion: Kinetics of Complex Micelle Formation Induced by the Hydrolysis of an Antibiotic Prodrug," *Molecular Pharmaceutics*, vol. 21, no. 8, pp. 4157–4168, 2024. doi: 10.1021/acs.molpharmaceut.4c00579 .

[80] O. Kuzminskaya, S. Riemer, R. Dalgliesh, L. Almásy, I. Hoffmann, and M. Gradzielski, "Structure and Phase Behaviour of Interpolyelectrolyte Complexes of PDADMAC and Hydrophobically Modified PAA (HM-PAA)," *Macromolecular Chemistry and Physics*, p. 2200276, 2022. doi: 10.1002/macp.202200276 .

[81] S. Antoun, J.-F. Gohy, and R. Jérôme, "Micellization of quaternized poly(2-(dimethylamino)ethyl methacrylate)-block-poly(methyl methacrylate) copolymers in water," *Polymer*, vol. 42, no. 8, pp. 3641–3648, 2001. doi: https://doi.org/10.1016/S0032-3861(00)00746-1 .

[82] D. Stawski and A. Nowak, "Thermal properties of poly(N,N-dimethylaminoethyl methacrylate)," *PLoS ONE*, vol. 14, no. 6, 2019. doi: 10.1371/journal.pone.0217441 .

[83] M. R. Telaretti Leggieri, T. Kaldéus, M. Johansson, and E. Malmström, "PDMAEMA from α to ω chain ends: tools for elucidating the structure of poly(2-(dimethylamino)ethyl methacrylate)," *Polymer Chemistry*, vol. 14, no. 11, pp. 1241–1253, 2023. doi: 10.1039/d2py01604d .

[84] X. Han, Z. Xiong, X. Zhang, and H. Liu, "Multi-tunable self-assembled morphologies of stimuli-responsive diblock polyampholyte films on solid substrates," *Soft Matter*, vol. 11, no. 11, pp. 2139–2146, 2015. doi: 10.1039/c5sm00025d .

[85] B. Hofs, I. K. Voets, A. de Keizer, and M. A. Cohen Stuart, "Comparison of complex coacervate core micelles from two diblock copolymers or a single diblock copolymer with a polyelectrolyte," *Physical Chemistry Chemical Physics*, vol. 8, pp. 4242–4251, 2006. doi: 10.1039/B605695D .

[86] Y. Li, T. K. Bronich, P. S. Chelushkin, and A. V. Kabanov, "Dynamic properties of block ionomer complexes with polyion complex cores," *Macromolecules*, vol. 41, no. 15, pp. 5863–5868, 2008. doi: 10.1021/ma702671w .

[87] S. Holappa, L. Kantonen, T. Andersson, F. Winnik, and H. Tenhu, "Overcharging of polyelectrolyte complexes by the guest polyelectrolyte studied by fluorescence spectroscopy," *Langmuir*, vol. 21, no. 24, pp. 11 431–11 438, 2005. doi: 10.1021/la051866r .

[88] Z. Gao, X.-F. Zhong, and A. Eisenberg, "Chain Dynamics in Coronas of Ionomer Aggregates," *Macromolecules*, vol. 27, no. 3, pp. 794–802, 1994. doi: 10.1021/ma00081a026 .

[89] J. Adelsberger, A. Kulkami, A. Jain, W. Wang, A. M. Bivigou-Koumba, P. Busch, V. Pipich, O. Holderer, T. Hellweg, A. Laschewsky, P. Müller-Buschbaum, and C. M. Papadakis, "Thermoresponsive PS-b-PNIPAM-b-PS Micelles: Aggregation behavior, segmental dynamics, and thermal response," *Macromolecules*, vol. 43, no. 5, pp. 2490–2501, 2010. doi: 10.1021/ma902714p .

[90] S. Ray, N. Singh, R. Kumar, K. Patel, S. Pandey, D. Datta, J. Mahato, R. Panigrahi, A. Navalkar, S. Mehra, L. Gadhe, D. Chatterjee, A. S. Sawner, S. Maiti, S. Bhatia, J. A. Gerez, A. Chowdhury, A. Kumar, R. Padinhateeri, R. Riek, G. Krishnamoorthy, and S. K. Maji, "α-Synuclein aggregation nucleates through liquid–liquid phase separation," *Nature Chemistry*, vol. 12, no. 8, pp. 705–716, 2020. doi: 10.1038/s41557-020-0465-9 .

[91] S. Kim, W. B. Lee, N. R. de Souza, and S. H. Choi, "QENS study on local segmental dynamics of polyelectrolytes in complex coacervates," *Polymer*, vol. 264, 2023. doi: 10.1016/j.polymer.2022.125525 .

[92] A. T. Boothroyd, *Principles of Neutron Scattering from Condensed Matter*. Oxford University Press, 2020. doi: 10.1093/oso/9780198862314.001.0001 .

[93] G. L. Squires, *Introduction to the Theory of Thermal Neutron Scattering*, 3rd ed. Cambridge University Press, 2012. [Online]. Available: https://www.osti.gov/biblio/6632171

[94] D. Sivia, *Elementary Scattering Theory: For X-ray and Neutron Users*. Oxford University Press, 2011. doi: 10.1093/acprof:oso/9780199228676.001.0001 .

[95] X. S. Brems, S. Mühlbauer, and R. Cubitt, "Pushing the limits of accessible length scales via a modified Porod analysis in small-angle neutron scattering on ordered systems," *Journal of Applied Crystallography*, vol. 57, no. 5, pp. 1358–1372, 2024. doi: 10.1107/S1600576724007295 .

[96] G. Beaucage, "Approximations Leading to a Unified Exponential/Power-Law Approach to Small-Angle Scattering," *Journal of Applied Crystallography*, vol. 28, no. 6, pp. 717–728, 1995. doi: 10.1107/s0021889895005292 .

[97] ——, "Small-angle scattering from polymeric mass fractals of arbitrary mass-fractal dimension," *Journal of Applied Crystallography*, vol. 29, no. 2, pp. 134–146, 1996. doi: 10.1107/S0021889895011605 .

[98] B. Hammouda, "Analysis of the Beaucage model," *Journal of Applied Crystallography*, vol. 43, no. 6, pp. 1474–1478, 2010. doi: 10.1107/S0021889810033856 .

[99] "Sasview documentation," http://www.sasview.org/.

[100] I. Breßler, J. Kohlbrecher, and A. F. Thünemann, "*SASfit*: a tool for small-angle scattering data analysis using a library of analytical expressions," *Journal of Applied Crystallography*, vol. 48, no. 5, pp. 1587–1598, 2015. doi: 10.1107/S1600576715016544 .

[101] T. Ando, T. N. Vu, T. Nishimura, R. Takahashi, and S. I. Yusa, "Synthesis and Characterization of Polyion Complex Micelles with Glycopolymer Shells for Drug Delivery Carriers," *Langmuir*, no. 49, 2024. doi: 10.1021/acs.langmuir.4c03795 .

[102] R. Pires-Oliveira, J. Tang, A. M. Percebom, C. L. Petzhold, K. C. Tam, and W. Loh, "Effect of Molecular Architecture and Composition on the Aggregation Pathways of POEGMA Random Copolymers in Water," *Langmuir*, vol. 36, no. 49, pp. 15 018–15 029, 2020. doi: 10.1021/acs.langmuir.0c02538 .

[103] E. Atay, M. J. Fabra, M. Martínez-Sanz, L. G. Gomez-Mascaraque, A. Altan, and A. Lopez-Rubio, "Development and characterization of chitosan/gelatin electrosprayed microparticles as food grade delivery vehicles for anthocyanin extracts," *Food Hydrocolloids*, vol. 77, pp. 699–710, 2018. doi: 10.1016/j.foodhyd.2017.11.011 .

[104] K. S. Singwi and A. Sjölander, "Diffusive motions in water and cold neutron scattering," *Physical Review*, vol. 119, no. 3, 1960. doi: 10.1103/PhysRev.119.863 .

[105] F. Volino, J. C. Perrin, and S. Lyonnard, "Gaussian model for localized translational motion: Application to incoherent neutron scattering," *Journal of Physical Chemistry B*, vol. 110, no. 23, 2006. doi: 10.1021/jp061103s .

[106] F. Mezei, "Neutron spin echo: A new concept in polarized thermal neutron techniques," *Zeitschrift für Physik A Hadrons and nuclei*, vol. 255, pp. 146–160, 1972. doi: 10.1007/BF01394523 .

[107] G. Williams and D. C. Watts, "Non-symmetrical dielectric relaxation behaviour arising from a simple empirical decay function," *Transactions of the Faraday society*, vol. 66, pp. 80–85, 1970. doi: 10.1039/TF9706600080 .

[108] R. R. Cheng, A. T. Hawk, and D. E. Makarov, "Exploring the role of internal friction in the dynamics of unfolded proteins using simple polymer models," *Journal of Chemical Physics*, vol. 138, no. 7, 2013. doi: 10.1063/1.4792206 .

[109] B. S. Khatri and T. C. McLeish, "Rouse model with internal friction: A coarse grained framework for single biopolymer dynamics," *Macromolecules*, vol. 40, no. 18, pp. 6770–6777, 2007. doi: 10.1021/ma071175x .

[110] O. Kuzminskaya, "Solubilisation of organic compounds of different polarity by interpolyelectrolyte complexes based on copolymer micelles," Ph.D. dissertation, Technische Universität Berlin, Berlin, 2023. doi: 10.14279/depositonce-17060 .

[111] A. Sokolova, A. E. Whitten, L. de Campo, J. Christoforidis, A. Eltobaji, J. Barnes, F. Darmann, and A. Berry, "Performance and characteristics of the BILBY time-of-flight small-angle neutron scattering instrument," *J. Appl. Cryst.*, vol. 52, no. 1, pp. 1–12, 2019. doi: 10.1107/S1600576718018009 .

[112] M. Chamchoum, O. Czakkel, S. Prevost, and M. Gradzielski, *Characterization of the structure and dynamics of the hydrophobic domains in interpolyelectrolyte complexes*. Institut Laue-Langevin (ILL) doi:10.5291/ILL-DATA.9-11-2116, 2023.

[113] M. Darge, A. Das, N. Martin, A. W. G. Michel-Busch, and M. Gradzielski, *The Effect of Surfactant Addition on the Structure of Hydrophobically Modified Interpolyelectrolyte Complexes (IPECs)*. Institut Laue-Langevin (ILL) doi:10.5291/ILL-DATA.9-11-2223, 2024.

[114] M. Chamchoum, O. Czakkel, T. Seydel, S. Prevost, and M. Gradzielski, *Characterization of the dynamics of interpolyelectrolyte complexes*. Institut Laue-Langevin (ILL) doi:10.5291/ILL-DATA.9-11-2151, 2024.

[115] C. J. Garvey, B. P. Kumar, K. A. Ramya, and V. Apostolos, *Concentration, pH and ionic strength dependence of Mucin polymer coilconformation.*. Institut Laue-Langevin (ILL) doi:10.5291/ILL-DATA.8-03-1098, 2024.

[116] M. Chamchoum, O. Czakkel, S. Prevost, and M. Gradzielski, *Characterization of the dynamics of interpolyelectrolyte complexes for different mixing ratios.* Institut Laue-Langevin (ILL) doi:10.5291/ILL-DATA.TEST-3314, 2023.

[117] M. A. De Jesús-Téllez, D. M. Sánchez-Cerrillo, P. Quintana-Owen, U. S. Schubert, D. Contreras-López, and C. Guerrero-Sánchez, "Kinetic investigations of quaternization reactions of poly[2-(dimethylamino)ethyl methacrylate] with diverse alkyl halides," *Macromolecular Chemistry and Physics*, vol. 221, no. 9, p. 1900543, 2020. doi: https://doi.org/10.1002/macp.201900543 .

[118] H. Lee, S. H. Son, R. Sharma, and Y. Y. Won, "A discussion of the ph-dependent protonation behaviors of poly(2-(dimethylamino)ethyl methacrylate) (pdmaema) and poly(ethylenimine-ran-2-ethyl-2-oxazoline) (p(ei-r-eoz))," *Journal of Physical Chemistry B*, vol. 115, no. 5, pp. 844–860, 2011. doi: 10.1021/jp109151s .

[119] P. Van de Wetering, N. J. Zuidam, M. J. Van Steenbergen, O. A. G. J. van der Houwen, W. J. M. Underberg, and W. E. Hennink, "A mechanistic study of the hydrolytic stability of poly(2-(dimethylamino)ethyl methacrylate)," *Macromolecules*, vol. 31, no. 23, pp. 8063–8068, 1998. doi: 10.1021/ma980689g .

[120] R. Yañez-Macias, I. Alvarez-Moises, I. Perevyazko, A. Lezov, R. Guerrero-Santos, U. S. Schubert, and C. Guerrero-Sanchez, "Effect of the Degree of Quaternization and Molar Mass on the Cloud Point of Poly[2-(dimethylamino)ethyl methacrylate] Aqueous Solutions: A Systematic Investigation," *Macromolecular Chemistry and Physics*, vol. 218, no. 10, 2017. doi: 10.1002/macp.201700065 .

[121] S. H. Min, S. K. Kwak, and B. S. Kim, "Atomistic simulation for coil-to-globule transition of poly(2-dimethylaminoethyl methacrylate)," *Soft Matter*, vol. 11, no. 12, pp. 2423–2433, 2015. doi: 10.1039/c4sm02242d .

[122] B. D. Ermi and E. J. Amis, "Domain Structures in Low Ionic Strength Polyelectrolyte Solutions," *Macromolecules*, vol. 31, no. 21, pp. 7378–7384, 1998. doi: 10.1021/ma980579+ . [Online]. Available: https://doi.org/10.1021/ma980579+

[123] E. Spruijt, F. A. Leermakers, R. Fokkink, R. Schweins, A. A. Van Well, M. A. Cohen Stuart, and J. Van Der Gucht, "Structure and dynamics of polyelectrolyte complex coacervates studied by scattering of neutrons, X-rays, and light," *Macromolecules*, vol. 46, no. 11, pp. 4596–4605, 2013. doi: 10.1021/ma400132s .

[124] J. K. Percus and G. J. Yevick, "Analysis of Classical Statistical Mechanics by Means of Collective Coordinates," *Physical Review*, vol. 110, no. 1, 1958. doi: 10.1103/PhysRev.110.1 .

[125] N. W. Ashcroft and J. Lekner, "Structure and resistivity of liquid metals," *Physical Reviews*, vol. 145, pp. 83–90, 1966. doi: 10.1103/PhysRev.145.83 .

[126] T. Noda and Y. Morishima, "Hydrophobic association of random copolymers of sodium 2-(acrylamido)-2-methylpropanesulfonate and dodecyl methacrylate in water as studied by fluorescence and dynamic light scattering," *Macromolecules*, vol. 32, no. 14, pp. 4631–4640, 1999. doi: 10.1021/ma990202j .

[127] Tanford, "Micelle Shape and Size," *The Journal of Physical Chemistry*, vol. 392, no. 21, p. 29, 1964. doi: 10.1021/j100665a018 .

[128] M. Uchman, M. Štěpánek, S. Prévost, B. Angelov, J. Bednár, M.-S. Appavou, M. Gradzielski, and K. Procházka, "Coassembly of poly(ethylene oxide)-block-poly(methacrylic acid) and n-dodecylpyridinium chloride in aqueous solutions leading to ordered micellar assemblies within copolymer aggregates," *Macromolecules*, vol. 45, no. 16, pp. 6471–6480, 2012. doi: 10.1021/ma301510j .

[129] C. Tondre and R. Zana, "Apparent molal volumes of polyelectrolytes in aqueous solutions," *The Journal of Physical Chemistry*, vol. 76, no. 23, pp. 3451–3459, 1972. doi: 10.1021/j100667a026 .

[130] B. Jerman, M. Breznik, K. Kogej, and S. Paoletti, "Osmotic and volume properties of stereoregular poly(methacrylic acids) in aqueous solution: Role of intermodular association," *Journal of Physical Chemistry B*, vol. 111, no. 29, pp. 8435–8443, 2007. doi: 10.1021/jp0676080 .

[131] B. Hofs, A. De Keizer, and M. A. Stuart, "On the stability of (highly aggregated) polyelectrolyte complexes containing a charged-block-neutral diblock copolymer," *Journal of Physical Chemistry B*, vol. 111, no. 20, pp. 5621–5627, 2007. doi: 10.1021/jp0714318 .

[132] M. Sedlák, v. Koňák, P. Štěpánek, and J. Jakeš, "Semidilute solutions of poly(methacrylic acid) in the absence of salt: Dynamic light-scattering study," *Polymer*, vol. 28, no. 6, 1987. doi: 10.1016/0032-3861(87)90156-X .

[133] B. Hammouda, *SANS from homogeneous polymer mixtures: A unified overview.* Berlin, Heidelberg: Springer Berlin Heidelberg, 1993, pp. 87–133. doi: 10.1007/BFb0025862 .

[134] J. Teixeira, "Small-angle scattering by fractal systems," *Journal of Applied Crystallography*, vol. 21, no. 6, pp. 781–785, 1988. doi: 10.1107/S0021889888000263 .

[135] A. Stenstam, G. Montalvo, I. Grillo, and M. Gradzielski, "Small angle neutron scattering study of lysozyme-sodium dodecyl sulfate aggregates," *Journal of Physical Chemistry B*, vol. 107, no. 44, pp. 12 331–12 338, 2003. doi: 10.1021/jp0352783 .

[136] B. H. Zimm, "Apparatus and Methods for Measurement and Interpretation of the Angular Variation of Light Scattering; Preliminary Results on Polystyrene Solutions," *The Journal of Chemical Physics*, vol. 16, no. 12, pp. 1099–1116, 1948. doi: 10.1063/1.1746740 .

[137] J. S. Pedersen, "Determination of Size Distributions from Small-Angle Scattering Data for Systems with Effective Hard-Sphere Interactions," *Journal of Applied Crystalography*, vol. 27, pp. 595–608, 1994. doi: 10.1107/S0021889893013810 .

[138] N. Carl, S. Prévost, R. Schweins, and K. Huber, "Ion-selective binding as a new trigger for micellization of block copolyelectrolytes with two anionic blocks," *Soft Matter*, vol. 15, no. 41, pp. 8266–8271, 2019. doi: 10.1039/c9sm01138b .

[139] S. W. Provencher, "Contin: A general purpose constrained regularization program for inverting noisy linear algebraic and integral equations," *Comp. Phys. Comm.*, vol. 27, no. 3, pp. 229–242, 1982. doi: https://doi.org/10.1016/0010-4655(82)90174-6 .

[140] A. Scotti, W. Liu, J. S. Hyatt, E. S. Herman, H. S. Choi, J. W. Kim, L. A. Lyon, U. Gasser, and A. Fernandez-Nieves, "The CONTIN algorithm and its application to determine the size distribution of microgel suspensions," *Journal of Chemical Physics*, vol. 142, no. 23, p. 234905, 2015. doi: 10.1063/1.4921686 .

[141] O. Anthony and R. Zana, "Interactions between water-soluble polymers and surfactants: Effect of the polymer hydrophobicity. 2. amphiphilic polyelectrolytes (polysoaps)," *Langmuir*, vol. 12, no. 15, pp. 3590–3597, 1996. doi: 10.1021/la960184o .

[142] U. P. Strauss and N. L. Gershfeld, "The transition from typical polyelectrolyte to polysoap. i. viscosity and solubilization studies on copolymers of 4-vinyl-n-ethylpyridinium bromide and 4-vinyl-nn-dodecylpyridinium bromide," *The Journal of Physical Chemistry*, vol. 58, no. 9, pp. 747–753, 1954. doi: 10.1021/j150519a013 .

[143] F. Horkay, P. Falus, A. M. Hecht, and E. Geißler, "Length scale dependence of the dynamic properties of hyaluronic acid solutions in the presence of salt," *Journal of Physical Chemistry B*, vol. 114, no. 47, 2010. doi: 10.1021/jp106578f .

[144] Raymond M. Fuoss and Hussein Sadek, "Mutual Interaction of Polyelectrolytes," *Science*, vol. 110, pp. 552–554, 1949. doi: 10.1126/science.110.2865.552 .

[145] W. S. Loo, A. Faraone, L. S. Grundy, K. W. Gao, and N. P. Balsara, "Polymer Dynamics in Block Copolymer Electrolytes Detected by Neutron Spin Echo," *ACS Macro Letters*, vol. 9, no. 5, pp. 639–645, 5 2020. doi: 10.1021/acsmacrolett.0c00236 .

[146] J. M. Y. Carrillo and A. V. Dobrynin, "Polyelectrolytes in salt solutions: Molecular dynamics simulations," *Macromolecules*, vol. 44, no. 14, pp. 5798–5816, 2011. doi: 10.1021/ma2007943 .

[147] P. Anton and A. Laschewsky, "Solubilization by polysoaps," *Colloid and Polymer Science*, vol. 272, no. 9, pp. 1118–1128, 1994. doi: 10.1007/BF00652381 .

[148] X. Li, M. Zamponi, K. Hong, L. Porcar, C. Y. Shew, T. Jenkins, E. Liu, G. S. Smith, K. W. Herwig, Y. Liu, and W. R. Chen, "PH Responsiveness of polyelectrolyte dendrimers: A dynamical perspective," *Soft Matter*, vol. 7, no. 2, pp. 618–622, 2011. doi: 10.1039/c0sm00671h .

[149] B. Wu, Y. Liu, X. Li, E. Mamontov, A. I. Kolesnikov, S. O. Diallo, C. Do, L. Porcar, K. Hong, S. C. Smith, L. Liu, G. S. Smith, T. Egami, and W. R. Chen, "Charge-dependent dynamics of a polyelectrolyte dendrimer and its correlation with invasive water," *Journal of the American Chemical Society*, vol. 135, no. 13, pp. 5111–5117, 2013. doi: 10.1021/ja3125959 .

[150] S. V. Ghugare, E. Chiessi, M. T. F. Telling, A. Deriu, Y. Gerelli, J. Wuttke, and G. Paradossi, "Structure and dynamics of a thermoresponsive microgel around its volume phase transition temperature," *The Journal of Physical Chemistry B*, vol. 114, no. 32, pp. 10 285–10 293, 2010. doi: 10.1021/jp100962p .

[151] B. Frick, E. Mamontov, L. Van Eijck, and T. Seydel, "Recent backscattering instrument developments at the ILL and SNS," *Zeitschrift für Physikalische Chemie*, vol. 224, no. 1-2, pp. 33–60, 2010. doi: 10.1524/zpch.2010.6091 .

[152] I. Mosca, K. Pounot, C. Beck, L. Colin, O. Matsarskaia, C. Grapentin, T. Seydel, and F. Schreiber, "Biophysical Determinants for the Viscosity of Concentrated Monoclonal Antibody Solutions," *Molecular Pharmaceutics*, vol. 20, no. 9, pp. 4698–4713, 2023. doi: 10.1021/acs.molpharmaceut.3c00440 .

[153] M. Grimaldo, F. Roosen-Runge, F. Zhang, F. Schreiber, and T. Seydel, "Dynamics of proteins in solution," *Quarterly Reviews of Biophysics*, vol. 52, p. e7, 2019. doi: 10.1017/s0033583519000027 .

[154] J. Colmenero, A. Arbe, F. Alvarez, A. Narros, D. Richter, M. Monkenbusch, and B. Farago, "Hydrogen motions and the α-relaxation in glass-forming polymers: Molecular dynamics simulation and quasi-elastic neutron scattering results," *Pramana - Journal of Physics*, vol. 63, no. 1, 2004. doi: 10.1007/BF02704047 .

[155] A. Narros, F. Alvarez, A. Arbe, J. Colmenero, D. Richter, and B. Farago, "Hydrogen motions in the α-relaxation regime of poly(vinyl ethylene): A molecular dynamics simulation and neutron scattering study," *Journal of Chemical Physics*, vol. 121, no. 7, 2004. doi: 10.1063/1.1772761 .

[156] A. Arbe, F. Alvarez, and J. Colmenero, "Neutron scattering and molecular dynamics simulations: Synergetic tools to unravel structure and dynamics in polymers," *Soft Matter*, vol. 8, no. 32, pp. 8257–8270, 2012. doi: 10.1039/c2sm26061a .

[157] A.-C. Genix and J. Oberdisse, "On the absence of structure factors in concentrated colloidal suspensions and nanocomposites," *The European Physical Journal E*, vol. 46, no. 6, p. 46, 2023.

[158] S. Fujiwara, "Dynamical Behavior of Disordered Regions in Disease-Related Proteins Revealed by Quasielastic Neutron Scattering," *Medicina (Lithuania)*, vol. 58, no. 6, 2022. doi: 10.3390/medicina58060795 .

[159] D. J. Bicout, "Influence of environment fluctuations on incoherent neutron scattering functions," *Physical Review E - Statistical Physics, Plasmas, Fluids, and Related Interdisciplinary Topics*, vol. 64, no. 1, 2001. doi: 10.1103/PhysRevE.64.011910 .

[160] A. M. Stadler, I. Digel, J. P. Embs, T. Unruh, M. Tehei, G. Zaccai, G. Büldt, and G. M. Artmann, "From powder to solution: Hydration dependence of human hemoglobin dynamics correlated to body temperature," *Biophysical Journal*, vol. 96, no. 12, 2009. doi: 10.1016/j.bpj.2009.03.043 .

[161] M. Bee, *Quasielastic neutron scattering*. Bristol: IOP Publishing Ltd, 1988. [Online]. Available: https://inis.iaea.org/records/y543b-r9h40

[162] M. Bée, "A physical insight into the elastic incoherent structure factor," *Physica B: Physics of Condensed Matter*, vol. 182, no. 4, 1992. doi: 10.1016/0921-4526(92)90034-P .

[163] M. Grimaldo, F. Roosen-Runge, M. Hennig, F. Zanini, F. Zhang, N. Jalarvo, M. Zamponi, F. Schreiber, and T. Seydel, "Hierarchical molecular dynamics of bovine serum albumin in concentrated aqueous solution below and above thermal denaturation," *Physical Chemistry Chemical Physics*, vol. 17, no. 6, pp. 4645–4655, 2015. doi: 10.1039/c4cp04944f .

[164] F. Fernandez-Alonso and D. L. Price, *Neutron Scattering–Applications in Biology, Chemistry, and Materials Science*. Elsevier, 2017. [Online]. Available: https://shop.elsevier.com/books/neutron-scattering-applications-in-biology-chemistry-and-materials-science/fernandez-alonso/978-0-12-805324-9

[165] M. Hennig, F. Roosen-Runge, F. Zhang, S. Zorn, M. W. Skoda, R. M. Jacobs, T. Seydel, and F. Schreiber, "Dynamics of highly concentrated protein solutions around the denaturing transition," *Soft Matter*, vol. 8, no. 5, 2012. doi: 10.1039/c1sm06609a .

[166] J. O. Daldrop, J. Kappler, F. N. Brünig, and R. R. Netz, "Butane dihedral angle dynamics in water is dominated by internal friction," *Proceedings of the National Academy of Sciences of the United States of America*, vol. 115, no. 20, 2018. doi: 10.1073/pnas.1722327115 .

[167] J. J. Portman, S. Takada, and P. G. Wolynes, "Microscopic theory of protein folding rates. II. Local reaction coordinates and chain dynamics," *Journal of Chemical Physics*, vol. 114, no. 11, 2001. doi: 10.1063/1.1334663 .

[168] D. Das and S. Mukhopadhyay, "Molecular Origin of Internal Friction in Intrinsically Disordered Proteins," *Accounts of Chemical Research*, vol. 55, no. 23, 2022. doi: 10.1021/acs.accounts.2c00528 .

[169] H. Nakagawa, M. S. Appavou, J. Wuttke, M. Zamponi, O. Holderer, T. E. Schrader, D. Richter, and W. Doster, "Nanosecond structural dynamics of intrinsically disordered β-casein micelles by neutron spectroscopy," *Biophysical Journal*, vol. 120, no. 23, pp. 5408–5420, 2021. doi: 10.1016/j.bpj.2021.10.032 .

[170] L. Verlet, "Computer "experiments" on classical fluids. i. thermodynamical properties of lennard-jones molecules," *Phys. Rev.*, vol. 159, pp. 98–103, 1967. doi: 10.1103/PhysRev.159.98 .

[171] N. Metropolis, A. W. Rosenbluth, M. N. Rosenbluth, A. H. Teller, and E. Teller, "Equation of state calculations by fast computing machines," *The Journal of Chemical Physics*, vol. 21, no. 6, pp. 1087–1092, 1953. doi: 10.1063/1.1699114 .

[172] W. Humphrey, A. Dalke, and K. Schulten, "VMD – Visual Molecular Dynamics," *Journal of Molecular Graphics*, vol. 14, no. 1, pp. 33–38, 1996. doi: 10.1016/0263-7855(96)00018-5 .

[173] A. P. Thompson, H. M. Aktulga, R. Berger, D. S. Bolintineanu, W. M. Brown, P. S. Crozier, P. J. in 't Veld, A. Kohlmeyer, S. G. Moore, T. D. Nguyen, R. Shan, M. J. Stevens, J. Tranchida, C. Trott, and S. J. Plimpton, "LAMMPS - a flexible simulation tool for particle-based materials modeling at the atomic, meso, and continuum scales," *Computational Physics Communications*, vol. 271, p. 108171, 2022. doi: 10.1016/j.cpc.2021.108171 .

[174] C. M. Sorensen, "Light scattering by fractal aggregates: A review," *Aerosol Science and Technology*, vol. 35, no. 2, pp. 648–687, 2001. doi: 10.1080/02786820117868 .

[175] A. J. Hurd and W. L. Flower, "In situ growth and structure of fractal silica aggregates in a flame," *Journal of Colloid and Interface Science*, vol. 122, no. 1, pp. 178–192, 1988. doi: 10.1016/0021-9797(88)90301-3 .

[176] M. Simon, P. Krause, L. Chiappisi, L. Noirez, and M. Gradzielski, "Structural control of polyelectrolyte/microemulsion droplet complexes (PEMECs) with different polyacrylates," *Chemical Science*, vol. 10, no. 2, pp. 385–397, 2019. doi: 10.1039/C8SC04013C .

[177] M. Simon, E. Schneck, L. Noirez, S. Rahn, I. Davidovich, Y. Talmon, and M. Gradzielski, "Effect of polymer architecture on the phase behavior and structure of polyelectrolyte/microemulsion complexes (PEMECs)," *Macromolecules*, vol. 53, no. 10, pp. 4055–4067, 2020. doi: 10.1021/acs.macromol.0c00236 .

[178] E. Kostyurina, J. U. De Mel, A. Vasilyeva, M. Kruteva, H. Frielinghaus, M. Dulle, L. Barnsley, S. Förster, G. J. Schneider, R. Biehl, and J. Allgaier, "Controlled lcst behavior and structure formation of alternating amphiphilic copolymers in water," *Macromolecules*, vol. 55, no. 5, pp. 1552–1565, 2022. doi: 10.1021/acs.macromol.1c02324 .

[179] J. H. Chen, L. Q. Lu, H. X. Zhao, Y. Yang, X. Shu, and Q. P. Ran, "Conformational Properties of Comb-shaped Polyelectrolytes with Negatively Charged Backbone and Neutral Side Chains Studied by a Generic Coarse-grained Bead-and-Spring Model," *Chinese Journal of Polymer Science (English Edition)*, vol. 38, no. 4, pp. 371–381, 2020. doi: 10.1007/s10118-020-2350-9 .